Cyclic variability of flame propagation and autoignition in supercharged and naturally aspirated SI engines

by

Graham Thomas Conway

BEng (Hons) MSc

Submitted in accordance with the requirements
for the degree of Doctor of Philosophy

UNIVERSITY OF LEEDS

School of Mechanical Engineering

August 2013

For Tom and Gwen

Acknowledgements

Here I identify and acknowledge those who have, in some way, contributed to the completion of this thesis. As you're wondering... yes! The length of this section is a true and representative reflection of the magnitude of support that has been wholly necessary in the culmination of this thesis.

- Horror stories from students who never see their supervisors, are pushed down the wrong path, or lambasted at every opportunity are common. I am pleased to say however, that my supervisor, Dr Alexey Burluka, Alex, is none of these; I could have asked for no better. In addition to the general discussion about combustion research; the conversations on Soviet Union history as well as discussions on bureaucracy, were personal highlights.

- I also wish to acknowledge Prof Chris Sheppard, although unfortunately my arrival coincided with his departure, I hold the information I was able to gleam from him in the highest regard.

- An unreserved thank you must go to my new colleagues in the Engines team at SMTC UK (most notably Iain Fleming for giving me time off to complete this work). Their understanding and commitment to my Ph.D. has, in short, allowed this work to be realised. With special thanks to George Houghton and George Corfield for offering to read this work in the quest for finding errors; in doing so, highlighting the deficiency that a spell-checker cannot differentiate, in context, between assess and asses.

- Jaguar Land Rover and the UltraBoost consortium for providing a fantastic opportunity to be a part of a cutting-edge research topic, as well as for the financial support. It was an invaluable insight into how the "real" world works. On that note, I must thank the University of Bath for providing a significant portion of Jaguar data to this project.

- The combustion group at Leeds comprises many able students who I have had the privilege of working alongside. I will refrain, mostly, from individual accolades, however I thank: Ahmed, Markous, Tawfiq, Navanshu, Amin, Faraz, Nini and Dominic. I must distinguish Mr Zhengyang Ling from the other students for two reason. Firstly, he provided a significant portion of the experimental data to this work. Secondly, he may well be my boss one day... soon. I also thank Dr Phil Roberts for "showing me the ropes" when I arrived, and for a willingness to discuss engines outside of work (to the detriment of social situations).

- Thanks to the IT staff at the School of Mechanical engineering for accommodating requests, no matter how trivial. A special thank you goes to John Hodrien for being a font of knowledge on all things "LINUXy"

- Thanks to the technical staff in the engine laboratory. Although, primarily situated at a work station I have ventured into the noisy bit on occasion and found the staff to be accommodating whenever a request has been made

- Jon, James; thanks for making sure I remained motivated. *"So motivated you don't even know."*

- My housemates, with whom I spent 2 very enjoyable years of my Ph.D., rightly get a special mention: To Heskey, thanks for being a source of enlightening conversation and introducing me to the delights of being "triangled". To Rick, thanks for the well stocked fridge and freezer (especially the Fabs) and for "putting me up" this year, where possible. To Dave, *thank you*. Additionally I must thank Mike and Steff for offering me the spare room in their humble abode.

Finally, (its outside of bullet points so it must be *really* important) I feel indebted to my family for providing support both emotionally and, perhaps more obviously, financially over the last 8 years of my "higher" education. Mum, Dad, Laura... Thank you. I can only apologise for the appearance of being AWOL this year and hope it will be the exception.

Abstract

The ever-changing demands from consumers for more fuel efficient vehicles necessitates automotive manufacturers developing ever more radical proposals for engine design. The latest trend from manufacturers is engine "downsizing"; where a smaller, more efficient, engine is pressure-charged to recoup the lost full-load performance. An effect of downsizing is that engines now run at significant intake pressures. Additionally, implementation of simulation techniques as an integral part of the research and design process is becoming commonplace in the automotive industry. Whether or not current models can be considered reliable for combustion prediction at significantly elevated pressures, such as those experienced by downsized engines, is a main focus of the current work, predominantly assessed through how the crank-resolved in-cylinder pressure traces from prediction, compare to experiment. Experimental data was provided by four different engines: two Jaguar Land Rover multi-cylinder engines, one naturally aspirated, the other heavily downsized, and two University of Leeds bespoke research engines operating under naturally aspirated, or high pressure conditions representative of downsized engines.

It was seen that the combustion models were not able to accurately predict combustion at different pressures without adjustment of the turbulence quantities, namely the length scale used to define the "after-burning" process. Additionally, it is known that variability of combustion limits the performance of engines significantly; a better understanding of variability which may lead to mitigation methods would result in significant efficiency gains. The magnitude of variability in the four different engines is investigated in this work as well as the current capability in predicting the variability. Once a mean cycle was successfully matched, the variability of the engine cycles is accurately predicted for all engines and conditions by a random-number model, invoking variability on two parameters, u' and ϕ, with Gaussian distribution. Moreover a novel method for assessing variability is proposed and is employed in a study to assess the influence of combustion variability at different stages of combustion. The variability of the combustion event was seen to be a strong function of the very early stages of combustion.

The propensity for autoignition is also known to increase with operating pressure and temperature. The predictive capability, of two autoignition models, was assessed against experimental data. It was observed that a chemical kinetic based autoignition model was more able to predict autoignition over all engines, vis-á-vis an empirically based model. In addition, it was also seen that a variability of autoignition within the engine existed, which was independent of burning rate. Finally, "knocking" cycles were identified within the heavily supercharged, multi-cylinder research engine which defined the calibration limit of the engine. It was seen, however, that the frequency of pressure oscillations was beyond that traditionally seen for knock cycles.

Contents

List of Figures

List of Tables

Nomenclature

Roman and Greek Symbols

Symbol	Units	Description
A	m^2,	Area
A	–	Zimont burning velocity model constant
a	m/sec	Speed of sound in a gas
α	1/sec	Stretch rate
α	m^2/sec	Thermal diffusivity
C_{l_i}	–	Integral length scale constant
C_{l_λ}		Taylor scale length constant
δ_x		Flame thickness
D	m	Engine bore
D	m^2/sec	Mass diffusivity
Da	–	Damkhöler number
fr_b	m	Radius of burnt gas
fr_e	m	Radius of entrained gas (flame)
Ka	–	Karlovitz number
k	m^2/s^2	Turbulent kinetic energy
Le	–	Lewis number
l_i	m	Turbulent integral length scale
l_λ	m	Turbulent Taylor length scale
l_η	m	Turbulent Kolmogorov length scale
P	Pa	Pressure
ϕ	–	Equivalence Ratio
m	kg	Mass
$\dot{m}$	kg/sec	Mass flow rate
ρ	kg/ m^3	Density
r	m	Radius

R_e	-	Reynolds Number
T	K	Temperature
t	sec	Time
τ_{tq}	N/m	Brake torque
U	m/sec	Flow velocity
u	m/sec	Burning velocity
u'	m/sec	Rms turbulent velocity
u'_k	m/sec	Effective rms turbulent velocity
S_p	m/sec	Instantaneous piston speed
$\bar{S}_p$	m/sec	Mean piston speed

Abbreviations

aTDC	After top dead centre
bTDC	Before top dead centre
^{o}CA	Degrees of crank angle rotation
COV	Coefficient of variation
CR_{static}	Static compression ratio
$CR_{dynamic}$	Dynamic compression ratio
DAQ	Data acquisition
DNS	Direct numerical simulation
ECU	Electronic control unit
EGR	Exhaust gas recirculation
EPC/EVC	Exhaust port closure / exhaust valve closure
FFT	Fast fourier transform
fps	Frames per second
HCCI	Homogeneous charge compression ignition
HWA	Hot wire anemometry
IMEP	Indicated mean effective pressure
IPC/IVC	Intake port closure / intake valve closure
IPS	Instantaneous piston speed
K	Kalghatgi octane index correction factor
LDV	Laser doppler velocimetry
LES	Large eddy simulation

LSPI	Low speed pre-ignition
LUPOE1/2-D	Leeds university ported optical engine (Mk I/II) disc configuration
LUSIE	Leeds university spark ignition engine (simulation software)
LUSIEDA	Leeds university spark ignition engine data analysis
MATLAB	Matrix Laboratory
MBT	Maximum Brake Torque
MON	Motor octane number
MPS	Mean piston speed
NTC	Negative temperature coefficient
ON	Octane Number
PIV	Particle image velocimetry
PRF	Primary reference fuel
rev / min	Revolutions per minute
rms	Root mean square
RON	Research octane number
S	Fuel sensitivity
SI	Spark ignition
TDC	Top dead centre
TKE	Turbulent kinetic energy
VVT	Variable valve timing
VVL	Variable vale lift
WOT	Wide open throttle

Subscripts

b	–	Burned
i	–	Intake
l	–	Laminar
t	–	Turbulent
r	–	Reaction (burnt)
u	–	Unburned

Chapter 1

Topic introduction and scope of thesis

1.1 Background introduction

The conversion of chemical energy to mechanical output, via heat, was the cornerstone of the 19^{th} century industrial revolution; a process no less valued today. Heat engines in various forms are still an integral part of day-to-day life. For the overwhelming majority of people, the obvious application of heat engines is found in transportation medium. Indeed, it has been reported that, as of 2010, over 1 billion cars now occupy the world's roads (Sounasis [2013]). On that basis, even if industrial and military applications are omitted, the fuel consumption figure, from the commercial vehicle sector alone is likely to exceed the trillion litre mark, annually. Owing to the inefficiency of internal combustion engines (ICE), as limited by both the Second Law of Thermodynamics as well as the non-isochoric combustion event, a considerable amount of the chemical energy contained in the fuel is wasted into the atmosphere as heat. While, as consumers, we have largely become desensitised to figures of such immensity, the situation still presents a huge responsibility for engineers to attain engines which operate closer to their maximum potential efficiency.

Consumers, in addition to requesting high efficiency travel demand more refined vehicles with more equipment, better drive-ability, enhanced performance and reduced base costs. Combining this situation with the additional targets, set by governments, to improve emissions results in a challenging situation for engineers. In response to meeting these opposing demands (with regard to efficiency) engineers have developed radical concepts and strategies in an attempt to improve the overall vehicle performance. One such innovation is engine "Downsizing", whereby a smaller capacity engine takes the place of a larger capacity engine with the intent of improving part-load efficiencies while at the same time retaining full-load performance through "artificially" increasing the engine displacement with external boosting systems. The associated increase in pressure[1] is the primary focus of the reported work.

Ideally, to achieve efficiencies closer to theoretical limits, the combustion should be as close to isochoric (instantaneous) as possible. A faster time for combustion to be completed, τ_{comb} will increase the rate of heat release, Q, as the chemical release of energy will occur over a smaller change in volume, V, limited by $\lim_{\tau_{\text{comb}} \to 0}, \frac{dQ}{dV} = \infty$; therefore time available for heat to transfer out of the system is reduced and more of the work can be transferred to the piston at the optimum crank angle. Unfortunately the increased temperature in the cylinder will induce autoignition of the unburned fuel-air mixture (end-gas). Where this event is severe enough (as is common) a damaging pressure wave will evolve, referred to as "knock", which can significantly damage engine components to the point of failure. It can be seen that there must exist a combustion process, started at a given crank angle, which gives the fastest possible combustion, without increasing the temperature to a point where autoignition is induced.

Methods to increase the rate of the combustion process are, on the whole, well understood. For instance it is known that the rate at which the heat from the fuel is released is a strong function of the level of turbulence in the system as well as the fuel's "natural" rate of combustion through molecular diffusion of the active species into the reaction zone. Unfortunately it is not possible to assumed that the highest turbulence levels will result in the fastest combustion rates because of complexities in flame structure and quenching limits of the flame. A final point on the rate of combustion is that, a greater release of heat from the process is likely to, again, increase the propensity of

[1]Throughout the current work downsizing is intrinsically linked with an increase in pressure, where the phrase downsized appears it should be assumed that it is referring to increased pressure, unless otherwise stated.

knock (known to be a strong function of the pressure-temperature-time history of the end-gas[1]).

Variability of combustion is another key limitation to engine performance. To simplify, if it is assumed (quite reasonably) that the fastest burning cycle will be the one which demonstrates autoignition. The solution is to adjust the operating parameters to achieve a cycle which has a burn-rate to heat-release relationship which does not promote autoignition but, to satisfy efficiency, is as fast as possible. In the "real" world however, a large amount of normally distributed variability can be seen in an engine operating with fixed parameters. The situation now results in the efficiency being driven by the mean cycle, which will be significantly slower than the optimum (owing to the Gaussian nature of variability) which only a statistically low number of cycles are able to attain. The causes of variability have primarily been attributed to variations in the flow-field and air-fuel homogeneity and stoichiometry.

1.2 Scope of the current work

As introduced in Section 1.1, the occurrence of autoignition limits engine efficiency. Increases in efficiency could be realised for reduced variability which would enable faster mean burning rates. To achieve the latter, the influence of turbulence characteristics on the combustion process of gasoline-like fuel combustion requires further investigation. Indeed Lipatnikov [2012] declares "*Target-directed research into the influence of the turbulence length scale on the flame speed and burning velocity is strongly needed*". The causes of variability are thought to be well understood, however interactions of the different elements which make up ICE combustion: autoignition, variability, combustion rates and turbulence have not directly been assessed. In addition, with the advent of downsized engines, a new variable, that of pressure, is introduced. While the influence of pressure has been studied on individual elements, it would not be unfair to say that such investigations are somewhat sparse, occasionally provide contradictory results and are seldom studied at high initial pressures (approximately 50 bar) as seen in downsized engines at the start of combustion. Moreover the interaction between the elements may be different at higher and lower pressures.

[1]Although a greater amount of heat will be released from the fuel, a faster combustion rate will reduce the time upon which the temperature can affect the end-gas. Naturally, one of these mechanisms will dominate and determine the autoignition outcome, the non-proportionality of fuel-oxidation rates, as a function of temperature, greatly increasing the complexity

The majority of the work is to assess the fidelity of a well developed, quasi-dimensional thermodynamic model, LUSIE ([the] **L**eeds **U**niversity **S**park **I**gnition **E**ngine [code]), which has been developed at the University of Leeds for almost three decades. The model used in this study additionally shares routines with commercially available ICE simulation packages. It is therefore of interest to see whether or not the model is able to accurately predict the interactions of various processes at higher pressures, where the industry focus appears to lie. A significant amount of experimental data was available for this project, enabling a good understanding of the model performance for each element.

The variability of combustion is also investigated in more detail. There are three main phases of combustion: initiation, a main phase and a termination phase. Through a novel account of variability using an R^2 correlation, the variability of combustion and its effect on the final cylinder pressure have been assessed at the three main phases. LUSIE is employed to model the experimentally observed trends.

1.2.1 Novel Contributions

The most novel aspects of this work can be identified as:

- Highlighting that a possible deficiency in the currently used model for turbulent premixed combustion in engines exists for highly boosted engines, which may be related to the definition of turbulence length scale used to predict the after-burning rates.
- Showing that by assuming a variability of mixture composition and flow-field velocity appears to be a valid method for predicting cycle-to-cycle variability for an array of engines operating at both low and high pressures.
- The conception of a method for quantifying cycle-to-cycle variability which highlights where in the combustion process the factors affecting variability become less influential. The method also highlights a variability of autoignition separate from the burn rate exists in the boosted single cylinder LUPOE2-D engine.
- Identifying a high frequency pressure oscillation phenomena, associated with a downsized engine; an observation easily mistaken for combustion related engine knock. It has been shown that this phenomena is highly unlikely to be engine knock and that potentially the high force within the cylinder of a boosted engine is enabling the oscillations.

1.3 Thesis outline

- Chapter 2 - In this chapter, a broader discussion and extended review of the elements (turbulence, combustion, autoignition and variability) is undertaken. Where possible peer-reviewed publications have been used to support statements of fact. Work has been critically reviewed where appropriate and issues relating to validity of studies have been highlighted. At the end of each section, in line with the fundamental scope of this work, the effects of pressure on each of the elements have been independently assessed.

- Chapter 3 - The model used to form the majority of the current work is introduced and described in detail. The Chapter includes a description and background of the variability model and 0-D$k-\epsilon$ turbulence models which were implemented as a part of the current work. Four distinct engines were used for model validation throughout the work[1], these four engines are also introduced although information regarding data acquisition was left to a minimum as any experimental work carried out by the author was limited.

- Chapter 4 - Results of the $k-\epsilon$ turbulence model fitted to three different engines are presented in this chapter, the comparison includes both experimental turbulence data as well as data predicted using CFD methods. The results of LUSIE predictions of crank-resolved in-cylinder pressure for the four different engine platforms are presented, the influence of pressure and engine-type is noted and discussed. The influence of turbulence scales used in the after-burning expressions are focused on in detail.

- Chapter 5 - Variability of combustion in low pressure and high pressure engines, as seen both experimentally and as predicted by LUSIE using the cycle-to-cycle variability model are given in this chapter. The influence of different parameters recognised to be the primary causes of variability are examined both individually as well as how they influence variability when combined. Variability between low pressure and high pressure engines has been assessed for both multi-cylinder engines as well as the single-cylinder research engines. Also discussed is an interesting observation seen in the multi-cylinder production engine with respect to its variable valve lift (VVL) mechanism and the effect it has on variability. The ability to predict variability in engines operating under boosted conditions is discussed. Finally, in this chapter, a novel method for variability of combustion is introduced;

[1] Although three base engines were used, there were essentially four different engines in operation once the Leeds University engine was modified for running at boosted conditions

the method is based on an R^2 correlation. The variability of combustion at different stages of a propagating turbulent premixed flame is investigated using the new method as well as by predictive methods.

- Chapter 6 - The focus of this chapter is autoignition. Some observations of experimentally seen anomalies are predicted in order to gain a further insight into their origin. Two types of autoignition model, kinetic and empirical, are used to predict autoignition in engines based on experimental data using a post-processing thermodynamic cycle analysis. The ability of each model to predict autoignition for the different engine types and operating conditions is presented. A look into the variability of autoignition and whether there exists a variability separate from the burning rate variability is presented. Finally, an assessment of an autoignition anomaly seen in the boosted production engine is assessed via a frequency analyses; the suggestion is that the engine had not been pushed to its "limits" as was initially thought.

- Chapter 7 - The key findings from the work are summarised, with a discussion on their implications for future combustion research generally. Recommendations for future research students at the University of Leeds with specific application to the equipment and models used in this study are given.

Chapter 2

Background to SI engine combustion

2.1 Downsizing concept

The primary aim of a downsized engine to reduce mechanical and pumping inefficiencies, specifically at low load; ultimately this leads to an improvement in efficiency as well as a reduction in CO_2 emissions. A reduction in engine displacement is usually achieved through a reduction in the number of, and/or size, of cylinders. The advantages of engine downsizing on part-load performance can be seen in three primary areas:

- Friction benefits: a reduction in the number and size of cylinders will reduce the amount of surface-to-surface interfaces and therefore friction; smaller cylinders will also reduce the surface area of the combustion chamber, minimising heat transfer loses.
- Pumping benefits: an engine with half the displacement will require twice the amount of air-fuel to achieve the same load request. A situation which, at part load, will reduce the amount of work required from the piston to create a pressure gradient across the engine intake system, i.e. reducing the so-called pumping loses.
- Impact on vehicle design: smaller engines, will be lighter and easier to package into a vehicle; a reduction in vehicle weight will reduce the amount of work required to

move the vehicle a certain distance. In addition lower frontal areas of vehicles and the associated reduction in drag will lead to more efficient vehicles[1].

Possible disadvantages of downsizing are increased cost and complexity of single-stage and multiple-stage boosting systems. Additionally, control strategies for complex boosting systems require significant development to permit high levels of transient performance. Also, high in-cylinder pressures can lead to increased mechanical mass for durability as well as larger bearing sizes; which can negate friction benefits.

It has been shown by numerous studies that downsizing results in increased efficiency at low engine loads whilst engine performance in terms of full-load torque and power is comparable to engines with larger displacements (Bozza et al. [2007, 2009]; Cruz et al. [2003]; Lake et al. [2004]; Lecointe and Monnier [2003]; Shahed and Bauer [2009]; Stokes et al. [2000]).

2.2 Turbulence

Turbulence can be described as a fluctuating flow arising at elevated fluid velocities; it is as difficult to understand as it is to accurately quantify. Its presence has confounded some of the greatest minds, with Einstein, Feynman and Heisenberg all alleged to have spoken with disdain regarding turbulence, the latter reportedly saying "When I meet God, I am going to ask him two questions: Why relativity, and why turbulence? I really believe he will have an answer for the first." (Marshak and Davis [2005]). Despite the complexity surrounding turbulent flows they are an important part of every-day life; some turbulent flows being directly observable while others are visible only from their effects, i.e. the unpleasant sensation experienced by aircraft. A widely accepted, but by no means definitive, definition of turbulence is given by Hinze [1975]:

> *"Turbulent fluid motion is an irregular condition of flow in which the various quantities show a random variation with time and space coordinates, so that statically distinct average values can be discerned."*

[1]Complex boosted systems on vehicles, especially those employing a hybrid of two or more supercharger devices will increase vehicle weight and be more difficult to package, therefore the benefit of smaller engines may not be so obvious in terms of packaging depending on the vehicle-engine platform as a whole

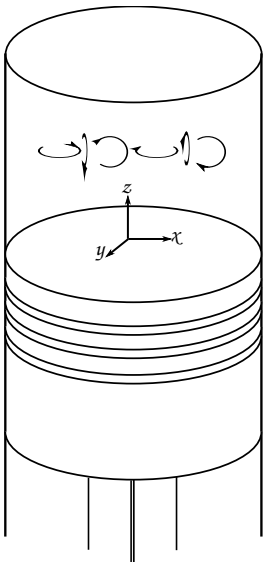

Figure 2.1: A representation of the 3-D flow field of individual eddies within a cylinder.

Turbulence can further be described as the motion of randomly[1] distributed vortices of varying sizes in three dimensions which occur when instabilities are not damped sufficiently by viscous actions and the velocity of the fluid at a given point in the flow exhibits random fluctuations of the velocity (Tabaczynski [1976]; Turns [2000]). More developed definitions, and more mathematical definitions can be found in seminal turbulence texts such as Hinze [1975]; Reynolds [1974]; Tennekes and Lumley [1972].

2.2.1 Turbulent Flow in IC Engines

It is known that reciprocating internal combustion (IC) engines always operate under turbulent conditions, that is the three-dimensional (x, y, z) in-cylinder flow field being turbulent for all engine speeds and inlet port/valve configurations (Acroumanis et al. [1984]), see Figure 2.1. It is a common knowledge that the combustion process is strongly affected by turbulence (Liou and Santaviccia [1983]; Liou et al. [1984]). Turbulence in engines increases the heat and mass transfer rates between burned and unburned zones, over and above molecular diffusion resulting in higher flame speeds (Heywood [1988].

In an engine, turbulence is primarily generated by the break-up of the intake-jet of reactants flowing into the cylinder during the induction process (Tabaczynski [1976]. The induction of air and fuel into the cylinder results in complex and apparently random

[1]The term random should be used with caution when describing turbulence. Although seemingly random in nature, the phenomena conforms to the laws of conversation and is predictable by Navier-Stokes equations and is therefore not wholly random Lipatnikov [2012]

fluid motion. This can be relatively ordered in a bulk motion such as swirl (axial rotation) or tumble (perpendicular to the cylinder axis); a representation of swirl and tumble flow motion can be seen in Figure 2.2. The engine geometry and inlet design will largely determine the turbulence characteristics for a given engine. It is also worth noting that, *generally*, the same mean flow events will occur for concurrent cycles in ICE cycles owing to the geometric profile of the intake system, as well as the dynamic profile of the valve lift[1], although, there are considerable variations in turbulence fluctuations within a given cycle which are further discussed in Section 2.7. Viscous shear stresses dissipate the vortices of the large scale fluid motion to smaller vortices, at rate governed by the internal energy of the turbulence, eventually being completely dissipated as negligible heat (Minter and Spangler [1996]). Within an engine cylinder, after the inlet valve/port closes turbulence decays as there is no more kinetic energy, being provided from the intake-jet, to "feed" it. A source of kinetic energy after valve/port closure may come from the piston motion which can induce turbulence, e.g. rapid distortion theory suggests that the compression of large scale eddies increases their rotational velocity, contributing to turbulence generation (Hill and Zhang [1994]). At the same time the large-scale eddies are being stretched and distorted, reducing in size until the largest fraction of the kinetic energy is of the order of the molecular scale and can no longer be reduced; then the energy is dissipated (converted to thermal energy).

2.2.2 Quantification of turbulence

When describing the influence of turbulence on process it is necessary to: 1) determine the quantities that are to be used in defining a) the turbulence itself b) the influence 2) determine how to handle these quantities statistically given the pseudo-random nature of turbulence. The two most important turbulent quantities are that of a velocity and a scale; with respect to IC engines these quantities are the turbulent fluctuating velocity (around the mean velocity) and 3 length and time scales, discussed in Section 2.2.3.

2.2.2.1 Turbulent velocity

Quantification of the "turbulent" velocity is achieved by statistical decomposition of a set of measured, instantaneous velocities. For simplification, an initial example will consider an isotropic Eulerian, time resolved case for steady flow e.g. the flow through a pipe

[1]The use of the word "generally" is applied as modern intake systems and valvetrain can include geometries which vary with operating condition which may alter flow type under transient operation.

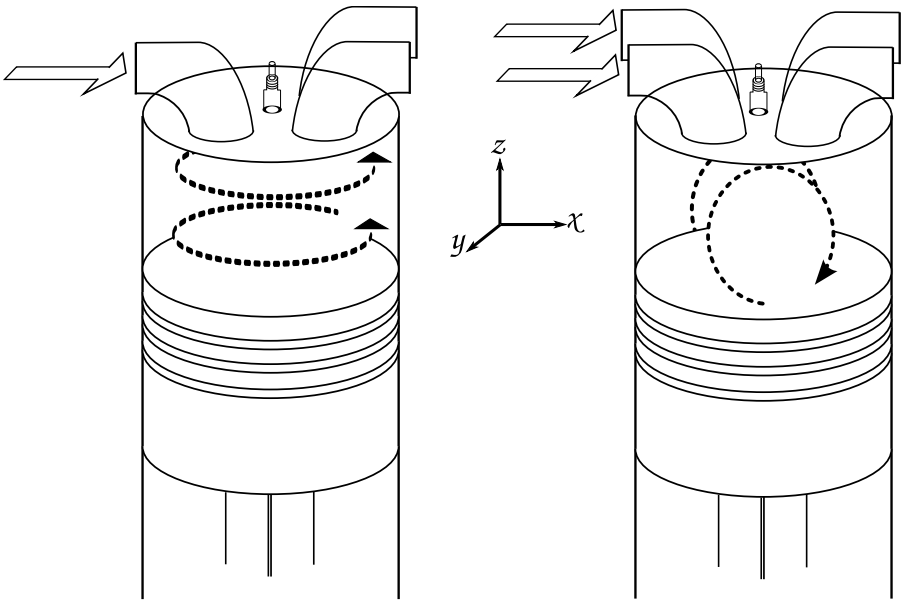

Figure 2.2: A representation of swirl and tumble motion within an engine cylinder-piston assembly.

measured continuously at a single spatial location. The *mean* velocity, $\bar{U}$ is therefore the mean of all the velocities measured at a fixed point in space over time, $U(t)$. Of course at any given time, owing to turbulence, it is unlikely that the condition $U(t) = \bar{U}(t)$ will be realised; therefore the instantaneous velocity can be related to the mean velocity and the "level" of turbulence, $u(t)$ by Reynolds decomposition:

$$U(t) = \bar{U}(t) + u(t) \tag{2.1}$$

Where the flow is considered steady, clearly $\bar{U}$ in reality has no dependence on time and can be found from the time average of $U(t)$.

$$\bar{U} = \lim_{\tau \to \infty} \frac{1}{\tau} \int_{t_o}^{t_o+\tau} U dt \tag{2.2}$$

The fluctuating velocity, u, is defined by the root mean square (rms) value to avoid the time-average zero mean.

$$u' = \lim_{\tau \to \infty} \left[\frac{1}{\tau} \int_{t_o}^{t_o+\tau} (U^2 - \bar{U}^2) dt \right]^{1/2} \tag{2.3}$$

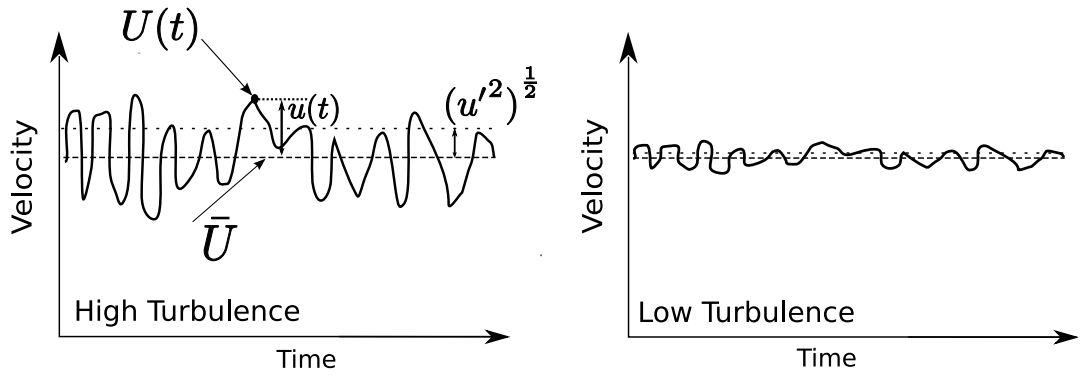

Figure 2.3: Two time-dependent flow cases detailing the decomposition of velocities for both high and low turbulence conditions.

It can be thought of as the standard deviation of the fluctuations around the mean. The value is generally termed "turbulent intensity" in literature. Strictly speaking however, the term "turbulence intensity" should be reserved for the ratio - $u'/\bar{U}$.

An example of the above description can be seen in Figure 2.3 where a theoretical, steady flow system produces two different turbulence levels for the same velocity, here it will be assumed for the example that a variation in density or pipe diameter makes the situation of identical velocity but different turbulence more feasible.

Naturally, flow in engines is neither steady state nor isotropic because of the piston motion, as well as the non-constant induction event with respect to the intake orifice area. The non-steady flow prevents the use of the time-based Reynolds decomposition (Eq. 2.1 to 2.3). In such cases a different averaging approach is used, ensemble averaging; which can be thought of as a discrete averaging process compared with the continuous averaging achieved by the time-based approach.

An instantaneous velocity in the i_{th} cycle at crank angle θ is described as follows:

$$U(\theta, i) = \bar{U}(\theta, i) + u(\theta, i) \tag{2.4}$$

Where, as before $\bar{U}(\theta, i)$ and $u(\theta, i)$ are the mean and fluctuating components of the instantaneous velocity. The ensemble-averaged velocity is defined as:

$$\bar{U}_{EA}(\theta) = \frac{1}{N_c} \sum_{i=1}^{N_c} U(\theta, i) \tag{2.5}$$

Where N_c is the total number of cycles used in the averaging. The number of cycles required to determine a u' value has been investigated by Hussin [2012] who assessed

the impact of the number of cycles used for ensemble-averaging techniques. He used Laser Doppler Velocimetry (LDV) techniques to determine u' values in the LUPOE2-D engine at 750 rev/min and 1500 rev/min with a varying amount of cycles (50-500 for the 750 rev/min case and 100 to 900 for the 1500 rev/min case). It was concluded that although there was a dependency of turbulence quantities on the number of cycles used for ensemble-averaging, it was not significant where more than $N/7.5$ cycles were used (where N is the engine speed in rev/min); thus at the engine speed of 750 rev/min 100 cycles are thought to give a good statistical sample.

It should be noted that the proposed ensemble averaged relationship has been accepted by numerous academics, however it is not considered to be a definitive solution to the problems of attaining average quantities in unsteady anisotropic flows. If the physical process in engines is analysed it can be seen that there exists two main fluctuations: 1) variations in velocity which occur "naturally" from one cycle to the next 2) turbulence fluctuations themselves. When the aim is to obtain turbulence quantities alone, which must be derived from the Reynolds decomposition, then the superimposed variation of the cycle-to-cycle fluctuation must be separated (Heywood [1988]).

2.2.2.2 Turbulent kinetic energy

One of the more important variables used to study turbulence is the specific Turbulent Kinetic Energy, (TKE). It represents the kinetic energy in the turbulent part of the flow while the Mean Kinetic Energy (MKE) relates to the kinetic energy in the "average" flow. From Eq. 2.1 & Eq. 2.3 it can therefore be seen that for a 3-Dimensional flow field:

$$\text{MKE} = \frac{1}{2}\left(\bar{U}_x^2 + \bar{U}_y^2 + \bar{U}_z^2\right) \tag{2.6}$$

$$k = \frac{1}{2}\left(u'^2_x + u'^2_y + u'^2_z\right) \tag{2.7}$$

When considering an isotropic case of turbulence alone, as is often the approach used in engines, Eq. 2.7 is reduced to:

$$k = \frac{3}{2}u'^2 \tag{2.8}$$

The energy contained within individual eddies determines their turbulence; eddies with more energy will be more turbulent. From a modelling perspective within engines, it is

the turbulent kinetic energy which is predicted and then converted to a level of turbulence by rearranging Eq. 2.8:

$$u' = \sqrt{\frac{2}{3}k} \tag{2.9}$$

2.2.3 Turbulent scales in engines

If the velocity associated with an eddy can be thought of as the amount of energy it contains and therefore its turbulence; the scale of the eddy can approximately be considered the time for which that scale will be active before the energy is passed onto smaller and smaller scales, dissipating as it does so according to Eq. 2.10 until eventually the viscous forces dissipate all kinetic energy into heat.

$$\epsilon = \frac{u'^3}{\iota} \tag{2.10}$$

Three key implications of Eq. 2.10 are as follows:

- The dissipation rate is controlled by the largest scales only
- The rate of dissipation is independent of viscosity
- The rate of dissipation is proportional to k

Three defined scales exist in engines; the largest scale, which is constrained only by the system boundary, is know as the integral scale, l_i. The smallest scales known as the Kolmogorov length scale, l_η is the smallest scale permissible, a scale which is smaller would be "smeared" out by viscous transport. An intermediate scale between the two is called the Taylor scale l_λ. A discussion of which scale is the most relevant to use in combustion modelling has been included in Section 3.4.3 as well as investigated in Chapter 4.

The definition of the integral and Taylor scales will be expanded upon as they are both used throughout the current work. The integral scale derives its name from its definition. Although it has been implied that the integral scale has a unit of dimension which identifies a length, it can also be considered as a time scale. A definition of the time-scale could follow that it is the time for an eddy to perform one revolution.

Determining the scale, either by time or length, depends on the method used to capture data. Where the flow can be measured at more than one fixed point, a length

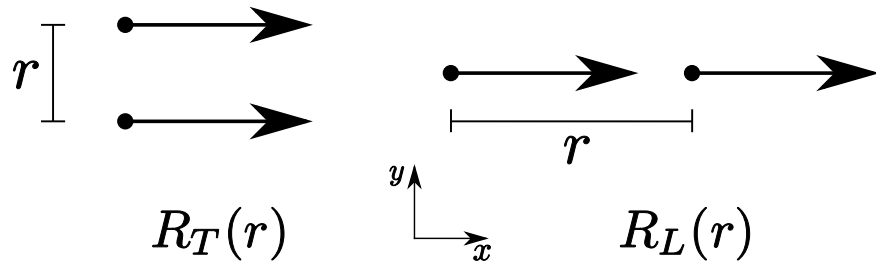

Figure 2.4: Transveral and longitudinal spatical velocity correlations for the defined flow-field.

scale can be directly obtained via simultaneous measurement of the flow-field at two different points, U and $U + r$. When only one position can be measured at any one time, results can be compared at different times, $U(t_0)$, $U(t_0 + t)$. The integral of the area under the autocorrelation coefficient, R, which for the spatial case is a measure of how much the velocity changes over the distance, r, between the two measuring points or the change in velocity at two discrete times, t. The autocorrelation coefficient can, for a temporal solution of τ_l be given as:

$$R_t = \frac{1}{N_c - 1} \sum_{i=1}^{N_c} \frac{U(t_o)U(t_o + t_)}{u'(t_o)u'(t_o + t)} \tag{2.11}$$

The integral time-scale, τ_l, can be determined as (Tennekes and Lumley [1972]):

$$\tau_l = \int_0^\infty R(t)dt \tag{2.12}$$

It therefore follows that the integral length scale, l_i can be related to the time scale by:

$$l_i = u'\tau_l \tag{2.13}$$

For spatial determination, the orientation of the linear relationship, with respect to the flow field, between the two points, must be acknowledged. For a two-dimensional flow-field, both a longitudinal and transversal integral length scale, l_{iL} & l_{iT} respectively, exist when spatial correlations are determined; as illustrated in Figure 2.4.

The two scales can be related, in the case of isotropic and homogeneous flows by Hinze [1975]:

$$l_{tL} = 2l_{iT} \tag{2.14}$$

It has been rationalised that owing to the weak dependence of burning rates on l_i compared to u' as well as the inability of combustion models to determine between the orientation of length scales, it is permissible to state the condition $l_{iL} = l_i T$ (Lipatnikov [2012]). The dependence of the after-burning rates on l_i in the current study has been seen to be stronger vis-á-vis previous studies where a two-zone combustion model (Section 3.2.6.1) was employed, (Hattrell [2007]). Burluka et al. [2012a] identifies that the transversal scales are only slightly smaller than the longitudinal one and that no discernible systematic difference between fast and slow cycles in either correlation length-scales can be observed. The choice of the correct scale to use appears to be unresolved, and until accurate measurements of time scales can be gauranteed it is unlikely the issue will be resolved in the near future.

The Taylor scale as a physical quantity is ambiguously defined in literature, with the consensus being that it is a scale which lies somewhere between the largest eddies and the smallest eddies (Hinze [1975]; Tennekes and Lumley [1972]; Turns [2000]). The most descriptive definition offered is by Law [2006], who defined the Taylor scale as the length scale which represents the distance covered by a Kolmogorov eddy during its lifetime when it is transported by an integral scale eddy. It is proposed that the Taylor time scale can additionally be determined from the same autocorrelation curve as used to determine the temporal integral scale by:

$$l_\lambda = -\frac{1}{2}\frac{d^2R}{dt^2}\bigg|_{t=0} \tag{2.15}$$

In practice though, the relationships seen in Eq. 2.16 & Eq. 2.17 can be used to relate the Taylor and Kolmogorov scales to a predicted integral scale (Law [2006]). It is seen in Section 3.4.3 that a proportionality constant, F_λ is often included into the relationships based on empirical data for an individual combustion vessel.

$$\frac{l_i}{l_\lambda} = C_\lambda \mathrm{Re}_L^{0.5} \tag{2.16}$$

$$\frac{l_i}{l_\eta} = \mathrm{Re}_L^{3/4} \tag{2.17}$$

2.2.4 Modelling of turbulence

A good prediction of turbulence is the key to successful SI engine models owing to the reliance of the combustion process on such quantities as u' and l_i and/or l_λ. Turbulence modelling is, for all practical purposes, approached with averaging and simplification techniques to reduce computational time. The ultimate aim for turbulence models could be a full numerical solution of the Navier-Stokes equations on an almost infinitely fine grid, for very turbulent flows in relatively large volumes. The closest current approach to realising the ideal model is the Direct Numerical Simulation (DNS) where a full solution of the Navier-Stokes equations is achievable but, to date, only at low Reynolds numbers and small volumes. The refinement of the mesh is determined by the size of the scales so the upper bound of the grid must be constrained by the combustion chamber (to account for l_i), while the smallest mesh size should contain a scale of size l_η. It can be seen that for a typical value of l_η, on the order of 10μm, which we will assume as a sphere/cube with a volume $\propto {l_\eta}^3$, will require the solution of almost 750 billion cells[1] in a typical engine cylinder at the start of the compression stroke. In addition, the computational power required for DNS solution, in floating point operations per second (flops) scales as Re^3 as l_i/η is proportional to $\mathrm{Re}^{3/4}$, in three directions ($\mathrm{Re}^{9/4}$) and the timescale relationship leads to $\mathrm{Re}^{11/4}$ which is approximately Re^3 ; Re number in turbulent flows in engines, combined with the relatively large non-stationary volume in engines, suggests that DNS methods for engines are still a number of years away from being realised.

Removal of these smallest scales, will increase the speed of computation significantly. A solution of this type is called Large Eddy Simulation (LES) where scales smaller than a certain size Δ_l are filtered and the only scales solved (l_x), are those which satisfy $\Delta_l < l_x \leq l_i$. Assuming Δ_l is $l_i/2$ then the previous example case for DNS can be reduced to under 10 million cells, still a significantly large number, but more approachable computationally. Indeed, when considering that, during combustion, the cylinder volume is significantly less than at the start of compression, then both the total volume and l_i will reduce and further cell reduction will occur to cell sizes of approximately 1 million - a value which is in line with some recent engine turbulence prediction (Gosman [2012]).

Predictions by LES methods, however, are still well beyond practical application of providing turbulence data to thermodynamic models where computational time is a key consideration and high powered computers are not feasible. A further simplification can be seen in Reynolds Averaged Numerical Simulation (RANS), as with Reynolds

[1]This approximation assumes an ideal spherical mesh shape rather than a commonly seen tetrahedral shape, from this any lattice packaging criteria associated with fitting spheres into a cylinder are ignored for the sake of brevity.

decomposition of classical turbulence theory, a similar approach can be applied to the Navier-Stokes equations for a temporally averaged case. Here *only* the largest scales of the flow are solved and all others are resolved with one of the numerous sub-models. Further coarsening of the spatial and temporal "grids" is allowed by a RANS approach reducing computational times further. A number of RANS-based solutions are available with differences arising from the approach used to close the Reynolds stress tensor equation system, see for example Versteed and Malalasekera [2007]. Such models include: zero-equation models, such as Baldwin-Lomax, one-equation models, of which the best known is probably the Spallart-Allmaras model, two-equation models such as the $k-\epsilon$[1] model, the $k-\omega$ model and Reynolds stress models (RSM). For a discussion of the intricacies between each solution the work of Versteed and Malalasekera [2007] discussed, in detail, a number of different aspects of turbulence modelling; the work of Sjeric et al. [2012] provides an excellent summary.

2.2.5 Influence of pressure on turbulent quantities

There has been a significant amount of research devoted to the effects of pressure on laminar, and to a lesser extent, turbulent flames for a variety of hydrocarbon fuels; there does, however, appear to be an apparent lack of literature regarding the effect of pressure on the properties of turbulence within engines. Cruz et al. [2003] used hot wire anemometry (HWA) techniques to determine information on the flow-field in a turbocharged engine. A constant temperature anemometer was used to determine the velocity normal to the probe wire. The anemometer was calibrated only up-to temperatures of 450 K, after which data was extrapolated; cylinder temperatures, even restricted to motoring operations, would be expected to exceed 750 K even for a modestly downsized engine. Another potential issue with the methods used is the lack of correction procedure on the velocity signal. A correction would be necessary because of the sensitivity to pressure experienced by a velocity signal compared to a temperature signal; such a correction is based on the Nusselt and Reynolds numbers of the flow, which requires the measurement of temperature and velocity simultaneously (Bruun [1985]). Using the averaged temperatures gives inaccurate fluctuation values, and thus erroneous u' measurements; consequently the results produced are unconvincing (Figure 2.5) with the u' values being minimum at the point of IVC followed by a rise, with a maximum occurring approximately 30^o aTDC. The overall conclusion of the work suggested a 10% increase in u' for

[1]It should be noted, that the $k-\epsilon$ model in this section is not related to the $k-"\epsilon"$ model referred to throughout this work, introduced in Section 3.4.2, which predicts the mass-averaged time-evolution of k only, while dissipation ϵ is not separately calculated.

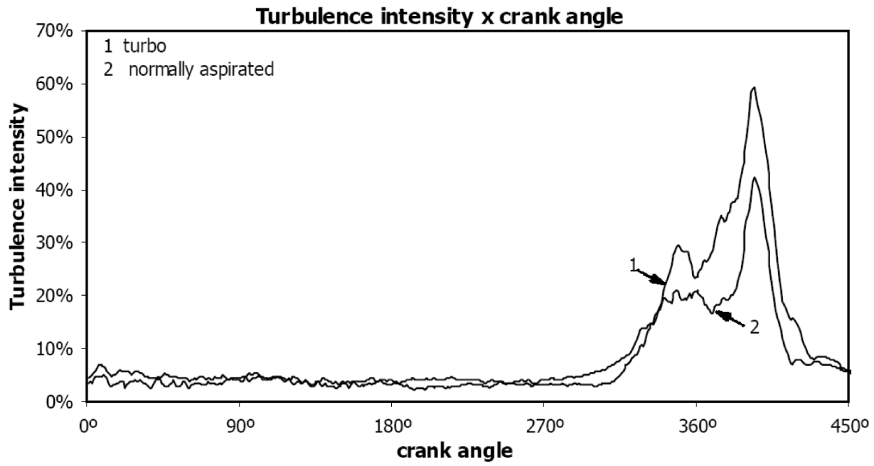

Figure 2.5: HWA measured u' values for a naturally aspirated and turbocharged, from Cruz et al. [2003].

an engine with a 50% increase in P_{ivc}, though the source of this increase is not identified with no suggestion as to whether extra turbulence was generated in the turbocharger, or by the increase in pressure.

Pressure also affects the viscosity and density of a fluid; Landry et al. [2008] investigated the effect of increased pressure on u' and l_i; Particle Imaging Velocimetry (PIV) measurements were used to characterise the flow field within a single cylinder research engine. Although they showed that values of u' and l_i varied with pressure, they also found that u' is maximum at P = 1 bar while l_i is minimum though these trends were not strong enough to suggest a relationship between pressure and turbulent properties. It was also not clear if the inlet velocity was measured to ensure TKE was not affected by the inlet jet. Work by Kobayashi et al. [1997] attempted to analyse u_t at high pressures as well as observing turbulence properties, u' and l_i; this was achieved using a nozzle-type burner with a turbulence generator installed inside a high-pressure chamber. The mean flow rate was maintained at 2.0 m/sec while pressure was increased from 0.1 to 3.0 bar, while turbulent properties were measured using a constant temperature hot wire. The trend of u' against P was the opposite to the one observed by Landry et al. [2008], i.e. u' was minimum at P = 1 bar. Turbulent small scales were found to be inversely proportional to pressure as seen in Figure 2.6 where it is clear that as pressure increases, the sensitivity of smaller scales increases, so that at the highest pressure l_η has undergone the largest percentage decrease compared to the l_i and l_λ scales. The relationship between the three scales, $\text{Re}_\eta^4 \propto \text{Re}_\lambda^2 \propto \text{Re}_{l_i}$ demonstrates why the sensitivity to pressure is proportional to 1/scale size (Bray [1980]). The reduction in l_i with pressure is a remarkable

observation as τ_l is considered to be a function only of the flow size, i.e. combustion vessel geometry.

Lawes et al. [2012] investigated pressure effects on laminar and turbulent flames using constant a volume combustion "bomb". It was seen that increasing the pressure altered some of the turbulent scales and the laminar flame properties. For the testing, pressure was increased while u, controlled independently of flow by internally mounted fans, was kept constant. It was noted, that different turbulent scales have different reactionary behaviours as the system pressure increases; l_i, primarily a function of the vessel size, remained constant. However, the Taylor and Kolmogorov scales fell; this was a trend also seen by Larsson [2009], simply a consequence of the decreasing viscosity.

Prediction of turbulence at different pressures was undertaken as part of an investigation into combining a simplified $k-\epsilon$ turbulence model to fractal combustion by Sjeric et al. [2012]. The study took place at both full and part-load conditions, thus accounting for a change in pressure. The exact change in pressure between each case is not known as only a part-load BMEP value is provided for the low pressure case. It can be assumed that the difference in initial pressure between the full load and part load cases would be approximately 0.7 bar $\pm$ 0.2 bar depending on the full load performance of the engine and assuming a linear relationship between intake pressure and BMEP. Nevertheless the results which can be seen in Figure 2.7 suggest that there is a negligible effect of pressure on turbulent kinetic energy for both a simplified $k-\epsilon$ turbulence model and the traditional two equation $k-\epsilon$ model.

2.3 Combustion in engines

Discussed in the previous section was an overview of turbulent flow in engines. Until now, combustion has been purposely omitted in this text with a view to decoupling the effects of both phenomenon on engine performance. The addition of combustion into discussion leads to further complexity; it is possible to simplify the discussion however by concentrating on the specific type of combustion mechanism found in SI engines, that is, a subsonic, localised flame which is premixed. Subsonic flames are termed deflagration flames.[1] A localised flame is where the flame occupies only a portion of the combustible medium at any one time, as opposed to homogeneous distributed reactions. Premixed flames form a flame front moving through a medium where the oxidiser and fuel are

[1]Propagation which occurs at supersonic speeds is said to be detonation, a topic of large interest in its own right, but outside of the scope of this study.

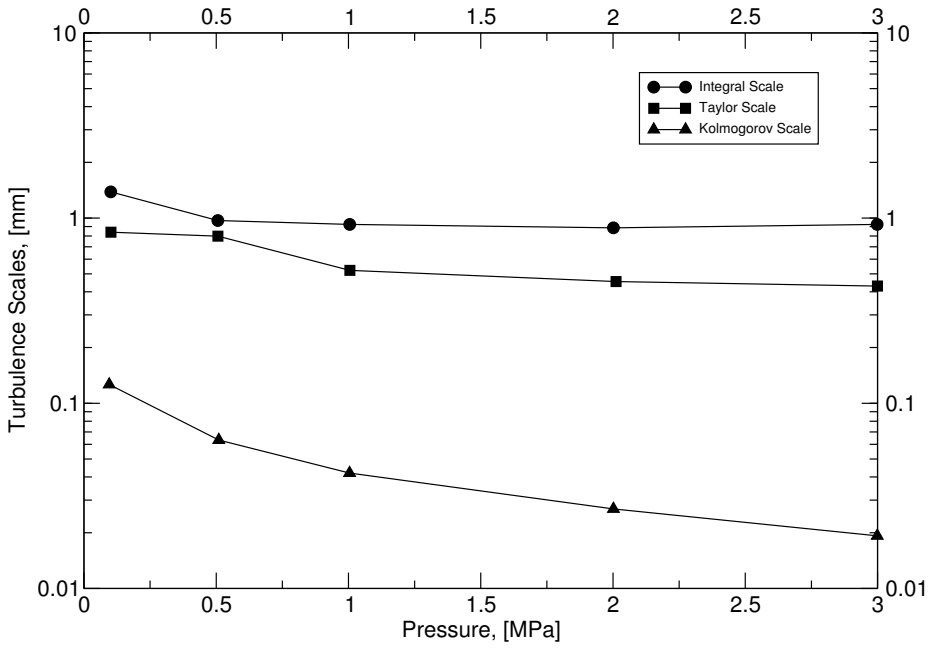

Figure 2.6: The influence of pressure on length scale as measured. Recreated from Kobayashi et al. [1997].

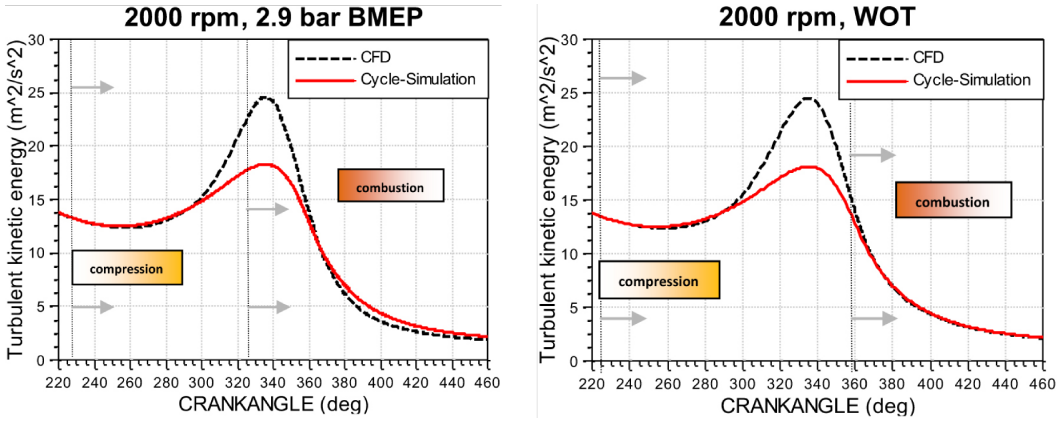

Figure 2.7: Turbulence as predicted by a 0-D$k-\epsilon$ model (Cycle-Simulation) and a CFD $k-\epsilon$ model (CFD). Adapted from Sjeric et al. [2012].

already mixed; this is in contrast to a non-premixed (diffusive) mode where combustion rates are driven by the fuel and oxidiser diffusing into one another, the latter regime occurring in a traditional diesel engine.

2.3.1 Laminar premixed flames

As already alluded to (Section 2.2.1), the flow field within an SI engine is highly turbulent, therefore the transition between laminar and turbulent flame propagation occurs very quickly. Despite the relatively short period spent at laminar conditions, the laminar burning velocity, u_l is a vital parameter for premixed turbulent combustion calculations. Since it is used as a foundation to predict turbulent burning velocity (see Section 3.2.8.1), as well as controlling the burn-rate of fuel behind the flame front. It is therefore prudent to discuss the phenomena before turbulent premixed flames are introduced.

Historically, the first description of premixed laminar flame structure was introduced by Mallard and Le Chatelier [1883]. They proposed that the conduction of heat from the hot products to the cold reactants was the controlling mechanism for flame propagation. Later Zel'dovich and Frank-Kamenetskii [1938] identified the influence of molecular transport processes on the laminar burning velocity, u_l, and introduced the dependency of reaction rate to flame temperature. Following the seminal work by Semenov [1935] the appreciation of the involvement of flame chemistry on intermediate radical species increased. An analytical expression for laminar burning velocity was derived by Zeldovich et al. [1985].

2.3.1.1 Propagation of laminar premixed flames

A premixed laminar flame is comprised of a thin reaction zone; the reaction zone itself is highly complex, even more so when the situation becomes turbulent. Despite the complexity, the mechanism by which propagation occurs can be illustrated by the simplified one-dimensional adiabatic flame; the simplified, unstretched structure can be seen, diagrammatically, in Figure 2.8.

The simplified structure consists of four main zones: reactant zone, preheat zone, reaction zone and product zone. The reactant zone contains the "cold" reactants, i.e. an oxidiser and a fuel. The preheat zone is dominated by heat conduction and mass diffusion of the reactants, the conductive heat flow into the cooler region is greater than the corresponding heat loss and therefore the gas temperature increases. In the reaction

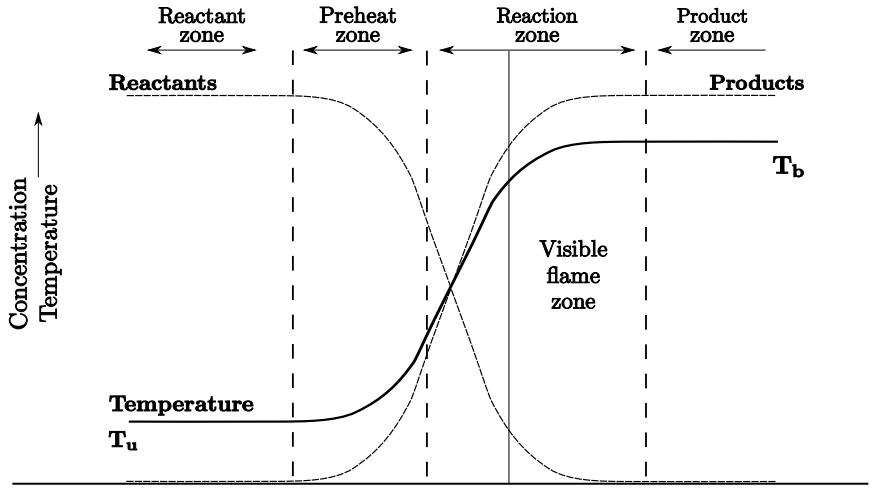

Figure 2.8: Concentration and temperature profiles associated with one-dimensional premixed adiabatic flames. Modified from Griffiths and Barnard [1995]. NB zone sizes are not to scale with respect to each other.

zone, conductive heat transfer is less while the reactants have now reached temperature to support self-sustaining reactions; the linear increase in temperature is the net result of the opposing processes. Eventually, the reactants are completely consumed. The emission of electronically excited species such as CH, CN, C_2, CHO and CO_2 emit light, in the reaction zone, as they return to their ground state (Griffiths and Barnard [1995]).

2.3.1.2 Laminar burning velocity and flame thickness

A laminar flame will propagate through a gas at a characteristic velocity, termed the burning velocity (Griffiths and Barnard [1995]). Heywood [1988] defines the one-dimensional unstretched laminar burning velocity, u_l, as "the velocity, relative to and normal to the flame front, with which the unburned gas moves into the front and is transformed into the products under laminar flow conditions". The unstretched laminar burning velocity, depends on the mixture composition, pressure and temperature. Practical flames are rarely one-dimensional and therefore do not conform to the example given in Section 2.3.1.1. Determining the local-stretched burning velocity, u_n requires an account of the flame stretch (see Section 2.3.1.3). A full discussion on determination of laminar burning velocities which account for stretch effects can be found in the work of Tripathi [2012].

The flame thickness, δ_L, represents the depth of the reaction zone (Griffiths and Barnard [1995]). Technically the thickness should reflect the depth of the total system where heat is released, however as the reaction zone is much thinner than the preheat zone, the flame thickness is approximately equal to the thickness of the preheat zone

(Lipatnikov [2012]). Quantification of this distance is not trivial due to the non-linear heat release. Owing to this situation, there are a number of definitions for flame thickness; again a discussion on flame thickness definitions can be found in Tripathi [2012].

2.3.1.3 Laminar flame stretch

When a flame propagates into a laminar flow-field which is not uniform, it is subjected to strain and curvature effects leading to changes in frontal area. The original one-dimensional assumption is no longer completely adhered to once the flame surface becomes stretched, as the transverse and tangential velocity components are no longer equal and hence the one-dimensional assumption is no longer valid. The increase in strain rate increases heat flux which reduces the flame thickness and burning velocity. This deviation affects the rate of change of temperature and species concentration, and therefore the thickness and velocity.

Study into the effect of stretch on premixed flames was started by Karlovitz et al. [1953]. The importance of straining and flame-front instability, specifically at the early stages of combustion, on flame propagation was demonstrated. The total stretch rate, α, acting at a point on the flame surface is defined as the rate of change of the flame area, A, of an infinitesimal element surrounding that point over the infinitesimal area (Lipatnikov [2012]), given by:

$$\alpha = \frac{1}{A}\left(\frac{dA}{dt}\right) \tag{2.18}$$

2.3.2 Turbulent premixed flames

The combustion process in SI engines is understood to a degree which allows the formulation of numerical models describing the process. Certain intricacies are not fundamentally understood owing to experimental difficulty in observing the reaction zone of turbulent flames. Accurate measurement of turbulence scales, specifically those smaller than the integral scale and in the capture of flame propagation in 4 dimensions (x, y, z, **t**). Basic principles allow the formulation of theories of combustion characteristics for regimes not yet tested; however the need for experimental data to corroborate theory is as relevant as ever.

Extrapolation of data is often performed; however with numerous processes occurring which react differently to a change in initial conditions, it is not always prudent

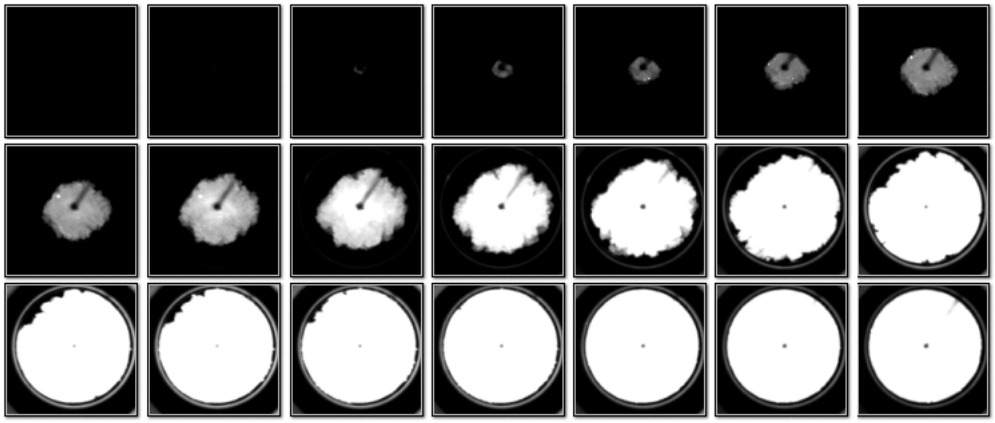

Figure 2.9: A developing flame captured in an optical disc-shaped research engine via natural light techniques. The time between each frame is 200μs or 1.8^{o}CA at 1500 rev/min.

to assume that these models are valid at all conditions as the interactions are not well understood.

A substantial amount is known, about the overall and individual phases making up the combustion process. It could be generalised that a "normal" cycle in an SI engine is initiated by an electrical arc grounded by the spark plug electrode. If enough energy is released in this process to allow self-sustaining chemical reactions, then a propagating flame will follow. The flame will accelerate as it experiences different scales of turbulence before slowing as it nears the wall and finally quenches completely. The described process can be seen in Figure 2.9 where natural light images of a combustion event have been captured using a high speed camera, as described in Section 3.6.2.

Although not captured by the natural light images, a turbulent flame has three primary regions associated with it: the flame has a leading edge (front), $\mathrm{fr_e}$ a reaction zone (thickness), δ_t and a trailing edge (burned gas radius), $\mathrm{fr_b}$ as is illustrated diagramatically in Figure 2.10 and should be considered the definitions used throughout this study. The average radius, $\mathrm{fr_{av}}$, seen in the Figure is included for clarity, it does not however take part in the models used in this study.

The level of turbulence, u', experienced by a turbulent flame will increase its burning velocity, u_t, up to a point where the ideal (maximum) turbulence level is reached ($u' = u'_{\mathrm{m}}$) after which ($u' > u'_{\mathrm{m}}$) the burning velocity will reduce as can be seen in Figure 2.11; eventually the flame will quench when $u' = u'_{\mathrm{q}}$. The optimum level of turbulence is not the same for each flame; the threshold varies for different stoichiometry and fuel composition, see for example Lipatnikov and Chomiak [2002].

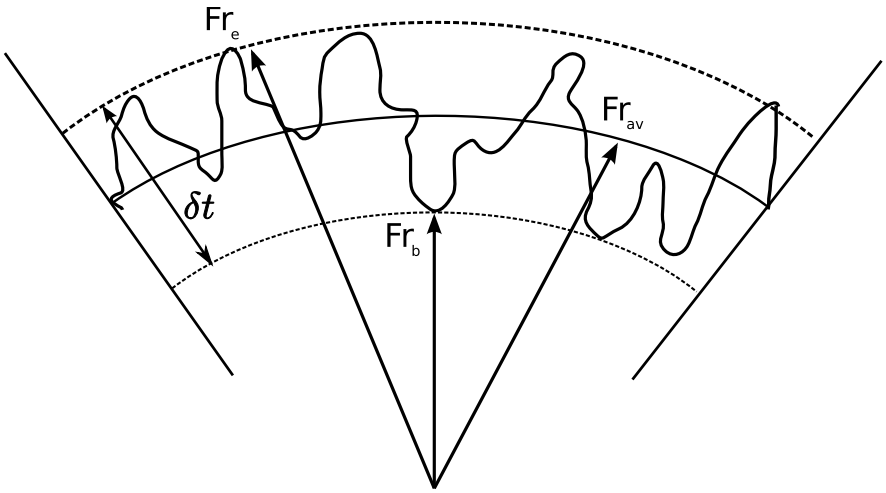

Figure 2.10: The different radii definitions which are traditionally attributed to a propagating turbulent premixed flame.

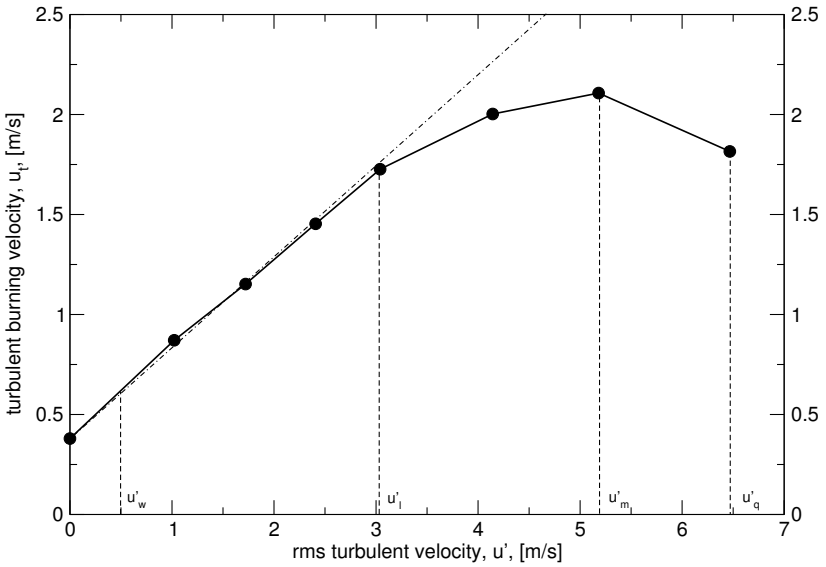

Figure 2.11: Effect of rms turbulent velocity on turbulent burning velocity for a propane-air mixture, reproduced from Lipatnikov [2012].

Lipatnikov and Chomiak [2002] reviewed experimental data based on turbulent flame speeds and burning velocities at moderate turbulence. The following generalisations were made:

- An increase in turbulent flame speeds and burning velocities by rms turbulent velocity at moderate turbulence.
- An increase in turbulent flame speeds, burning velocities, and slope du_t / du' by the laminar burning velocity.
- An increase in turbulent flame speeds and burning velocities by pressure despite the decrease in the laminar burning velocity.
- The dependence of turbulent flame speeds and burning velocities on the integral scale is much less pronounced than that of the laminar burning velocity, i.e. weak dependence.
- A decrease in turbulent flame speeds and burning velocities by the molecular heat diffusivity.

2.3.2.1 Turbulent combustion parameters

Combustion in engines is defined by a turbulent propagating flame which experiences different turbulence scales as it grows. While a laminar burning velocity is defined by the flame speed, S_l, and flame thickness, δ_L with respect to the unburned gas, a turbulent flame is dependent on both S_l as well as turbulence properties, namely l_i and u'. Dependence of u_t on S_l depends on mixture composition and it can be said that within the linear range of turbulence dependence u_1' (Figure 2.11) the dependence is at its strongest. Owing to this strong dependence, it is often desirable to decompose flame progression into the influence of both laminar and turbulent effects. In addition, it is important to see whether the turbulence penetrates the laminar flame thickness ,where the turbulence will affect the chemical processes and molecular transport of heat and mass. For that reason it is common to compare the laminar flame thickness to the characteristic turbulent length scales to see if penetration is likely. The effect of turbulence on a flame's structure can be expressed by the Karlovitz stretch factor, *Ka*.

$$Ka = \left(\frac{u'}{l_\lambda}\right)\left(\frac{\delta_L}{u_l}\right) \tag{2.19}$$

Karlovitz number is often thought of as the stretch factor in a turbulent flow field since it is the ratio of the rms turbulent strain rate to the chemical strain rate i.e. the ratio of Taylor eddy lifetime to the chemical lifetime. Put simply, it can be thought of a dimensionless number which expresses whether or not there is enough time for the flame structure to become severely distorted by turbulence. Where $Ka > 1$ it can be said that the flame surface is likely to be disturbed by the turbulence before combustion is complete. It has been proposed that at high values of *Ka* the small-scale turbulent stretching effect on the structure of thin reaction zones in the thickened-preheat-zone sub-regime is an area of research to be investigated; see for example Lipatnikov [2012].

Similar to *Ka* is the Damkhöler number, *Da*. It is an inverse measure of the influence of the turbulent flow on the chemical processes occurring in the flame. It is equal to the ratio of the time it takes a fluid to flow some characteristic distance, to the time it takes some chemical reaction or other physical process to be completed.

$$Da = \left(\frac{l_i}{u'}\right)\left(\frac{u_l}{\delta_L}\right) \tag{2.20}$$

Comparing Eq. 2.19 Eq. 2.20 it can be seen that:

- $Ka \propto 1$ / *Da*
- $Ka = \sqrt{\mathrm{Re}_{l_i}}$ / *Da* owing to the relationship between the Taylor and Integral length scale, (Eq. 2.16)[1]

These two dimensionless values can be used to quantify the structures of common flames. Diagrammatically, the role of *Da* and *Ka* on flame structure can be seen on a Borghi diagram, shown in Figure 2.12 (Borghi and Destriau [1998]). The Reynolds number, Re_l, is also identified on this diagram indicating the boundary of laminar flames.

Combustion in SI engines, with premixed flames, will generally fall within two regions on the diagram, at the boundary of the thickened, wrinkled flames (distributed reaction zone) and wrinkled flames with pockets (wrinkled flamelet) (Gillespie et al. [2000]), i.e. $Ka \approx 1$. An increase of pressure will affect both the laminar burning velocity and the laminar flame thickness as discussed in Section 2.3.3. As the turbulence is weakly affected by pressure, then a pressure increase will increase *Ka* owing to relationship of thermal diffusivity; on the Borghi diagram (Figure 2.12) the change is reflected

[1]It should be stressed that *Ka* has its own physical meaning and in the area $Ka = <1$ then the turbulent stretching of the inner structure of laminar flamelets requires consideration, Lipatnikov [2012].

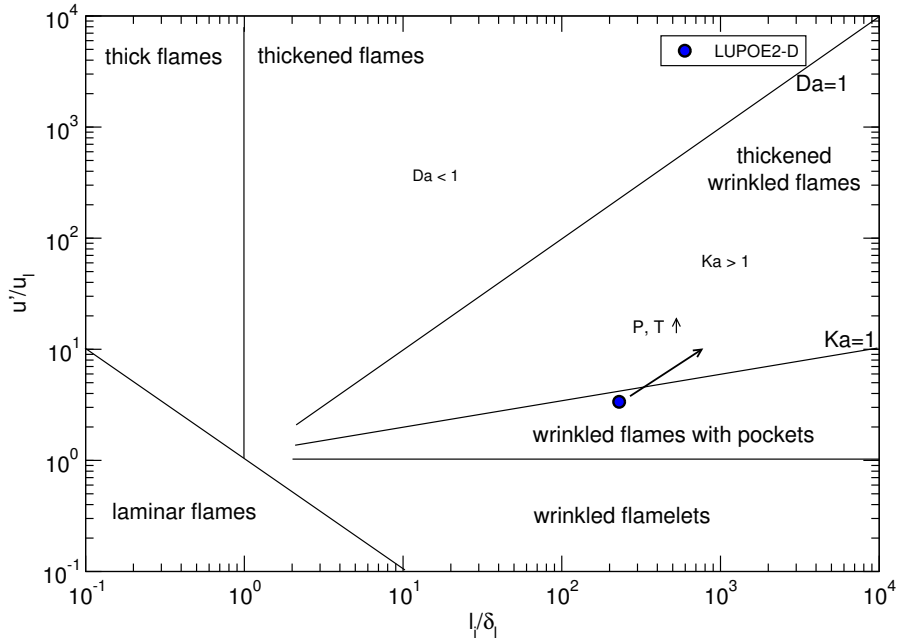

Figure 2.12: A Borghi diagram highlighting the different turbulent combustion regimes as well as the expected change in regime with downsized engine operation.

by the solid arrow. Research suggests that l_i and u' are largely independent of pressure; it can then be seen the general direction in which engine operation will take at higher pressures in engines. If a reduction in u_l is predicted by an increase in pressure, then it is surprising to see the operating regime predict a faster dimensionless burning velocity. In engines however, it must be assumed that a greater heat release will be associated with higher density combustion, therefore the increase in temperature vastly outweighs the increase in pressure and the net result is an increase burning velocity (Turns [2000]).

One final combustion parameter to be introduced here is the Lewis number Le. It represents the diffusivity ratio (α/D), where α is the thermal diffusivity of the mixture and D is the mass diffusivity of the reactant. (Law [2006]):

$$Le = \frac{\alpha}{D} \tag{2.21}$$

Lewis number becomes significant when discussing instability in flames (Section 2.3.5).

2.3.3 Influence of pressure on laminar premixed combustion

The inlet conditions will be different for naturally aspirated and pressure-charged downsized engines. The composition of the mixture will be similar (negating any increase in burned gas residual caused by increased back pressure). The higher pressure, temperature and subsequently density will result in a downsized engine running at remarkably different conditions.

Landry et al. [2008] estimated values of u_l under engine-like conditions at different pressures using the PREMIX code of the CHEMKIN package. They found that u_l remained constant through a range of pressures from 0.7-1.5 bar; fairly typical of downsized operating conditions. These results do not however agree with previous data where an increase in P results in a reduction in u_l; the reason that u_l remained constant is because each increase in pressure was met with an increase in temperature, known to increase u_l.

An increase in pressure will result in an increase in density for the same temperature; it has been suggested by Syed et al. [2010] that $u_l \propto 1/\rho$, which is in agreement with the work of Andrews and Bradley [1972] who propose u_l = 0.34P / $P_0^{-0.5}$ and Turns [2000] who suggests $u_l \propto P^{(n-2/2)}$ where the exponent, n is the overall reaction order. The reason for this dependency, according to Nomura et al. [2007], is that the quantity of liquid fuel per unit volume increases with pressure as the liquid equivalence ratio is held constant. Therefore as downsized engines have higher inlet charge densities it could be concluded that u_l of these mixtures is lower than seen in non-downsized counterparts. Another possible explanation for the reduction in u_l is that the decrease in u_l is said to be related to the termolecular recombination reactions, $H + O_2 + M \rightarrow HO_2 + M$ whose reaction rate is proportional to the pressure; see for example Glassman and Yetter [2008]; Kobayashi et al. [1997]. Lipatnikov [2012] notes that observations by Andrews and Bradley [1972] are in agreement within the framework of activation-energy asymptotic (AEA) theory[1]. Clearly, in conventional engines, an increase in pressure comes always with some increase in temperature; hence it is different from steady-state operation. Additionally, higher pressures are also known to reduce the laminar flame thickness. From AEA theory the mixtures' thermal diffusivity is proportional to $1/P$ and as δ_L is proportional to diffusivity then it follows that the flame thickness will reduce with an increase in pressure. Thus it can be seen that with the ratio of the relationship of thermal diffusivity to chemical timescale, τ_c, of $u_l = \frac{\alpha}{\tau_c}$, a reduction of pressure will realise a decrease in u_l. Measurement of the laminar

[1] AEA theory is a classical theory developed by Zel'dovich and Frank-Kamenetskii [1938]. It describes the theory of laminar premixed flames in a simple way, using single-step chemistry.

thickness of a flame is however made difficult because of the onset of cellularity which occurs at increased pressure (Tripathi [2012]) and therefore further study into effects of pressure are inhibited .

2.3.4 Influence of pressure on turbulent burning velocity

As discussed in Section 2.3, the turbulent burning velocity is a strong function of the laminar burning velocity; a reasonable assumption would be that because of lower u_l, u_t would also be lower. It has however been reported that unlike u_l, u_t increases with pressure (Turns [2000]).

Landry et al. [2008] undertook an investigation into the effect of pressure and dilution on the turbulent burning velocity, in an engine running on iso-octane, for intake pressures between 0.70 to 1.50 bar with diluted mixtures in the range of 10 to 35% EGR (by volume). The turbulent burning velocity was estimated from the mean flame front displacement velocity, u_d, and the mean flow field velocity, U, which was determined from the laser tomography images and Particle Image Velocimetry (PIV). It was found that for a constant EGR rate, u_t increased only slightly with an increase in pressure in a linear manner, with the relationship of (R^2 = 0.98).

$$u_t = 0.00045P \; + \; 2.116 \tag{2.22}$$

Turbulence levels in the engine were however low, $u' \approx 1.1$ m/s at N = 1200 rev/min; simulations were only performed at this speed.

A trend of low pressure influence on turbulent burning velocity (when turbulence levels are also low) was reported by Lawes et al. [2012] at the University of Leeds. An investigation into the effects of pressure on the turbulent burning velocity of iso-octane was undertaken in a fan-stirred combustion vessel. The integral length scale, l_i, was measured by two-point correlation to be 24 mm, at 500 rev/min, and was seen to be independent of all operating speed from 1000 to 10,000 rev/min. Initial pressure was increased from 1 to 10 bar, while the equivalence ratio and rms turbulent velocity were also changed. The effect of increasing pressure can be seen in Figure 2.13. As alluded to earlier, it is seen that the influence of pressure does not appear to greatly alter the low turbulence turbulent burning velocity, while for the more turbulent case u' = 4 m/s a greater influence of pressure is clearly seen. Flame curvature and wrinkling was attributed to the increase in pressure, in turn increasing the burning velocity.

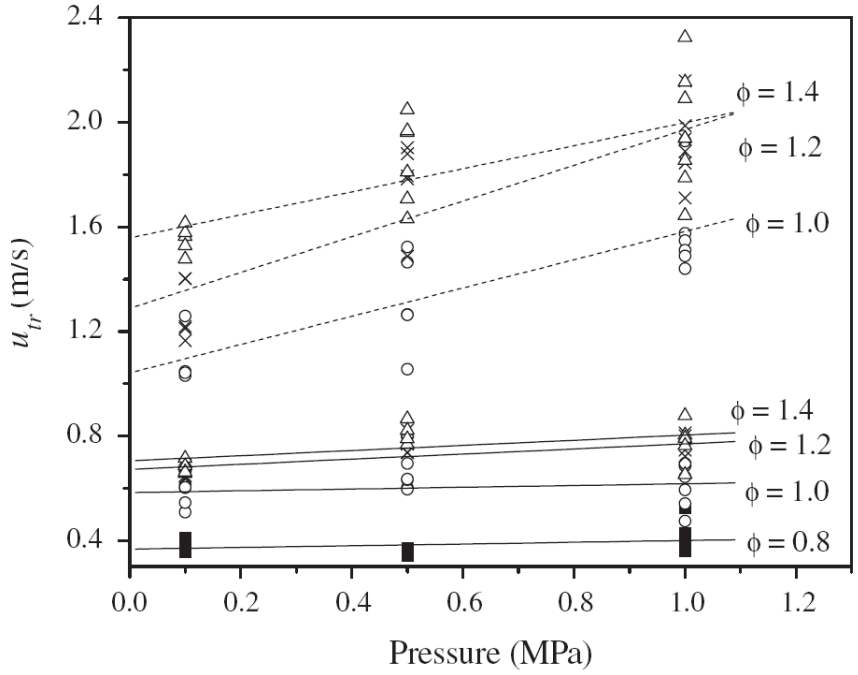

Figure 2.13: The influence of pressure, equivalence ratio and turbulence on turbulent burning velocity, solid lines represent cases at u' = 1.0 m/s while the dashed lines are with u' = 4.0 m/s (Lawes et al. [2012])

Work by Haq et al. [2002] supports that an increase in wrinkling will occur with an increase in pressure, as can be seen in Figure 2.14. Laser induced fluorescence (LIF) images of the flame were taken in a fan stirred bomb. For the same turbulence and mixture composition two tests with initial pressures of 1 and 5 bar were performed; both cases were tested with an initial temperature of 358 K. There was an obvious increase in the wrinkling of the flame for the lower pressure case. At higher pressure the flame is seen to be wrinkled on a large scale; it is clear in this case that significantly increased wrinkling is present resulting in a larger flame surface area vis-á-vis the lower pressure case.

If it is considered that $u_t \propto u_l\, C_{\text{turb}}$, where C_{turb} is considered *a* measure of turbulence, then,while u_l decreases with an increase in pressure, it follows that the turbulence effects must compensate for, and indeed, be greater than the reduction in u_l if the turbulent velocity is increased over and above the laminar condition (as is well known).

Therefore if the relationships: (Liu et al. [2013])

$$u_t \propto u' \text{Da}^{0.25} \tag{2.23}$$

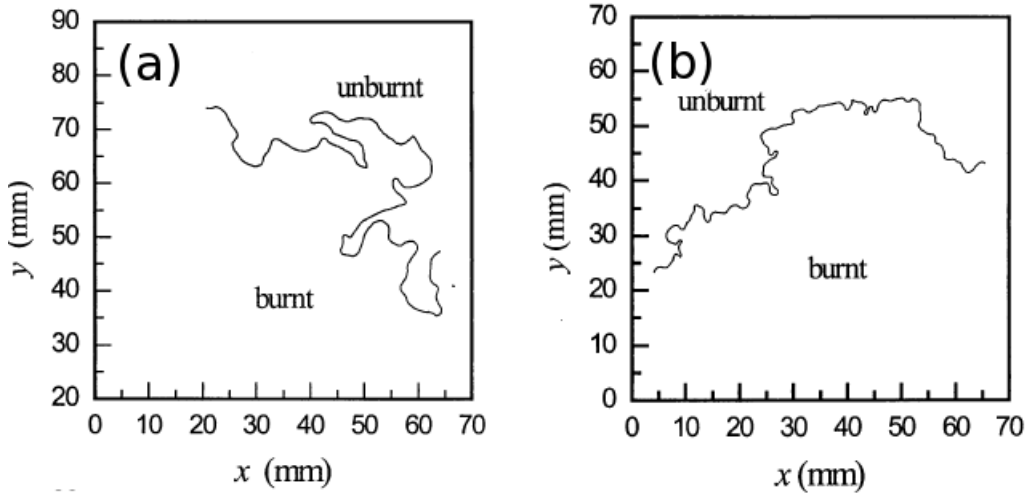

Figure 2.14: LIF image showing flame edges of stoichiometric iso-octane-air flames at ϕ = 1, u' = 1.2 m/s, (a) P = 1 bar, (b) P = 5 bar. Modified from Haq et al. [2002]

$$u_t \propto u' \mathrm{Ka}^{-0.31} \tag{2.24}$$

are assumed, then a larger value of *Da* or a smaller value of *Ka* is required to increase the turbulent burning velocity for a given pressure as u' is considered to be independent of P. From Eq. 2.20 and Eq. 2.19 it can be seen where pressure has influence. Considering Eq. 2.20 only, the LHS is considered independent of pressure, therefore the chemical timescale (RHS) must be responsible for an increase in pressure. The only condition which satisfies a larger τ_{ch} where both values must decrease, is that $d\delta_l/dp$ is $> du_l/dp$. This hypothesis is supported by the work of Haq et al. [2002] who observed that δ_l decreased approximately 1.9 times more than u_l for a 5 fold increase in pressure while all other parameters remained the same. For *Ka* the same situation holds true. However, on the LHS of the expression it is considered that l_λ can be affected by an increase in pressure, $l_\lambda \propto 1 \ / \ P$ In this case the value of *Ka* will decrease for the same $d\delta_l/dp$ to du_l/dp relationship, where this time the RHS term will reduce. The resulting decreased *Ka* results in an increased turbulent burning velocity if Eq. 2.24 is to be satisfied. It appears that the account of pressure influences the turbulent time scale for *Ka* but not *Da* while *Da* will be more influenced by pressure as the LHS of 2.20 does not change with pressure while for *Ka* there is an increase which is opposed to the decrease on the LHS of Eq. 2.19.

Also of consideration is the difficulty in separating temperature from pressure experimentally, and although it is possible to control the initial temperature, the greater density of the mixture will result in higher heat release and higher temperature of the unburned gas mixture which will influence u_l. To satisfy the ideal gas law condition, if

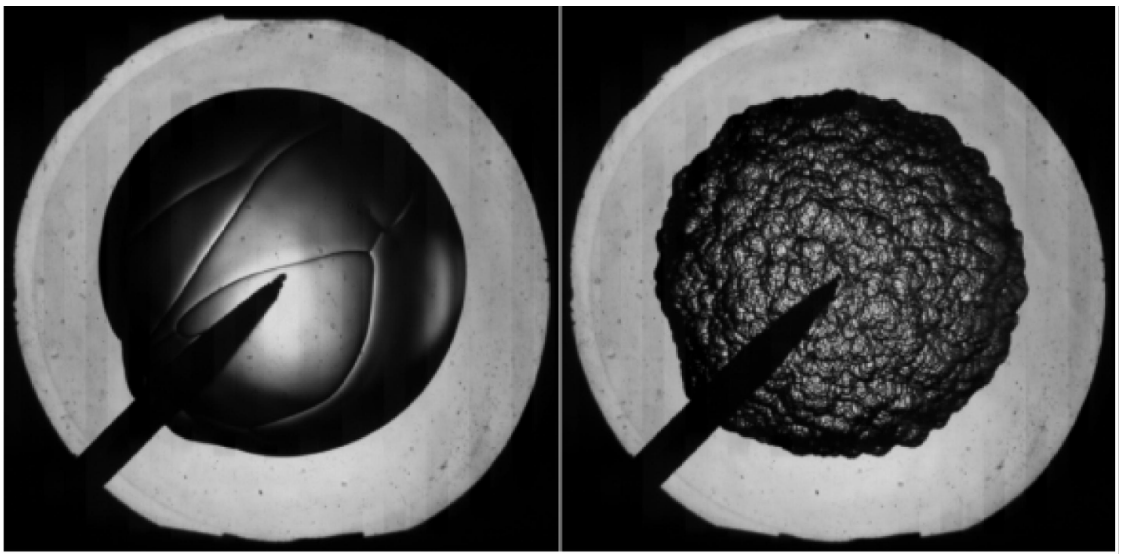

Figure 2.15: Schlieren images of (left) stable heptane-air flame, ϕ = 0.8 and b) (right) cellular heptane-air flame, ϕ = 1.6. Reproduced from Mandilas [2008].

the number of moles and temperature are to be kept constant for an increased pressure, then the volume must reduce (potentially reducing l_i, introducing a different variable into the experiment).

2.3.5 Instability of propagating flames

Laminar flames propagating into a reactive medium can be perturbed by instability and are therefore deemed unstable. For the current work, instability was neither observed or directly predicted. It has however previously been identified that; for the conditions at which the engines in this study were operated (high pressure and with heavy hydrocarbon fuels) the occurrence of instability is highly likely (Mandilas [2008], Tripathi [2012]). It is for this reason that the topic is introduced here while a fuller description can be found in the thesis of Tripathi [2012] or the text of Lipatnikov [2012].

The instabilities can be seen on the topography of the surface in the form of defined cells and ridges (Figure 2.15 (right)); where such a flame is in contrast to a stable flame with few cracks on the surface (Figure 2.15 (left)). Such cellular flames have a larger area vis-á-vis a stable flame and therefore have a larger area - resulting in an increased flame speed. The phenomena which lead to cellularity onset of flames have been identified as hydrodynamic and / or thermo-diffusive instabilities.

The hydrodynamic instability framework was first proposed by Darrieus [1938] and Landau [1944]; as such the instability is referred to as (D-L) hydrodynamic instability.

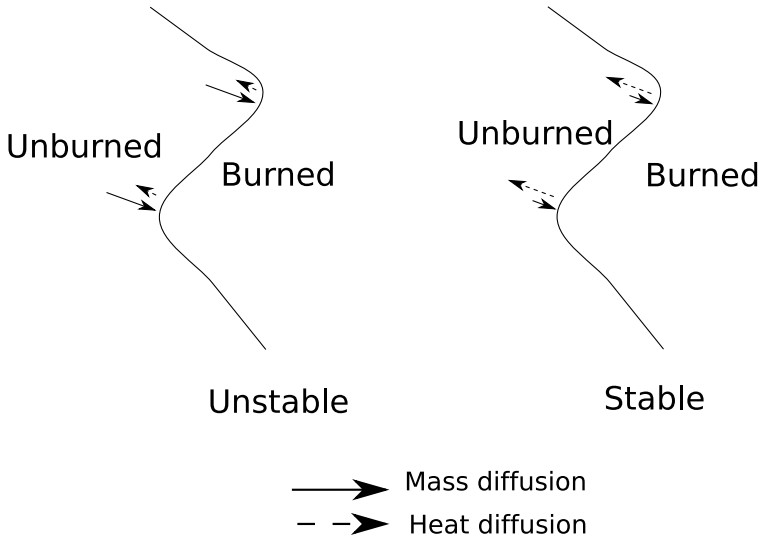

Figure 2.16: Schematic diagram of the thermo-diffusive instability mechanism. Reproduced from Law [2006].

This instability occurs due to the convex and concave nature of a propagating flame; which invokes an imbalance on the rates at which the reactants move towards the flame front depending on whether they approach a concave or convex surface. As the reactant flow slows (at a convex surface) but global burning velocity remains constant, the convex surface protrudes further (Lipatnikov [2012] and Tripathi [2012]).

The thermo-diffusive mechanism involves converging and diverging mass and thermal fluxes at the peaks and troughs of the flame surface. Where the heat diffusion to the unburned reactants is greater than the mass flux to the flame then the flame is stable and vice-versa (see Figure 2.16). Lewis (see Eq. 2.21) number defines a stable and unstable flame where; $Le > 1$ then the flame is stable as the thermo-diffusive instability effects can suppress the hydrodynamic instability. Conversely when $Le < 1$, the flame is unstable as the two instabilities enhance each other (Lipatnikov [2012]). As an unstable flame has an increased surface area, it follows that u_l increases with a decrease in Le. Finally, it has been seen that an increase in pressure and equivalence ratio also increase the tendency for instability; thus it could be said that an increase in pressure should result in an increase burning velocity.

2.4 Autoignition in SI engines

The term autoignition covers numerous events within an engine where the air-fuel mixture spontaneously ignites. Numerous sub-categories can be used to further define spe-

cific types of autoignition events depending mainly on the timing and mechanism by which they occur. Most autoignition events in SI engines are considered undesirable as they can lead to damaging knock which is almost always associated (see Section 2.4.1.1). Spontaneous autoignition of the air-fuel mixture within an engine, is ultimately detrimental to performance and efficiency. If left undiagnosed, continuous knock events will reduce the longevity of components significantly[1]. Autoignition is primarily influenced by the pressure / temperature / time relationship of the combustible mixture. Discussed in this section are the different modes of autoignition as well as factors which influence the onset of autoignition.

The current trend of engine downsizing results in engines which operate under increasingly extreme conditions and the probability of encountering autoignition events is increased. The predominant cause is the increase in pressure that comes from the boosting strategy commonly associated with downsizing, along with the inevitable temperature increase where inter-cooling is not ideal. The ability to predict autoignition is of key importance to the design and calibration stages of an engine program. Completely accurate prediction of autoignition is, however, not currently possible for a number of reasons, examples include: surface hot-spots, oil-fuel interaction as well as mixed distributions amongst others.

2.4.1 Modes of autoignition

The occurrence of autoignition in engines can be defined as the onset of combustion in a reactive medium raised to a definite temperature and pressure, T, P, (Sokolik [1963]). The composition of the mixture is also a crucial factor in the autoignition propensity, however it is the pressure / temperature / time history of the unburned mixture which ultimately determines whether a mixture will autoignite or not. The timing of the onset of autoignition and the events which follow are key factors in determining the mode of autoignition and can suggest the severity of any post autoignition events such as knock.

As detailed in Section 2.3, ”normal” combustion in SI operation involves a flame front which propagates outwards from a point of ignition entraining and burning the unburned air-fuel mixture as it does so. Termination of this flame front occurs by quenching due to the boundary of the chamber. Assuming the propagation of the flame is statisti-

[1]In some engines the onset of autoignition is beneficial, such as in Homogeneous Charge Compression Ignition (HCCI) combustion where the rapid rate of heat release is more efficient; typically HCCI engines operate at very lean mixtures to avoid high amplitude knock waves forming.

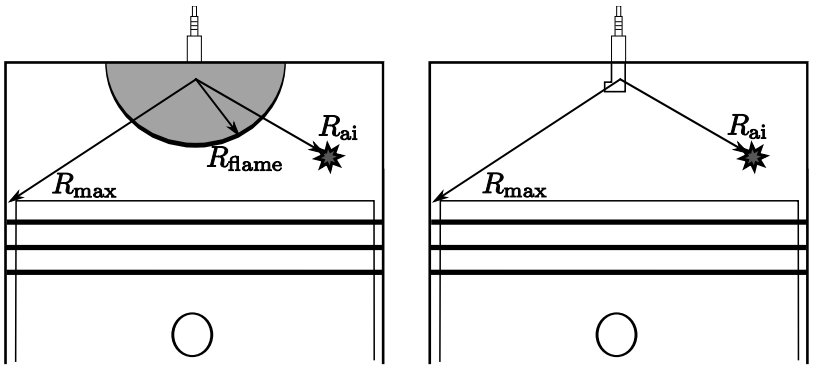

Figure 2.17: Definition of autoignition and pre-ignition; pre-ignition occurs before a flame initiated by the spark plug occurs. Drawing not to scale.

cally spherical[1] then there becomes three distinct radii which can be used for the classification of autoignition; the flame front radius, r_{flame}, the maximum boundary of the system, r_{max} and any given point of a secondary combustion site r_{ai}, separate from the controlled site of ignition or subsequent propagating flame. The three radii, from a 2-D representation can be seen in Figure 2.17. It should be noted that r_{max} is not a stationary point as the transient nature of engine operation results in piston motion and as such a constantly moving boundary. If the temperature and pressure of the unburned fuel-air mixture ahead of the flame front, herein referred to as end gas, are such that a site in the end gas ignites spontaneously, then autoignition has occurred, i.e. r_{ai} can only occur when $r_{flame} < r_{max}$.

2.4.1.1 End gas knock

The onset of autoignition by itself is not necessarily detrimental depending on the timing of the event. It is the onset of propagating pressure waves caused by the rapid heat release which leads to knock. The term "knock" refers to the sound made by the pressure wave oscillating across the combustion chamber caused by the energy release during autoignition. A representative diagram of this process can be seen in Figure 2.18, while a typical pressure trace of a knocking cycle can be seen in in Figure 2.19. The pressure wave amplitude of an associated knock event is said to be proportional to heat release rate and the rate of change of unburned gas temperature; see for example Bradley et al. [1993]; Konig and Sheppard [2004]. It has been said that under high load in Homoge-

[1]Research at Leeds by Abdi Aghdam [2003] and Cairns [2001] found that flames, in engines, seldom propagate in a spherical manner and generally have a preferred propagation path, biased by spark plug orientation and vicinity to valves. However, the assumption of homogeneous and isotropic turbulence within the quasi-dimensional model means the influence of flame shape is less critical than may be assumed.

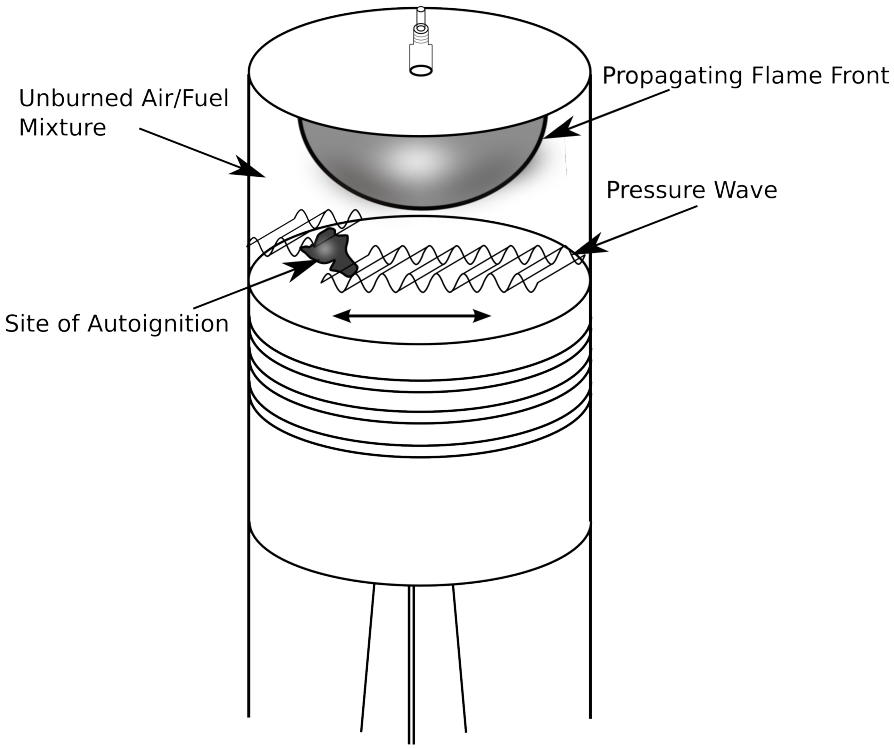

Figure 2.18: A representation of an autoignition site in a disc-shaped combustion chamber. Note, diagram not drawn to scale.

neous Charge Compression Ignition (HCCI) applications when the chemical reactions are too fast, and the combustion is too rapid, the result is a pressure wave that travels back and forth in the combustion chamber (Dahl et al. [2011]). It has been proposed that the pressure waves in HCCI combustion arise from the very fast combustion of a parcel of the air-fuel mixture when the required expansion rate of such a parcel exceeds the speed of sound, resulting in an increase in local pressure; see for example Yelvington and Green [2003].

2.4.1.2 Pre-ignition

Pre-ignition is an autoignition event which occurs prior to the initiation of a flame from a spark, as such $r_{flame} = 0$. In Figure 2.17 a typical pre-ignition event (where autoignition occurs before a spark has been initialised) can be seen. Pre-ignition in SI engines is arguably the most destructive mode of autoignition as the available chemical energy contained within the air-fuel at the point of ignition is at its maximum. Spontaneous release of this energy will result in very high rates of heat release and very high corresponding cylinder pressures. The violent nature of a pre-ignition cycle vis-á-vis a normal combus-

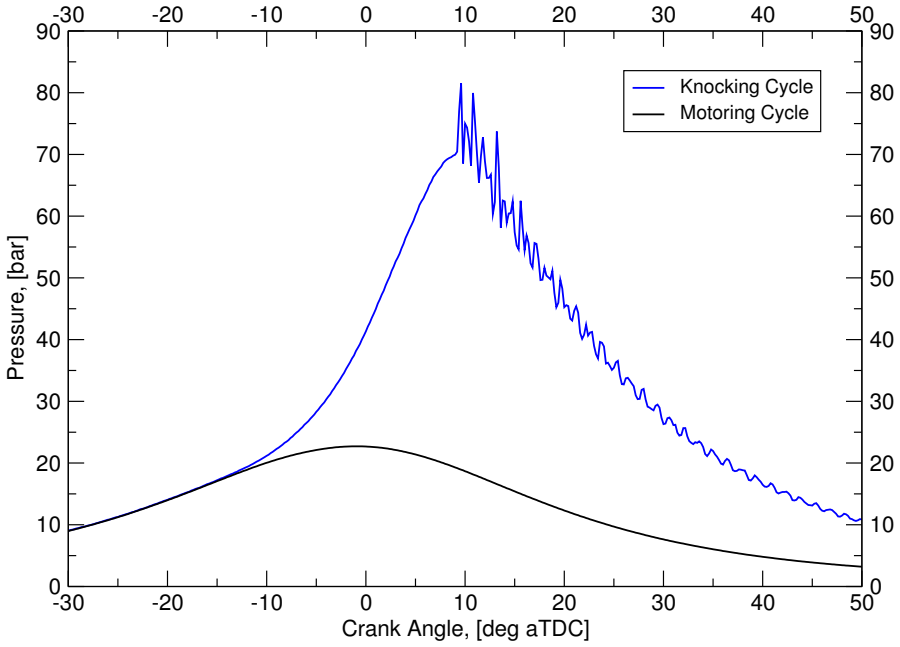

Figure 2.19: A cylinder pressure trace from the LUPOE2-D engine from a "knocking" cycle showing high frequency oscillation. ϕ = 1.0, spark advance 20^o bTDC, 1500 rev/min, iso-octane fuel.

tion cycle can be seen in Figure 2.20. The data presented in the figure was obtained from a four cylinder research engine, introduced in Section 3.6.6.

A feature of these pre-ignition cycles is that, generally, the earlier the pre-ignition event the more intense the pressure oscillations. The release of the chemical energy, and therefore temperature, of a fuel into a smaller volume will result in an increased knock intensity; in an engine the autoignition event is commonly seen to occur near TDC, where the cylinder volume is small. Perhaps the most important feature of all of the pre-ignition cycles is that, although the pressure rise is faster vis-á-vis non-pre-ignition cycles, it is not quasi-instantaneous as is in HCCI combustion; examples of HCCI combustion can be found in the work of Roberts [2010]. This realisation suggests that a self-sustaining flame is initiated, from which a combustion event ensues at an increased rate. Additionally, it allows the type of pre-ignition generally seen to be determined as hot-spot pre-igniting rather than gas-phase pre-ignition. In gas-phase pre-ignition, the pressure and temperature of the fuel-air mixture reaches the point of autoignition, followed by a very rapid pressure rise to maximum as with HCCI combustion.

Two types of hot-spot autoignition exist. The first is caused by local heating of the fuel-air mixture by a surface at elevated temperature; sources include: Exhaust valves, carbon deposits or the spark plug itself. Another type of hot-spot pre-ignition is that

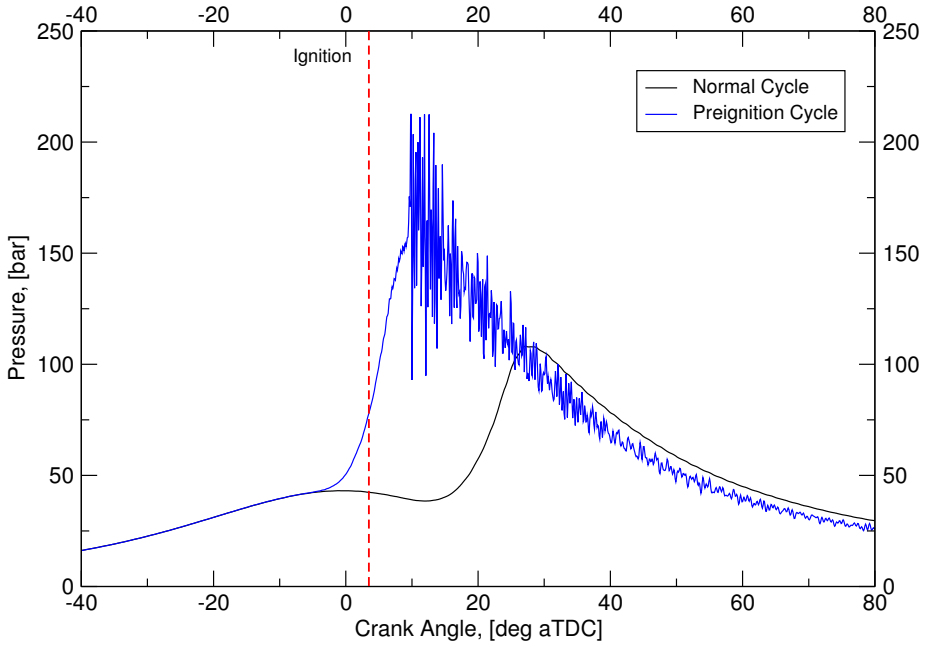

Figure 2.20: An example of a pre-ignition cycle compared to a "normal" combustion cycle. A distinct pressure rise before the spark timing is seen.

which occurs in the fuel-air mixture but not at a fixed location. This could include a heated oil droplet or a pocket of oil-fuel-air which has a reduced autoignition delay time.

It is clear that at higher pressure, as found in downsized engine, pre-ignition becomes significantly worse (Dahnz and Spicher [2010]; Hülser et al. [2013]; Kalghatgi and Bradley [2012]; Peters and Kerschgens [2103]; Zahdeh et al. [2011]). The term "Low speed pre-ignition" (LPSI) has been used in industry owing to the observation that the pre-ignition appears predominantly at low speed full load operation. A significant effort by academia and industrial parties to mitigate pre-ignition is currently being undertaken. The latest findings suggest that it is the interaction between oil-fuel droplets in the gas itself which is causing pre-ignition; see for example Dahnz and Spicher [2010]; Hülser et al. [2013], while Kalghatgi and Bradley [2012] acknowledges the oil driven pre-ignition mechanism. They also suggest that a significant lack of data regarding the autoignition delay times of engine-like oils is a barrier to better understanding of the role that oil may have in LSPI; it follows that research into the oxidation of heavy hydrocarbons (such as lubricant oil) is urgently needed. Despite the better understanding of the mechanism causing pre-ignition, a globally accepted solution to the issue has not yet been found and warrants a heavy industry focus to its solution.

2.4.1.3 Super-knock

The term super-knock has been attributed to the pressure oscillation which follows a pre-ignition event. No specific threshold in terms of an amplitude or $P_{\max}$ has been set to rigidly define an autoignition event. The violence of a super-knock event has been attributed to a developing detonation event (Kalghatgi and Bradley [2012]) The violence of the event is based on the pressure-temperature-time history of the air-fuel mixture, or, more correctly the steepness of the slope where the history of the fuel lies on the autoignition delay time curve, $d\tau/dt$, at the point of autoignition onset.

2.5 Autoignition chemistry

The chemical mechanism of self-ignition of hydrocarbons includes many hundreds of intermediate species formed and consumed in thousands of elementary reactions. The self-ignition occurs when a sufficient amount of active short-living radical species are accumulated in the air-fuel mixture and reactions proceeds rapidly afterwards. For an illustration purpose, fast reaction may mean that the rate of temperature increase exceeds 10^4 K/sec.

The chemical structure of radical species, the accumulation of which leads to self-ignition, depends of the temperature; for low temperatures, below 800-850 K these alkyl peroxides for somewhat higher temperatures, say 800-900 K, these may be hydroperoxides; above this, the autoignition is determined by aldehydes, this is a fairly gradual shift in relative importance of these types of substances with temperature increase (Sokolik [1963]); their importance also depends on the fuel composition.

It should, however, be noticed that under SI engine conditions, the autoignition ahead of the propagating flame commonly occurs at relatively low temperatures and high pressures, corresponding to the alkyl and hydroperoxide mechanism. Below follows a more detailed outline of autoignition chemistry from Griffiths and Barnard [1995]

2.5.1 Reaction mechanism for hydrocarbon oxidation

In this section a simplified reaction mechanism for hydrocarbon oxidation at cool flame and high temperature is presented.

The initiation of the chemical reaction involving a hydrocarbon (RH) and oxygen (O_2) is the abstraction, typically a β-scission of the H atom from the fuel shown by reaction mechanism Eq. 2.25 (Cox and Cole [1985]; Griffiths and Barnard [1995] & Sokolik [1963]).

$$RH + O_2 \longrightarrow \dot{R} + HO_2 \tag{2.25}$$

The radical (RO_2) is the principal propagating species for subsequent acceleration of further reactions with increasing temperature:

$$\dot{R} + O_2 \rightleftharpoons RO2 \tag{2.26}$$

In the low/intermediate temperature region (500-860 K), Alkyl hydroperoxides $(ROOH)$ are formed from the flow intermolecular abstraction by alkylperoxy radicals $(RO2)$:

$$R\dot{O}O + RH \longrightarrow ROOH + \dot{R} \tag{2.27}$$

It is believed that this reaction presents the main reduction in forward rate in the low/intermediate temperature region. Decomposition of the alkyl hydroperoxide is promoted at the weak peroxide bond $(O = O)$:

$$ROOH \longrightarrow R\dot{O} + OH \tag{2.28}$$

The resulting hydroxyl radicals are OH are the major intermediates in high temperature oxidation.

In the higher temperature region, Reaction 2.26 is reversed and $RO2$ generally forms more stable molecules. The combination of oxygen and alkyl radical forms hydrogen peroxides $(HO2)$ which become the principle propagating species.

$$R\,O_2 \longrightarrow alkene + HO_2 \tag{2.29}$$

This results in fuel oxidation as follows:

$$HO_2 + RH \longrightarrow HOOH + R \tag{2.30}$$

$$HOOH \longrightarrow HO + OH \tag{2.31}$$

The resulting hydroxyl radicals are OH, the major intermediates in high temperature oxidation.

A change of the kinetic mechanism from peroxide to aldeyhyde pathways manifests in some intermediate temperature interval where the rate of reaction is seemingly decreased with temperature increase; this interval is commonly referred to as the "Negative Temperature Coefficient" (NTC) region; see for example Burluka et al. [2012b].

2.6 Engine design considerations

The criteria for autoignition or knock has been discussed above in detail, however it is important to conclude that autoignition itself is dependent on the rate of heat release from various reactions occurring during the oxidation of the fuel and the subsequent reactions which follow. Owing to the nature and inclusion of the reaction rates it is implied that the autoignition phenomenon is very much a time dependent one. The end gas heats up because of the cool flame reactions occurring within, as well as from compression by the piston and flame. If, however, the propagating flame were to reach the flame before these cool flame reactions had a chance to develop then autoignition would not occur. Therefore, increasing the speed of the flame would reduce the time that a knocking process had available. The time taken for the flame to travel is influenced by engine design parameters such as the engine bore, spark plug position, piston shape, and cylinder head shape (Poulos and Heywood [1983]).

Compression ratio is a significant factor in the development of autoignition and knock; an increase in compression ratio, above some critical value, will induce autoignition and knock as a result of higher compression temperatures. To achieve very high thermal efficiencies, combustion should be very fast in order to approach the idealised Otto cycle, where heat release occurs at constant volume. However, this is not possible with SI engines owing to the fact that the flame is one which propagates from a point in the chamber to boundaries and to avoid the extreme rates of heat release that would occur if this were possible. Therefore, in reality for a given fuel/air mixture there is a highest useful compression ratio before autoignition and knock reduce power output and efficiency.

2.6.1 Kalghatgi K factor

In the work of Kalghatgi [2001a,b, 2004, 2005]; Mittal and Heywood [2009] the relevance of fuel ratings to ”modern” engines is highlighted. The work draws attention to difficulties in using primary reference fuels (PRFs) to characterise the autoignition propensity of a fuel when it is used in gasoline engines which operate with relatively low temperatures compared to the pressures that they operate at. Mittal and Heywood [2009] explains that the octane index (OI) is defined as the volumetric percentage of iso-octane in the PRF blend (an iso-octane and n-heptane blend) that exhibits similar knocking characteristics. The OI is formally the average of the research octane number (RON) and motor octane number (MON), however it is also correctly expressed as (Kalghatgi [2001a]):

$$OI = (1 - K)RON + KMON = RON - KS \tag{2.32}$$

Where S is the fuel sensitivity (RON - MON) and K can be calculated based on the temperature of the gas when the pressure inside the engine on the compression stroke is 15 bar, T_{comp15}.

$$K = (T_{comp15}0.0056) - 4.68 \tag{2.33}$$

It has been said that when the original RON and MON tests were devised, values of K were approximately 1 (Mittal and Heywood [2009]); therefore the OI was the average of the RON and MON. With modern engines operating lower temperatures compared to their pressure, owing to materials technology, direct injection and turbocharging, values of K are falling; therefore when K is 0, the MON test is no longer relevant. More importantly for the latest series of downsized engines, K values can be negative, which brings about the situation of having increased OI values for a fuel of high sensitivity. In the work of Mittal and Heywood [2008] it is identified that K should increase with engine speed as the RON and MON tests are undertaken at different engine speeds, (900 and 600 rev/min respectively).

2.7 Cycle-to-cycle variability

Cycle-to-cycle variability, (c.c.v) has long been recognised as limiting the range of operating conditions in spark ignition engines(Heywood [1988]) by; eliminating cyclic vari-

ation power would increase by 10% for the same amount of fuel used (Soltau [1960]). Variations in SI engines could be further reduced (in theory) via tighter control of EGR and fuelling, either through tolerances in manufacturing or calibration; high frequency closed loop control systems could also reduce c.c.v by tightly constraining the input variables. The stochastic nature and presence of turbulence however will always introduce an uncontrollable element to the process; by 'persuading' turbulence, at least in terms of bulk flow, to follow a set repeatable pattern, such as swirl and tumble then c.c.v, to an extent, could be reduced (Hill and Zhang [1994]).

2.7.1 Causes of variability

The causes of variability in the combustion process from one cycle to the next, for a given cylinder under "steady-state" operation can be categorised into primary and secondary causes. Primary causes will give rise to a variability in engine performance owing to the stochastic nature of combustion defining variables, primarily, mixture composition (spatially and globally), and variations in the flow field, primarily u' (Burluka et al. [2012a]; Larsson [2009]; Stone [1999]). Secondary causes can be given as being those which will have an influence on the combustion rate of the next cycle; primarily residuals not expelled from the cylinder during the exhaust stroke of one cycle and are therefore present for the following. Such prior cycle residuals can become relevant in forthcoming cycles for several reasons: a reduction of u_l will naturally induce increased variability owing to reduced chemical lifetimes, an increase in heat for the intake charge reducing density are usually observed at lean combustion conditions.

A comprehensive literature review by Ozdor et al. [1994] has identified that cycle-to-cycle variations are especially influential in the local region around the point of ignition because of their influence on early flame propagation. These fluctuations lead to imperfect mixing, partial stratification, random convection of the spark kernel away from electrodes and random heat transfer from the burning kernel to the spark electrodes. When the flame is in its infancy, it is heavily influenced by the local environment, and more relevantly stochastic variations in the local vicinity. As the flame radius grows the effect of locally rich/lean high/low turbulence zones cancel out owing to LLN theory[1] (Larsson [2009]). In Figure 2.21 an illustration of LLN theory applied to a growing flame

[1]LLN theory (Law [of] Large Numbers) states that for a given experiment which has a probability <1 then the observed probability should converge to the expected probability (i.e. the mean value) for a larger trial set. This theorem can equally be applied to local inhomogeneity in engine combustion

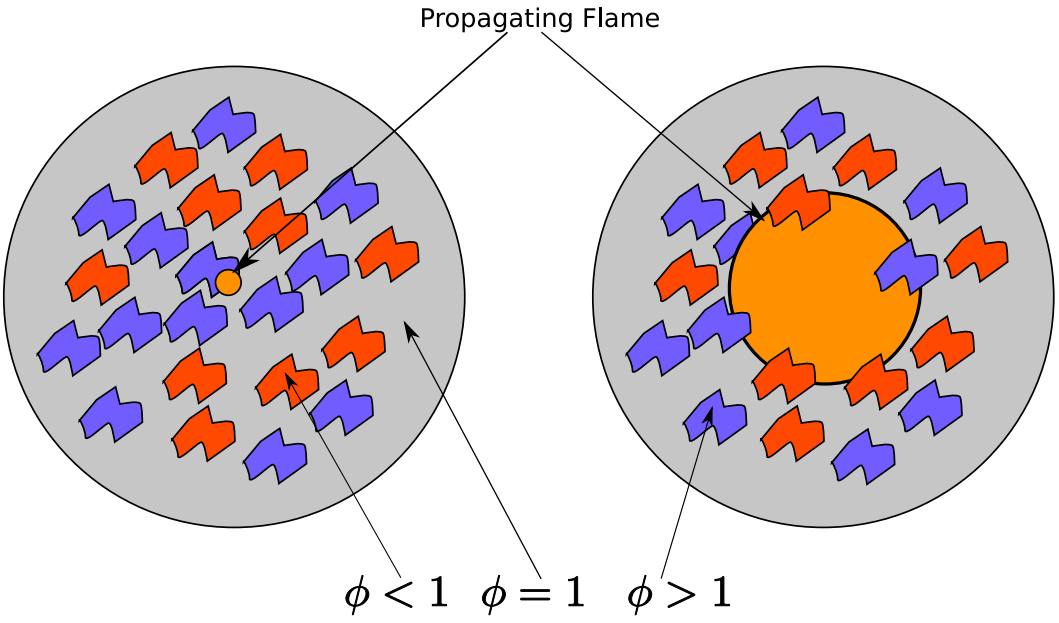

Figure 2.21: The interactions of the flame fronts of a small flame and a larger flame with locally rich and lean pockets of air-fuel mixture.

in a cylinder can be seen. The flame front of the larger flame will statistically experience a global ϕ closer to the mean value of 1 than the smaller flame.

On the discussion of the influence of ϕ work by Gürbüz et al. [2013] identifies a strong relationship between ϕ and variability for both "gasoline" and hydrogen. The culmination of the work can be seen in Figure 2.22 where the leanest $\phi = 0.8$ and richest $\phi = 1.3$ gasoline mixtures are seen to exhibit a larger level of variability, based on the distribution of maximum pressure P_{max} and crank angle location of maximum pressure, θP_{max} , than the lowest distribution case, $\phi = 1.1$ this would suggest a link between variability and u_l, also known to have a maximum value at the slightly rich conditions. The "Slow-burn" and "Fast-burn" labels on the figure appear to be erroneous however as they suggest a low pressure cycle with a late θP_{max} are "Fast" cycles.

Lipatnikov and Chomiak [1998] applied a simplified turbulence diffusion model to investigate the effects of turbulence on the early stages of combustion, with the aim of showing that the active eddy size, l_x is on the order of $fr_{ign} > l_x > \delta_L$ where fr_{ign} is the radius of the flame kernel. For engines it could be assumed that this is a value in the range of a small l_i or large l_λ scale. The investigation focused on:

- The straining of the kernel as a whole by random velocity gradients, increasing/decreasing the strain of a flame will increase/decrease heat transfer where a flame which is too cool may quench, a strain rate which is too large may cause a convec-

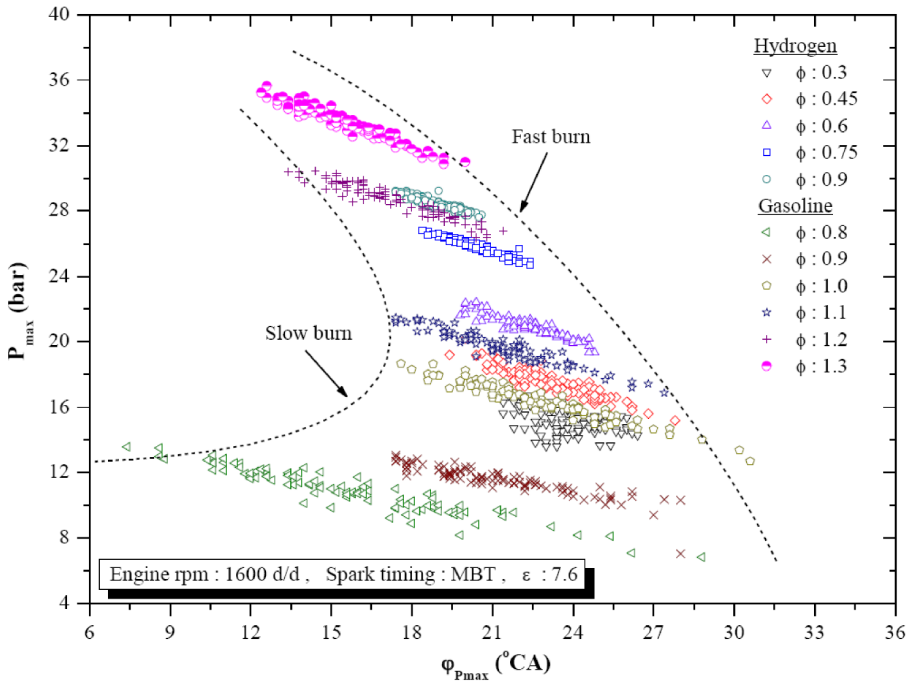

Figure 2.22: Influence of ϕ on peak pressure and location of peak pressure distributions for gasoline and hydrogen air-fuel mixtures. Modified from Gürbüz et al. [2013].

tion of the flame away from a point of high strain for laminar flame (Darabiha et al. [1986]).

- Random fluctuations of small-scale turbulent diffusivity.

It was predicted that there exists a strong relationship between small-scale turbulent diffusivity and the kernel growth history. A strong dependence of burning rates on small scale turbulence was also seen, experimentally, by Hill [1988] who noted that the deviation in burning times were dependent on l_λ which was estimated based on l_i (as in Eq. 2.16). Recent studies however using Particle Imaging Velocimetry (PIV) on a quiescent flow engine at the University of Leeds has suggested that small scale motion is possibly not the dominant cause of variability in engines, it was seen that u_t is strongly dependent on u', but less so on length scale.

Variability of combustion is not solely limited to the influence of small scale eddies which will affect early flame growth, although it is reported to be the primary cause of variability. The effect of large scale motion and the mean flow field into which the flame propagates has also been seen to have considerable influence on burn rates . An observation confirmed by the work of many researches; see for example Burluka et al. [2012a]; Matekunas [1983]; Ozdor et al. [1994]; Stone [1999]. It is also proposed that the mean flow may have a superior influence on slow flames vis-á-vis faster ones as reviewed

by Hussin [2012] where he reports of experimental work that shows larger bulk motion (swirl or tumble) reduces variability. The reason for increased variability is owing to the longer time for slow flames to experience the flow field.

A final interaction upon which variability can be reported is the flame-wall interaction. Owing to the non-spherical nature of propagating flames in engines (Cairns [2001]) it is clear that there will be regions of the flame that contact and quench on the wall before others, this will be especially true for convected flames. It has been reported by Hill [1988] that interactions with the wall modify the standard deviations in the pressure but do not wholly account for, or greatly contribute towards cyclic variability in engines.

2.7.2 Modelling of variability in SI engines

Modelling of premixed combustion variability can taken on several forms which can be generalised:

- Models which account for the primary and secondary causes of variability discussed in Section 2.7.1 from first principles and whose outlet conditions become boundary conditions for subsequent cycles.
- Empirical relationships based on experimental data for a given set of conditions.

Larsson [2009] identifies three categories for variability modelling, CFD models, flow dispersion models and finally, calibrated models. CFD models are considered to be of limited practicality to variability studies for the indirect reduction of applicability by reduction of computational time, that is, reducing the CFD to a RANS model (see Section 2.2.4 for RANS and other turbulence models discussed here) which use averaged values of turbulence by definition will be of little applicability to variability models. Similarly LES models simplify the flow field to contain only the largest scales, unreliable for the solution of sub-grid scales based on the observations discussed in Section 2.7.1. However the work by Burluka et al. [2012a] may lead to renewed research in this area. DNS models would be impractical owing to solution times. The use of the deterministic LES solution would require variability of the boundary conditions to invoke variability in the turbulence quantities.

For a discussion on flow dispersion model, the interested reader is directed towards Larsson [2009] (Section 3.3.3 in the aforementioned work). The use of calibrated models, that is to say, a model which one or two variables (considered to have the largest

effect on variability) are randomly varied from cycle-to-cycle to statistically match the averaged values of an experimental data set (a further discussion on the variability quantification is presented in Section 5.2). A model of this type is the focus of the present study and a detailed overview of the model can be found in Section 3.4.4.

Dai and Lu [1995] assesses numerous model types and their application to variability modelling. They dismissed a Monte Carlo[1] based approach owing to computational time, although they noted that to accurately replicated variability seen experimentally it was necessary to vary: kernel size, kernel displacement by convection and global u'. They determined that a random number generator approach was feasible provided the exact perturbation of each variable was well quantified. They determined that a regression model approach gave the best correlation with experimental data. The use of such a model, although useful in industry, is not ideally suited for research purposes. The model they tuned to engine data ultimately consisted of 6000 data points from 13 engines. Seven main parameters were used as inputs including: engine speed, IMEP, ϕ, EGR, Burn 10%, Burn 90% and CA50. In this sense the model is not predictive for engine conditions or configurations outside of those used for data input; intake pressure was not a parameter used.

Aghdam et al. [2007] introduced a variability model within the quasi-dimensional combustion model, LUSIE; the detailed description of which is reserved for Chapter 3. In their work, a variation of two parameters, ϕ and u', at the point of ignition was invoked. The subsequent effect on the rate of combustion was seen to be in-line with experimental cycles. Variation of ϕ and u′ was Gaussian with standard deviation of 5% and 12.5% for ϕ and u' respectively. The work by Aghdam et al. [2007] is extended in this thesis; a discussion of the model used is in Section 3.4.4, whilst predictions of variability for four different engines can be found in Chapter 5.

2.7.3 Influence of pressure on variability

In downsized engine applications, where higher pressures are present, there will likely be an influence on variability. Literature on the subject of pressure and variability in boosted engines is sparse. From a fundamental view however it has been reported that small scale turbulence is responsible for combustion variability; small scale turbulence

[1]In Monte Carlo simulations a number of possible results for a given situation are assessed by substituating values with a certain probability distribution for a factor that has uncertainty. The simulation then calculates the results over and over again, for each new calculation a different set of values from the distribution are used. Monte Carlo simulations can become extremely computationally heavy as they may involve tens of thousands of recalculations prior to completion.

on the order of l_λ is known to scale inversely with pressure. Additionally, faster burning rates are said to positively reduce variability; it is known that an influence of p on u_l and u_t exists, which will likely result in a change in variability. Simulation results from Lipatnikov and Chomiak [1998] show that early flame development effects are enhanced with a decreasing laminar burning velocity, suggesting an increased pressure will have a negative effect on the early stages of combustion.

Samuel et al. [2010] investigated cyclic variability on a boosted and non-boosted engine. The former operating with a gasoline direct injection system, while the non-boosted engine operates with a single-point throttle-body mounted fuel injector (TBI). A simple COV analysis of several combustion parameters, BMEP, CA50, peak pressure and location of peak pressure were performed in addition to crank resolved variability. The conclusions were as follows:

- COV analysis using COV of pressure against crank angle provided more insight into the cyclic variations that happen during different sections of the cycle which could not be seen with the conventional mode of analysis. It also showed that the minimum value for COV of pressure at the end of compression stroke is independent of the engine load and type.
- The maximum value of COV of pressure during combustion had a strong relationship with the load and speed for the boosted engine while it had a weaker relationship for the TBI engines.

A comparison of 30 cycles (from a 200 cycle set) captured on a boosted research engine, called UB100, (introduced in Section 3.6.6) and a non-boosted production engine, called AJ133, (introduced in Section 3.6.5) can be seen in Figure 2.23 and Figure 2.24 used in the main body of this work (see Section 3.6.4). Variability is clear to see between concurrent cycles, most notably, the maximum pressure value. It can be seen that there is a reduced variability in P_{max} for the boosted condition; the reduction in variability is discussed further in Chapter 5, while it is thought that the faster turbulent mass burning velocities in the UB100 engine lead to a reduction in the variability.

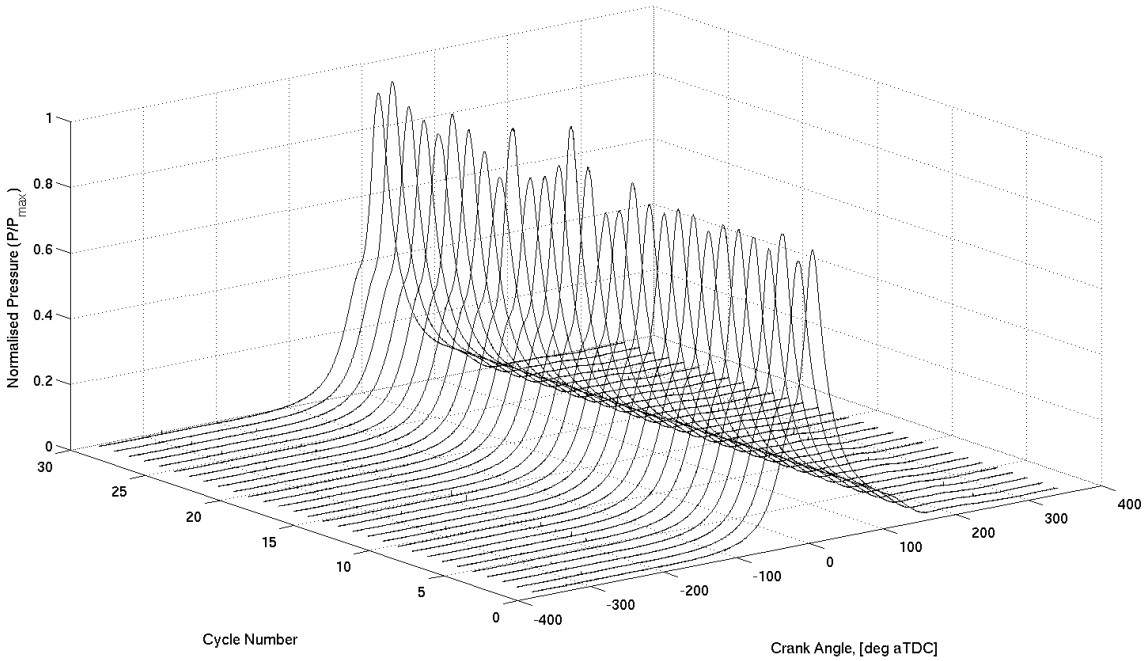

Figure 2.23: 30 cycles from a non-boosted GDI production engine. The variation in the normalised pressure (by maximum pressure) is seen to be large, COV_{IMEP}=2.4% (200 cycles).

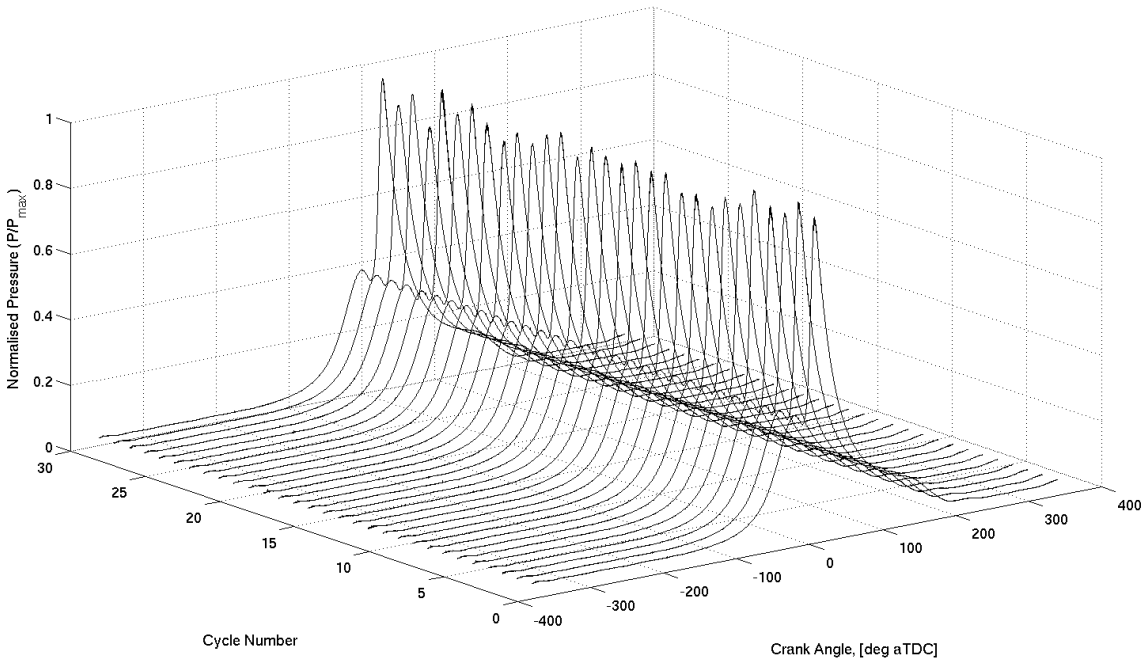

Figure 2.24: 30 cycles from the boosted UB100 production engine. The variation in the normalised pressure (by maximum pressure) is seen to be smaller than the non-boosted AJ133 engine, COV_{IMEP}=1.8% (200 cycles).

Chapter 3

Combustion code and engine description

3.1 Introduction

A quasi-dimensional thermodynamic code for use in the prediction of combustion in spark ignition (SI) engines has been under development at The University of Leeds for the past 30 years. The culmination of the compiled code is referred to by the acronym LUSIE ([the] **L**eeds **U**niversity **S**park **I**gnition **E**ngine [code]).

Thermodynamic modelling of engine cycles before the inception of the LUSIE code at Leeds was limited to equilibrium cycle models for single and divided chamber engines (Desoky [1981] and Al-Mamar [1986]). The limitations of assuming instantaneous heat release to account for a highly transient process were realised during the early modelling work at Leeds. It was not until an account for combustion-rate and heat transfer processes were included by Hynes [1986], that the foundations of the LUSIE code were set out. Since the inaugural work, LUSIE has been developed significantly and now includes two zonal model types as well as expressions for flame development. In addition, a number of supplementary routines have been included to more accurately quantify the combustion process. These include accounting for: blow-by, flame geometry, turbulence, autoignition

as well as multiple ignition sources[1] (Bradley et al. [1988], Abdel-Salam [1992] Merdijani and Sheppard [1993], Langridge [1995], Cairns [2001], Abdi Aghdam [2003] and Hattrell [2007]).

3.2 LUSIE Simulation Software

3.2.1 Overview of the software

The primary application of the LUSIE code is to predict thermodynamic processes which occur in two and four-stroke spark ignition engine cycles. Of the five main phases which make up the four-stroke cycle, the LUSIE code iteratively models only the compression, combustion and expansion strokes i.e. a closed system[2]. The intake and exhaust processes are modelled in terms of the inducted mass, assuming the flow rate into the engine is constant throughout the intake and exhaust periods. The inclusion of mass rates is to provide initial conditions to the zero-dimensional (0-D) $k - \epsilon$ turbulence model.

The LUSIE code is governed by thermodynamic laws and is therefore grouped into the zonal modelling set. This is in contrast to fluid-dynamic governed models, generally solved via techniques found in CFD solvers. Moreover, LUSIE can be classified as a quasi-dimensional model, a sub-set of thermodynamic models. A quasi-dimensional model is not limited to an exact "dimension" as such, for example, it would use the 3-D flame geometry information and convert it to a single value of flame volume in 1-D. It is correct to classify LUSIE as a quasi-dimensional model when the two or three-zone models are used for solution (Section 3.2.6.1 and 3.2.6.2 respectively). When the Wiebe model (Section 3.2.5) is used for "predicting" the burn-rate, it is a 0-D model where no attempt to quantify the physical processes during combustion is made.

A full account of the numerous thermodynamic, fluid dynamic and dynamic processes occurring within an engine cycle is beyond even the most detailed simulation techniques. The functionality of the LUSIE code is to separate a "real" combustion process into a number of sub-processes, as well as discretizing the cycle into smaller time-steps, for which solutions are found; it is the sum of the sub-processes which accounts for the

[1] This specific area of modelling is currently a work-in-progress. The intention is to have a robust account of the propagation of separate flames within the cylinder, this particular work requires the use of GGEOM, (Section 3.2.12).

[2] Although the system is theoretically closed, the occurrence of blow-by in engines means this cannot be realised. An account of this is included within LUSIE and discussed further in Section 3.2.10.

cycle as a whole. Although these processes occur simultaneously in the actual engine cycle, numerically, they are solved consecutively.

The most recent significant contributions to existing LUSIE code, by this author, include the 0-D $k - \epsilon$ turbulence model (discussed in Section 3.4.2) and the inclusion of a cycle-to-cycle variability model, based on the polar Box-Muller transform (Section 3.4.5). Other researchers have included a routine to account for flame-geometry in complex pent-roof applications (LUSIE was previously limited to idealised pent-roof systems only) (Hattrell [2007]) and recently, a more comprehensive kinetic autoignition model to account for surrogate fuel use (Khan [2013]).[1]

The LUSIE code is compiled with either Intel or Sun compilers and until recently, was primarily written in Fortran 77 (though Hattrell has since migrated almost all of the code to Fortran 90). There are a number of features in Fortran 90 not available in Fortran 77, a list of which can be found on the National Supercomputer Centre website [accessed 28^{th} April 2013]. The primary reason for the upgrade to Fortran 90 was to account for the modular programming framework (Hattrell [2007]); presumably for reasons such as introducing an alternative for the potentially problematic 'COMMON' statement, which requires careful tracking in relatively large compiled codes such as the LUSIE software. Fortran versions later than 90 were considered, however it was felt that the new features would not enhance the operation of the LUSIE code significantly enough to warrant a second migration of the code.

3.2.2 LUSIE software operation

Operation of the LUSIE code is currently via command line interface which, when combined with a Unix environment, provides the potential for powerful pre-processing and post-processing. A number of input files, in text format, are used to specify: the engine geometry, input conditions, model types and flame geometry tables. The output files are also in text format and are column separated, allowing them to be exported to a spreadsheet environment or processed directly from the raw output file.

[1] At the time of writing the latest generation of autoignition models are currently being integrated within LUSIE and are undergoing validation but have not been included in any autoignition studies presented in this thesis.

3.2.3 Motoring process

The motoring cycle, simulated by the LUSIE code involves the prediction of the crank-resolved compression and expansion phases, assumed to be isentropic. The use of a motoring cycle as a pre-requisite to a firing cycle within a LUSIE simulation has, historically, been because of the need to establish a non-combustion event heat transfer profile over the cycle as used by the Woschni heat transfer model described in Section 3.2.11, when the system is split into more than one zone. With the introduction of the 0-D $k-\epsilon$ turbulence model, described in Section 3.4.2, a further application of the motoring cycle was utilised. The motoring process now takes the final Turbulent Kinetic Energy (TKE) value from the motoring cycle prediction and uses it as the initial condition for the preceding firing cycle. In addition to calling the heat transfer and turbulence routines, the blow-by routine is also called during the motoring process as a pressure difference exists between combustion chamber and piston rings, albeit at a reduced magnitude vis-á-vis a firing simulation.

3.2.4 Firing process

Provided the equivalence ratio is non-zero, then a firing cycle will proceed the motoring one. As with the motoring cycle, the solution of the firing cycle is achieved by solving individual routines sequentially. Unlike the motoring cycle where the calculation of compression or expansion does not include any timing marks, checks are required to be made on the current crank angle, θ, to determine whether or not the combustion specific routines should be invoked, i.e. when $\theta = > \theta_{ign}$. Once the condition for ignition has been met, then a routine which creates a spark kernel of pre-defined size, is accessed. An initial "delay period" follows, intended to account for a delay seen experimentally, where the formation of a kernel and subsequent time taken to form a self-sustaining flame to form is of transient nature. The delay time is specified as an input value based on experimental analysis, rather than calculated (Abdi Aghdam [2003]).

The combustion process in an engine operates in a turbulent regime, as well as in a system where the boundary conditions are different at each time-step. Quantifying this process is, therefore, non-trivial; nevertheless there are a number of solution methods available within LUSIE which can be applied to this problem as briefly mentioned previously. A high-level overview of the different models will be included here. A more comprehensive and descriptive review found in the thesis of Hattrell [2007].

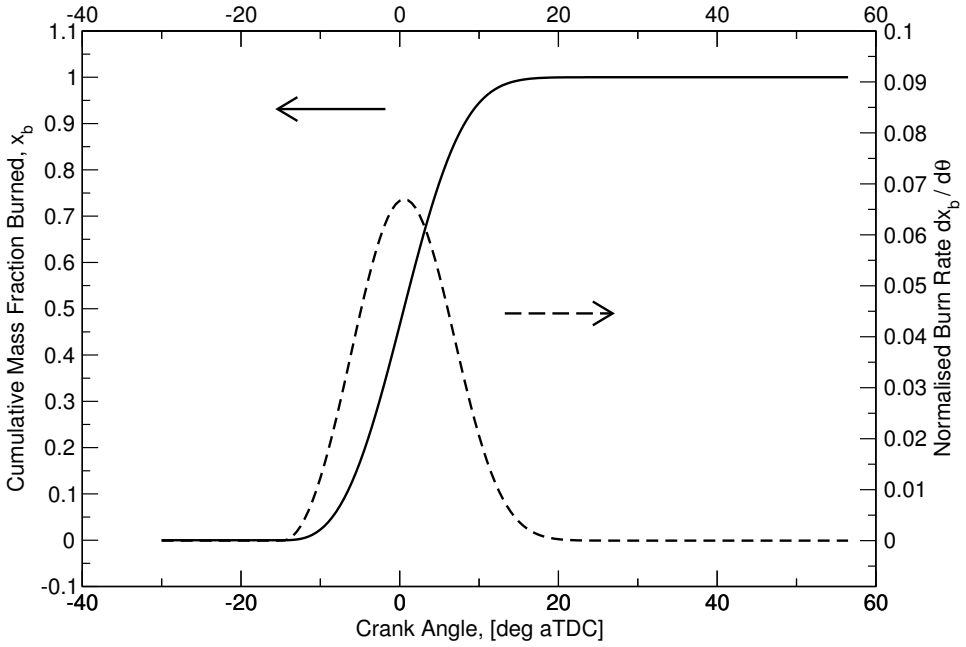

Figure 3.1: Fuel burn rate and cumulative mass fraction of fuel burned, as given by the Wiebe model. Constants of a and m are 5 and 2 respectively. Ignition is set at 12^o bTDC

3.2.5 Zero dimensional modelling

The zero dimensional model used within LUSIE is the Wiebe (more correctly it is Vibe after the original author) model (Vibe [1964]), shown in Eq. 3.1.

$$x_b = 1 - \exp\left[-a\left(\frac{\theta - \theta_{ign}}{\Delta\theta}\right)^{m+1}\right] \tag{3.1}$$

$x_b(\theta)$ is the cumulative mass fraction (of fuel) that has been burnt since the point of ignition θ_{ign}[1], $\Delta\theta$ is the total burn duration, while m and a are constants. The fraction of fuel burned, as a function of crank angle, produces an "S-shaped" profile which can be tuned to an experimentally derived, crank-resolved mass fraction burned (MFB) curve by adjustment of the model constants. An example of a predicted mass fraction burned curve, and associated burn rate curve is shown in Figure 3.1.

The Wiebe model has limited use in predictive simulations as, it requires prior knowledge of the burn rate to correctly fit a prescribed profile. It is however computationally efficient and can be used to great effect if experimental data is available. The

[1]Caution should be used when considering the point of ignition. The Wiebe model will "predict" that the start of mass burn is at the point of ignition, while it has been seen experimentally that there exists a delay in time between the point of ignition and the time at which the fuel begins to be burnt.

predicted mass fraction burned, at a given time-step, can be used to predict the gas temperature rise which can then be related to the in-cylinder pressure via the first law of thermodynamics.

3.2.6 Zonal modelling

Zonal modelling, as the name suggests, involves splitting the combustion chamber into discrete zones[1]. With flow motion assumed to be isotropic, the primary identifier for different zones is the state of composition, i.e. whether the fuel-air mixture is burned or unburned in a particular section. There are sub-models which are common to both zonal models, but which are not used in the Wiebe model (Section 3.2.5). Both of the zonal models predict the rate at which unburned fuel-air mixture is converted to heat by considering the process physically. In the case of the two-zone model this is expressed as a mass rate of fuel burned, Δm_b. The three-zone model, with the additional zone has two separate mass based rates, Δm_b as well as a mass based rate at which the fuel is entrained into the flame front, Δm_e, see Figure 3.2. Intricacies of these two rates, will be discussed in more detail in Sections 3.2.6.1 and 3.2.6.2.

The model operation is similar between the two zonal models as such they share routines. Information required for exclusive use by the three-zone model includes: the entrained flame radius, $\mathrm{fr_e}$, as well as a characteristic combustion time τ_b, discussed further in 3.2.6.2. Somewhat unintuitive is the situation where the flame properties are required in both models, for example the flame area[2]. The main sub-routines shared by both zonal models are: Laminar burning velocity, u_l, rms turbulent velocity, u', integral scale, l_i, a turbulent burning velocity; either of the burned gas, or the entrainment velocity (u_{tr}, u_{te} respectively), the flame development factor f_d and flame deceleration factor, f_w. Each of these individual models will be introduced in further detail in the following sections.

[1]Splitting the chamber into zones should not be confused with a meshing process such as used in CFD where the volume is split into small, but finite, packages of information define the system and are solved by continuity equations

[2]Although there is no flame, as such, predicted in the two-zone model. A knowledge of the flame area is required to represent the boundary between burned and unburned gas for use in Eq. 3.2

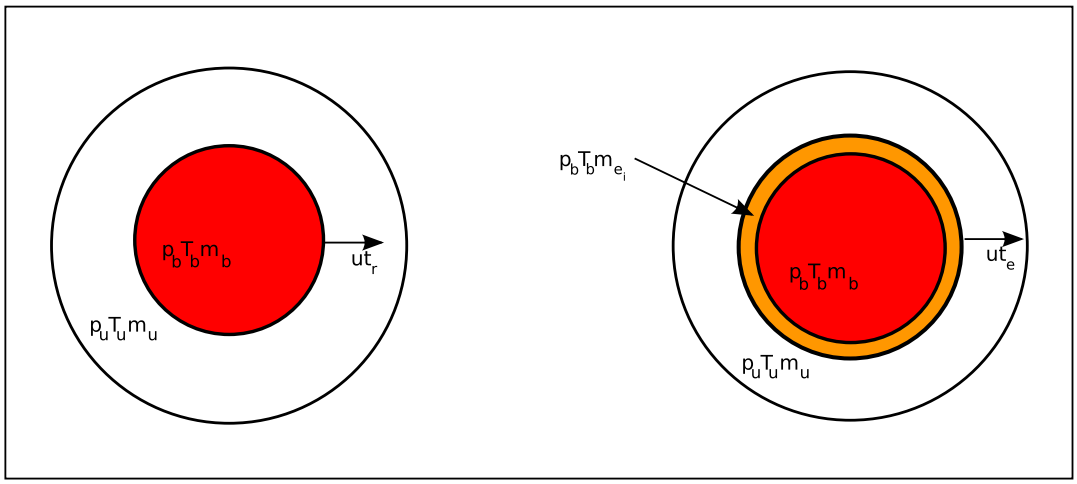

Figure 3.2: A figure representing the two-zone and three-zone modelling definitions used within LUSIE.

3.2.6.1 Two-zone modelling

The two-zone model is the simpler of the two zonal models within LUSIE. As suggested by the model name, the combustion chamber is split into two separate zones; one containing burnt gas, the other containing the unburned fuel-air mixture. An account of the flame itself is not made and therefore any interaction involving a flame is not actively considered. The rate at which the unburned mixture is converted to burned products is determined by a turbulent mass burning rate, u_{tr}. As the combustion process is lumped into a single rate reaction, prediction is strongly dependent on the expression used to determine u_{tr}. The amount of fuel burned at a given time-step, Δm_b, is given by :

$$\Delta m_b = \rho_u A_{fr} u_{tr} \tag{3.2}$$

Where u_{tr} is the developing burning velocity with the active area of the burnt gas front, A_{fr} and density of the unburned gas, ρ_u.

3.2.6.2 Three-zone modelling

The three-zone model formulation is an extension of the two-zone model and is based on the work of Blizard and Keck [1974]. Like the two-zone model, it predicts burned and unburned gas zones. In addition to these two zones, the three-zone model also accounts for the existence of a flame, across which combustion takes place. The introduction of a flame of finite thickness, δ_t, is an attempt to improve accuracy by predicting the physical

processes occurring across the flame. The assumption is that individual eddies of a fuel-air mixture are entrained, i.e. brought into the propagating flame front which is travelling at a progressing velocity, u_{te}. After being entrained, they are "burned" at a rate controlled by the characteristic "burn-up" time, τ_b, which is controlled by the ratio of turbulent eddy size to the laminar flame speed (Eq. 3.5). There exists two separate burning rates in the three-zone mode a) the velocity of the flame front, b) the velocity of the burned gas. The rate at which the fuel-air mass is entrained into the flame at a given time step, is defined according to:

$$\Delta m_e = \rho_u A_{fe} u_{te} \tag{3.3}$$

The noticeable differences between Eq. 3.2 and Eq. 3.3 are that the burning velocity driving rate is based on the rate of entrainment and therefore represented by the flame front, rather than the burned gas reaction front. Clearly the active area definition also changes to represent the flame. The rate at which fuel is burned, for a given time-step, is given by:

$$\frac{dm_b}{dt} = \frac{m_e - m_b}{\tau_b} \tag{3.4}$$

where τ_b is given by

$$\tau_b = C_{\tau b} \frac{l_e}{u_l} \tag{3.5}$$

Where $C_{\tau b}$ is a proportionality constant and is the second user-definable constant in the three-zone model. The characteristic burn-up time can be defined as the time taken for a turbulent eddy to burn. It is a function of the size of a turbulent eddy, l_e, and the laminar burning velocity, u_l. The choice of the size of eddy to use in the burn up definition has been a point of discussion both within the University of Leeds as well as in the combustion modelling community. Work at Leeds has previously used the integral scale, l_i, to define the burn-up time (Abdi Aghdam [2003] and Hattrell [2007]). The original model proposers Blizard and Keck [1974] correlated their model to experimental data and used a scale size which varied with the intake valve lift. Later, Keck adapted the model by taking the integral length scale to be the characteristic eddy size (Keck et al. [1987]). The turbulence structure suggested by Tennekes and Lumley [1972] was introduced into the entrainment model which considered the involvement of the three major scales, integral, Taylor, l_λ and Kolmogorov, l_η in the entrainment and burn process. The Taylor scale

was assumed to be the characteristic size at which laminar diffusion was an important consideration and was therefore used by Tabaczynski et al. [1977] and Tabaczynski et al. [1980] in their burn-up definition. The Taylor scale, is also used in commercial software packages Gamma-Technologies [2012]; the application of this scale to boosted engines is considered in Section 4.3.1.

3.2.6.3 Zonal modelling discussion

Work conducted by Hattrell [2007] using the LUSIE code, concluded that the two-zone model offered simplicity above the three-zone model, not only computationally, but also in terms of data input as the two-zone model is not so sensitive to turbulent length scale information (which is difficult to obtain experimentally). Additionally the two-zone model could, philosophically, be seen as possessing higher integrity by limiting the adjustable constants to only one, A, in Eq. 3.12.

The two-zone model calculation of turbulent burning velocity, u_{tr}, is more sensitive to flame acceleration vis-á-vis the three-zone model. It may appear philosophically awkward that the model, which is devoid of a direct account of the flame should be sensitive to its predicted progression, while the model which implicitly includes it, is less so. It should be remembered however that in the two-zone model the rate of mass burned is directly proportional to u_{tr}. In the three-zone model however, the mass of fuel burned (therefore heat release) is based on both u_{te} and also burn rate. It can be thought of that u_{te} (influenced by the flame development) determines the upper limit of the amount of fuel that could be burned, while the amount that is burned is driven by eddy size and laminar flame speed. The burning rate will only be influenced by the entrainment rate if dmb/dt $>\Delta m_e$. The entrainment and burning processes will proceed at different rates in the three-zone model. Conversely, in the two-zone model, development of burning velocity, is directly proportional to the mass of fuel burned (Eq. 3.2).

3.2.7 Laminar burning velocity

The unstretched laminar burning velocity, u_l, is used in both zonal models for the calculation of a turbulent burning velocity in Eq. 3.12 as well as being used in Eq. 3.3 to control the rate of mass burn in the three-zone model. A number of studies have been undertaken using various fuels to determine unstretched laminar burning velocity correlations (Al-Shahrany et al. [2005]; Bradley et al. [1998]; Metghalchi and Keck [1982]; Ormsby [2005]; Rhodes and Keck [1985]; Ryan and Lestz [1980] and Muller et al. [1997]).

Obtaining laminar burning velocities under "engine like" conditions is experimentally complex owing to the high pressure and temperatures present in internal combustion engines. In addition, relatively heavy hydrocarbons such as those used in SI engines suffer from instabilities and, as such, are seldom wholly laminar (Gillespie et al. [2000]). Where data has been obtained at these conditions, there exists a large scatter. Previous work by Hattrell [2007] who investigated the validity of a number of laminar burning velocity correlations, suggested that at atmospheric pressures and temperatures a good agreement exists between the models; however at engine like conditions the situation changes significantly. Although Hattrell [2007] makes no recommendation as to the most acceptable model to use, based on the conditions at which the relationships were derived (P_{int} 0.4-50 atm, T_{int} greater than 350 K and 0.8 $<\phi<$1.5) the correlation proposed by Metghalchi and Keck [1982] is used in the present study. It is as follows:

$$u_l = u_{l,o}\left(\frac{T_u}{298}\right)^{\alpha}\left(\frac{p}{p_o}\right)\beta(1-2.1f) \tag{3.6}$$

where the laminar burning velocity, u_l, is given in cm s^{-1}, f is the diluent mass faction, T_u is the unburned gas temperature (K) and p is pressure in atmospheres. For an iso-octane-air mixture of a given equivalence ratio, ϕ, the values of $u_{l,o}$, α and β are calculated as follows:

$$u_{l,o} = 33.72 - 110.82(\phi - 1.13)^2 \tag{3.7}$$

$$\alpha = 2.18 - 0.8(\phi - 1) \tag{3.8}$$

$$\beta = -0.16 + 0.22(\phi - 1) \tag{3.9}$$

The performance of the Metghalchi and Keck relationship can be seen in Figure 3.3; this figure includes a comparison of both the original experimental results as well as the regression model created from the original data. In this specific case there appears to be a good correlation between the two sets of results; there have however been repeats of this experiment at identical (or very similar) conditions which produce significantly different results (Hattrell [2007]; James [1987] and Lipatnikov [2012]). The source of error is most likely to be a failure to understand stretch and instability mechanisms (Bradley et al. [2000] and Lipatnikov [2012]). Lipatnikov [2012] states that the influence of per-

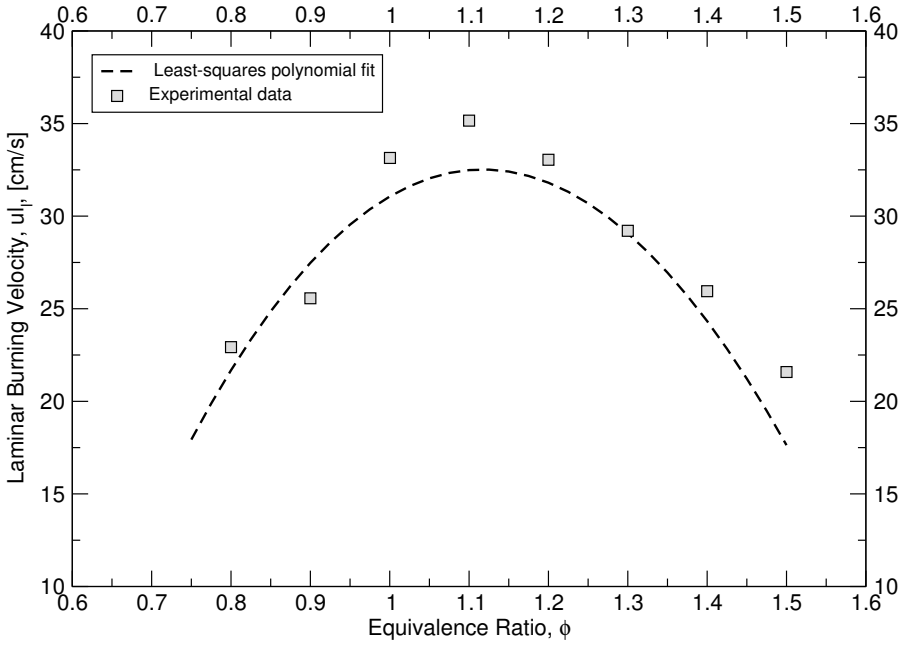

Figure 3.3: A comparison between experimental and predicted laminar burning velocities. Experimental results are from Metghalchi and Keck [1982]. P = 1 atm, T = 350 K

tubations on flame speed were not addressed in the Metghalchi and Keck work owing to deficiencies in techniques used at the time. It appears however, that the results for flame speed are comparable to other results (see Page 56 in Lipatnikov [2012]) around the stoichiometric mixture region, as is the case for the work undertaken in this thesis.

3.2.8 Turbulent burning velocity

As discussed previously, laminar flames are highly unlikely to exist in SI engines owing to the instability brought about by the high pressure and temperatures of the environment, the high weight carbon fuel and the turbulent flow field. As such, the turbulent burning velocity is required for an accurate prediction of the combustion process. A number of studies by researchers at the University of Leeds as well as other works have attempted to formulate a model for expressing the turbulent burning velocity in engines. Abdi Aghdam [2003] investigated the performance of three turbulent burning velocity expressions; two developed at the University of Leeds - the Leeds Ka (Abdel-Gayed et al. [1987]) and Leeds $KaLe$ (Bradley et al. [1992]) correlations as well as the Zimont model (Zimont [1979]). This model was later developed by Lipatnikov and Chomiak [1997], who included a time based flame development discussed in Section 3.2.9, forming the Zimont-Lipatnikov burning velocity model (Section 3.2.8.1). The conclusion from

the work of Aghdam was that the Zimont-Lipatnikov model was preferable to either of the Leeds derived models when looking at variations in operating conditions.

3.2.8.1 Zimont turbulent burning velocity expression

The original Zimont model, before it was developed by Lipatnikov, was developed for high Reynolds and Damkhöler numbers which are present in highly turbulent combustion processes. The original Zimont model assumed that the small-scale turbulent eddies which enter into the periphery of the flame-front thicken it enhancing the mixture and increasing the burning rate[1]; whilst large-scale eddies also increase the burn rate by wrinkling the thickened flamelets, i.e. increase the area of the flame. The foundation of the model is built on the assumption that although the flame thickness increases, a fully developed burning velocity has been reached. The consequence of this is that, by assuming that eddies larger than the scale, l_x, (responsible for flame wrinkling and straining), which lie between the Kolmogorov and integral length scales ($l_\eta << l_x << l_i$), are only responsible for resulting in an increase of the area of thickening flamelets, thereby increasing the entrainment rate, but not the burning velocity itself. The fully developed turbulent burning velocity, $u_{t,\infty}$ can therefore be modelled as:

$$u_{t,\infty} = u_l \frac{\overline{A_t}}{\overline{A_o}} \tag{3.10}$$

Where A_t is the surface area of a thickened flamelet, while A_o is the area of the projection of this surface onto a plane normal to the direction of the flame propagation. An equilibrium between the increase in flamelet surface area and the area consumption due to flamelet self-propagation is rapidly reached, and while the flame continues to increase in area because of wrinkling by large scale eddies, this process is relatively slow. With the assumption that $(\overline{A_t}/\overline{A_o})$ is independent of flame-development time then the relationship for the developed turbulent reaction burning velocity, $u_{t,\infty}$ is dependant upon: the rms turbulent velocity, u', the unstretched laminar burning velocity,u_l, the thermal diffusivity α, and integral length scale l_i, given by:

$$u_{t,\infty} \propto u' Da^{1/4} \propto u'^{3/4} {u_l}^{1/2} \alpha^{-1/4} {l_i}^{1/4} \tag{3.11}$$

[1]It was later felt by Lipatnikov and Chomiak [2002] that this process violated the activation energy asymptotics (AEA) theory of laminar premixed flames as the burning rate should be controlled by diffusivity in the very thin reaction zone rather than turbulence quantities

Where Da is the Damkhöler number which is a ratio of the turbulent and chemical timescales (τ_t / τ_c) where the turbulent time scale $\tau_t = l_i/u'$ and the chemical time scale $\tau_c = u_l^2/\alpha$. The inclusion of the proportionality constant, A, brings about Eq. 3.12, the current expression for the fully developed turbulent burning velocity, $u_{t,\infty}$, in LUSIE:

$$u_{t,\infty} = Au'^{3/4} {u_l}^{1/2} \alpha^{-1/4} {l_i}^{1/4} = Au' Da^{1/4} \tag{3.12}$$

The proportionality constant, A, has traditionally required adjustment when using the two-zone or three-zone model for any given experimental data set (Abdi Aghdam [2003]). The velocity is either the turbulent mass burning velocity, u_{tr}, as originally intended by the Zimont model, or the entrainment velocity, u_{te} as used in the three-zone model; in the three-zone model, A, can be considered the ratio of mass burning velocity to entrainment velocity. In an attempt to quantify this relationship and align a single constant of A, regardless of whether the two or three-zone combustion model is used; the inclusion of the density ratio term, ρ_u / ρ_b, in Eq. 3.13 attempts to account for an expanding flame where the two-zone model does not consider a flame as such.

$$u_{t,\infty} = Au' Da^{1/4} \left(\frac{\rho_u}{\rho_b} \right) \tag{3.13}$$

Flames within engines, in addition to being turbulent, are also non-isochoric and have both an associated acceleration as well as a flame thickness, δ_t, which physically increases with time as it experiences different eddy sizes in the chamber. The effects surrounding the progressing flame can seperated into two categories:

- When the flame is unconstrained and progresses into the unburned air-fuel mixture, where that progress is largely governed by the turbulence scales encountered
- When the flame approaches the system boundary, in this case, the piston, cylinder liner and head components.

An account of the former process is included by Lipatnikov and Chomiak [1997] as an enhancement of the original Zimont model to include the transient effects of the progressing flame. This is accounted for with the addition of the progression (development) factor, f_d.

$$u_t = u_l + u_{t,\infty} f_d \tag{3.14}$$

In addition, the flame decelerates as it approaches and eventually quenches against the wall. This area of modelling is sensitive as it is where the majority of the mass is burned. The factor, f_w, is added to Eq. 3.14 to give the final expression in LUSIE for turbulent burning velocity:

$$u_t = (u_l + u_{t,\infty} f_d) f_w \tag{3.15}$$

The development factor f_d and the so-called "de-development" factor, f_w, are discussed in further detail in Section 3.2.9.

3.2.9 Flame development

As previously discussed, any given combustion event within an SI engine is neither steady, laminar or independent of time. It involves an initially spherical kernel of plasma stretching and wrinkling as it is subjected to varying sizes of turbulent eddies across the combustion chamber. The non-steady increase in flame area brings about an acceleration of the flame as it propagates into the combustion chamber. The rate at which the entrained fuel burns is not necessarily aligned with the rate of flame entrainment, therefore the thickness of the flame brush is also a transient phenomena (Larsson [2009]; Ormsby [2005] and Abdel-Gayed et al. [1987]). Indeed the impact of turbulence quantities, that is a velocity and a length scale, on flame propagation are even now not well understood when trying to differentiate between which of the two is the most influential property. What can largely be agreed upon is that, during the early stages of combustion, the flame is most influenced by the varying turbulence spectrum it experiences. Therefore, in flame development the early stages of acceleration are of great importance when attempting to fully understand the real *developing* turbulent burning velocity.

The assumption made by the Zimont model (Section 3.2.8.1) is that the turbulent burning velocity is independent of flame development time; combustion in SI engines however is known to be non-steady and has associated acceleration. The flame development must be considered if an accurate representation of the combustion process is to be achieved. A number of expressions to account for the development of flames in engines exist in literature and in LUSIE. Two of the models were developed at the University of Leeds and were based on experimental results by Abdel-Gayed et al. [1987] and Scott [1992] (one based on flame radius, the other being time based). Another three models have been included based on a literature review conduced by Hattrell [2007], who identified the work of Dai et al. [1995]; Wu et al. [1993] and Lipatnikov and Chomiak [1997] for

further study within LUSIE. It was found that the Leeds based models and the Lipatnikov model produced similar trends, whilst the Dai and Wu models appeared to over-predict the flame development in the early stages and go on to predict an infinitely accelerating flame unless met by an infinitely increasing length scale. A more comprehensive review of these models is available in the thesis of Hattrell [2007] whilst the Lipatnikov model, used in the current study, will be briefly outlined.

The development factor proposed by Lipatnikov and Chomiak [1997] considered a time-based development factor, f_d. That is, the "state" of the developed flame, t, seconds after ignition, and the influence that had on the fully developed turbulent burning velocity $u_{t,\infty}$ as below:

$$f_d = \left\{ 1 + \frac{\tau'}{t} \left[\exp\left(-\frac{t}{\tau'} \right) - 1 \right] \right\}^{1/2} \tag{3.16}$$

The turbulent time scale, τ', can be thought of as a turbulent timescale, which simplifies to $\tau' = 0.55(l/u')$ where the constant 0.55 is derived from the constants used in the $k - \epsilon$ model predicted turbulence (Verhelst and Sheppard [2009]). The model is based on the assumption that the fully developed flame can be related to the developing flame by comparison of the change to flame area vis-á-vis the laminar case. The relative increase in the turbulent case is denoted as δS, which is said to be proportional to the ratio of the length scales (the scales being normal and tangential to the the flame front, Σ and Λ respectively) by $\delta S \propto \Sigma \ / \ \Lambda$.

Although the model will predict a decreasing rate of flame acceleration, it does not predict the deceleration encountered by a flame in close proximity to the surfaces of the combustion chamber. The interaction of the flame and the wall is complex and difficult to capture experimentally; in part because of few full-bore optically accessed engines. It can be said that as the flame approaches the walls, the active flame area decreases as it is considered to be inactive once truncated by the walls. Once the flame is truncated then the rate of entrainment falls proportionally, as does the heat release and associated pressure rise; this can be seen in the associated rounding of the "S-shaped" mass fraction burned profile (for example see Figure 3.1). Experimentally captured cycles in the LUPOE2-D engine have shown that a similar trend can be seen in the flame radius, obtained by natural light (Figure 3.4). The predicted case here was run without any flame deceleration routines; the sharp cut off of $\mathrm{fr_e}$, not seen in the experimental cycles, highlights the need for flame deceleration to be considered.

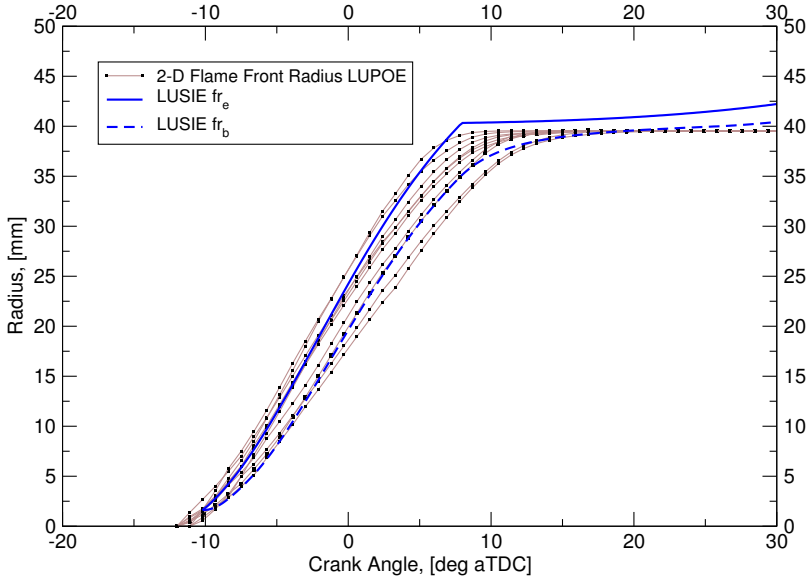

Figure 3.4: Predicted burned gas and entrained radii fr_b, fr_e compared to 10 experimental captured cycles within the LUPOE2-D engine at the SRC conditions without the de-development factor included.

As the flame approaches the walls, the increased heat losses from the flame due to its proximity to the walls reduces the flame's velocity (and therefore mass burning rate). Additionally the flame extinguishes due to exhaustion of reactants, or radical termination at the walls (Verhelst and Sheppard [2009]). The deceleration factor, used to define the "de-development" of the flame as it approaches the wall, was originally proposed by Lipatnikov and Chomiak [2000] based on observations of flame progression and has been used converted to engine co-ordinates by Aghdam et al. [2007] where reasonable accuracy was shown. The deceleration factor is based on experimental observations of the progress of the flame. The flame-wall factor, f_w, for engine-like conditions is given by:

$$f_w = \text{erf}\left(\frac{r_b - fr_e}{\delta_d(t)}\right) \tag{3.17}$$

Where r_b is the bore radius, fr_e is the flame radius, δ_t is the flame thickness, determined by either the difference between the entrained radius fr_e and burned gas radius fr_b or it can be assumed that the growth of the flame thickness with respect to time is controlled by turbulent diffusion (Lipatnikov and Chomiak [2000]), given by:

$$\delta_t(t) = u'\tau_l \left\{2t' \left[1 - \frac{1}{t'}\left(1 - e^{-t'}\right)\right]\right\}^{1/2} \tag{3.18}$$

Where $t' = t \ \tau_L$ is the dimensionless time elapsed since ignition and τ_l is the integral time scale.

3.2.10 Blow-by

During a firing or motoring cycle a pressure difference between the combustion chamber and the crankcase exists. Mass inside the cylinder will naturally move towards the area of lowest pressure, this process is largely prevented in an engine by the inclusion of piston rings which form a seal between the two systems. This seal is not, however, perfect under static or dynamic loading. With the lubricated-mechanical interference existing between piston components and cylinder walls, there inevitably exists gaps leading to leakage from the combustion chamber into the crankcase.

Blow-by can further be categorised into mass which escapes the combustion chamber, to be re-introduced on the expansion stroke, and mass which is lost to the crank case which in reality would end up in the breather system or will be mixed with lubrication oil. In modelling terms, the latter situation assumes that the mass is permanently lost for that individual cycle. The amount of mass transferred is modelled within LUSIE with the assumptions that the flow is compressible and isentropic; routines to account for this movement of mass were written by Abdi Aghdam [2003]. The mass lost is considered to be of unburned composition only, which can be considered valid for all cases within this thesis where the combustion chamber included a centrally mounted spark plug. Further discussion on the blow-by model can be found in the thesis of Hattrell [2007], while the formulation of the model can be found in the work of Abdi Aghdam [2003].

3.2.11 Heat transfer

The occurrence of heat transfer in an engine cycle has a strong effect on the combustion process (Ferguson and Kirkpatrick [2001]). There are two expressions programmed into LUSIE to predict heat transfer, which can be found in Annand [1963] and Woschni [1967]; both are based on the Nusselt-Reynolds type of heat-transfer solution; commonly found in quasi-dimensional codes. Forced convection is considered to be the dominant heat transfer mechanism, thus these equations are based on steady turbulent convection heat transfer. The wetted surface areas, which vary with piston motion, are required for the models and are calculated using the flame geometry routines (Section 3.2.12). For further detail on the heat-transfer models in LUSIE see Abdi Aghdam [2003]; Liu [2004] and Hattrell [2007].

3.2.12 Flame geometry

A number of models within LUSIE require a crank-resolved knowledge of the flame geometry (Sections, 3.2.6.1, 3.2.6.2, 3.2.8.1 and 3.2.11). Owing to the nature of varying combustion rates, as well as a varying point of ignition, it can be identified that there may exist more than one different flames geometries for any given crank angle in any given combustion chamber. Where the combustion chamber is idealised[1] the calculation of flame geometry and truncation can be derived analytically (Liu [2004]). It is assumed that the propagating flame is both spherical[2] and laminar, that is to say devoid of wrinkling and therefore complex surface area geometry. Where the idealised situation is not realised (as with most production engines), specifically ones with complex piston geometry to assist direct-injection flow motion, a euclidean analytical solution is not possible. For the work reported in the thesis, the bespoke GGEOM (Generalised flame GEOMetry) routine was used (Hattrell [2009]). GGEOM is stand-alone software, compatible with .gts (gnu triangulation) files which can be created from CAD data in .stl (stereolithography) format. It is written in C code and allows the user to create a set of lookup tables containing information regarding the flame geometry at a given discrete crank angle and flame radii depending on the pre-defined resolution. Visually the flame geometry in a given combustion chamber can be obtained, as seen in Figure 3.5 where a comparison of an idealised disc shaped flame geometry at three flame radii are compared to a non-idealised pent-roof combustion chamber constructed from .stl CAD data.

3.3 Autoignition models

Modelling of autoignition is essential for predicting the knock propensity of an engine during its inception and design phases. The ability to accurately predict the occurrence of autoignition and knock onset in a given cycle provides designers with the ability to increase engine operation to within closer tolerances of the restrictive limitations of abnormal combustion. The advancement in computing power and the creation of models relying on chemical reaction schemes has led to the real possibility of autoignition mod-

[1] Idealised geometry is the name given to a chamber which conforms to either a disc shape or pent shape which has featureless head and piston components, and ignition is central (on the x and y plane)

[2] Research at Leeds by Abdi Aghdam [2003] and Cairns [2001] shows that flames seldom propagate in a spherical manner and generally have a preferred propagation path, biased by spark plug orientation and proximity to valves, however the assumption of homogeneous and isotropic turbulence within the quasi-dimensional model means the influence of flame shape is less critical than may be assumed

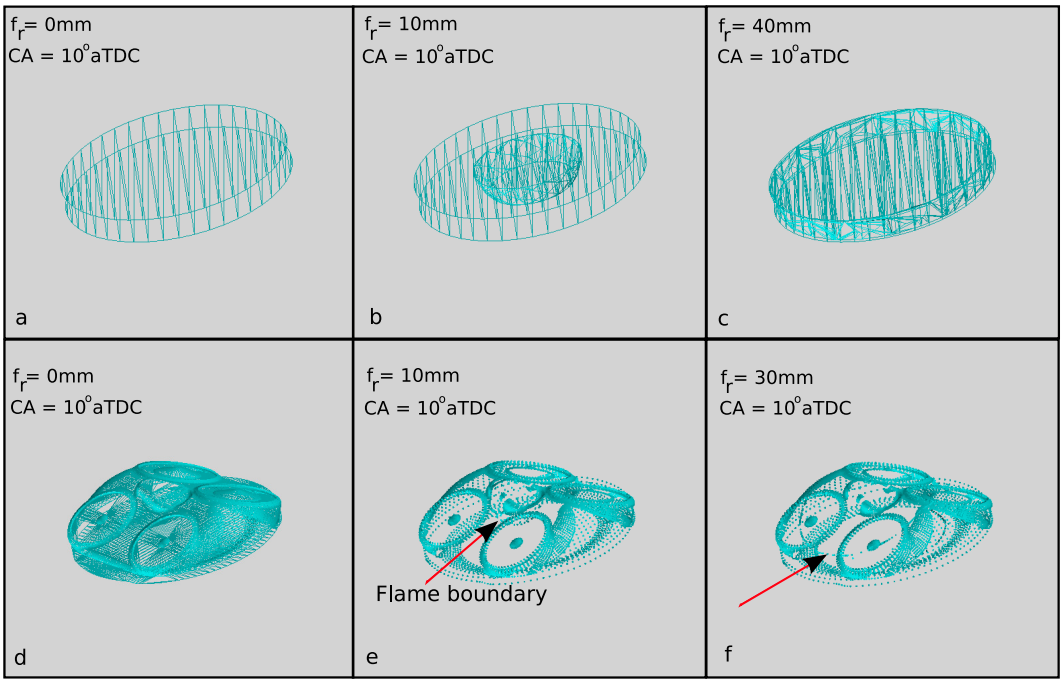

Figure 3.5: Six images illustrating the GGEOM software predicting flame geometry for idealised and non-idealised combustion chamber geometries. Images a,b and c are representative of the LUPOE2-D engine while images d,e and f are representative of the boosted production engine.

els being able to predict autoignition behaviour. A current limitation with these models is the cyclic variation occurring between consecutive cycles of the engine which, in real time alter autoignition onset.

Researchers have developed two distinct methods of modelling autoignition. The first method are based on empirical data which take autoignition delay times for individual fuel and air mixtures and relate them to the current model. The second are based on chemical reaction schemes varying in complexity which are predominantly driven by reaction rates occurring during hydrocarbon oxidation to predict temperatures of the gases involved in the reaction (Griffiths and Barnard [1995]).

Autoignition modelling within the thermodynamic LUSIE code is driven by the pressure and temperature history of the unburned composition ahead of the flame-front (end-gas). The temperature increase is based on the heat release from the mass of fuel that has burned at a given time-step, as described in Section 3.2.4. The temperature, pressure, volume and composition of the end-gas are passed to the autoignition routine within the LUSIE code. The pre-selected model type is invoked and solution is undertaken by either an empirical or kinetic model type until a threshold for autoignition has been achieved, the process can be seen in the flowchart, Figure 3.6.

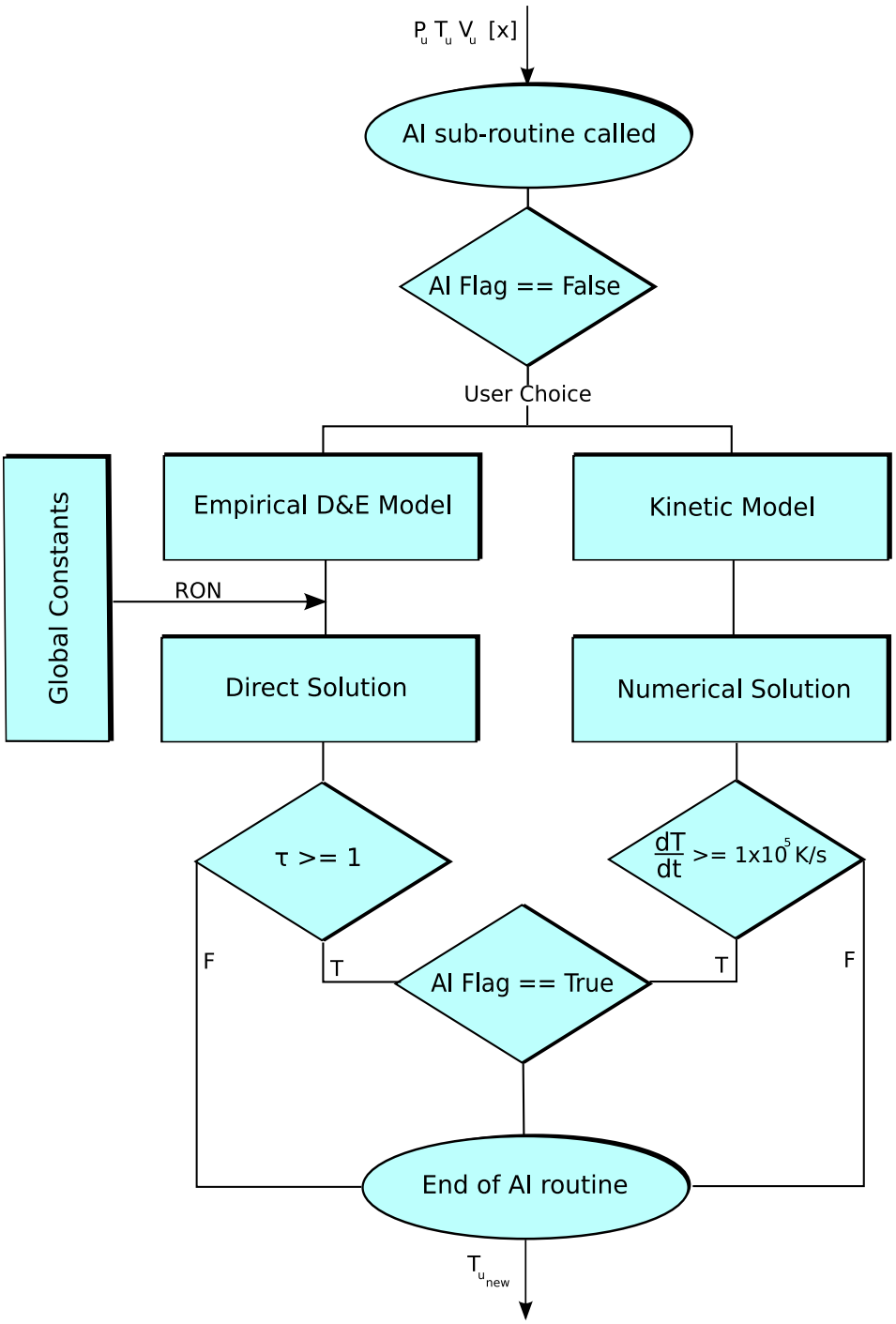

Figure 3.6: Flowchart showing the sequence of events during the autoignition subroutine of LUSIE.

3.3.1 Empirical DandE model

A widely used empirically based autoignition model[1] is that of Douaud and Eyzat [1978] (hence D&E); the D&E model is simple in terms of computational demand, compared with even reduced kinetic models. It is based on an Arrhenius function, which predicts the temperature dependence, T, on the rate constant in a chemical reaction. The rate constant in the case of the function is considered to be the ignition delay time, τ:

$$\tau = Ap^{-n} \exp\left(\frac{B}{T}\right) \tag{3.19}$$

Where *A*, *B* and *n* are user-adjustable model constant. The D&E expression developed for calculating the autoignition delay time in engines, as a function of temperature, pressure and octane number of primary reference fuels (comprising a mix of iso-octane and n-heptane) is as follows

$$\tau = 17.68 \left(\frac{ON}{100}\right)^{3.402} p^{-1.7} \exp\left(\frac{3800}{T}\right) \tag{3.20}$$

The model was validated for octane numbers values in the range $80 \leq$ON≤ 100. The model constants allows the user to achieve a better fit to the individual testing conditions. The autoignition delay time predicted is the instantaneous autoignition delay time predicted for a steady state pressure and temperature in a system. It can be thought of as the length of time a mixture, given the conditions of, P=x, T=y and ON=z would take to autoignite if it were brought to and left at those conditions. With the moving piston and transient combustion process in engines, the pressure and temperature vary constantly therefore having a single ignition-delay time is meaningless. To account for the delay time in engines it is necessary to consider the delay time at each crank angle given the state of the mixture at that time, thus:

$$\tau_\theta = 17.68 \left(\frac{ON}{100}\right)^{3.402} p_\theta^{-1.7} \exp\left(\frac{3800}{T_\theta}\right) \tag{3.21}$$

The autoignition onset point can then be determined by the Livengood and Wu integral (Livengood and Wu [1955]). Where the integrated τ_θ delay times between the point the

[1]The term autoignition modelling is commonly interchanged with knock modelling. It should be highlighted that the knock event itself, i.e. the high frequency pressure wave, is not modelled and therefore the term of a "knock" model is not strictly correct.

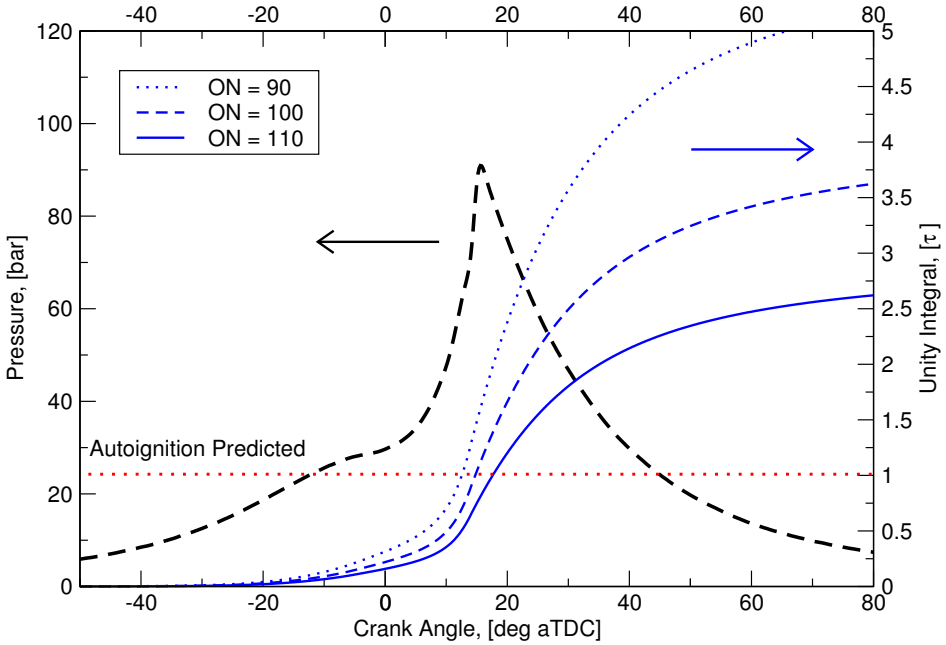

Figure 3.7: The influence of octane number on the prediction of autoignition using the D&E model. A smoothed in-cylinder pressure trace captured on the LUPOE2-D Boosted engine at 750 rev/min compared to predicted integrated autoignition delay times.

system becomes closed, θ_{ivc}, and the current crank angle are calculated. Autoignition is deemed to have occurred when the integral reaches unity.

$$\int_{\theta_{\text{ivc}}}^{\theta} \frac{1}{\tau_\theta} dt = 1 \tag{3.22}$$

To account for variations in fuel quality and composition the octane number can be adjusted. The octane number is typically the average of the RON and MON for a given fuel. The influence of the octane number on the predicted Livengood and Wu integral can be seen in Figure 3.7.

This model is computationally simple to solve analytically. Additionally, the input of numerous chemical reactions as is required by the more complex chemical kinetic schemes, is not necessary. It is because of this simplicity that it is a popular model used widely throughout the automotive industry, as well as in commercial combustion codes (Gamma-Technologies [2012]). The model has also been used to determine experimental HCCI combustion onset timings (Shahbakhti et al. [2007] and Roberts [2010]).

3.3.2 Kinetic modelling

The empirical model introduced in Section 3.3.1 has drawbacks when predicting autoignition at conditions outside of those used to validate the model, as well limitations in as predicting autoignition behaviour in fuels with a pronounced negative temperature (NTC) region (see Section 2.5.1). The alternative to empirical based autoignition modelling is to incorporate a model based on reaction rates and chemical heat release which are considered applicable to gasoline type fuels. This type of modelling is commonly referred to as kinetic modelling.

A number of kinetic models were reviewed by Griffiths and Barnard [1995], ranging from comprehensive models with 100s of species and 1000s of reactions, to reduced schemes with $<$100 species and $<$100 reactions. Implementing these types of schemes within LUSIE would be a time-consuming undertaking, owing to the need to input each species, each reaction and the subsequent reaction rate constants (see Eq. 3.23). In light of this, the autoignition models incorporated into LUSIE are known as skeletal kinetic models which are comprised of a number of species and reactions. Griffiths also notes that one of the primary purposes of the comprehensive model is to provide a starting point for reduced kinetic schemes. Moreover, he suggests that the accumulation of the errors invariably included into the individual reaction rates makes the use of such models no less relevant than a reduced model being used with adjustable constants which can be used to refine the model further.

3.3.2.1 Shell autoignition model

There are a number of kinetic autoignition models incorporated into LUSIE; the simplest model was developed by Halstead et al. [1975], known as the ”Shell” model. The Shell model is based on empirically measured autoignition times from rapid compression machines. Previous work at the University of Leeds (Roberts [2010]) has identified that, of all the available autoignition models available in LUSIE, the Shell model consistently gave the poorest correlation over a number of conditions. For the standard knocking reference condition (SKRC - see Section 3.5.2) on the LUPOE2-D engine, he identified a mean error of -5^o CA for the Shell model, i.e. autoignition was predicted to occur 5^o CA earlier than seen experimentally. Over-prediction was also seen by Smallbone [2004] on an earlier variant of the LUPOE engine, this time 3.4^o CA early for the 100PRF (iso-octane) fuel.

3.3.2.2 Cernansky autoignition model

Another autoignition model within LUSIE is the Cernansky autoignition model (Zheng [2001]). The model was originally developed for use with HCCI operation although the foundation of the model is based on the Keck model scheme developed by Cowart et al. [1990] (mentioned in Section 3.3.2.3) where the original 18 reaction and 13 species model was modified to account for the cool-flame reaction heat release and CO formation which is associated with HCCI combustion. The final model contained 31 reactions and 21 active species. The Cernansky autoignition model is by far the most comprehensive scheme within LUSIE, although it would still be considered sparse relative to the more comprehensive kinetic models available. Roberts [2010] observed that predictions of autoignition in the LUPOE2-D (operating in SI mode) were very encouraging when using the Cernansky Model. The mean error for the SKRC condition was -0.5^{o}CA, although there appeared a tendency for some cycles to be under-predicted i.e. autoignition occurred but it was predicted to occur later.

3.3.2.3 Keck autoignition model

A further autoignition model implemented with the LUSIE code, as the Keck model. There are three models which are categorised as "Keck" models in LUSIE, of interest to the current thesis is the one formulated by Chun et al. [1988] - the origins which can be traced back to the work of the Shell expression (Halstead et al. [1977]) which had been developed by Cox and Cole [1985] to include more realistic chemistry. The model by Chun et al. [1988], herein referred to as *the* Keck model comprises 17 active species and 19 reactions. It was used to reproduce experimentally seen "explosion" characteristics in a constant volume combustion vessel and ignition delay times in a rapid compression machine. The model was further refined to the autoignition performance specific in SI engines with encouraging predictions. The promising results and potential led to further refinement of the model by Cowart et al. [1990] who compared the model against both a comprehensive autoignition model, consisting of 324 active species and 1303 reactions as well as to experimental results obtained on a Ricardo Hydra research engine. The fuel used for these studies was a PRF with a RON of 94 as well as Indolene (RON97.4). To account for the performance of different fuels the forward rate constant of the isomeriation reaction $RO_2 \leftrightharpoons$ ROOH was adjusted to fit for the different fuels.

The autoignition routines implemented within LUSIE are rather antiquated compared to the rest of the LUSIE code as they are still in FORTRAN 77 format. The solver used within LUSIE is the Eulsim open-source Eulerian integrator with adaptive time-step

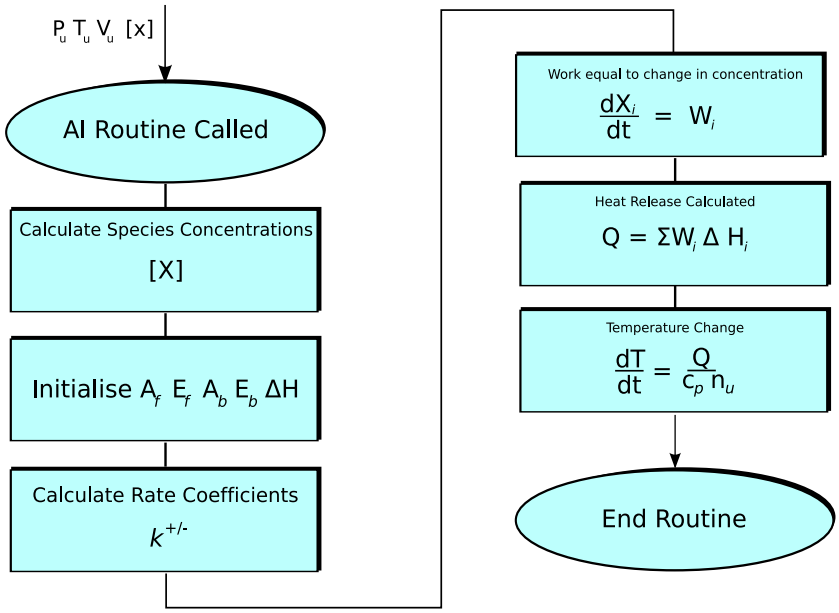

Figure 3.8: Flowchart showing the sequence of calculations for the Keck (Chun et al. [1988]) autoignition model within LUSIE.

built in, it is well suited to the stiff system of differential equations that are solved with the kinetic models where equations producing radicals can introduce instability. In addition Eulsim is not permitted for use with commercial projects and has recently been migrated to a different integrator (backward-difference) aligned with the work of Khan [2013]. The solution process within LUSIE for the Keck model can be seen in the flowchart (Figure 3.8); and is described in further detail below.

The unburned gas pressure and temperature, P_{u}, T_{u} as well as the molar composition of the gas, X_i, are passed as variables to the autoignition sub-routines. The constants for the jth reaction rate, k_j, are initialised based on the the data in Table 3.1, which are stored in the LUSIE sub-routine in the form of a "data" block;

$$k_i = Ae^{-E_i/RT} \tag{3.23}$$

the molar concentration of the ith gas, $[X_i]$ is calculated based on the unburned gas volume at the current crank angle, θ

$$[X_i] = \frac{X_i}{V_u(\theta)} \tag{3.24}$$

the change in the concentration of the gas, with respect to time is known as the instantaneous reaction rate, W_j where $\lim_{W_{i_{dt\to 0}}} = dX_i \ / \ dt$ is

$$\frac{dX_i}{dt} = W_j \tag{3.25}$$

the heat released or absorbed by the reaction, Q_j, can be determined by the reaction rate and enthalpy of formation ΔH_j

$$Q_j = W_i \Delta H_j \tag{3.26}$$

the rate of temperature change for a given reaction is then a function of the heat released in the reaction, for a given number of mols, and the specific heat capacity at constant volume, itself a function of, T_u

$$\frac{dT_i}{dt} = \frac{Q_j}{C_v n_j} \tag{3.27}$$

3.4 Turbulence

As alluded to in Section 2.2.1, the nature of operation of internal combustion engines results in high velocities and therefore turbulent flow regimes. It has also been seen that turbulence is responsible for increasing flame speed and therefore the rate of heat release - significantly greater than would be achieved in a laminar system. The importance of turbulence, in modelling terms is well understood and is included in the models used in LUSIE (Eq. 3.16, Eq. 3.5, Eq. 3.3 and Eq. 3.2), where turbulence is responsible for increasing the burning velocity, the rate of fuel burned and the rate of flame development. Models to predict turbulence in engines can consist of the numerically complex solution of Navier-Stokes equations, or some simplification of those based on the required turbulent scale resolution, i.e. Large Eddy Simulation (LES) as discussed in Section 2.2.4. Solutions of this type are beyond the scope of quasi-dimensional models such as LUSIE where the preferred solution type regards the flow as homogeneous and isotropic solvable by a 0-dimensional analysis. Two such solutions available within LUSIE are discussed below.

Reaction	ΔH_{300}	log A^+	E^+	log A^-	E^-
1. RH + $O_2 \leftrightharpoons$ R + HO_2	46.4	13.5	46	12	0
2. R+$O_2 \leftrightharpoons$ RO_2	-31	12	0	13.4	27.4
3. $RO_2 \leftrightharpoons$ ROOH (iso-octane)	7.5	11	21.4	11	11
4. ROOH + $O_2 \leftrightharpoons$ O_2RO_2	-31	11.5	0	13.4	27.4
5. $O_2RO_2H \rightarrow$ OROOH +OH	-26.6	11.3	17		
6. OH + RH $\rightarrow$ R+H_2O	-23.5	13.3	3		
7. OROOH $\rightarrow$ OH + ORO	43.6	15.6	43		
8. R + $O_2 \leftrightharpoons$ HO_2 +C = C	-13.5	11.5	6	11.5	19.5
9. $2HO_2 \rightarrow$ HOOH +O_2	-38.5	12.3	0		
10. HOOH + M $\rightarrow$ 2OH + M	51.4	17.1	46.0		
11. ORO $\rightarrow$R′CHO+R″O	8.5	14	15		
12. R″O+$O_2 \leftrightharpoons$ O_2R″O	-31.0	11.5	0	13.4	27.4
13. ROOH $\rightarrow$OH + R′CHO + C = C	-3	14.4	31		
14. RO_2 + R′CHO $\rightarrow$ ROOH + R′CO	-0.6	11.45	8.6		
15 .RO_2 + RH $\leftrightharpoons$ R+ ROOH	8	11.2	16	10.1	8
16. HO_2 + R′CHO $\rightarrow$HOOH + R′CO	-.06	11.7	16.0		
17. HO_2 + RH $\leftrightharpoons$ R + HOOH	8	11.7	16	10.8	8
18. HO_2 + C $\rightarrow$ C = Epox + OH	-0.23	10.95	10		
19. R + R $\rightarrow$ C = RH	-85.0	13.2	0.0		

Table 3.1: The Arrhenius parameters for the rate constants for iso-octane oxidation as used in the ″Keck″ model. Reproduced from Chun et al. [1988].

Constant	LUPOE1-D	LUPOE2-D
C_1	0.44	0.58
C_2	1.7	-0.25
C_3	0.043	0.0238

Table 3.2: Turbulence constants for the linear fit relationship as proposed by Atashkari [1997] (LUPOE1-D) and Hussin [2012] (LUPOE2-D).

3.4.1 Linear fit relationship

The simplest turbulence model within LUSIE is based on an empirically derived relationship between u' and crank angle, θ, for a given engine speed. Results have been obtained for different variants of the LUPOE family of engines, originally the LUPOE1-D engine (Atashkari [1997]), and more recently on the LUPOE2-D engine (Dawood [2010] and Hussin [2012]. Results from these experiments have identified that the crank dependant u' value decreases linearly around the TDC region. More specifically, the linear region in the disc-shaped LUPOE2-D engine was seen between -20 to 20^o aTDC. It was also seen that u' could also be related to engine speed by $u' \propto \bar{S}_p$. Based on his observations, Atashkari proposed the following relationship to predict u' in the LUPOE engines.

$$u' = C_1 \bar{S}_p + C_2 - C_3 \theta \tag{3.28}$$

Where the constants of C_1, C_2 and C_3 were related to actual physical processes occurring over the induction and compression cycle as follows: C_1 accounts for turbulence generation by the piston motion, although considered a mean motion across the cycle, C_2 was related to turbulence generated by the intake jet again considered to be constant over the cycle and C_3 is a dimensionless constant affecting the gradient of the fit. Hussin [2012] also defined the constants fitted for both engines which can be seen in Table 3.2. The largest variation between the constants for the LUPOE1-D and LUPOE2-D engines is in C_2, which is related to the turbulence generated by the intake jet, unsurprising owing to the difference in intake system configuration between the two engines.

Another relationship within LUSIE for predicting the linear u' relationship, was based on the work of Hall and Bracco [1987] who measured turbulence intensities and velocities via LDV measurements under both fired and motored conditions. The engine used was similar in configuration to the LUPOE family of engines in that it was a ”flat-pancake” chamber with ported intakes. It was seen that the intake velocity scaled more strongly with the engine speed rather than the speed of the intake jet itself. Additionally

it was seen that the turbulence in a firing cycle was similar to that seen in a motored cycle. Although not accounted for in the model it was also seen that the intensity of turbulence u' / U increased sharply near the cylinder wall, but not at the piston surface. The final relationship was as follows:

$$u' = C_1 \bar{S}_p \left[1 - 0.5 \left(\frac{\theta - \theta_{ign}}{45} \right) \right] \tag{3.29}$$

where C_1, again, requires a different value to those declared for the LUPOE variants, $\bar{S}_p$ is the mean piston speed and $\theta - \theta_{ign}$ gives the amount of crank angle which has elapsed since the point of ignition.

The linear relationships derived from experimental data is only valid around the TDC linear region. However, as this is the region where turbulence quantities are influential on the combustion process it has become an acceptable application of the model. The properties of the line, i.e. gradient and intercept are not predicted and are adjusted in the relationship by the inclusion of 3 constants in the case of the Atashkari [1997] and Hussin [2012] relationships. It can be seen in Eq. 3.28 that the number of user-adjustable constants exceeds the known variables which leads to an unsatisfactory situation in terms of a predictive model. In addition, the type of relationship allows for anomalous u' values, such as u' <0 after a certain time (crank angle). Moreover, the dependence of the relationship on $\bar{S}_p$ appears to suggest a large portion of production is because of the piston speed rather than the breakdown of the intake jet (lumped into the constant C_1), however in reality where the model is only concerned with u', around TDC then as $\lim_{\theta \to 0}, S_p = 0$ leading to the intake jet, not directly modelled, dominating the production predicting.

3.4.2 0-D $k - \epsilon$ turbulence model

The necessity for the inclusion of a turbulence model within LUSIE which has predictive capability existed because of the limitations posed by the linear fit models, see the discussion in Section 3.4.1). A zero dimensional $k - \epsilon$ model proposed by Lumley [2006] has been introduced into the existing LUSIE code. The model is based on equations that describe the evolution of turbulence in a field where the density is a function only of time. The model includes both the effects of strain in the shear flows driven by the mean piston motion and the effects of turbulence enhancement due to compression.

The turbulence model uses the equation for the mass averaged turbulent kinetic energy (TKE); mass averaged data is preferred when dealing with compressible flows,

such as those found in engines which undergo significant pressure and density changes (Rao [2010] and Chen and Riley [1991]). The initial k value is predicted based on the intake jet velocity:

$$k = \frac{1}{2}\left(u_x'^2 + u_y'^2 + u_z'^2\right) \tag{3.30}$$

The zero-dimensional model assumes that the turbulence is isotropic and hence, Eq. 3.30 reduces to:

$$k = \frac{3}{2}u'^2 \tag{3.31}$$

The time evolution of k is governed by the ODE, integrated from the PDE for turbulent kinetic energy over the cylinder volume (Morel and Mansour [1982]).

$$\frac{dk}{dt} = P - D + \frac{1}{M_c}\left(I - E - k\frac{dM_c}{dt}\right) \tag{3.32}$$

LUSIE simulates the closed part of the cycle which would negate the intake and exhaust terms. However the intake and exhaust terms account for the majority of the turbulence production in the engine and were therefore included (See Section 3.2.3) the production term, P, is the product of the strain rate of the mean motion and the Reynolds stresses of the turbulence. The turbulence production due to strain in the shear flow on the walls is represented by a length scale for the mean strain rate, a function of mean piston speed and the ratio of cylinder area to cylinder volume . The turbulence production due to compression is modelled with rapid distortion theory (Lumley [2006]). Thus, the total energy production is given by:

$$P = F_p\frac{A_w}{V_c}|S_p|^3 - \frac{2}{3}k\frac{1}{V_c}\frac{dV_c}{dt} \tag{3.33}$$

where F_p is an adjustable coefficient for calibration with experimental data, suggested to be 0.03 by Lumley [2006]. A_w is the exposed area of the chamber, V_c is the cylinder volume.

Studies have additionally shown that turbulence intensity at TDC has a maximum value equal to roughly half the mean piston speed for engines comparable to the LUPOE2-D engine in configuration; see for example Liou et al. [1984]. Also that gas flow velocity in the cylinder and inlets scale with mean piston speed; see for example

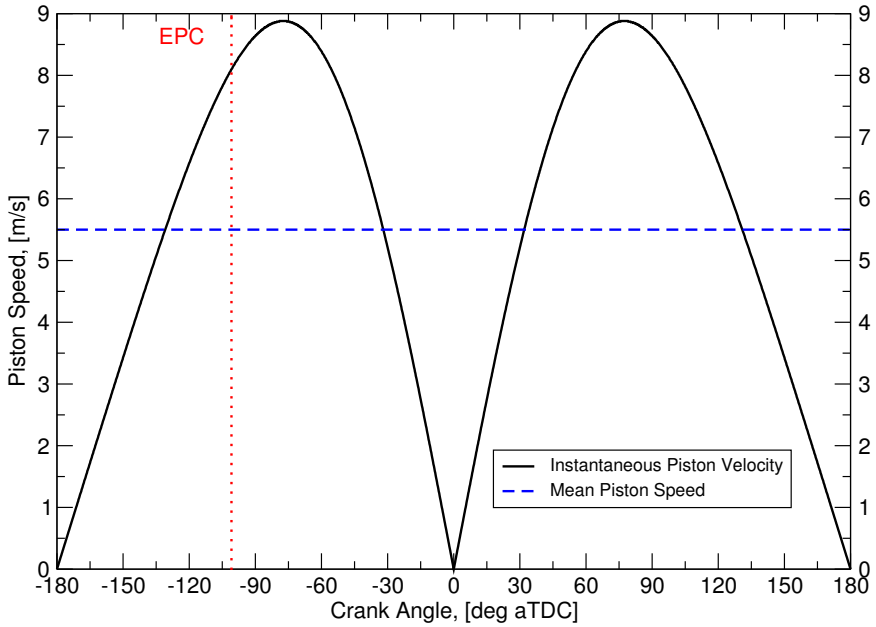

Figure 3.9: Mean piston speed compared with the actual instantaneous piston speed for the LUPOE2-D engine at 1500 rev/min.

Heywood [1988]. For these reasons the mean piston speed, $\bar{S}_p$ was compared to the instantaneous piston speed, S_p. The difference between the instantaneous piston speed and the mean piston speed can be seen in Figure 3.9 where the mean and instantaneous piston speeds for the LUPOE2-D piston at 1500 rev/min are given. It can be seen that before the exhaust port closes the piston speed is above the average. This is a critical time during the end of the inlet phase for turbulence production, so although there is a significant amount of time the piston operates below mean piston speed, the dynamics of the inlet phase change markedly during this regime.

The turbulence energy dissipation rate per unit mass, D, which according to turbulence theory should vary with turbulence length scale, as $\frac{u'^3}{l_i}$, where u' is the initial rms and l_i is a length scale of the largest eddies. Turbulence in an engine has a scale comparable with that of the cylinder, so the dissipation model is:

$$D = F_d \frac{k^{3/2}}{V_c^{1/3}} \tag{3.34}$$

F_d is, again, a user selected coefficient, suggested to be 0.05 (Lumley [2006]).

Flow visualisation experiments suggest that most of the kinetic energy of the mean flow entering through the valves is converted to turbulence energy in the cylinder. Therefore the model for the intake term is:

$$I = F_i \dot{m}_i \frac{U_i}{2} \tag{3.35}$$

similarly, flow out the cylinder through the exhaust is modelled by:

$$E = \dot{m}_e U_e \tag{3.36}$$

Where:

- F_i and F_e are user selected coefficients, suggested to be 0.01 and 0.02 respectively (Lumley [2006]).
- $\dot{m}$ variables represent the mass flow rates at the relevant conditions.
- $U_i U_e$ are the inlet and exhaust velocities respectively.

The mass flow rate through the inlets and exhausts can be expressed by one-dimensional isentropic flow analysis based on the initial mass inducted as constrained by the density. The initial k value can be obtained assuming

$$k = \frac{3}{2} u'^2 \approx \frac{3}{2} U_i^2 \tag{3.37}$$

Where U_i, the intake jet velocity, can be obtained from the averaged mass flow rate, $\dot{m}$, of the charge inducted during the cycle.

$$\dot{m} = \rho A U_i \tag{3.38}$$

The following assumptions are made with the $k - \epsilon$ model, they are as follows:

- The mass flow rates during the inlet and exhaust period are constant throughout the inlet and exhaust regardless of piston position
- Volumetric efficiency is 90% for the LUPOE2-D engine
- There is no backflow through inlet or exhaust

- Initial mass values are set based on the volumetric efficiency to avoid diving by 0 on the first timestep
- Inlet velocity is constant owing to the assumed constant flow rate.

The adjustable coefficients mentioned through the model description are given below for the LUPOE2-D engine. The constants were selected by matching model results to experimental cold-flow LDV measurements on the LUPOE2-D engine. Three points were selected throughout the compression phase, (IVC/IPC, -90^o aTDC and TDC). The constants were adjusted until the error at these three points was at a minimum.

- F_d = 0.017
- F_p = 0.035
- F_i = 0.005

A final point to note is that there is no pressure dependent terms in the 0-D $k-\epsilon$ model. While the density of the mixture is dependent on the pressure and therefore the mass terms used in the model, the increase in mass (and therefore influence of pressure) is negated by the assumption that mass flow into the cylinder is constant. As the velocity U_i is related by Eq. 3.38 to the density, ρ, then the increase in mass by the increase in pressure is, as said, negated by the increased density and therefor,e the intake velocity U_i which sets the initial, k values, remains constant. Once under a closed system, the RHS term of Eq. 3.32 is equal to 0.

3.4.3 Turbulent scale definition

There is a need for quantification of the turbulence scale, or scales, used in the turbulent burning velocity and flame development routines (Eq. 3.5 and Eq. 3.16). As it has not been determined experimentally with any certainty, the length scale chosen by the user to express the "burn-up" definition is not hard-coded into LUSIE and can be changed for each simulation. In addition, the model constant $C_\tau b$ in Eq. 3.5 provides another factor for which to tune a particular model. Owing to the apparent lack of clarity regarding the choice of turbulence scales, two have been defined in LUSIE, the integral and the Taylor length scale.

Despite the non-trivial nature of obtaining turbulence scales in engines, a number of rends have been identified through experiments, from which empirical models have

been formulated. Hussin [2012] reviewed a several papers relating to turbulent scale measurements in engines (Fraser and Bracco [1989]; Ghandi et al. [2005]; Hong and Chen [1997]; Ishima et al. [2008] and Heim and Ghandhi [2011]). Perhaps the most striking observation, pertaining to the integral scale, was that that essentially the integral scale is of the order of the clearance height C_h. An observation in line with the seminal work of Tennekes and Lumley [1972] who determined that the integral scale was a strong function of the vessel dimensions.

Based on these observations, the integral length scale calculation within LUSIE, is determined to be a function of the clearance height, or rather the distance between the piston surface and the head (for disc-shaped combustion chambers); itself a function of crank angle:

$$l_i = C_L C_h(\theta) \tag{3.39}$$

The constant C_L is typically of the order of 0.2; see for example Hattrell [2007].

For engines that do not have a disc-shaped combustion chamber configuration (likely to be most production engines) it is necessary to employ a different relationship for the integral length scale. The flame will experience a different effective combustion chamber size as it propagates from the source of ignition. In the case of a centrally ignited flame, it is related to the effective clearance height (a function of the flame radius $\mathrm{fr_e}$ and the crank angle). The integral scale definitions employed by LUSIE are displayed in Figure 3.10.

$$l_i = C_L C_h(\theta)(f_{re}) \tag{3.40}$$

The 0-D $k-\epsilon$ prediction for integral scale is based on the turbulence energy dissipation rate per unit mass given by Eq. 3.34. Turbulence theory indicates that dissipation should vary with u'^3/l_i; see for example Hinze [1975]; Lumley [2006] and Fluent [2006]. Therefore, combining with Eq. 3.34 the integral scale is given by

$$l_i = F_D V_c^{1/3} \tag{3.41}$$

Whether or not the integral length scale is the correct scale to use in the determination of burning velocity, flame development and mass burning rate is a topic open for discussion. Simulations undertaken during the course of this study have identified that

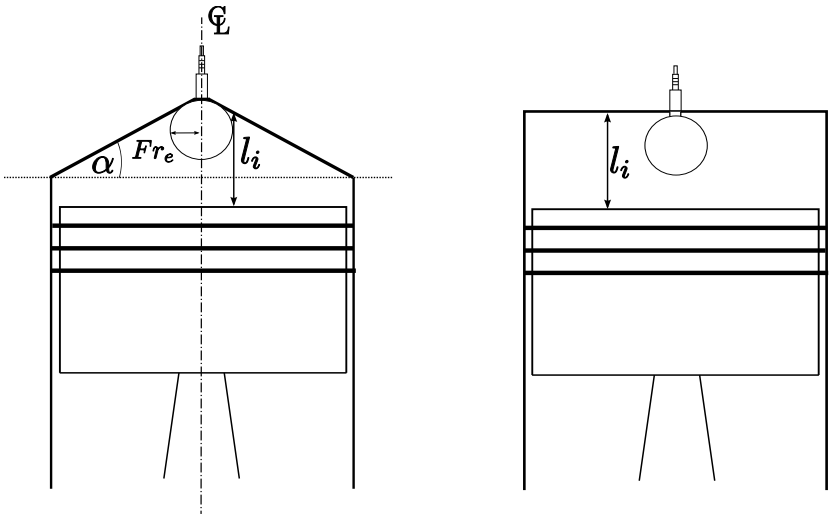

Figure 3.10: Integral length scale definitions used within LUSIE for pent-shaped and disc-shaped combustion chambers. Reproduced from Hattrell [2007].

use of the Taylor scale as the scale that drives the burn-rate 3.5, may be applicable to boosted engines (see Chapter 4). Obtaining the Taylor scale directly through measurement is not currently feasible, or at least this author has failed to find evidence to the contrary. Traditionally the Taylor scale is obtained from the curvature of the atuocorrelation function, see Section 2.2.1 for details. An empirical relationship between the Taylor scale and the integral scale was developed by Tennekes and Lumley [1972]:

$$l_\lambda = F_\lambda \frac{l_i}{R_e{}^{0.5}} \tag{3.42}$$

Where different values of F_λ have been proposed by different authors. For the study on the effect of Taylor scale on burning rates, discussed in Section 4.3.1 the constant is adjusted; the original values coded into LUSIE can be seen in Table 3.3, and R_e the Reynolds number is:

$$R_e = \frac{\rho l_t u'}{\mu_v} \tag{3.43}$$

Where μ_v is the dynamic viscosity, ρ_u is the unburned gas density. It can be suggested here that, unlike the integral scale, the Taylor scale will be influenced by the change in pressure because of change in density.

F_λ Value	Source
$\sqrt{40}$	Abdel-Gayed et al. [1987]
$\sqrt{15.0}$	Tennekes and Lumley [1972]
$\sqrt{16.0}$	Scott [1992]

Table 3.3: Turbulence constant, F_λ to determine the Taylor length scale from the integral length scale)

3.4.4 Cyclic variability modelling

The requirements for quantifying cyclic variability in SI engines are identified in Section 2.7. The model described in this section was introduced to LUSIE to account for the variation in equivalence ratio, ϕ, and u'. The variability has been identified as having a Gaussian distribution of a mean value μ and standard deviation σ, where the variation in standard deviation is 5% or 12.5% for ϕ and u' respectively based on the work of Aghdam et al. [2007]. The Gaussian distribution for a σ of 5% for ϕ over 100 cycles can be seen in Figure 3.11. It can be seen that the σ limits (σ to 3σ) produce a maximum ϕ variation of $\pm$ 0.15 for the 100 cycle set, where 68.2% of the data is contained within the σ variation, 95.4% is contained within a 2σ variation and 99.6% of cycles are within the 3σ limits.

The requirement of the model therefore is to generate the normally distributed equivalence ratio, $\phi_R(i)$, for the i_{th}cycle, in addition to generating the random multiplier for TKE at the point of ignition, $k_{ign}(i)R$; see for example Eq. 3.44. A number of methods exist which are capable of achieving this target; they are, two forms of the original Box-Muller transform (Box and Muller [1958]) known as *basic* and *polar*[1], as well as the Ziggurat algorithm described in Marsaglia and Tsang [1984]. The *polar* Box-Muller transform was selected for use in the variability modelling work conducted throughout this study owing to the low usage of the routine (called only twice per simulation) compared to the more rigorous Ziggurat method.

$$k_{ign}(i) = k_{ign} \cdot R(i) \tag{3.44}$$

[1]The *polar* form of the Box-Muller transform is also referred to in literature as the Marsaglia polar method (Marsaglia and Bray [1964]).

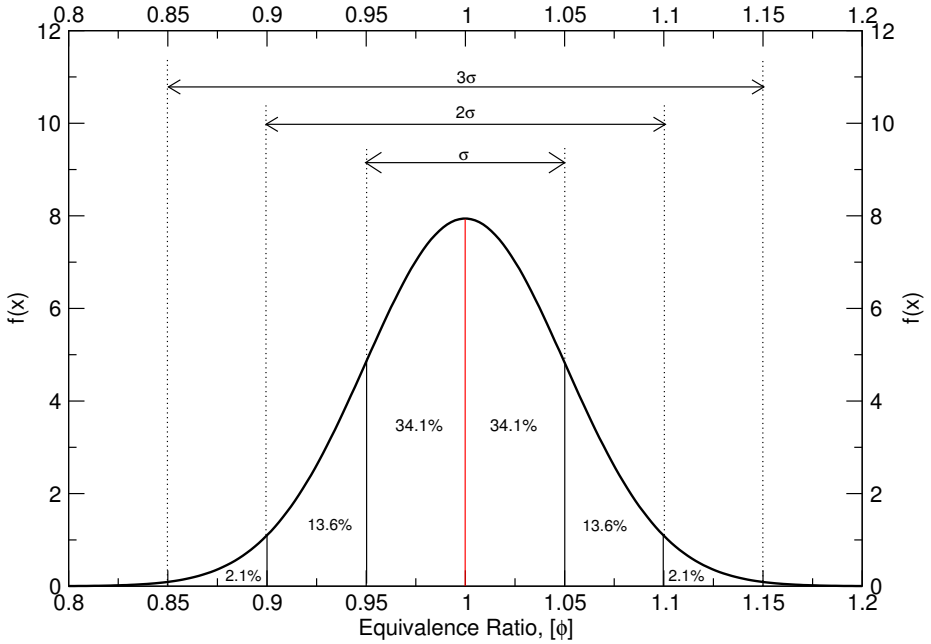

Figure 3.11: Gaussian distribution with included standard deviation, σ, limits for a 100 cycle data set. Equivalence ratio, ϕ, is expected to vary around μ=1 with σ=5%.

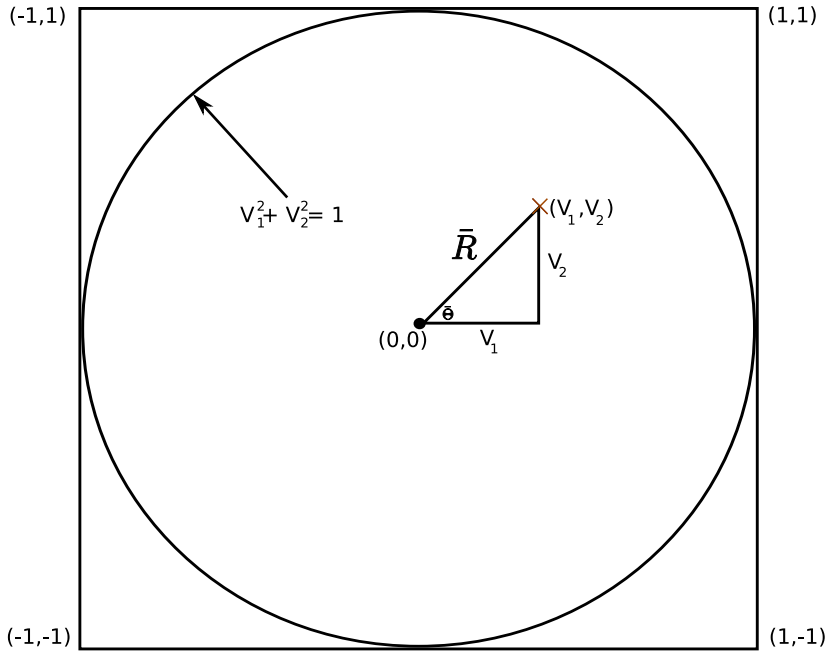

Figure 3.12: Representation of the polar coordinates definition within the confinement of the bounding square and circle for the limits (-1,1).

3.4.5 Box Muller Transform

The *basic* Box Muller Transform is a method for producing a pair of normally distributed (μ=0,σ=1), independent, random numbers Y_1, Y_2. It can be seen that their polar coordinates $R = \sqrt{Y_1^2 + Y_2^2}$, $\Theta = tan^{-1}(v_1 \backslash v_2)$ are independent, with R^2 being exponentially distributed (μ = 2 and Θ being uniformly distributed on (0,2π)) (Marsaglia and Bray [1964]). It can also be said that where two variables, v_1 and v_2, are generated at random and are uniformly distributed (all possible discrete values along a continuous line are equally probable) then the relationship:

$$R = (-2\log(U_1)^{0.5} \tag{3.45}$$

$$\Theta = 2\pi U_2 \tag{3.46}$$

can be used to obtain the unit normal variables Y_1 and Y_2 where, with another randomly generated variable U_2.

$$Y_1 = R\cos\Theta = (-2\log U_1)^{0.5}\cos(2\pi U_2) \tag{3.47}$$

$$Y_2 = R\sin\Theta = (-2\log U_1)^{0.5}\sin(2\pi U_2) \tag{3.48}$$

The *basic* Box-Muller approach is limited by the requirement to determine sine and cosine values which can be computationally expensive, although this is not a significant issue for the intended application. The *polar* method transforms the coordinates to polar ones and can therefore remove the trigonometric limitation of the model by the use of the ratios see Figure 3.12, where

$$\cos\Theta = \frac{v_1}{\bar{R}} \tag{3.49}$$

$$\sin\Theta = \frac{v_2}{\bar{R}} \tag{3.50}$$

the *polar* Box Muller transform requires uniformly distributed variables, v_1, v_2 along (-1,1) rather than (0,1) as with the *basic* approach. Initially two independent, uniformly

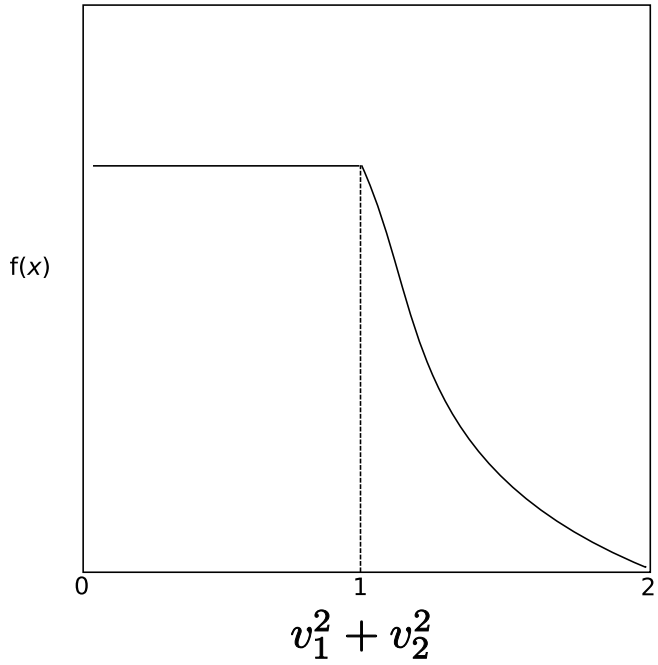

Figure 3.13: Sketch of the behaviour of the frequency of (S) for values in the range (0,2) where only the uniformly distributed values are required.

distributed variables, now called x_1, x_2 are generated on (0,1) see Figure 3.14a where 1000 points have been plotted within these limits within a square of area 4 and a unit circle with origin (0,0). Transforming these two variables to (-1,1) (see Figure 3.14b) by:

$$v_1 = 2x_1 - 1 \tag{3.51}$$

$$v_2 = 2x_2 - 1 \tag{3.52}$$

Yields a uniformly distributed spread in the unit square of area 4. For $\bar{R}^2$ to be uniformly distributed, only the coordinates which lie within the disk $v_1^2 + v_2^2 \leq 1$ are valid, see Figure 3.13. Removal of randomly generated variable pairs which lie outside the limits can be achieved by the relationship:

$$S = R^2 = v_1^2 + v_2^2 \tag{3.53}$$

A loop within the random number generator routine generates the two independent variables, v_1, v_2 and checks that $S \leq 1$ and $\neq 0$. If this condition is not satisfied then the two new variables are generated. Figure 3.14c contains a plot where the check has

been performed on 1000 cycles, 789 meet the criteria (S≤1 and S≠0), where 785 would be the theoretically expected value as the ratio of the area of a square to the area of a circle bounded by a square is $\pi/4$. Having obtained the required polar coordinates with $\bar{R}^2$ being uniformly distributed on (0,1) and Θ uniformly distributed on (0,2π) the polar expression can be formed:

$$\cos\Theta = \frac{v_1}{\bar{R}} = \frac{V_1}{\sqrt{v_1^2 + v_2^2}} \tag{3.54}$$

$$\sin\Theta = \frac{v_2}{\bar{R}} = \frac{V_2}{\sqrt{v_1^2 + v_2^2}} \tag{3.55}$$

From substitution of 3.54 and 3.55 with 3.47 and 3.48 the two independent unit normals, Y_1, Y_2, can be produced:

$$Y_1 = \sqrt{\frac{-2\log S}{S}} v_1 \tag{3.56}$$

$$Y_2 = \sqrt{\frac{-2\log S}{S}} v_2 \tag{3.57}$$

Only one of these variables is required to produce the random multiplier, $R(i)$, required for use in LUSIE. It can be related to the pre-determined μ and σ used as input variables to the routine, by $R(i) = Y_1\sigma\mu$. The relationship between one half of the initially generated uniform variable pair, x_1, and the final normal variable Y_1 can be seen in Figure 3.14. The asymptotic behaviour around 0.5 can be explained by Eq. 3.51, Eq. 3.52 and Eq. 3.53 as when $\lim_{x_1 \to} 0.5$ and $\lim_{x_2 \to} 0.5$, S=0 and when the logarithm is taken in Eq. 3.56 $\lim_{S\to\infty}$, Y_1=∞.

It can be seen in Figure 3.15 that a normally distributed ϕ value with μ 1 and σ 5% has been generated using the two independent uniformly distributed variables. A Gaussian trend can be seen even with only a small sample size of 100 cases and a large bin size in the histogram plot. There are not enough cases to fully appreciate the normal distribution behaviour which is therefore given in Figure 3.16 where 100 000 cycles have been predicted. Of note is the fact that the random number generator used to create the initial x_1, x_2 variables does not appear to create the random variable uniformly, the exact cause for this is unknown. It can be seen however, from Figure 3.14 that the pseudo-

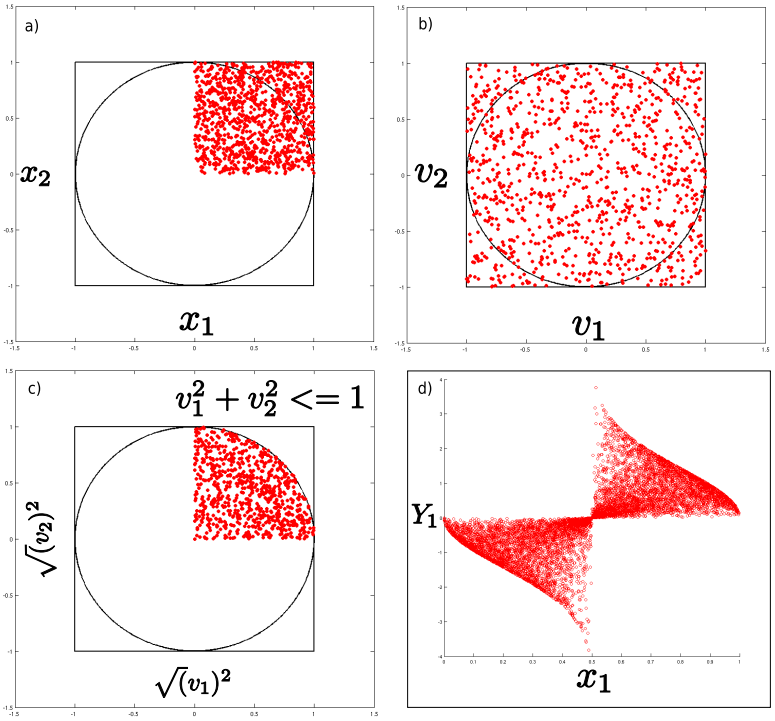

Figure 3.14: Four figures representing the separate processes involved in the *polar* Box Muller method to generate the required normal unit variables (Figures a-c) - 1000 cycles, Figure d) - 10 000 cycles).

uniform random variable generation should not impact the magnitude of the predicted range of the normal unit variable as the variables at the extremity of the initial generation of x_1 and x_2 appear to only influence values of high frequency. Although it may however increase the relative frequency at which an extreme cycle will appear.

3.5 SI combustion code validation

The LUPOE2-D engine (Section 3.6.2) was available to perform experiments throughout the initial stages of this research, it was decided to capture a well defined experimental data set for validation purposes . This included motoring tests, firing tests and observation of the combustion process via optical methods.

3.5.1 Motoring cycle validation

The first set of tests, the motoring cycles, were used to check the fundamental input conditions of the engine and specifically the blow-by parameters. The geometric compression

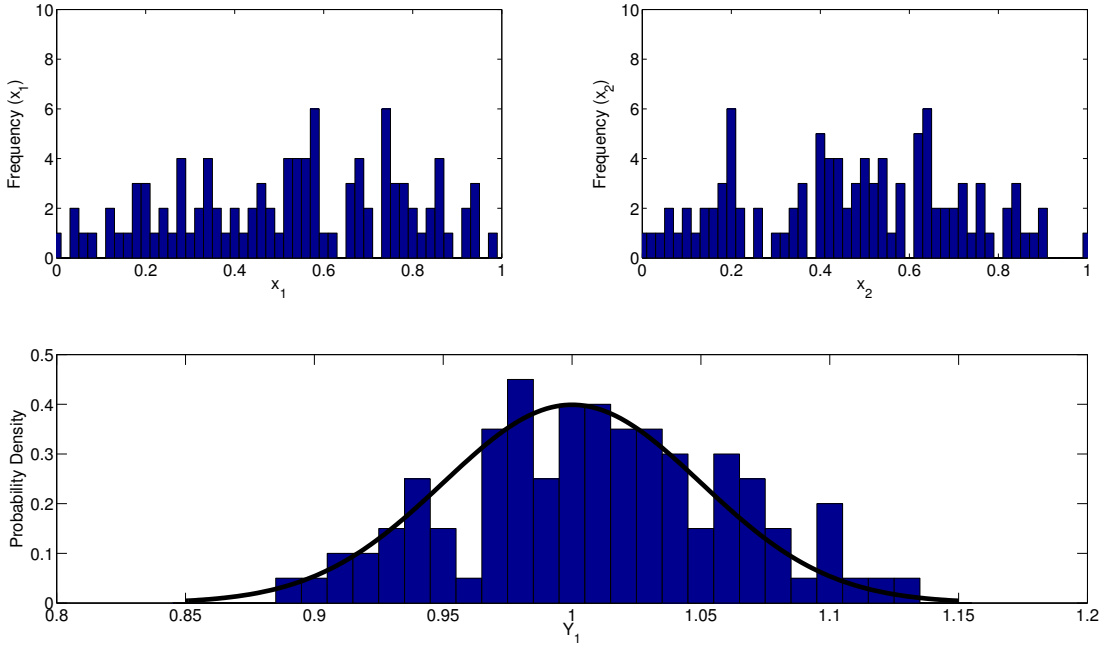

Figure 3.15: Histogram plots of the two initially generated uniform variables x_1 and x_2, for 100 cycles, with the Gaussian distribution of one of the associated randomly generated normal pairs, Y_1.

ratio was calculated both from CAD drawings of the engine and also by measurement. The effective compression ratio, used by LUSIE, was obtained by calculation from piston position at the point of exhaust port closure; itself a measured parameter along with the inlet port opening / closing.

Having adjusted the blow-by parameters (top land crevice volume increased by 30%) and by matching the inlet pressure to that seen in the experimental cycle at the point of Exhuast Port Closure (EPC) a good agreement between predicted and experimental motoring cycles was achieved. It can be seen in Figure 3.17 that the pressure rise agrees with the experimental data well, as does the peak pressure.

3.5.2 Reference condition LUPOE2-D

It is discussed in Section 5.2 that the variability of certain parameters can be reduced by operating the engine at maximum brake torque (MBT). A reference condition was therefore determined experimentally which would operate at the MBT condition for a stoichiometric mixture, at a given engine speed; this condition is herein referred to as the standard reference condition (SRC). Indeed it may provide a useful benchmark for future

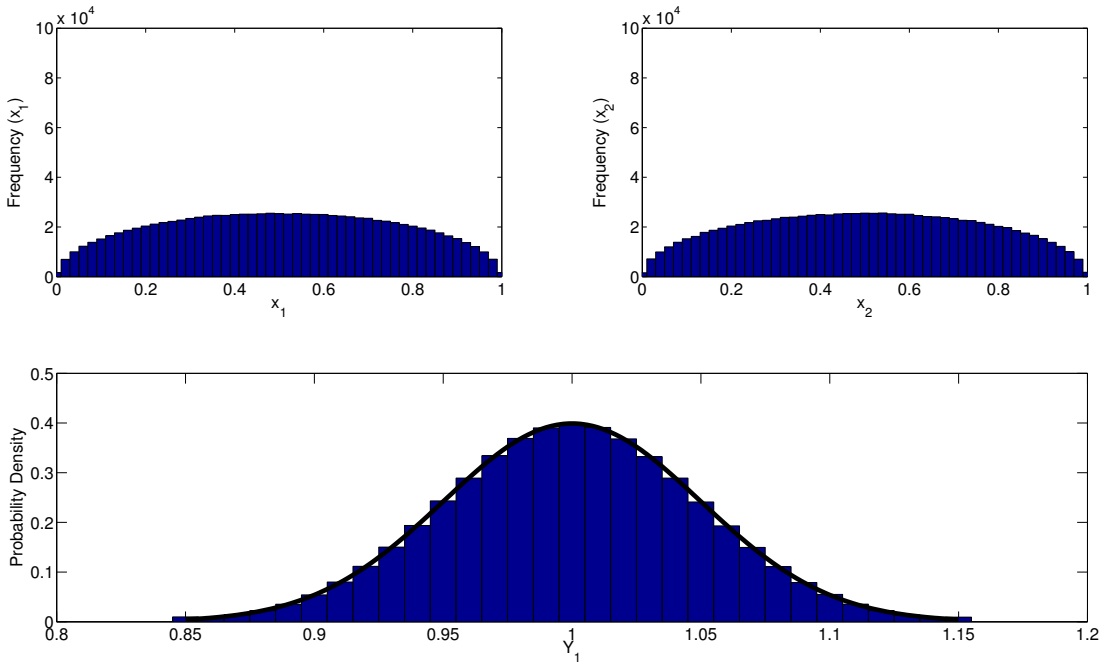

Figure 3.16: Histogram plots of the two initially generated uniform variables x_1 and x_2, for $1{\cdot}10^6$ cycles, with the Gaussian distribution of one of the associated randomly generated normal pairs, Y_1.

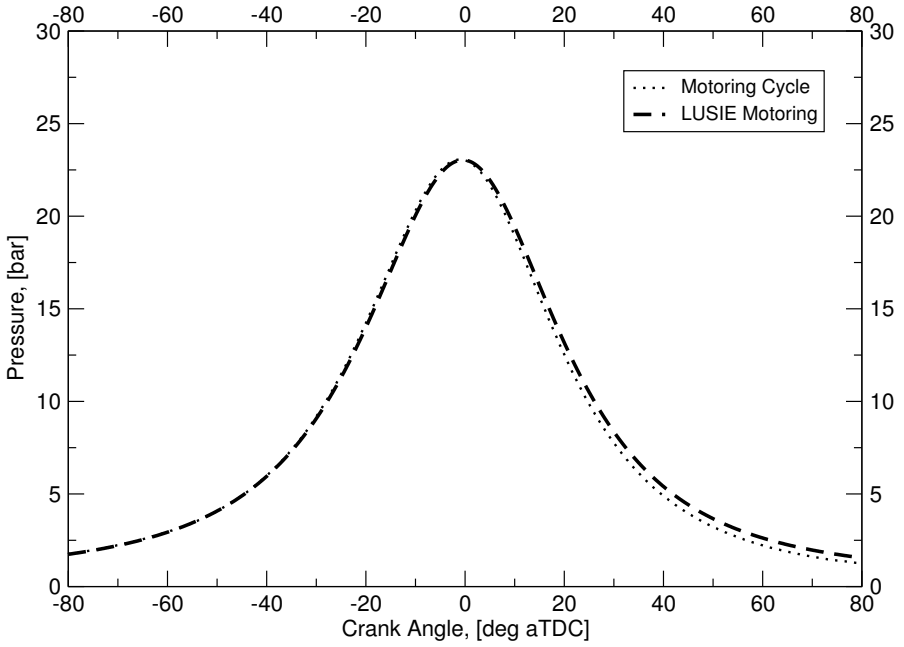

Figure 3.17: Cylinder pressure trace of motoring cycles from the LUPOE2-D engine and the curve predicted using the LUSIE code.

Engine Parameter (Unit)	SRC	SKRC
Equivalence Ratio	1.00	1.00
Spark Advance (° aTDC)	-12.00	-22.00
Intake Pressure (bar)	1.18	1.18
Intake Temperature (K)	323.15	363.15
Engine Speed (rev/min)	1500.00	1500.00
Fuel	iso-octane	iso-octane

Table 3.4: Engine setup parameters for the standard reference condition and standard knocking reference condition for the LUPOE2-D engine.

researchers to test the performance of the engines as they age, as well as the effect of changes in configuration. The operating conditions were determined in an earlier work (Conway [2010]) and are in line with previous work to identify the MBT operating point on the engine with the same configuration; see, for example Roberts [2010]. Additionally a standard knocking reference condition (SKRC) has been created based on the work of Roberts [2010]. The chosen conditions can be seen in Table 3.4.

3.5.3 Firing cycle validation

Having established a baseline for the motoring cycles with derived blow-by parameters it was necessary to asses the ability of LUSIE to accurately model a combustion event. This was achieved by comparison of the predicted crank resolved cylinder pressure in a firing cycle to that seen experimentally at the SRC. Ten tests were run in total, during each test 10 firing cycles were captured with a skip fire ratio of 9:1, resulting in 100 cycles worth of data. Five fast, middle and slow cycles were selected for comparison with the predicted cycle, (see Section 5.2.5 for a discussion on selecting cycles), the results can be seen in Figure 3.18. The predicted ”middle” cycle falls into the faster region of the experimentally seen ”middle” cycles with an acceptable comparable maximum pressure value P_{max}.

3.5.4 Flame radius validation

In addition to analysing the cylinder pressure of the firing cycle, it was also necessary to validate the latest LUSIE version with regards to flame speed To achieve this, a high speed camera utilising natural light conditions was placed directly above, and on the same plane as, the cylinder bore. The quartz optical window, gave full bore access to the

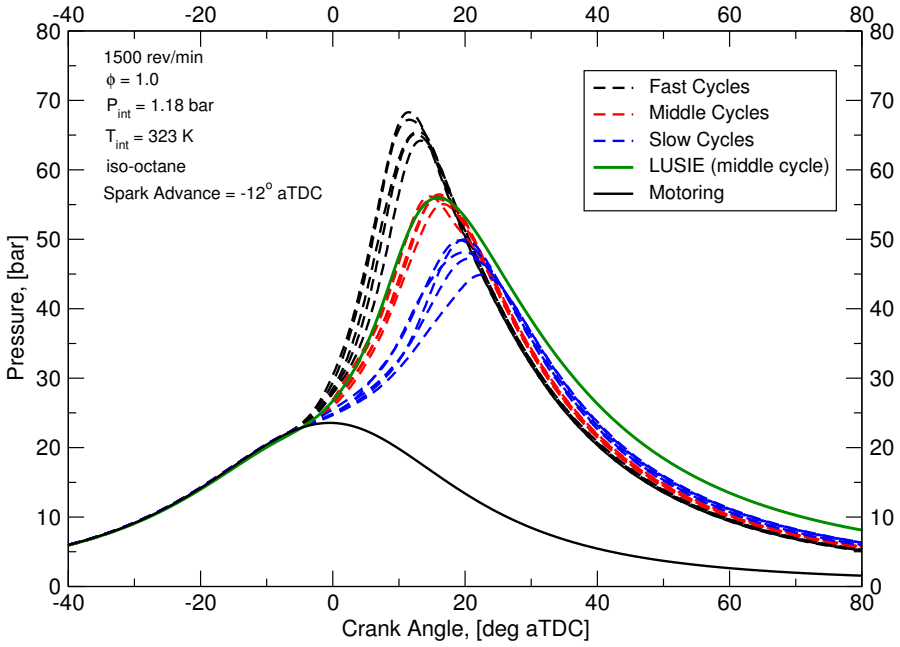

Figure 3.18: The fast, middle and slow defined experimental cycles captured on the LUPOE2-D engine are compared against a "middle" cycle predicted by LUSIE. The operating conditions are at the SRC.

combustion event. The camera was synchronised with the LabVIEW acquisition program to start capturing images on ignition, (see Section 3.6.2). The camera was set to capture at 10 000 frames per second with a shutter speed of 1/capture rate, in this case 100μsec. During the optical tests, 80 individual frames were captured per firing cycle, (72° CA at 1500 rev/min). The raw images captured for a given cycle were related to a flame radii via a MATLAB script with image processing. The script was originally written by a former combustion group member (Mandilas [2008]) and then modified by the author for the specific application within engines. The visualisation toolbox within MATLAB converted the 256 colour greyscale images into binary images; the point at which the black pixels and white pixels form a boundary is used to determine an averaged radius of the flame. The sequence of binarised images representing the combustion process for a single cycle can be seen in Figure 3.19.

The crank-resolved flame radii for the fast, middle and slow cycles seen in Figure 3.18 are presented in Figure 3.20 along with the predicted burned gas radius fr_b and entrained radius, analogous to the laminar flame front radius fr_e. It can be seen that the flame radius initially follows the slow cycle rate of change but then appears to increase in speed during the development phase at a rate greater than was seen experimentally; culminating in a flame radius which is close to a middle cycle while not accounting for either phase individually; the flame thickness can be seen to be increasing throughout the

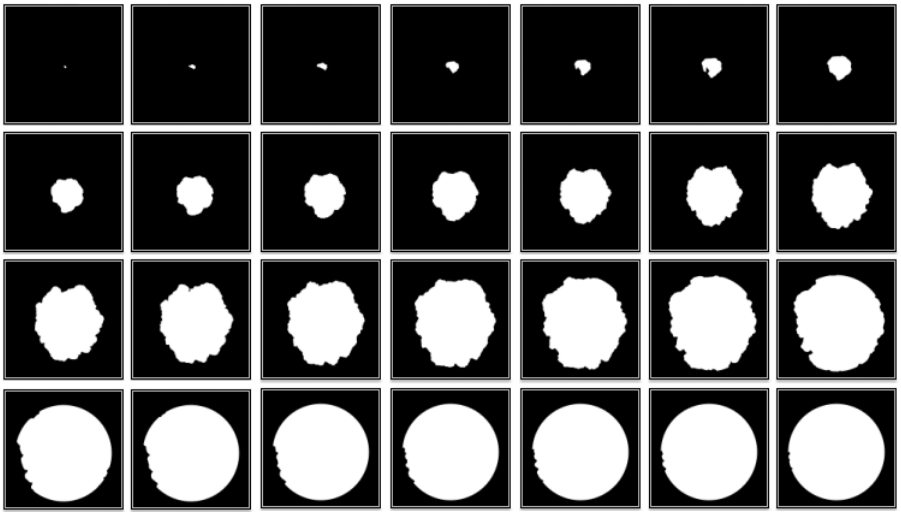

Figure 3.19: Processed and binarised images of flame development during one cycle captured in the LUPOE2-D engine at the SRC. The images are taken 1.11^o CA apart.

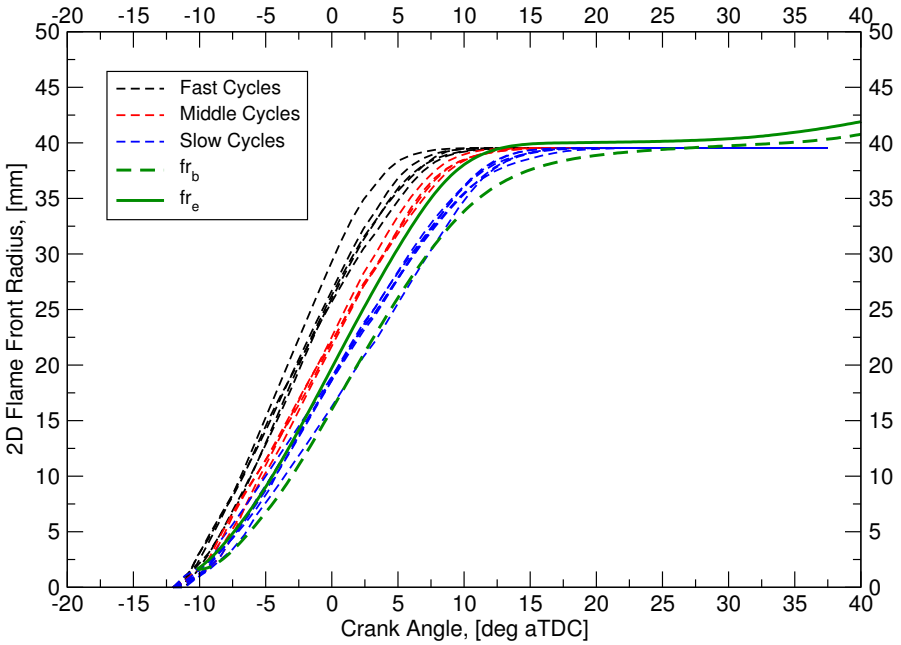

Figure 3.20: The flame radius against cylinder pressure data determined using optical techniques comparing experimental, fast, middle and slow cycles against a simulated middle cycle at SRC.

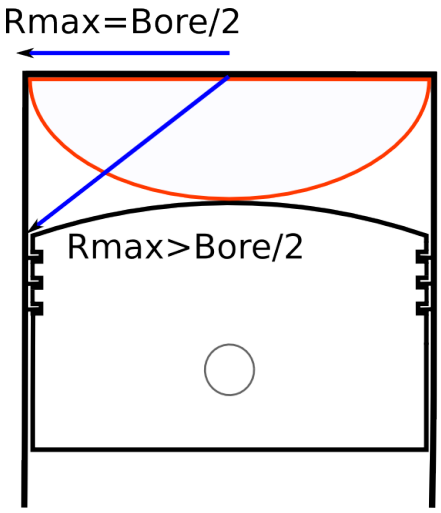

Figure 3.21: R_{max} is equal to half the bore when looking down on top of the engine. LUSIE can predict side projection where $R_{max} > R_{bore}$.

cycle. The deviation of the predicted cycle from the experimental cycle occurs during the phase where the burning velocity is considered to be fully developed, i.e. no longer accelerating over and above the acceleration caused by the flame experiencing different sizes of the turbulent spectrum. It appears that the predicted flame development is initially too slow and that the flame deceleration is not being correctly treated, i.e. the experimentally captured flames are slowing down at a greater than predicted, a consequence of close proximity to the walls.

The increase in flame radius and burned gas radius beyond the limits of the vessel, (40 mm bore), is an additional observation. This effect can be attributed to the projection of LUSIE compared with the projection achieved through the visualisation technique looking at a 2D plane of the cylinder bore. It can be seen in Figure 3.21 that with the assumed spherical flame growth the R_{max} changes dependent on the projection.

3.6 Description of experimental engines

During the reported work a large amount of experimental data were available from four engine platforms; both specific research engines as well as engines designed and built to production specifications. Having a large amount of experimental data is advantageous when modelling for validation purposes; the wealth of data does have an associated caveat however. Since the experimental data was not gathered by the current author, the exact working procedures was not well known. It is hoped however, that robust experimental techniques were used so so level of confidence in the resulted used to validate the

model can be drawn. Where data was gathered at the University of Leeds it was possible to track the process, while it is assumed that a large OEM (Original Equipment Manufacturer) will have well regimented working procedures. However it can not be said with certainty that all possible sources of error are quantified.

A total of four engines were used in the generation of data for this thesis; two University of Leeds single cylinder research engines[1], one boosted OEM research engine and one naturally aspirated OEM engine which has been in production since 2009.

3.6.1 SI engine testing at Leeds

The University of Leeds possess an array of equipment specifically used for fundamental combustion research. With the application of SI and HCCI combustion in engines the LUPOE (Leeds University Ported Optical Engine) series of engine is well suited. The LUPOE engine has gone through the LUPOE iterations in the past 10 years to its current form; the LUPOE2-D (Abdi Aghdam [2003]; Cairns [2001]; Hattrell [2007]; Ling [2011]; Roberts [2010] and Hussin [2012]). A detailed discussion of all aspects of the LUPOE2-D engine is beyond the scope of this work, which is predominantly focused on modelling. An overview of an engine's capabilities and any key technology relevant to modelling will be discussed. For an extended analysis of the LUPOE2-D engine, data acquisition and hardware the reader is encouraged to pursue the work of Roberts [2010] and Hussin [2012] for the LUPOE2-D engine, while the work of Ling [2011] details the LUPOE2-D boosted variant.

3.6.2 Optical research engine

The LUPOE2-D engine block is based on the agricultural Lister-Petter-PH1 single cylinder diesel engine, while the cylinder head, piston, barrel are bespoke components designed and manufactured at the University of Leeds. An overview of the engine setup and the associated analysis equipment can be seen in Figure 3.22,while a engineering drawing of the cross section of the barrel, and intakes can be seen in Figure 3.23. A number of modifications have been made to the engine in order to minimise cyclic variability. The addition of 4 exhaust "rings", or sets of ports which open at prescribed points in the

[1]In reality there is only 1 engine, the LUPOE2-D, however it was converted mid-way through this research to operate under a higher-pressure inlet conditions, known as LUPOE2-D boosted. The inaugural work for this was undertaken by this author, however it became the main focus of a colleges who further enhanced the boosting capability (Ling [2011]).

cycle (a change from single square ports in previous variants), determined by the piston motion. The addition of these was made to improve the efficiency of the cylinder-to-exhaust gas exchange process reducing residual concentration on following cycles which would affect the burn-rate and autoignition performance but mainly to allow for an unambiguous definition of the charge mixture, prior to combustion. Additionally the intakes are diametrically opposed, and the angle at which they meet the barrel has been chosen to reduce bulk flow motion and provide a quiescent flow field near TDC. The LUPOE2-D engine is a n stroke engine which means it can be fired when desired with an unlimited number of "motoring" cycles in between "firing" cycles, designed to further purge the cylinder of residual gases. The full specification of the engine can be seen in Table 3.5 where a comparison with the LUPOE2-D boosted engine, discussed in Section 3.6.3, is made.

The engine can be operated with a metal cylinder head, or with the head containing a transparent quartz disc to allow for optical filming; the disc size is of the same radius as the engine bore allowing for flame development at the wall to be captured. Care must be taken when operating the engine with the quartz head as cycles which exhibit extreme knock can damage the window.

The engine is controlled by operation of a bespoke timing rack consisting of a number of I/O cards used to control the dynamometer and peripherals itself while the data is collected from the same timing rack by a LabVIEW control system. The raw data taken from the LabVIEW data acquisition system has to be converted into usable data with meaningful units. The conversion is achieved by use of a MATLAB script, written by Roberts [2010], detailed in the work of Hussin [2012], which takes the data from the LabVIEW system and is able to split the cycles into individual cycles and correlate them with the correct cylinder pressure and crank angle.

Cylinder pressure is obtained via two in-cylinder pressure transducers, one dynamic the other is static. The dynamic transducer is a Kistler 601A piezoelectric sensor which is mounted in the cylinder head (see Figure 3.23 and used to record the voltage (later related to a cylinder pressure) throughout the entire cycle. Issues can occur with this setup because of the continual high-temperature exposure at the cylinder head location. It has been seen that this can lead to thermal drift over time and regular calibration is required to ensure accuracy (Hattrell [2007]). The static or reference pressure transducer is the Kistler 4045A20 piezoresistive sensor, primarily used to measure the pressure rise during the early part of compression. It is mounted into the cylinder barrel, and is considered far enough away from the high temperature region, to avoid thermal drift. It has however been seen to be susceptible to thermal shock at EPO (Roberts [2010]).

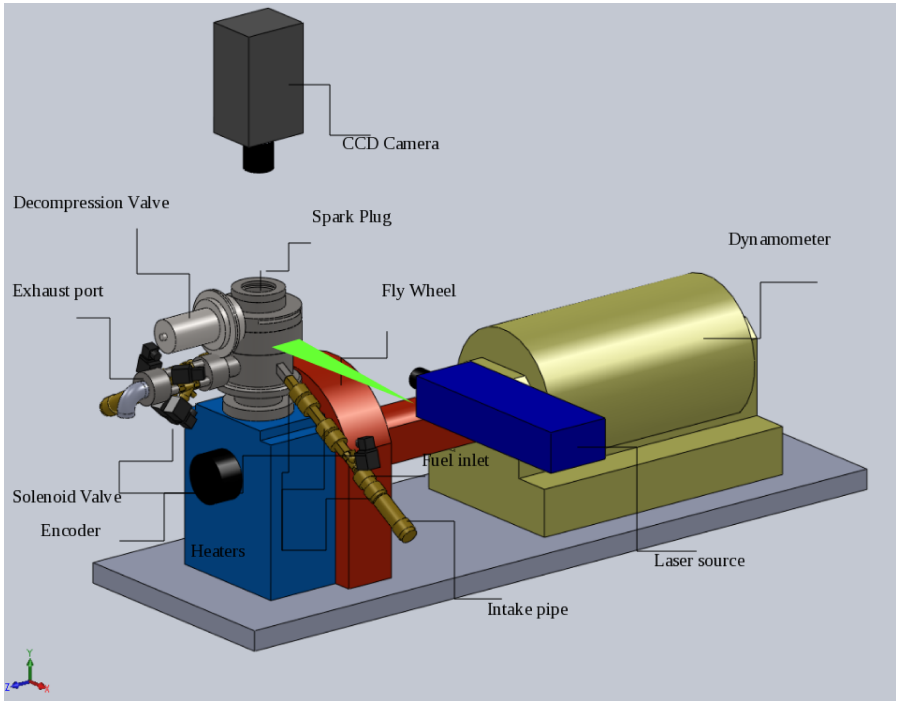

Figure 3.22: An annotated CAD drawing of the LUPOE2-D engine layout and associated equipment, including optical access and laser positioning for LDV and PIV experiments. Modified from Ling [2011].

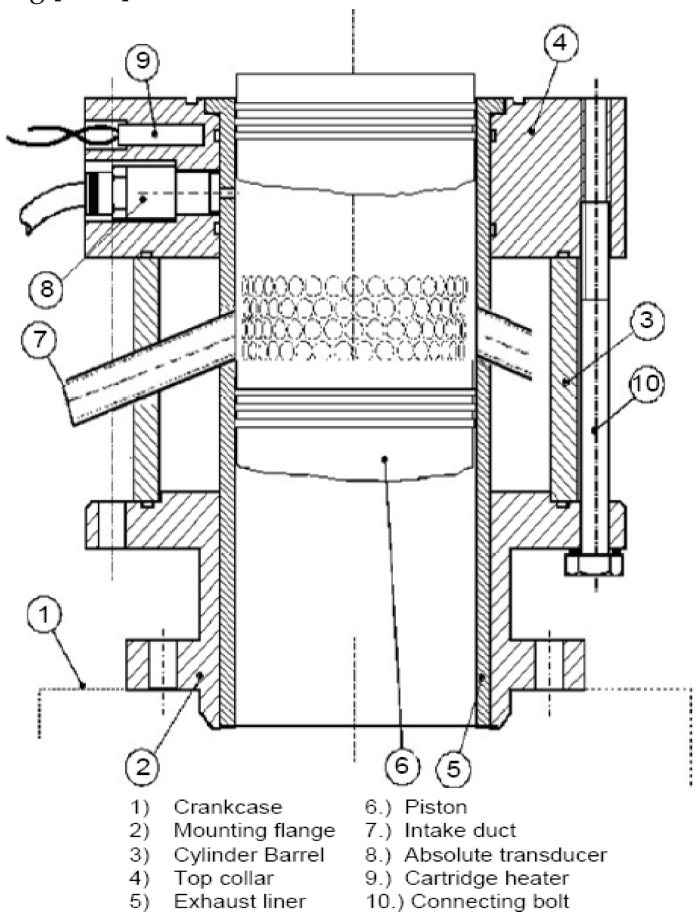

Figure 3.23: An annotated cross-section view of the LUPOE2-D engine (non boosted). Modified from Abdi Aghdam [2003].

Optical access, granted by the quartz windows, allows the in-cylinder combustion process to be captured. This is achieved using the natural light from a flame captured by a Photron Ultima APX-RS high speed digital camera. The camera is positioned directly above the cylinder, and on the same plane as the cylinder bore. The camera trigger and ignition timing are linked so as to avoid unnecessary cycles being captured. A fuller description of the techniques used to capture cycles optically can be found in the work of Roberts [2010].

3.6.3 Boosted LUPOE2-D engine

The LUPOE2-D engine is supplied by a compressed air line providing a constant mass flow rate of air at 4 bar, mass flow could be regulated to reduce pressure. The maximum achievable initial pressure, p_{int} however was approximately 1.2 bar at 1500 rev/min. The engine clearly required modification to be fit for study into the effect of high intake pressures on combustion. Two short-term solutions were devised: 1) Increase the compression ratio by geometric modification to the barrel. 2) modify the barrel by removing rows of the exhaust "rings" so that the piston would not reject charge on the compression stroke between intake port closure (IPC) and exhaust port closure (EPC), thus increasing the trapped mass and therefore increasing the pressure. Increasing the compression ratio would have resulted in an associated increase in intake temperature as the temperature increase is dictated by the volume ratio, between the clearance volume and volume at the start of compression (V_2 / V_1); an undesirable situation as it was hoped to separate the pressure-temperature dependency within engines (from boosting systems not employing ideal inter-cooling). It was therefore decided that the cylinder barrel should be re-manufactured with the removal of the top two exhaust rings. The effect on the relative port closing positions can be seen more clearly in Figure 3.24, where the intake now closes *after* the exhaust ring as the piston ascends, resulting in a higher P_{int} of approximately 1.5 bar at 1500 rev/min (peak motoring pressure increased from 23 to 32 bar). The difference made by the removal of two exhaust rings can be seen in Figure 3.25, while the exact effect of the geometric change on the port closing times can be found in Table 3.5. Clearly the scavenging efficiency of the engine is compromised with this setup, subsequently the number of skipped cycles, must be increased to ensure the cylinder is purged of exhaust gases. Additionally it is seen that the dynamic compression is increased by approximately 0.8 by removal of the two exhaust rings.

The engine was then further modified by Ling [2011] who introduced independently controlled exhaust valves, as opposed to the geometrically controlled port on the

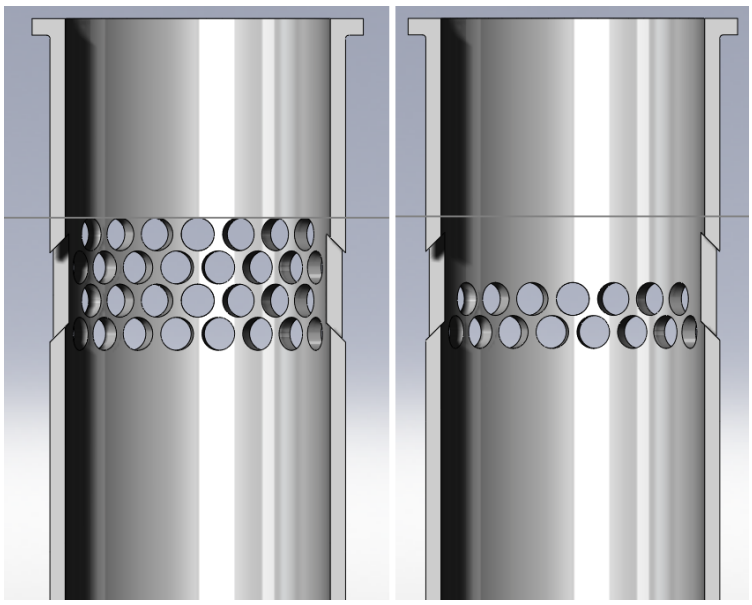

Figure 3.24: A figure highlighting the cross-sectional area of the non-boosted and boosted LUPOE2-D cylinder liners. The change is the removal of two "rings" of the exhaust ports. LUPOE2-D is on the left, LUPOE2-D boosted is on the right.

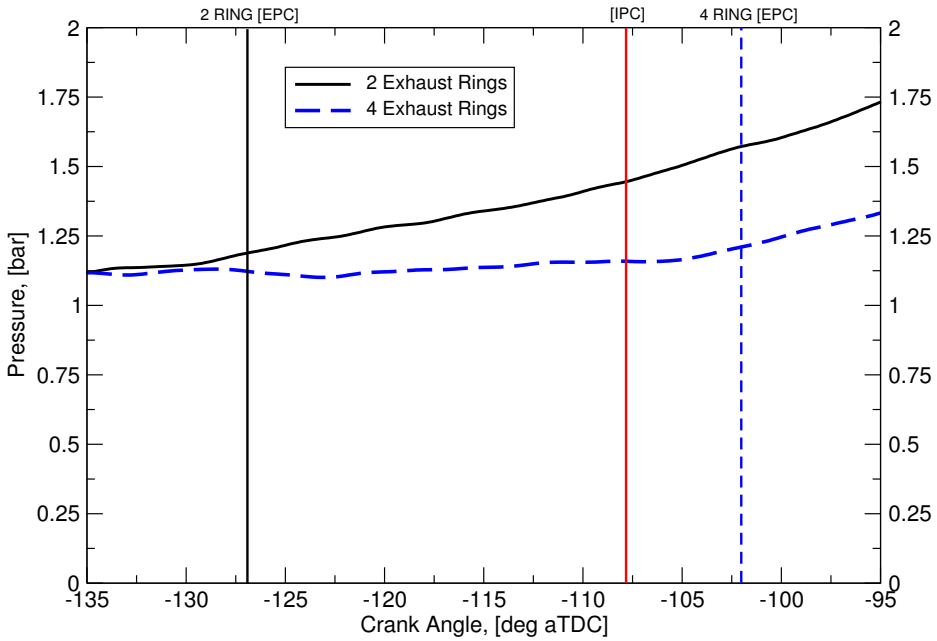

Figure 3.25: Pressure at the point of IPC for the 2 ring and 4 ring variants of the LUPOE2-D engine. Theoretical compression of the closed system begins at IPC for the 2 ring setup and EPC (4 ring) for the 4 ring setup.

Engine Parameter	LUPOE2-D	LUPOE2-D Boosted
Bore (mm)	80.0	80.0
Stroke (mm)	110.0	110.0
Clearance Height (mm)	8.0	8.0
Connection-Rod Length (mm)	232.0	232.0
CR_{Static} / $CR_{Dynamic}$	15.2 / 10.5	15.2 / 11.3
IPO/IPC° aTDC	-101.2	-101.2
EPO/EPC° aTDC	107.0	127.6

Table 3.5: A comparison of the more important engine parameters between the LUPOE2-D and LUPOE2-D boosted engines.

non boosted LUPOE. The new valve control system enables the intake mass flow rate, and the initial pressure to be independently varied; an important consideration when analysing the effect an increase in pressure has on say, turbulence quantities, known to be heavily influenced by intake velocities. The engine, at the time of writing is capable of almost achieving the 4 bar maximum intake pressure (as limited by the compressed air feed) at intake port closure, sufficient for study into high pressure combustion.

3.6.4 Jaguar Land Rover engines

In addition to results obtained through use of research engine, experiments were also performed on two engines under the control of an OEM, referred to as either the production or research engines in this work. These tests were performed where the LUPOE engine capabilities are limited; such as handling large quantities of data, useful for cyclic variability. In addition, the production engine was used as the primary testbed for high pressure testing owing to the ongoing development of the LUPOE2-D boosted engine.

3.6.5 Naturally aspirated production engine

The naturally aspirated, 5.0L V8 production engine, officially designated AJ133, has been publicly available since 2008 in both supercharged and naturally aspirated forms. The latter produces 515 Nm of brake torque, τ_{tq}, meaning it achieves 13 bar BMEP. The application of this engine to the current study is predominantly on cyclic variability. The author's knowledge of the engine is limited to literature as the testing was undertaken off site by the another University as part of a consortium involved in downsized engine

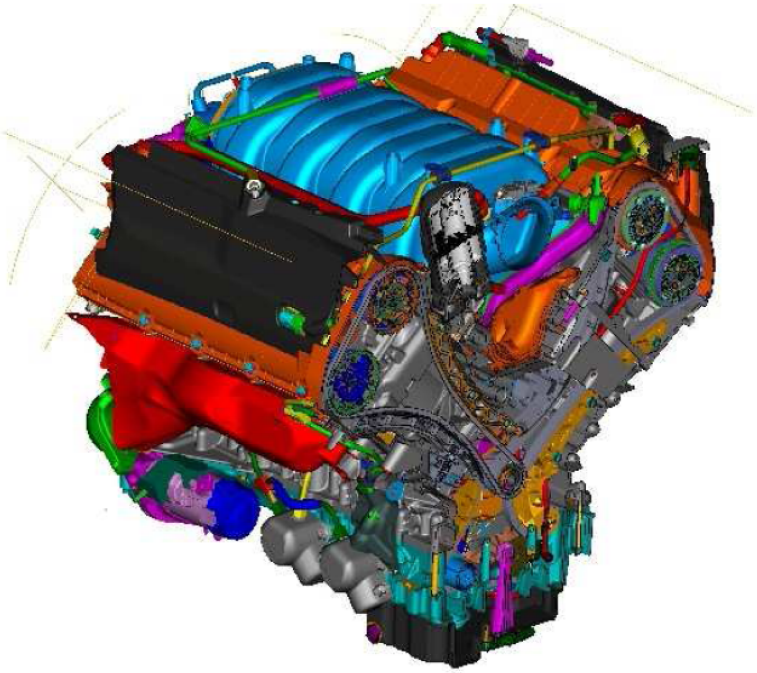

Figure 3.26: An isometric, CAD generated, view of the non-boosted production engine, from the ancillary end with a cross sectioned view showing the two banks of cylinders and valve train. Taken from Sandford et al. [2009].

research (Zolfagharifard [2013]). The technology relevant to this work includes variable cam position phasers which will change the timing of the intake and exhaust valve opening and closing points with respect to piston position; a technology commonly referred to as variable valve timing (VVT). Additionally the engine operates with variable valve lift (VVL); VVL on the AJ133 engine changes the intake valve lift at varying operating conditions depending on load and engine speed. Such a system also likely alters turbulence characteristics (predominantly rms turbulent velocity). In addition the engine includes a knock controller which identifies knocking cycles and then implements a control strategy of spark retard for subsequent cycles to prevent damaging ”run-on” knock occurring, i.e. where knock from one cycle is responsible for the knock event occurring in the following cycle.

3.6.6 Heavily boosted research engine

The boosted research engine is a part of the UltraBoost project; a project undertaken by JLR to determine the limits of SI downsizing (Zolfagharifard [2013]); it is refereed to, in

this report, as UB100[1]. One of the engine targets was to retain the naturally aspirated full load performance of 515 Nm of brake torque - which translates to a BMEP figure of 32 bar for the 2.0 L in-line 4 cylinder engine. A figure of 32 bar BMEP requires significant boosting, in this case a "turbo-super" layout was proposed (a boosting system consists of both a turbocharger and supercharger) which provides maximum boosting over the entire engine speed range as well as having good transient performance.

Despite having a boosting system proposed, throughout the duration of this work the engine was operated under idealised inter-cooling conditions, on a test-bed fed by compressed air. The primary reason for operating the engine under idealised conditions was that the boosting system was still being selected and designed into the engine package for a large proportion of the project time. The situation does however present the ideal opportunity to study the effects of increased intake pressure without the usually associated increase in temperature. The engine on the test bed running under idealised-intercooling can be seen in Figure 3.27. Data available from the engine would be in the form of crank-resolved cylinder pressure traces. It was felt that this would provide enough information for the proposed study into high pressure combustion. The ability to fully study the combustion process was limited as optical analysis or turbulence characterisation techniques were not feasible.

Apart from the difference in displacement and aspiration, there are other noteworthy differences between the two engines, the specification of the two engines can be seen in Table 3.6. Firstly the static compression ratio CR_{static} is lower in the boosted engine, a common design feature to avoid high temperatures that could lead to knock; although the theoretical peak thermal efficiency, η_{th} is also limited by this reduction[2]; see for example Pulkrabeck [2004]. The other interesting design difference is the difference in stroke between the two engines. The implications of having different strokes is that, for a given engine speed, N, there will exist a different mean piston speed, $\bar{S_p}$. Tt has been seen that the mean piston speed is influential in the generation of turbulence in engines 3.4.2. Additionally, the different connecting-rod lengths will lead to different locations of peak instantaneous piston speed, S_p.

Of particular relevance to this study is that the engines employ direct fuel injection strategies. The naturally aspirated variant is "spay-guided", whilst the boosted variant

[1]Although referred to in this report as UB100 the engine has gone through two other iterations, however the build and specification throughout this work is relevant only to the UB100 configuration.

[2]More correctly it is the expansion ratio (ϵ_R=V_1 / V_2) which dictates the efficiency of the cycle as it determines the amount of useful work that can be converted from the chemical heat release. Although geometrically linked in all non-Atkinson cycle engines, it is possible to independently alter the dynamic expansion and compression ratios with variable valve timing (VVT) systems.

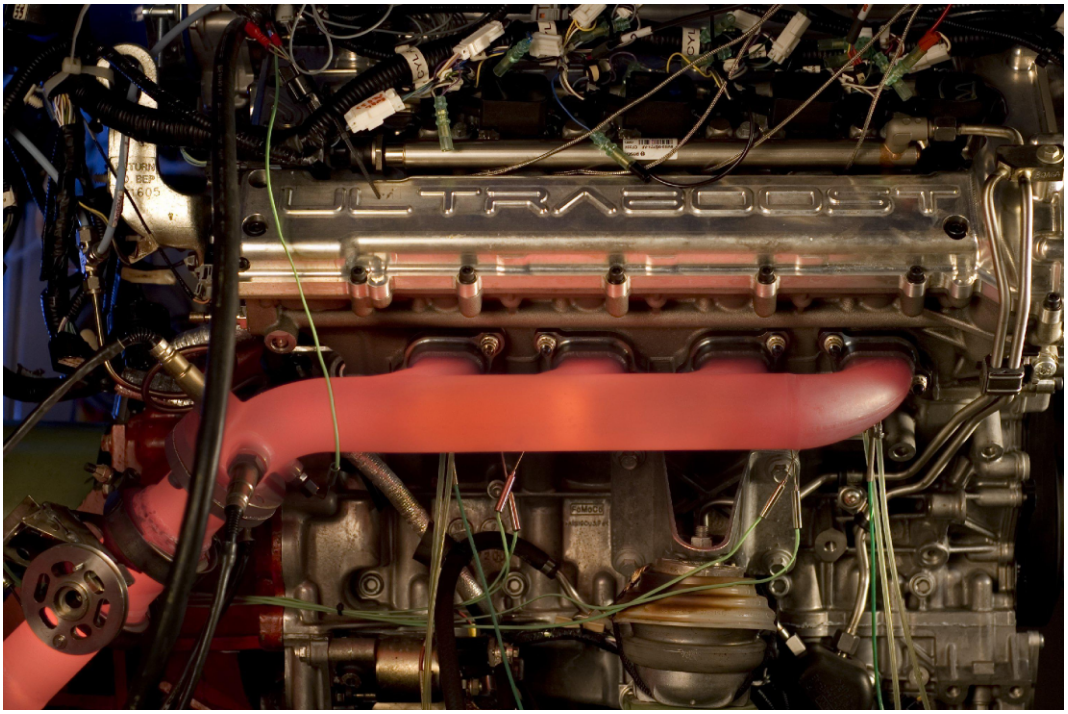

Figure 3.27: A picture of the UB100 engine running on the testbed at the University of Bath; note the lack of turbocharger. Taken from Lotus [2013].

Engine Parameter	AJ133	UB100
Bore (mm)	92.5	82.9
Stroke (mm)	93.0	92.0
No. Cylinders	8	4
Connection-Rod Length (mm)	150.0	148.05
Displacement (cc)	4999	1990
CR_{Static} / $CR_{Dynamic}$	11.5 / Variable	9 / Variable
IPO/IPC° aTDC	VVT	VVT
EPO/EPC° aTDC	VVT	VVT
Injection Type	Spray-guided GDI	Wall-guided GDI

Table 3.6: A comparison of the more important engine parameters between the non-boosted and boosted production engines.

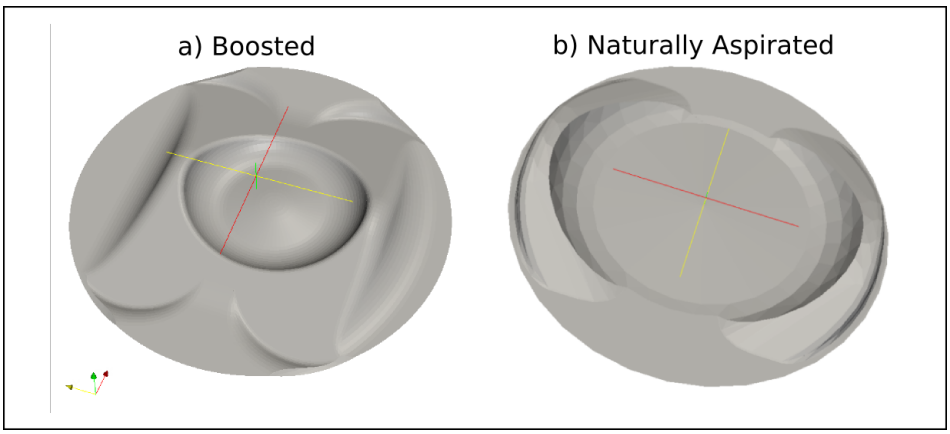

Figure 3.28: Isometric view of the UB100 and AJ133 piston surfaces from CAD files. The bowl in the centre of the UB100 piston is a requirement for direct injection engines to direct fuel toward the spark plug in wall-guided systems.

is "wall-guided". There are implications that the different strategies may have on engine performance, such as the ability to run at leaner conditions with wall-guided systems. Perhaps the biggest consideration is the different requirements for combustion chamber design, the two different piston topologies can be seen in Figure 3.28. In the wall-guided chamber (as in the boosted engine) requires features on the piston to guide the spray towards the spark-plug; this feature is not required in a spray-guided setup. The piston shape can have a significant influence on the propagation of combustion, as well as turbulence conditions at TDC (Miyamoto et al. [2006]).

3.7 LUSIEDA

The experimental engines yielded a significant amount of crank-resolved cylinder pressure data. From these data, it was necessary to extract information regarding the gas temperature, burned fuel mass and turbulent mass burning velocity for the variability studies in Section 5.7 as well as for comparing the performance of autoignition models for the four engines in section 6.3.1. The code used to determine the outputs was LUSIEDA (**L**eeds **U**niversity **S**park **I**gnition **E**ngine **D**ata **A**nalysis). LUSIEDA assesses the closed part of the engine cycle and derives the mass fraction of the burnt gas from the pressure signal. Essentially, LUSIEDA is a reverse of the LUSIE code. The crank-resolved cylinder pressure obtained experimentally is input into LUSIEDA, from which the contributing processes which sum to make that pressure are determined. For the purposes of combustion investigation, the important pressure required is the pressure rise which is

solely caused by the heat-released by the fuel burned i.e. the combustion event ΔP_{comb}; given by:

$$P_{i+1} = P_i + \Delta P_{pm} + \Delta P_{ht} + \Delta P_{lg} + \Delta P_{comb} \tag{3.58}$$

where P_i and P_{i+1} are the experimental cylinder pressures at two consecutive crank angles, θ_i and θ_{i+1}, ΔP_{pm} is the pressure change as determined by isentropic expansion or compression by the change in volume caused by piston motion ΔP_{ht} is the change in pressure caused by heat transfer modelled by the Woschni heat transfer model (see Section 3.2.11, ΔP_{ig} is the change in pressure caused by mass leaving (or re-entering) the system throughout the cycle, and is calculated by the blow-by model (Section 3.2.10). The change in pressure deemed to be caused by combustion is caused by a certain amount of fuel being burned. The amount of fuel burned is determined from the adiabatic flame temperature. An iterative method, based on a minimum error, is used to determine the mass fraction of fuel burned. Once the amount of fuel burned has been determined, then the turbulent mass burning velocity can be determined from Eq. 3.2. LUSIEDA has been introduced and summarised here; a fuller description can be found in Liu et al. [2013] or the theses of Hattrell [2007] or Roberts [2010]

Chapter 4

Turbulence Properties in SI Engines

4.1 Chapter Overview

The work presented in this chapter is focused on characteristics of turbulence, namely length scales and rms turbulent velocity, u', modelled using a 0-D $k-\epsilon$ model incorporated into the existing quasi-dimensional combustion model, LUSIE (detailed throughout Chapter 3). Model predictions were compared with experimental data and the commercially available engine simulation package, GT-Power (for the LUPOE2-D engine), as well as CFD predictions of turbulence in two production engines. Combustion predictions were made for the four engines of interest, LUPOE2-D, LUPOE2-D boosted, AJ133 (non-boosted production engine) and UB100 (boosted production engine). Experimental data obtained from these engines was at different operating conditions, with different levels of boosting. In addition, the combustion chamber geometries of the AJ133, UB100 and LUPOE2-D engines were significantly different to each other; the LUPOE2-D and LUPOE2-D boosted chamber geometries were identical. The ability of LUSIE to predict combustion in these engines is of significant interest in this chapter; the requirement to predict a cycle that was in good agreement with experimental cycles is to enable variability and autoignition modelling studies (see Chapter 5 and Chapter 6 respectively).

4.2 Turbulence model validation

The 0-D $k-\epsilon$ turbulence model implemented into LUSIE was used throughout the current work for the prediction of turbulence characteristics. Validation of the turbulence model was an essential first step in determining the fidelity of the combustion model as a whole. The need for a turbulence model is necessary where experimental data for the reported engines was not made available.

4.2.1 Single cylinder engine

Rms turbulence velocity, u', values have been predicted for the LUPOE2-D using the 0-D $k-\epsilon$ turbulence model, described in Chapter 3. The performance of the model was compared directly with the predictions from the GT-Power $k-\epsilon$ model, as well as experimentally obtained turbulence data from the LUPOE2-D engine.

The u' values, for the LUPOE2-D were experimentally captured using Laser Doppler Velocimetry (LDV) techniques; a very brief discussion of LDV techniques will be introduced here, though the reader is encouraged to read the fuller description of LDV techniques, with specific application to the LUPOE2-D engines, presented in the Ph.D. thesis of Hussin, 2012. LDV techniques are used to determine flow velocities by analysing the frequency of the light scattered by particles (seeds) which have been introduced into the gas flow. The underlying assumption is that the particles will follow the flow field motion in the same manner as dry air would. Thus permitting the local velocity of the seed at the LDV probe to be determined. The seeding used in the LUPOE engines took the form of Titanium dioxide (TiO_2) particles of 0.5 μm in diameter. The seeds were introduced into the system by a fluidised bed arrangement which has been used by previous LUPOE engine operators (Abdel-Gayed et al., 1987 and Atashkari, 1997). This arrangement was modified by Dawood, 2010 with the introduction of a heating system which prevented agglomeration of the particles.

In addition to validating the model against experimental LDV data and against turbulence predictions from GT-Power, the piston speed term in the 0-D $k-\epsilon$ turbulence model used in LUSIE and discussed in Section 3.4.2, was simplified using the mean piston speed, $\bar{S_p}$, as opposed to the instantaneous piston speed, S_p (Eq. 3.33; the comparison of the turbulence results can be seen in Figure, 4.1.Here it is noticeable that there is a considerable difference in u' values during the inlet and compression phases (between -108^o and 0^o aTDC), when comparing the GT-Power prediction with the 0-D $k-\epsilon$ model prediction of turbulence. It is important to note that the model within LUSIE has been

"fitted" to the experimentally derived data by way of adjustment of the inlet, production and dissipation coefficients, F_i, F_p and F_d, respectively.

The predicted initial turbulence value at the start of the cycle is of a far higher magnitude in GT-Power compared to both LUSIE and experimental data. The intake velocity, determines the initial k value for both models, on the first iteration. The definition of the initial k value (Eq. 3.37) is the same for both the 0-D $k-\epsilon$ turbulence model in LUSIE and that used in GT-Power (Morel and Mansour, 1982). Assuming the initial value of k is the same for both models then it can be determined that the over prediction of the GT-Power model at θ = -180 aTDC appears to be caused by a higher predicted intake charge velocity during in the gas exchange phase in the LUPOE2-D engine, vis-á-vis the experimental results. GT-Power simulates velocity at each crank angle step based on the changing profiles of intake and exhaust ports, while the 0-D $k-\epsilon$ model takes an average velocity based on the total mass transfer during the period the ports are open/closed, i.e when mass in transferred to and from the system; in theory, will result in an increase in velocity as the ports begin to close for the GT-Power prediction, based on isentropic flow. It can be seen from Figure 4.1 that there is a surge in u' close to Intake Port Closure (IPC); it is likely to have been caused by the reduction in flow area and resultant increase in velocity, not seen in the 0-D $k-\epsilon$ model prediction because of the averaged flow velocity; the port area closing surge, is also not visible in the experimental observations. Generation of u' in the LUPOE2-D appears to occur quickly at Exhaust Port Open (EPO) and no further turbulence is generated by the inlet jet after around 120^o aTDC. The experimental data also shows another maximum in u' shortly after TDC, at approximately 20^o aTDC; though not proven, it has been attributed to a spatial phenomenon within this engine seen when measurements are taken close to the cylinder walls (Hussin, 2012).

4.2.1.1 Piston speed definition

The effect of using the instantaneous or mean piston speed, IPS or MPS, respectively, in the production terms of the 0-D $k-\epsilon$ model can also be seen in Figure 4.1 where both definitions show good agreement during the compression phase vis-á-vis experimental data, the difference between using the IPS or the MPS useage is more pronounced during the later stages of compression and into the crank angle window that represents the combustion phase.

The primary area of interest for modelling is the crank angle window in which the bulk of combustion takes place; the combustion phase is where the turbulence properties are called by entrainment and burning routines. It can be seen in Figure 4.2 that during

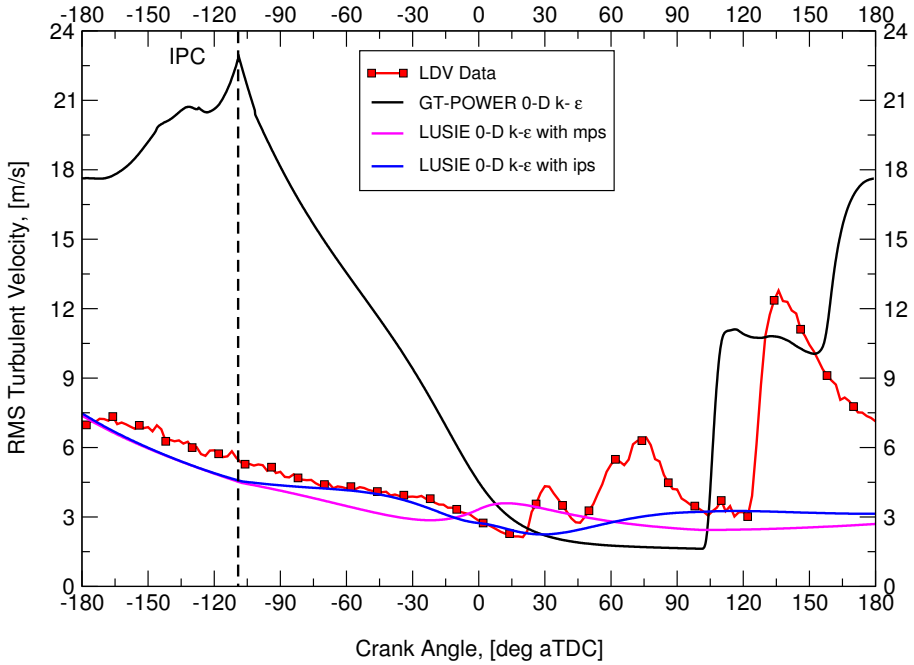

Figure 4.1: Comparison of different models used to predict u' during intake, compression and expansion phases for the LUPOE2-D under motored conditions at standard operating conditions for the LUPOE2-D engine of 1500 rev/min, ϕ = 1.0 and $\bar{P}_i$ = 1.18, bar, experimental rms turbulence data was obtained using the LDV method.

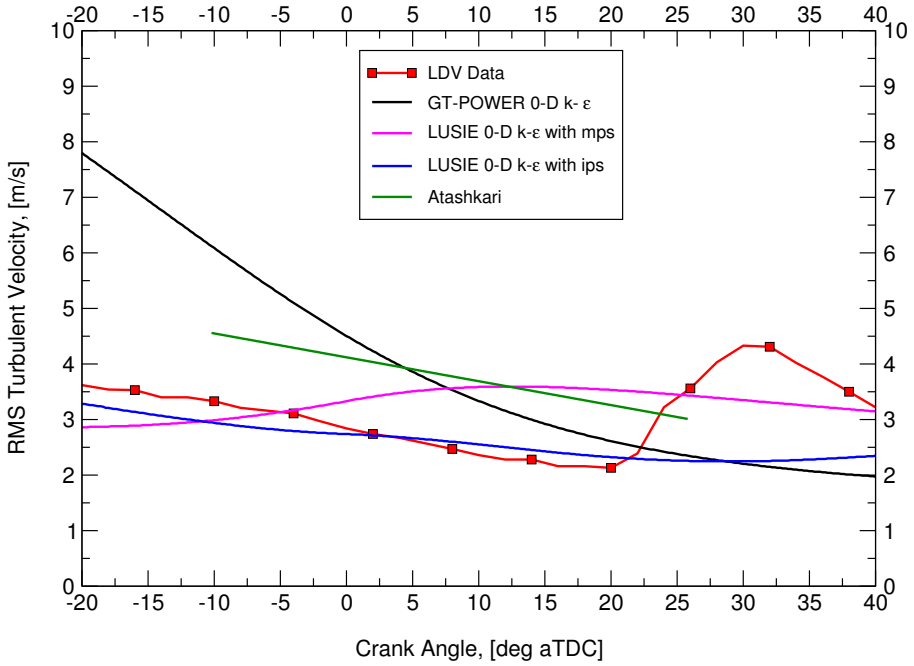

Figure 4.2: Comparison of different models used to predict u' during crank angle window where combustion is likely to occur in the LUPOE2-D engine. The experimental data was collected on the LUPOE2-D engine.

the combustion window, approximately -20^o to 40^o aTDC, the agreement between the 0-D $k-\epsilon$ model prediction and experimental data is good, with u' values far lower than the GT-Power prediction, possibly as a result of the very high initial u' value at the start of the cycle as previously discussed. The values predicted by the 0-D $k-\epsilon$ model are also closer to experimental data that those predicted by the Atashkari empirical data fit introduced in Section 3.4.1. The Atashkari results was omitted from Figure 4.1 as they are only validated for the combustion phase. In addition, the engine used by Atashkari, the LUPOE1 engine, although being fundamentally the same as the LUPOE2-D used in this study, has a number ofl key differences to the intake and exhaust geometry and port configuration which will affect the turbulence generation. The net result is that the least squares linear fit proposed by Ataskari, using the constants previously validated for the previous LUPOE1 engine generation, are no longer relevant for studies on the latest iteration LUPOE2-D engine.

The variation between IPS and MPS can be seen more clearly in Figure 4.3. Differences between the use of the two definitions begin to occur at IPC, after this point, the intake term becomes 0 as there is no mass entering the cylinder, $I = 0$ (Eq. 3.35) and $\frac{dM_c}{dt} = 0$ (Eq. 3.32). This leads to domination of the production term, P. As seen in Eq. 3.33 P is comprised of two parts. Taking the RHS term, the following limit can be seen as the piston approaches TDC, $\lim_{\theta \to 0}$, $\frac{dV_c}{dt}$ = 0. The LHS of Eq. 3.33 contains piston velocity, $|S_p|$ raised to the third power. In reality, however, as was seen in Figure 3.9, as $\lim_{\theta \to 0}$, $|S_p|$ = 0 and $\lim_{\theta \to 180}$, $|S_p|$ = 0. It is for this reason that the differences between IPS and MPS are found to increase either side of θ = 0 and θ = 180 as seen in Figure 4.3; the use of the IPS leads to a smaller error during the intake and compression phase compared with experimental data as seen in Figure, 4.4. All subsequent results presented in this thesis, which use the 0-D $k-\epsilon$ model in LUSIE, use the IPS for the definition of piston speed.

The influence of the mean and instantaneous piston speeds, on the production term, P, (Eq. 3.33) in the 0-D $k-\epsilon$ model can be seen in Figure 4.5. The influence of piston speed definition on the dissipation term, D, (Eq. 3.34) in the 0-D $k-\epsilon$ model can be seen in Figure 4.6. The earlier mentioned increase in production (caused by the decrease in the RHS of Eq. 3.33) can clearly be seen by the larger value of the production term when using the MPS definition. Hence, the dissipation term (also a function of k) has a maximum at θ = 0.

The intake jet velocity, more specifically its breakup into turbulent kinetic energy (TKE), is the primary influence behind turbulence generation in engines. A reduction in engine speed, which reduces the mass flow rate into the engine, results in a drop in the intake velocity by as governed by Eq. 3.38 . Present automotive vehicles require engines

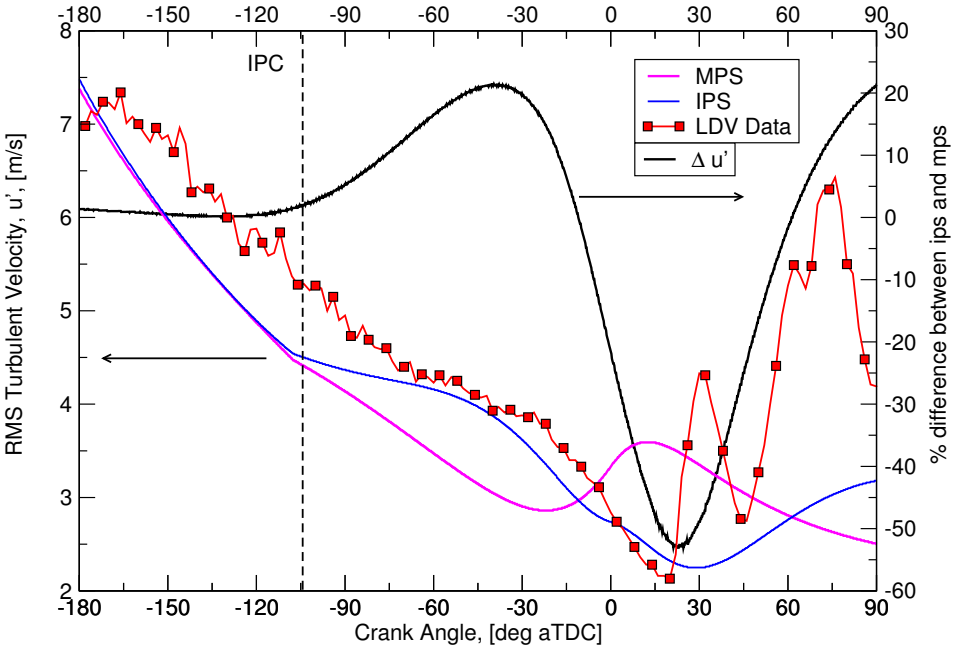

Figure 4.3: The influence of the piston speed definition used within the 0-D $k-\epsilon$, on the u' during the intake, compression and combustion phases, compared with the LDV experimental results.

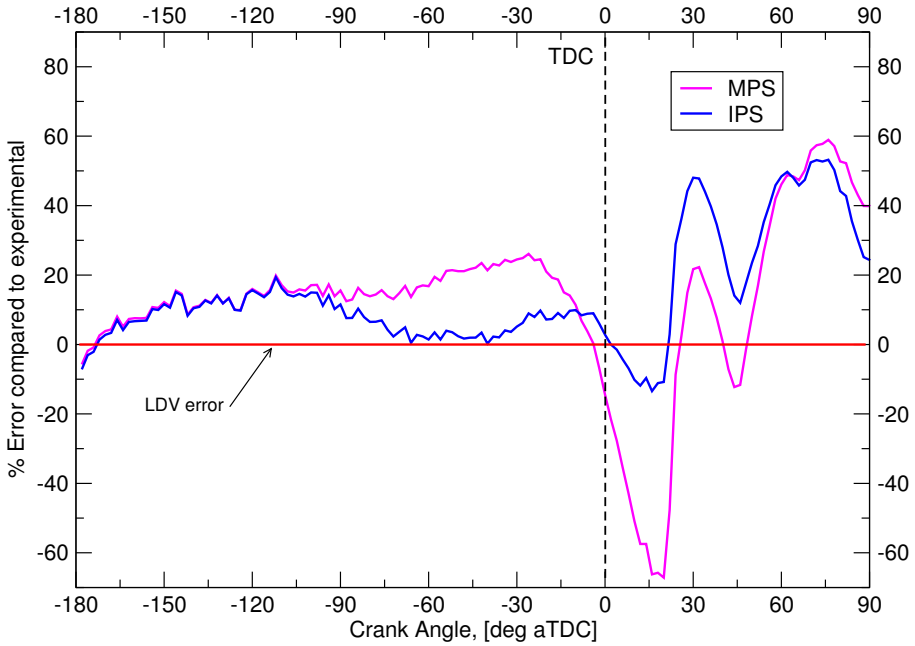

Figure 4.4: The influence of the piston speed definition, within the 0-D $k-\epsilon$ model, on the overall error of u' when compared with the LDV experimental results.

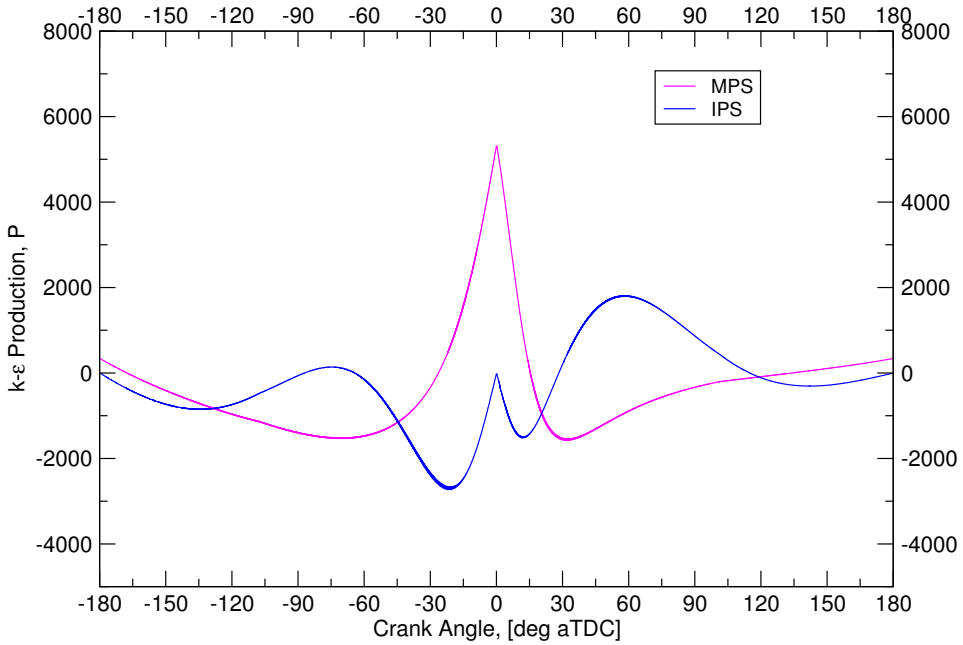

Figure 4.5: The influence of the piston speed definition used within the 0-D $k-\epsilon$, on the producing term, P.

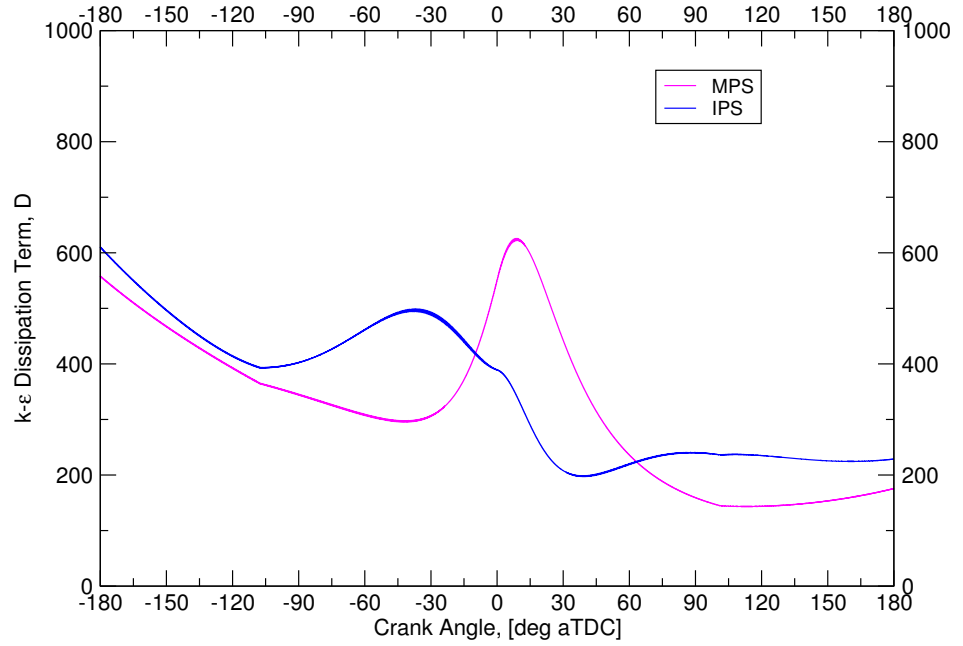

Figure 4.6: The influence of the piston speed definition used within the 0-D $k-\epsilon$, on the dissipation term, D.

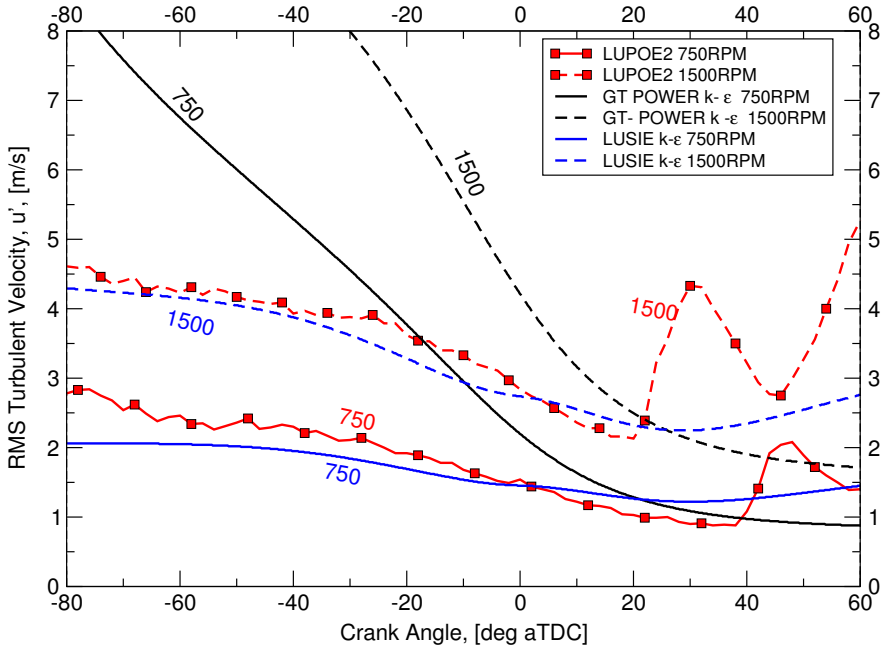

Figure 4.7: Comparison of u' for two turbulence models with LDV data from the LUPOE2-D for two different speeds, 750 rev/min and 1500 rev/min. The model constants have not been altered for any of the simulations. The instantaneous piston speed definition has been used for the LUSIE predictions.

which operate at varying speeds because of current geared transmission systems which have proportional speeds for the input and output shafts[1]; therefore it is crucial that any turbulence model is able to account for varying engine speeds. Predictions of u' at 750 rev/min, half the original 1500 rev/min were performed to check the ability of the 0-D $k-\epsilon$ model to account for varying speeds. Experimental data are available at this lower speed condition for LUPOE2-D, in addition a GT-Power prediction was performed. It can be seen by Eq. 3.35, Eq. 3.37 and Eq. 3.38 that the 0-D $k-\epsilon$ model accounts for the reduction in mass flow rate and therefore intake velocity, showing strong correlation with experimental data, still displaying the rapid increase in u' this time around 40^o aTDC suggesting there is potentially a time influence on the maximum somewhere in the system as it occurs approximately 20^o CA later, than for the 1500 rev/min condition (i.e. half the time in terms of crank angle after TDC).

[1]Continuously variable transmission (CVT) allows the input shaft (engine speed) to maintain a constant angular velocity over a range of output velocities (vehicle speed). Such systems are becoming more common, however fixed ratio transmission systems are still preferred.

4.2.1.2 Length scale analysis

LUSIE requires both u' and a turbulent length scale to calculate the characteristic burn-up time τ_b (Eq. 3.4) used in the mass burning rate calculation; for now only the integral scale is discussed as it is the most commonly used variable in both modelling and experiments (Hattrell, 2007). In the case of CFD, modelling of the length scale is primarily based upon a factor of the dissipation rate, i.e. in the case of the mass averaged l_i as calculated by CFD for use in the AJ133 and UB100 engines, is given by: $0.4\frac{\text{TKE}^{\frac{3}{2}}}{\epsilon}$. Another common prediction method is by attributing the integral scale to a characteristic length in the combustion chamber, as is done by the 0-D $k-\epsilon$ model used by LUSIE (Eq. 3.41) for example, as well as the original definition of length scale in LUSIE (Eq. 3.39) as used by Abdi Aghdam, 2003 and Hattrell, 2007. The two different methods share certain characteristics of results, such as exhibiting a parabola shape of the crank resolved integral scale, as they are a function of the chamber volume, with the minimum at TDC. From a physical point of view it is suggested that the smallest characteristic length can be found when the piston is at TDC, when the clearance volume, and therefore any clearance height is at a minimum. Many attempts at predicting length scales in engines rely on the geometric properties of the engine to determine the length scale, usually by way of clearance height and a given proportionality constant, five different definitions were found in the literature showing the vast amount of error surrounding length scale prediction when using a geometric prediction; the five selected definitions are:

1. l_i= 0.2l_{cht} (Section 3.39)
2. l_i= $V_c^{1/3}F_d$ (Section 3.41)
3. l_i= $V_c^{1/3}0.04$ (Bozza et al., 2007)
4. l_i= MIN ($\frac{l_{\text{cht}}}{6}$, $\frac{\text{bore}}{6}$) (Lumley, 2006)
5. l_i= MIN ($\frac{l_{\text{cht}_{\text{TDC}}}}{6}$, $\frac{\text{bore}}{6}$) (Lumley, 2006)

These five models are compared with experimental results from the LUPOE2-D engine, the results can be seen in Figure 4.8. It can seen that there is a large difference between the theoretical definitions of the scale as well as the disparity with the experimental results; the magnitude of the results is agreeable for all definitions, vis-á-vis experimental results. The second major observation to be seen in Figure 4.8 is the trend of the integral scale as a function of crank angle, generally the prediction of integral scale is that the minimum is at TDC, as discussed previously, where the available space for a

characteristic length is at the minimum. This can be seen in the definitions which either use the cylinder volume or clearance height, both functions of crank angle, in predicting the integral scale. The constant scale definition, shown as line number 5, does not appear to conform to the adopted theory that the integral scale is a function of some height in the chamber, which is dependent on the piston motion, it does however provide the best average fit to the experimental data throughout the closed cycle region, EPC-to-EPO. The length scale predicted by the 0-D $k-\epsilon$, with "fitted" constants as described in 3.4.2 results model in a good agreement with experimental data. The prediction using the legacy LUSIE definition (Eq. 3.39) results in a scale which is too large.

The influence of different integral scale definitions on the resulting predicted cylinder pressure can be seen in Figure 4.9, where the five different l_i definitions have been used to predict a LUPOE2-D cycle at standard reference conditions (SRC); all predictions use the crank-resolved u' values as calculated by the 0-D $k-\epsilon$ model. The predicted cycles are compared against 100 firing cycles captured in the LUPOE2-D engine. It can be seen that the definitions which predict the smaller integral scales also predict the fastest cycles, this is expected because of the reduction in the characteristic burn-up time for entrained fuel as the integral scale decreases (Eq. 3.4) The spark was initiated at -12^o aTDC while peak pressure occurs between approximately 10 and 20^o aTDC, this gives a window where the influence of the integral scale on combustion will be strongest. It can be seen in Figure 4.8 that using the original LUSIE definition of a length scale, l_i, (definition 1) results in combustion which is too slow. As the 0-D $k-\epsilon$ model had "fitted" u' and l_i values, it is unsurprising to see that the predicted "firing" cycle has a pressure which matches well to a mean cycle seen experimentally.

4.2.2 Naturally aspirated production engine 0-D $k-\epsilon$ and CFD predictions

4.2.2.1 Turbulence prediction for the AJ133 engine

With the 0-D $k-\epsilon$ turbulence model validated against the LUPOE2-D it was of interest to see whether or not the model, with the same constants, could be applied to a set of productions engines. The differences between the two engines are numerous, specifically that the AJ133 engine uses a traditional four-valve, pent-roof combustion chamber, as opposed to the two-stroke style breathing system and disc shaped combustion chamber used in the LUPOE2-D engine. For the calculation of u' however, the linear fit model is

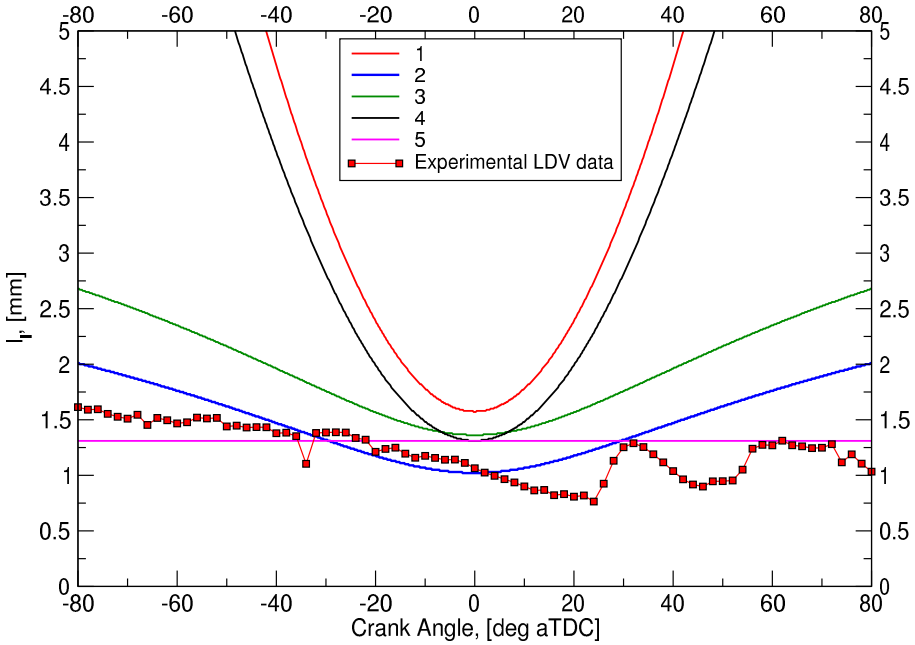

Figure 4.8: A comparison of different integral length scale definitions found in literature used to predict the integral length scale within the LUPOE2-D at 1500rm, compared with experimental data, the transverse, spatial, integral scale is calculated from the integral time scale measured using LDV methods.

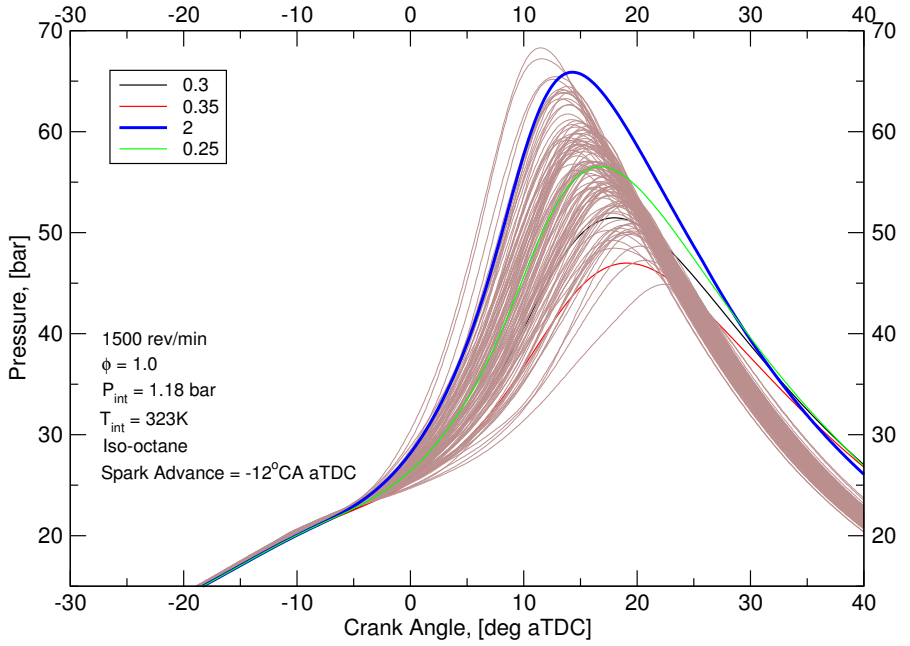

Figure 4.9: The influence of integral scale definition on combustion - as shown by cylinder pressure curves predicted in LUSIE and compared to 100 cycles obtained experimentally on the LUPOE2-D engine.

not directly dependent on cylinder volume, while the 0-D $k-\epsilon$ model does not depend on specific geometry, only the instantaneous total cylinder volume.

The primary difficulty encountered in trying to obtain turbulence data for the production engines is that it was generally not within the scope of the commercial projects to collect them experimentally owing to the cost and time constraints it would impose on a testing program. Where it was not feasible to obtain turbulence data experimentally for the production engines, they were obtained using more the rigorous numerical solution using CFD as the computational tool. CFD data was available for the production engines, and was provided by CD-Adapco. Data provided included the mass averaged total kinetic energy and integral length scale, this allowed for direct comparison with the 0-D $k-\epsilon$ model at a given condition for the non-boosted and boosted production engines. Validating data obtained from models against date obtained from other types of models is noted as being not entirely fulfilling. It is hoped, however, that trends and differences between simulations will be repeatable between models, while the definitive numeric(s) should be treated with caution.

The comparison between the non-boosted production and the 0-D $k-\epsilon$ model can be seen in Figure 4.10, which contains a direct comparison with CFD data using both the IPS and MPS variations of the same model 0-D $k-\epsilon$ model; constants were kept the same as they were for the LUPOE2-D comparison. As with the results for the LUPOE2-D it is clear that the piston speed has a large influence on the results and, as before, the usage of the IPS definition for piston speed, shows better correlation with the benchmark CFD data predicting the rise in u' during compression and the drop off in u' before TDC. The performance of the model after TDC is unknown as the CFD data was truncated at TDC. the increase in turbulence predicted by the 0-D $k-\epsilon$ model after approximately 30^o aTDC is not explainable by turbulence theory. Turbulence generation on the *compression* stroke is commonly attributed the piston stroke, as reducing the size of eddies results in an increase in their rotational velocity, increasing turbulence. The receding piston should not be responsible for increasing turbulence by this same process. Despite the increase in u' after TDC, encouraging conclusions can be made from the results, these being; the IPS definition has again been seen to be more applicable than taking the MPS value and that the model, in terms of u', shows an acceptable fit to both the LUPOE2-D and a production engine without further adjustment of the model constants.

Conversely, for the prediction of l_i, it can be seen in Figure 4.11 that the previously used 0-D $k-\epsilon$ definition with, F_d = 0.17 predicts a length scale that is far too low compared to CFD data. Indeed the constant was adjusted F_d to match the CFD predicted l_i, however, it was not possible to attain an accurate match with just adjustment of F_d, the

final value chosen, F_d = 0.6, has a matched value at TDC, however away from this region the error between the 0-D $k-\epsilon$ prediction and CFD increased significantly. Additionally, after such a large adjustment to the F_d value, the prediction of u' was adversely affected, as can be seen in Figure 4.12.

The original definition of integral length scale, based on the clearance height (Eq. 3.39) was used for prediction of l_i in the AJ133 engine where C_L was set to 0.26. It can be seen that using this definition, the agreement between CFD and prediction is improved.

It can be concluded from the results between the AJ133 and LUPOE2-D engine that the use of the 0-D $k-\epsilon$ model to predict u' is viable, however the prediction of l_i is poor and model constants have to be adjusted to better fit the engine.Whether or not the pent-roof, accounted for by CFD, is the cause in the erroneous 0-D $k-\epsilon$ model predicting requires further investigation. A possible solution to the erroneous l_i prediction would be to add an additional model constant in the 0-D $k-\epsilon$ model which affected only the integral scale, the definition of Bozza et al. [2007] employs this methodology, where they attempt to match a 1-D $k-K$ turbulence model (proposed by Poulos and Heywood [1983]) to 3-D CFD data.

4.2.2.2 Turbulence prediction for the UB100 engine

For a new version of 0-D $k-\epsilon$ model to be considered a viable alternative to CFD or experimental data, in terms of predicting u', it needs to be correlated to a number of different engines, and the performance assessed; clearly it was desirable for the model constants to remain just that, constant, throughout the correlation exercise. Having validated the model against experimental data for the LUPOE2-D and the AJ133 engine to a lesser extent it was necessary to check whether or not the model would still predict, with an acceptable degree of accuracy, u' for other engines, specifically those at boosted conditions.

The engine, which best represented the criteria of being a boosted engine, with the largest amount of available turbulence data, was the UB100 engine. The turbulence data was again provided by CD-Adapco. Figure 4.14 contains three separate results: mass averaged TKE over the whole chamber, instantaneous TKE values taken at theoretically placed probe positions along the head axis at the line of symmetry for the intake and exhaust valves, see Figure 4.13, and finally the prediction from the 0-D $k-\epsilon$ model. The model required adjustment of the constants (F_p, F_d, F_i) in order to achieve an acceptable agreement around the combustion phase vis-á-vis the CD-Adapco CFD prediction, see Table 4.1 for further details. It can be seen that the match between the 0-D $k-\epsilon$ model

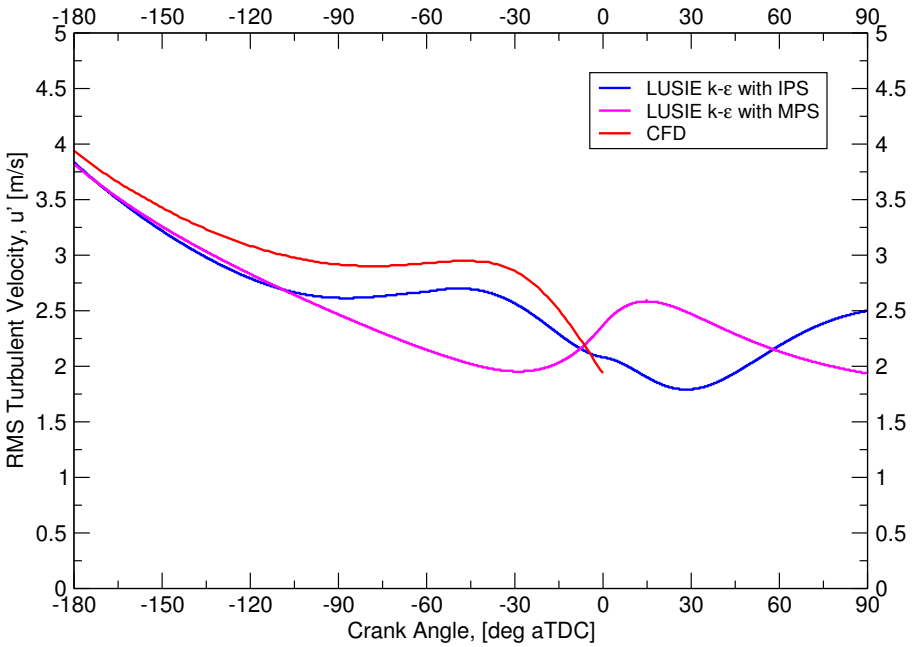

Figure 4.10: A comparison of the influence of piston definition influence on u' for the AJ133 engine predicted by the 0-D $k-\epsilon$ model; CFD data was provided by Jaguar Land Rover using Ford's MESIM software.

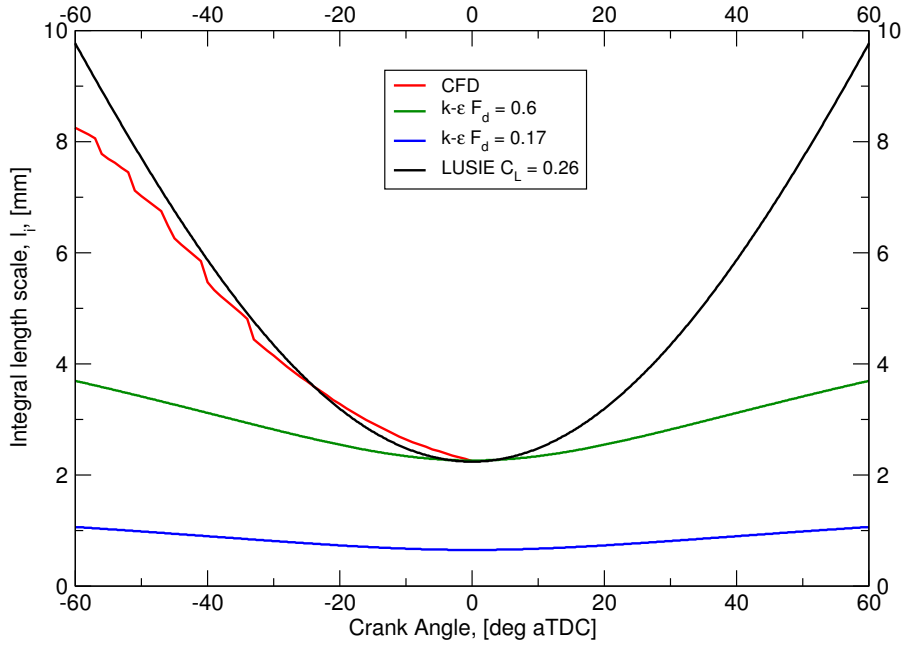

Figure 4.11: A comparison of the integral scale predictions within the AJ133 pent-roof production engine for the cold-flow integral length scale; CFD data was provided by Jaguar Land Rover using Ford's MESIM software.

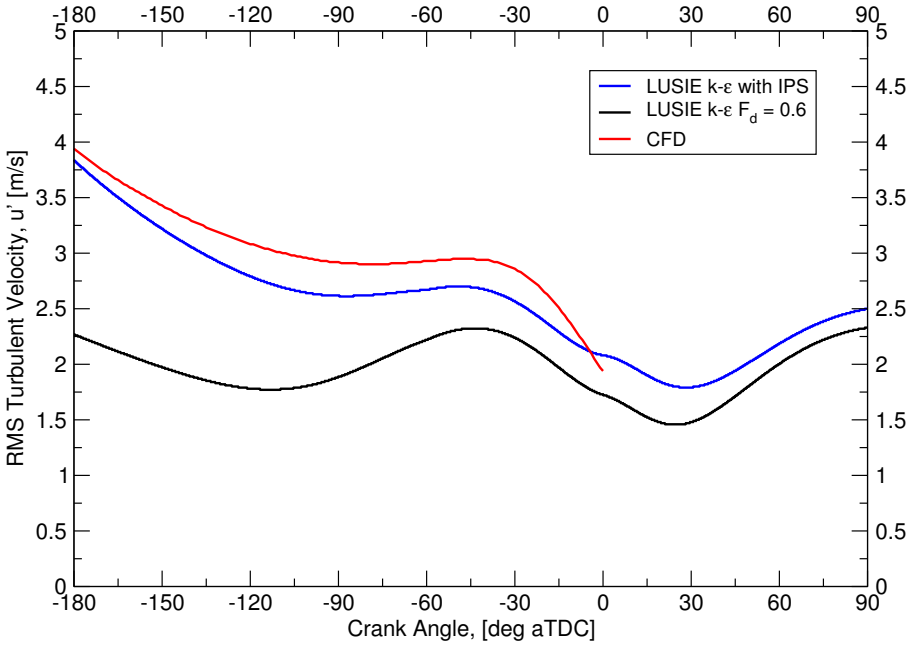

Figure 4.12: A comparison of the 0-D $k-\epsilon$ model prediction of u' with increased dissipation, compared against the CFD prediction of u'.

	LUPOE2-D	AJ133	UB100
F_p	0.035	0.035	0.025
F_d	0.017	0.017	0.030
F_i	0.005	0.005	0.005

Table 4.1: Model constants used within the 0-D $k-\epsilon$ model to fit u' of 3 different engines to experimental or CFD data. (Eq. 3.33, Eq. 3.34 and Eq. 3.35 for where constants are used by the model).

and the CFD predictions is not in good agreement during the majority of the compression and expansion phases, importantly however, the agreement around TDC and during the window for combustion the match between the 0-D $k-\epsilon$ model and the bulk average is acceptable. Better resolution around the combustion phase can be seen in Figure 4.15; as before the 0-D model predicts an increase in TKE shortly after TDC again around 30^oaTDC, which is not reflected in the CFD data, the predicted rise in the 0-D $k-\epsilon$ model is because of turbulence generation predicted by piston motion.

The integral scale predicted by CFD and LUSIE is presented in Figure 4.16 where there is a good agreement between the two curves after the model constant, C_L (Eq. 3.39) have been altered, the primary alteration was to apply an offset in the Y axis, where the length scale predicted by LUSIE and that predicted by CFD had a magnitude offset error of approximately 3.3 mm, with the CFD data predicting the larger of the two values.

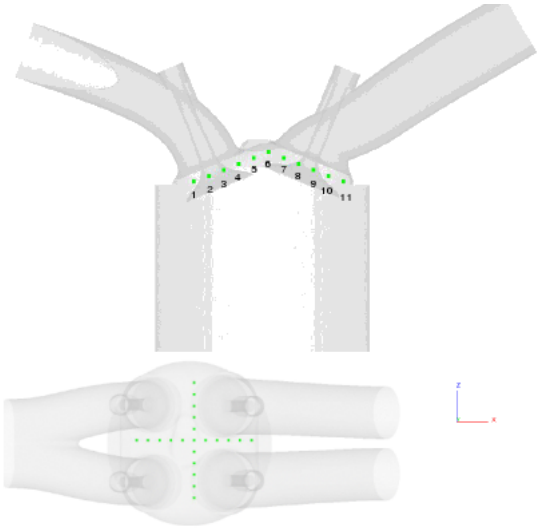

Probe number	X (mm)	Y (mm)
1	31.297	1.500
2	25.497	1.500
3	19.697	1.500
4	13.897	1.500
5	8.097	1.500
6*	2.297	1.500
7	-3.503	1.500
8	-9.303	1.500
9	-15.103	1.500
10	-20.903	1.500
11	-26.703	1.500

* Spark plug location (point alo the spark plug axis and in the g between the electrodes)

Figure 4.13: Position of theoretical probes in the 3-D combustion chamber for instantaneous u' as predicted by CD-Adapco using CFD solution methods. Probes are located along the Y axis, by drawing definition which represented the line of symmetry between the exhaust and inlet valve.The simulated engine is the UB100.

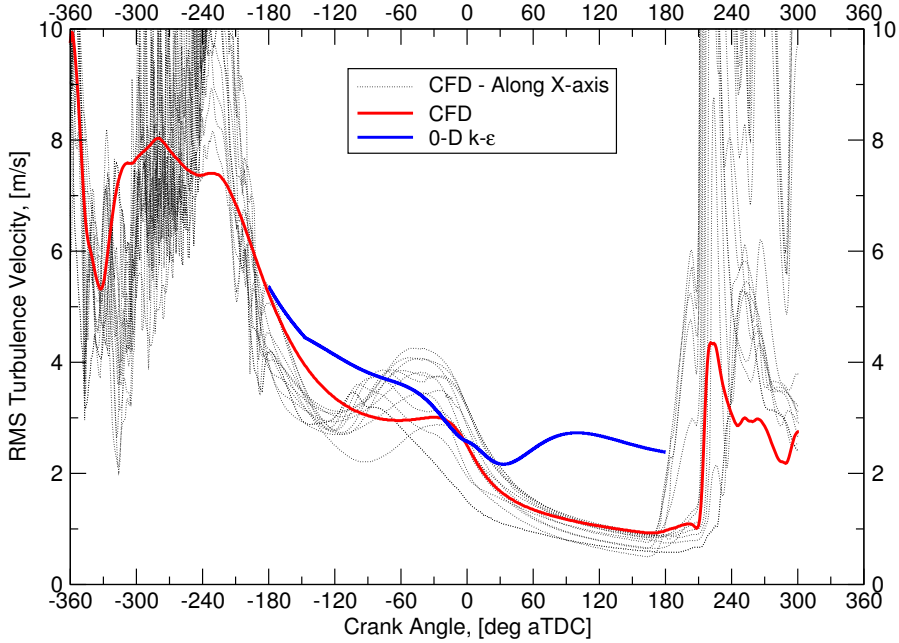

Figure 4.14: u' data for the UB100 engine predicted by the 0-D $k-\epsilon$ model, with modified constants compared to CFD data generated by CD-Adapco using Fluent. The red line represents the mass averaged turbulent rms velocity over the whole cylinder charge. The thin dotted line represents the turbulent kinetic energy at equally spaced, theoretical probe locations, along the head on the line of symmetry between the intake and exhaust valve.

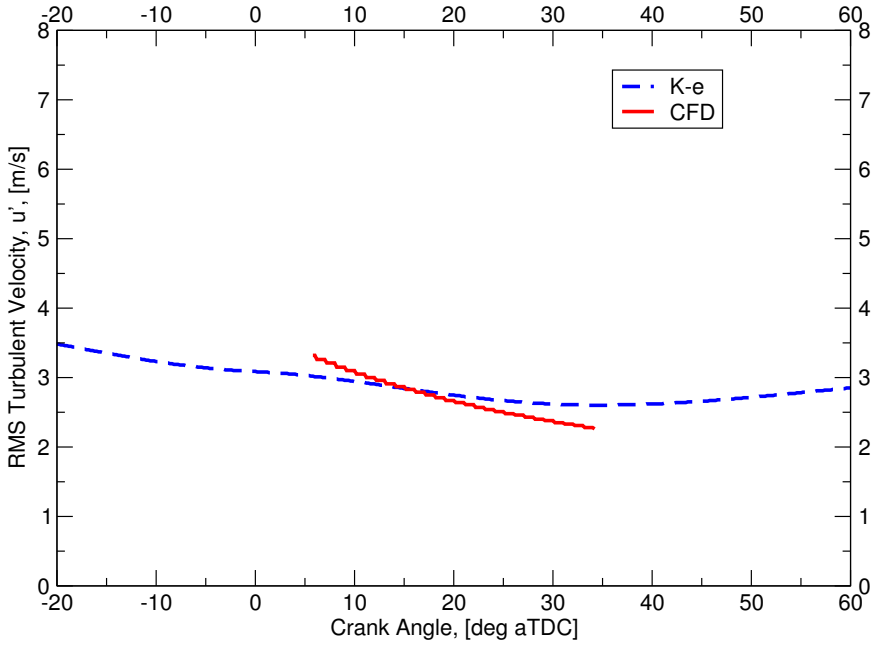

Figure 4.15: Comparing the mass averaged u' for the UB100 engine predicted by the 0-D $k-\epsilon$ model against the CD-Adapco CFD simulation.

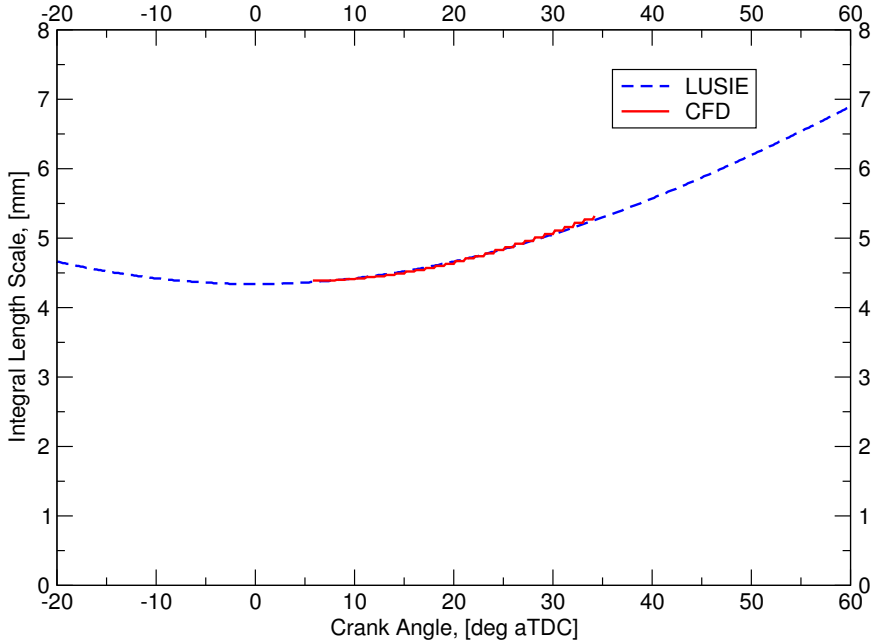

Figure 4.16: Comparing the integral length scale for the UB100 engine predicted by the 0-D $k-\epsilon$ model against a CFD simulation performed by CD-Adapco where the integral scale is defined by $0.4\ \dfrac{\mathrm{TKE}^{3/2}}{\epsilon}$.

Applying this additional 3.3 mm to the LUSIE definition brings the two curves into close alignment. The resultant Taylor scale, which can be seen in Figure 4.17, is based on the integral scale by the relationship (Eq. 3.42); as the integral scale values were fitted, the Taylor scales also show similar correlation. The large spike in the $k-\epsilon$ model is caused because LUSIE converts all unburned gas temperature to burned gas temperature once combustion is complete.

The resulting effect of the difference imposed by turbulence predictions between the 0-D $k-\epsilon$ and the CFD data on the combustion prediction can be seen in Figures 4.18 and 4.19. It is important to note here that in-cylinder pressure predicted here, by LUSIE, uses the Taylor scale after-burning definition as detailed in Section 4.3.1, the purpose of this Section is to compare the prediction of combustion using turbulence generated by the 0-D $k-\epsilon$ model to the combustion predicted by using turbulence predicted by CFD. The burn rate, observed by the burned, $\mathrm{fr_b}$, and entrained, $\mathrm{fr_e}$, radii are similar for both turbulence models; this is unsurprising because of the tuning of model constants to fit the CFD data. There are however minor differences in the data which result in differences in the burn rates observed; the 0-D $k-\epsilon$ appears to have a slower initial burn, through the developing phase (Eq. 3.16), but a faster main combustion period to termination (Eq. 3.17, where the majority of the fuel is burned because of the greater density of the fluid at the wall, i.e. at large flame radii. The influence of the faster main combustion phase can be seen in the pressure trace where a slightly larger peak pressure is realised by approximately 1 bar or 0.9%, this error is small compared to others and is deemed acceptable.

4.3 Influence of turbulence scales on burning rates

The 0-D $k-\epsilon$ turbulence model was seen to give a reasonable prediction of the cylinder pressure for the LUPOE2-D engine, dependent on the integral scale definition employed. The interest for the current study was, which definition, if any, would give a reasonable agreement with engines operating under boosted conditions, for examle, the UB100 or boosted LUPOE2-D engines. The first prediction made on the UB100 engine, was using the definition employed for the LUPOE2-D which was seen to give good agreement with a middle predicted cycle.

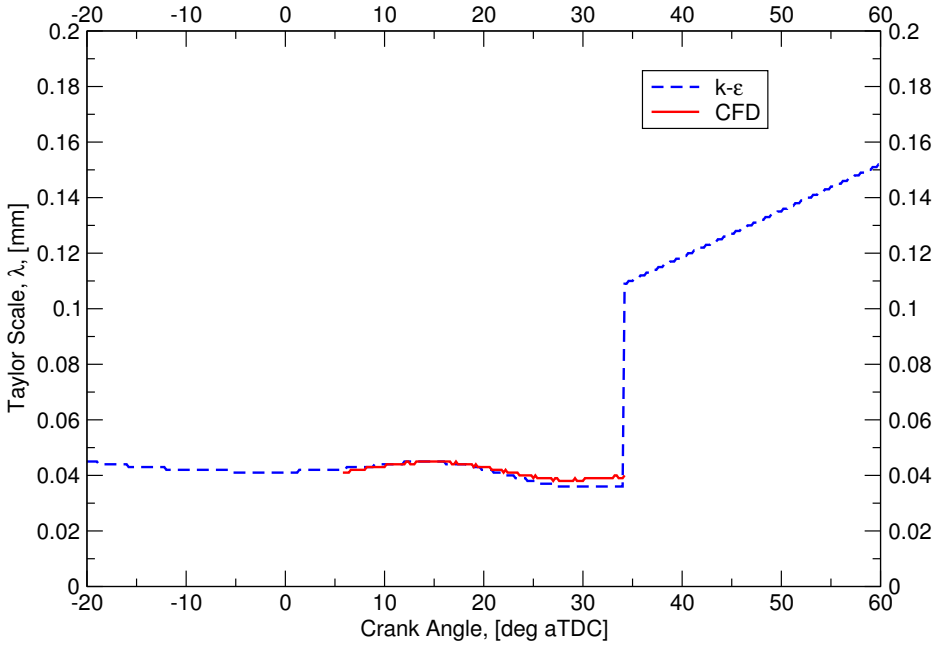

Figure 4.17: Comparing the Taylor length scale, λ, based on LUSIE predicted integral scale and λ based on integral scale predicted by CFD.

4.3.1 Combustion prediction of the UB100 engine

Figure 4.20 contains data of 100 firing cycles from the UB100 engine compared with a predicted cycle from LUSIE. It can be seen from it that the characteristic burn-up definition based on the integral length scale, with the after-burning proportionality constant, C_{l_i} = 0.8, as used for the LUPOE2-D engine, results in predicted combustion rates that are considerably too slow; the reason for this is unknown.There are a number of potential causes that explain the discrepancy. One possible reason is that characteristic scales in the boosted production engine responsible for driving combustion maybe considerably smaller than in the LUPOE2-D engine, i.e. smaller than the integral scale, resulting in faster combustion than predicted, though the reason for this cannot be ascertained easily. The two major differences between the engines, which may have an influence on turbulent length scales, are geometric variances such as using valves rather than ports, which will induce bulk motions like tumble, as well as the difference in the shape of the combustion chamber, one being a disc the other being pent-roof shaped. The pent-roof geometry may ultimately result in differences in the length scale owing to variations in the flow field at the boundary layers which will be different for pent and dome combustion chambers. It is assumed that the CFD predictions have accounted for this, though the predicted integral scale in the UB100 engine (and to a lesser extent AJ133) is far higher than for the LUPOE2-D engine.

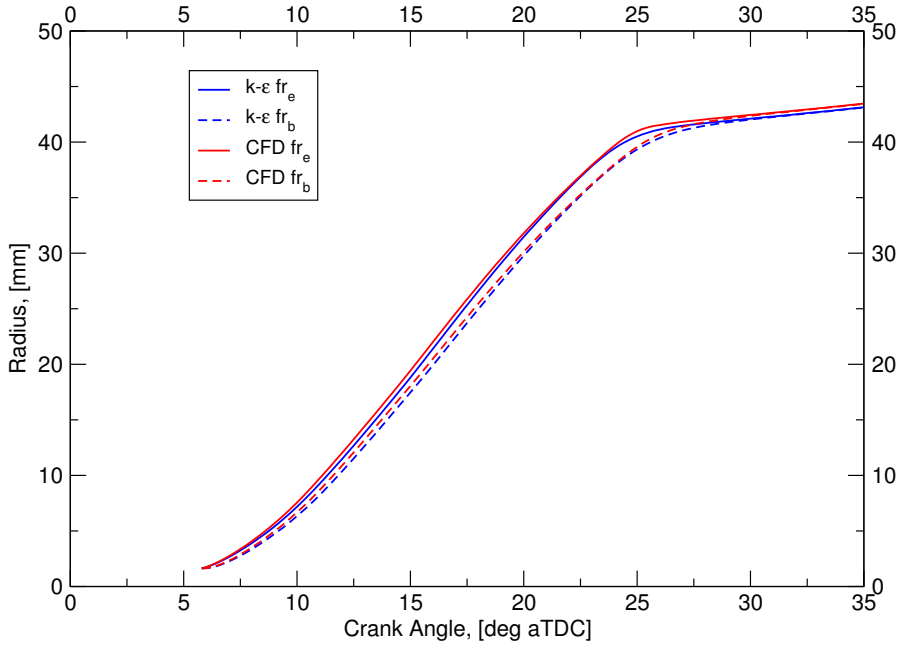

Figure 4.18: Comparing the burning rates of a 'mean' cycle in the UB100 engine, predicted by LUSIE using a) the internal 0-D $k-\epsilon$ model, b) CFD data provided by CD-Adapco. The burning rates are expressed by the burned gas and flame entrainment radii.

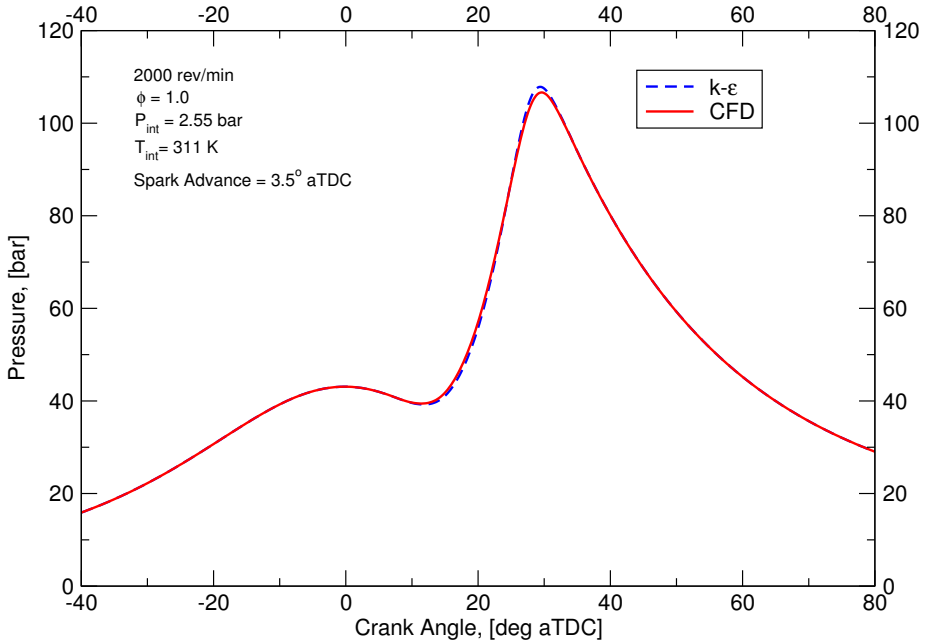

Figure 4.19: Comparing the cylinder pressure for the UB100 engine predicted by LUSIE using a) the internal 0-D $k-\epsilon$ model with modified constants, b) CFD data provided by CD-Adapco.

In contrast, it can be seen in Figure 4.21 that using the Taylor scale definition for the characteristic burn-up results in combustion rates which give a much closer prediction to experimental data, a range of proportionality constants on the Taylor characteristic burn-up time, C_{l_λ} have been explored here, from 0.5 to 10. As predicted, a larger proportionality constant results in slower combustion, as essentially it is predicting a larger length scale. It was found that for the boosted production engine a proportionality constant of 3 gave the most reasonable match to experimental data. Data from the boosted production engine was available at full load and part load conditions, with intake pressures of 2.55 bar and 1.46 bar respectively. After tuning of the proportionality constant to the full load condition it was not known whether the constant would still be valid for part load operation; indeed the constant of 3 led to an over-prediction of cylinder pressure at the part-load condition as seen in Figure 4.22. An overprediction was unsatisfactory as it was believed that the turbulence length scale properties were dependant on engine geometry rather than operating condition. Further analysis of the part-load condition, using GT-Power, suggested that the engine, at this condition, was operating with approximately 5% exhaust gas residuals, effectively slowing the rate of combustion vis-á-vis a residual free set of cycles. Including 5% EGR within a LUSIE predicted cycle resulted in a reduction of the burn rate in line with a mean experimental cycle, as seen in Figure 4.23, again with the proportionality constant of 3, thus bringing the part load condition in line with the full load condition. Matching the part and full load conditions allowed a reasonable confirmation of the assumption that it is the geometric differences within the engine which affect turbulent length scale properties rather than the varying operating conditions.

The performance of LUSIE in predicting the burn-rate at increased engine speed was of interest, and with the data provided it was possible to compare the performance of the predictive model, and more importantly the after-burning rate definition, at an increased engine speed of 3000 rev/min; the results from this prediction can be seen in Figure 4.24, where the proportionality constant appears to be predicting combustion that is in line with the fastest cycles seen experimentally. A slightly higher peak pressure can be seen compared to the experimental cycles (neglecting those that exhibit pre-ignition characteristics); although the burn rate is faster for the 3000 rev/min it can be seen that the 50% increase in engine speed has not radically altered the combustion rates outside of the expected range of experimental cycles.

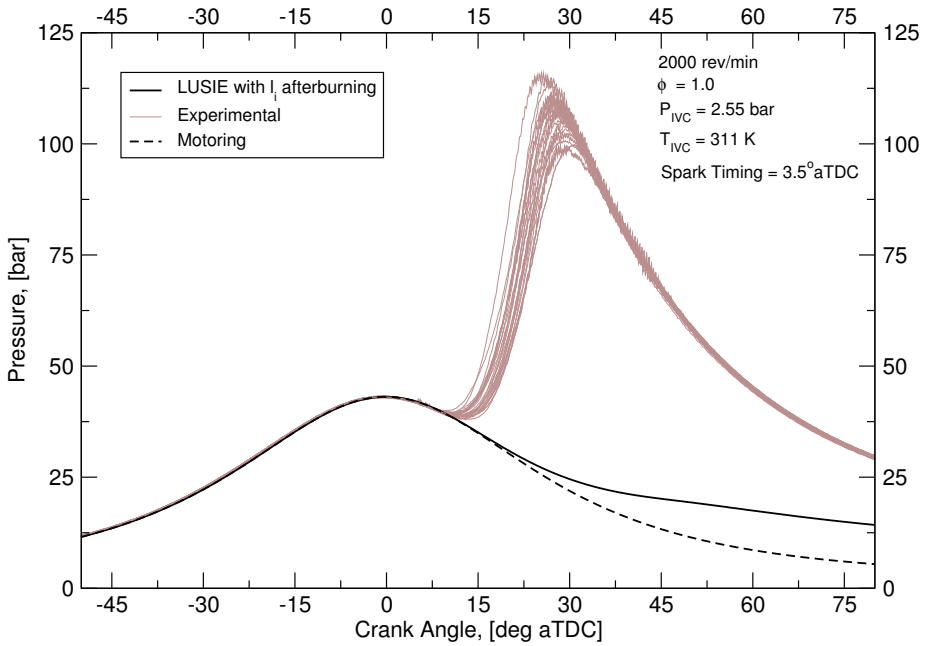

Figure 4.20: Performance of LUSIE in predicting a highly boosted firing case for the UB100 engine at the shown conditions. The model is using the standard after-burning prediction model using integral length scale, l_i, which was used for the LUPOE2-D engine.

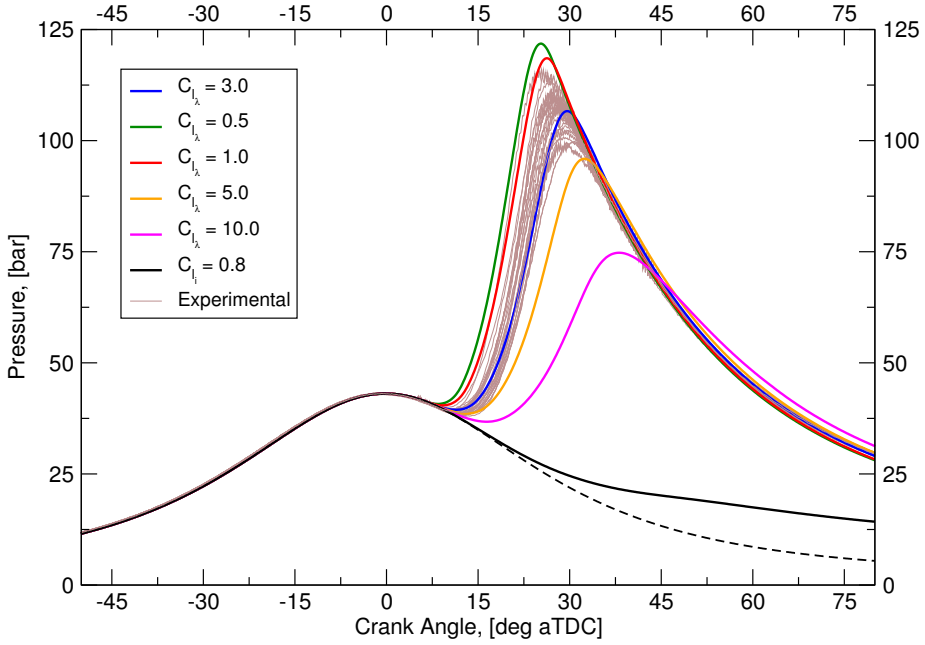

Figure 4.21: Influence of after-burning rate definition and constants on combustion, shown by cylinder pressure, for the UB100 engine operating at high pressure conditions. Predictions are made by LUSIE using CFD turbulence data. After-burning is predicted using a) Taylor scale Cl_λ with a range of constants and b) integral scale l_i with the constant 0.8 which was validated for the LUPOE2-D engine.

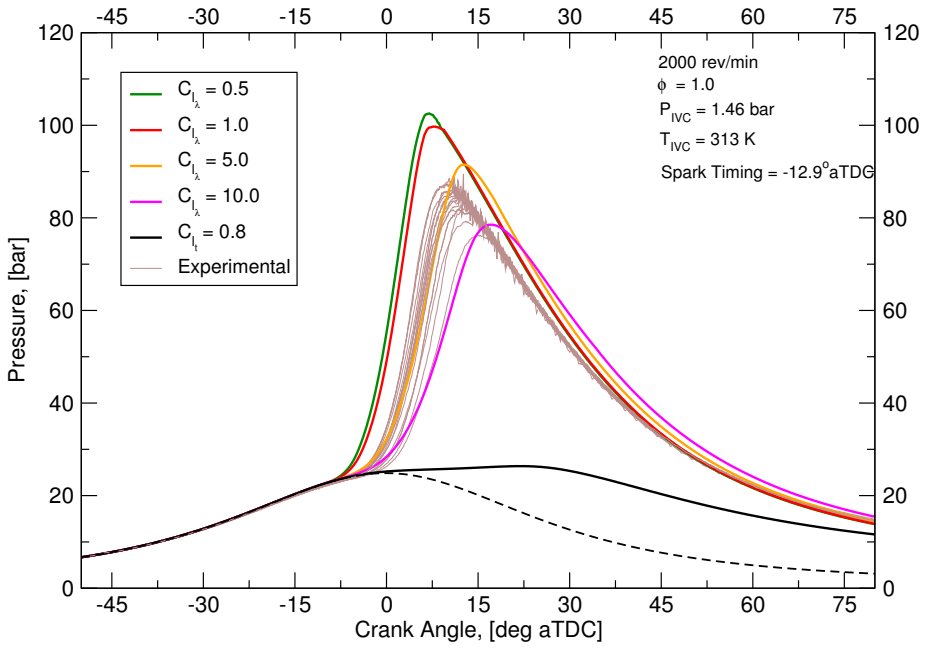

Figure 4.22: Influence of after-burning rate definition and constants on combustion, shown by cylinder pressure, for the UB100 engine operating at moderately boosted conditions. Predictions are made by LUSIE using CFD turbulence data. The after-burning is predicted using a) Taylor scale C_{l_λ} with a range of constants and b) integral scale l_i with the constant 0.8 which was validated for the LUPOE2-D engine.

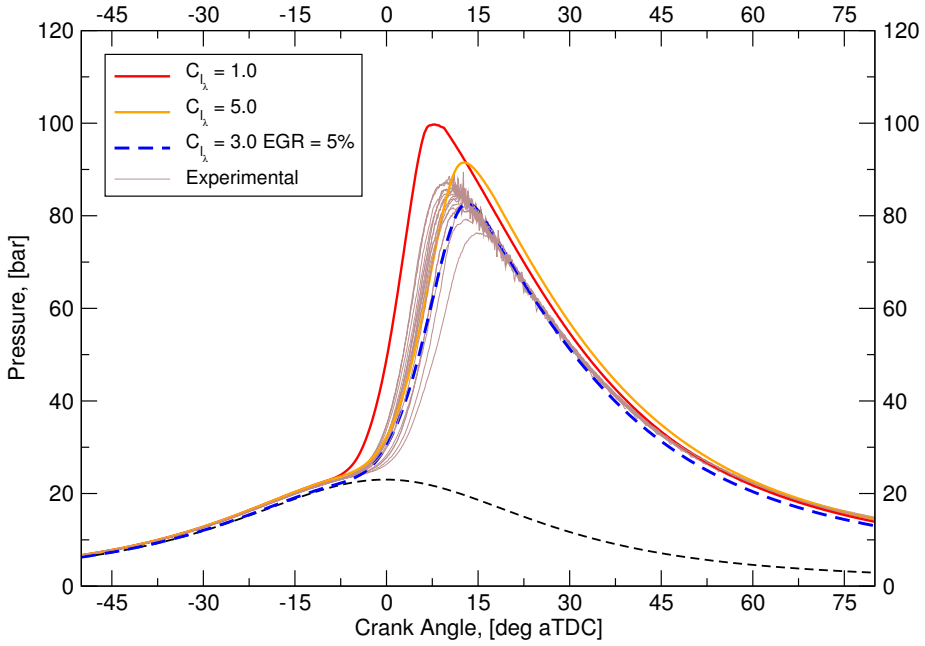

Figure 4.23: Influence of after-burning constants and residual levels on combustion, shown by cylinder pressure, for the UB100 engine operating at moderately boosted conditions. Predictions are made by LUSIE using CFD turbulence data. The after-burning is predicted using the Taylor scale C_{l_λ} with a range of constants with the inclusion of 5% EGR as predicted by GT-Power.

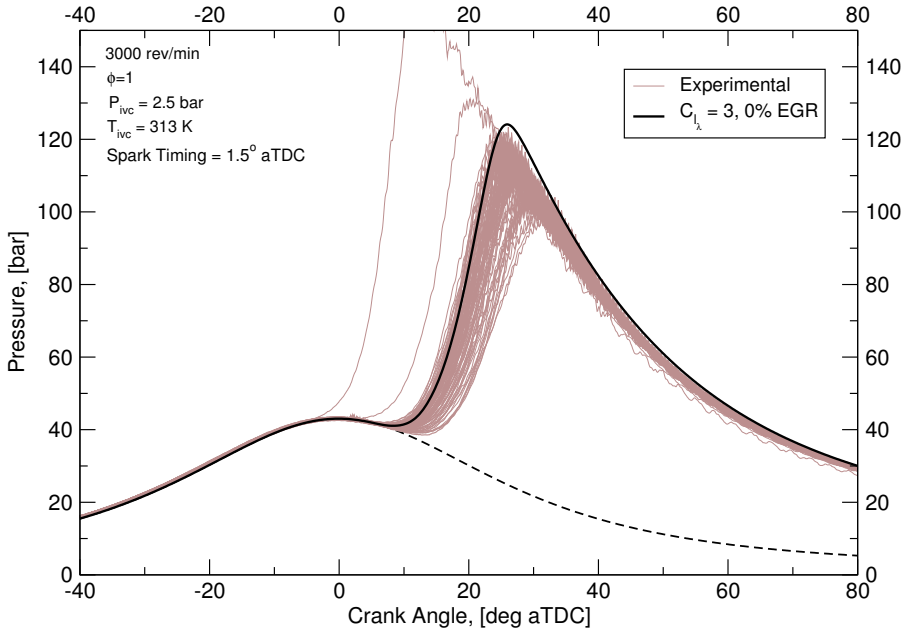

Figure 4.24: Influence of engine speed on predicted burn rate in the UB100 engine using the Taylor scale proportionality constant of 3, as was found to give good correlation to the 3000 rev/min data. Turbulence data, here were predicted by the 0-D $k-\epsilon$ model within LUSIE.

4.3.2 Combustion prediction of the AJ133 engine

The proportionality constant for the Taylor scale in the definition of after-burning, was shown to require adjustment to allow good correlation between experimental and predicted burning rates for the UB100 engine. It was assumed that the vast difference in burning rates between the UB100 engine and the LUPOE2-D was a result of turbulent length scale variation between the two engines, possibly caused by the pent-roof style combustion chamber as well as the 4 valve configuration. Available data from the AJ133 engine allowed comparison between similar engine types. The AJ133 engine, having a 4-valve pent head configuration, should closely resemble the flow pattern of the UB100 engine, therefore it is expected that the predictive burn rate model should, using the same burn rate definition of Taylor scale, be in agreement with the boosted production engine, having previously seen that it did not appear to be load dependent, i.e. independent of intake pressure.

A LUSIE prediction was run for the AJ133 engine using the same proportionality constant as was used for the UB100 engine, that of $C_{l_\lambda} = 3$; it can be seen in Figure 4.25 that using the Taylor scale-based definition (Eq. 3.5) burn-rate definition, combustion is significantly overpredicted and the resultant pressure signal peak is almost twice the value of the fastest experimental cycle It is implausible to attribute this error to the difference

in engine speeds between the AJ133 and UB100 engines as, based on the comparison between the UB100 engine at two difference engine speeds, little variation was seen with a 50% increase in speed of 2000 rev/min to 3000 rev/min. The proportionality constant had to be increased by a factor of approximately 8, resulting in C_{l_λ} = 25, for a realistic pressure signal to be predicted in the AJ133 engine; in addition to the Taylor scale burn-rate prediction, the predicted burn rate using the integral scale definition and after-burning proportionality constant validated for the LUPOE2-D engine, C_{l_i} = 0.8, was also plotted where, combustion rates are considerably too slow compared to experimental cycles. It can be seen that crank resolved flame radii (equivalent to fr_e) predicted by LUSIE and seen in Figure 4.26 suggests a slower predicted entrainment velocity in the AJ133 engine which combined with slower after-burning definition (C_{l_λ} = 25 compared to C_{l_λ} = 3), results in a greater flame thickness vis-á-vis the UB100 engine. One can hardly draw a definitive conclusion from this initial observation because of the multiple variables which could cause the large difference in burn rates. As an example, the in-cylinder charger was richer in the AJ133 simulation compared to UB100 hence the laminar flame thickness will also be increased, (Heravi et al., 2007). The increase in laminar flame thickness will reduce the mass burning rate and thereby increase the turbulent flame thickness. Similarly the laminar flame thickness should also increase with a decrease in pressure (Metghalchi and Keck, 1980) lowering the mass burn rate.

Fundamentally, modification of the proportionality "constant" between engines and conditions may be required for a number of reasons, such as, unreliable experimental engine data, the model itself not accounting for all physical variables, or the CFD data from which the turbulence model was validated are not reliable. The experimental data are obtained using accepted techniques, on calibrated equipment, in addition to the experiment being repeated a number of times, to ensure repeatability. With some assumption the experimental data can be considered the least likely source of error. This leaves the most likely source of error to be either the model itself, or the turbulence properties used for the input predicted by CFD, or indeed a combination of both. CFD predictions of turbulence properties included rms turbulence velocity and integral length scale, both mass averaged quantities. As discussed previously, the Taylor length scale is used in the burn-rate definition to give a more feasible burn-rate prediction, however, the Taylor scale is calculated from the input integral scale data, thus a further error may be introduced by doing this, in addition to the possible error in the initial integral scale prediction.

The rms turbulence velocity prediction for the UB100 and AJ133 engines can be seen in Figure 4.27; the 0-D $k-\epsilon$ model prediction for the AJ133 engine at 2000 rev/min

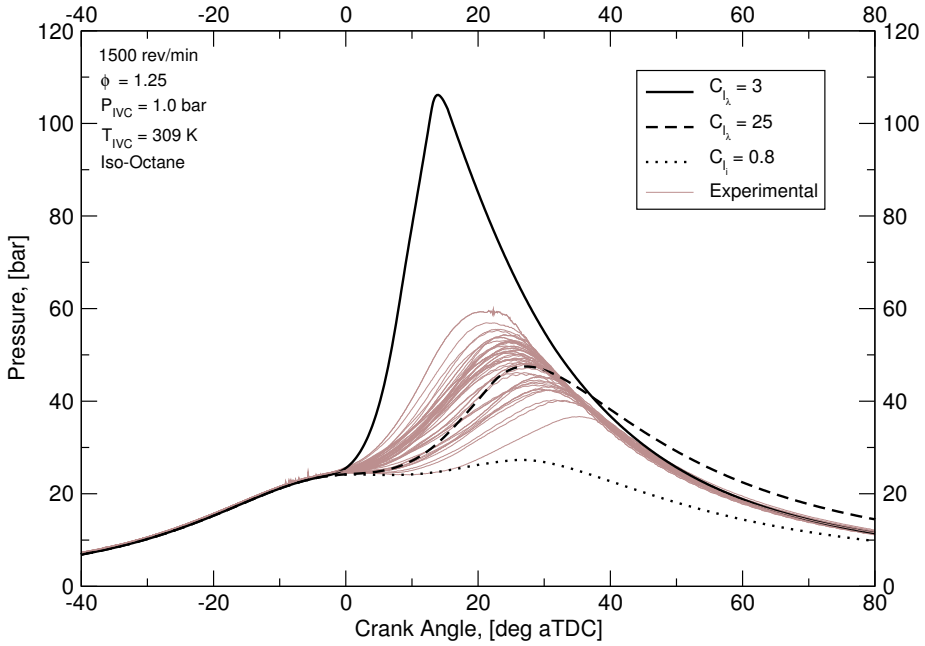

Figure 4.25: The influence of the Taylor scale and integral scale after-burning definition used within LUSIE, on the rate of combustion in the AJ133 engine, using constants fitted for the UB100 and LUPOE2-D engines, $C_{l_\lambda} = 3$ and $C_{l_i} = 0.8$ respectively.

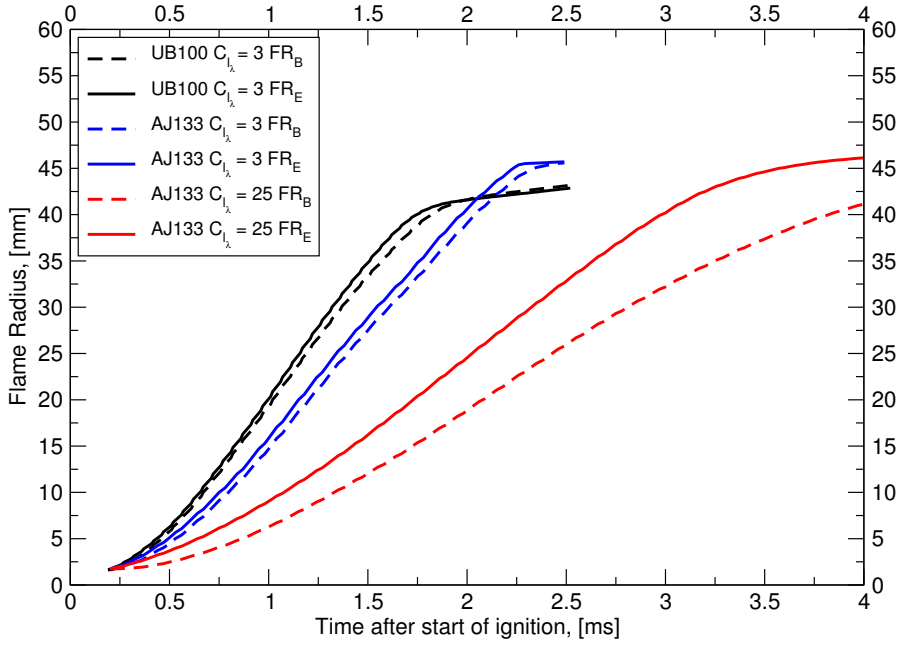

Figure 4.26: Comparing the flame propagation for the two engines represented by the burned gas and flame entrainment radii. Radii are predicted by LUSIE; the UB100 engine uses CFD turbulence data predicted by CD-Adapco, while the AJ133 turbulence data are provided by Jaguar Land Rover CFD data. Two Taylor constants are used for these simulations.

is included to demonstrate that, generally, the u' within the AJ133 engine is lower than that in the UB100 engine at like-for-like conditions i.e. the same engine speed and throttle position. This is possibly because of differences in the intake geometry of the two engines as well as the different piston geometries which may well influence turbulence properties. The u' is around 19% lower in the AJ133 engine, a value that suggests combustion will be slower in the AJ133 engine, whilst the predicted length scale, as seen in Figure 4.28, is predicted to be 50% of the characteristic length scales in the UB100 engine. It is suggested that the lower u' should be dominating factor here (Lipatnikov and Chomiak, 2002) and thus would explain, to an extent, the slower burn-rate prediction. Nonetheless, it should not explain the overly slow burn-rate predicted by using the integral rather than the Taylor scale burn-up definition, or the large variation in burn-rate between the AJ133 and UB100 engines. The shape of the piston surface is different between the two engines, see Figure 3.28. It has been said, Miyamoto et al., 2006, that the slanted squish style of piston (AJ133) will promote acceleration of the flame towards the end of combustion, as the flame reaches the angled profile towards the edge of the piston. It can be seen that a squish-piston-like profile can be seen in the centre of the UB100 profile, any acceleration of the flame here will occur early in the combustion process and it will yield an overall faster combustion.

It is unclear as to the reason for the vast difference in engine performance; the variation is possibly due to differences in the engine operating parameters, the higher pressure in the UB100 resulting in a faster than expected burning velocity, not predicted by the existing models which use iso-octane as the fuel; iso-octane is known to burn slower than gasoline-like PRF fuels (Zhao et al., 2003) and therefore the slow combustion may be exaggerated by the slow laminar burning velocities. The difference in u_l between a gasoline and iso-octane is approximately 10% at engine-like pressures according to a study by Jerzembeck et al., 2009. Also possible is that the geometric differences between the two engines results in spatially sensitive turbulence values which are not accounted for with the mass-averaged turbulence data. In order to rule out one of these possible causes, without the possibility to run the UB100 engine at equivalent conditions to the AJ133, it was decided to run the LUPOE2-D at higher intake pressures, as this would allow the influence of pressure to be investigated separately to geometric differences.

4.3.3 LUPOE2-D-Boosted

The LUPOE2-D-Boosted engine has identical combustion chamber geometry to the LUPOE2-D engine, thus the only difference in operating conditions should be caused by the in-

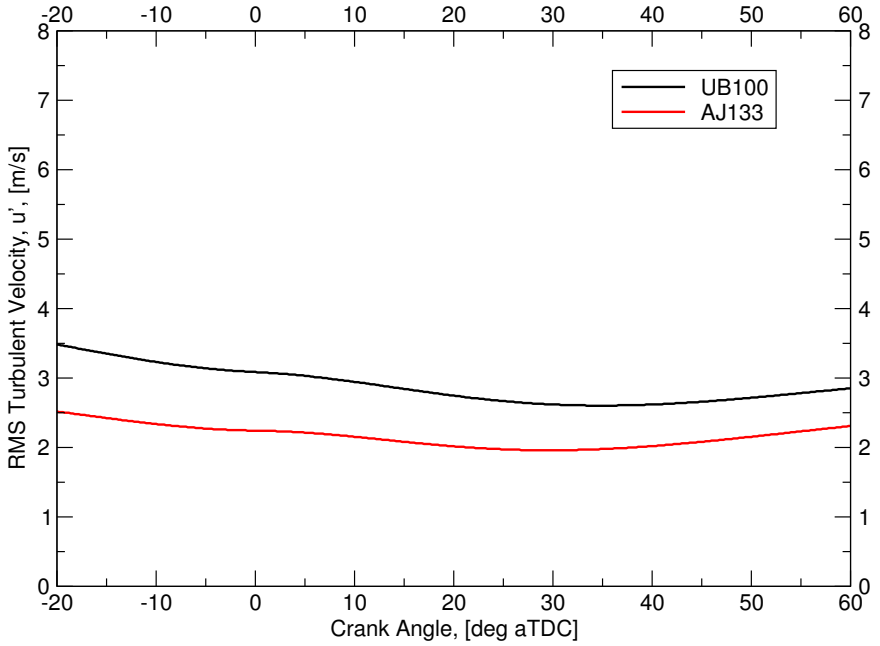

Figure 4.27: Comparing the crank resolved u' between the UB100 and AJ133 engine at their respective experimental speeds, 2000 rev/min and 1500rev/min as well as the predicted AJ133 u' at 2000 rev/min. The data presented for the UB100 are taken from LUSIE prediction using the 0-D $k-\epsilon$ model.

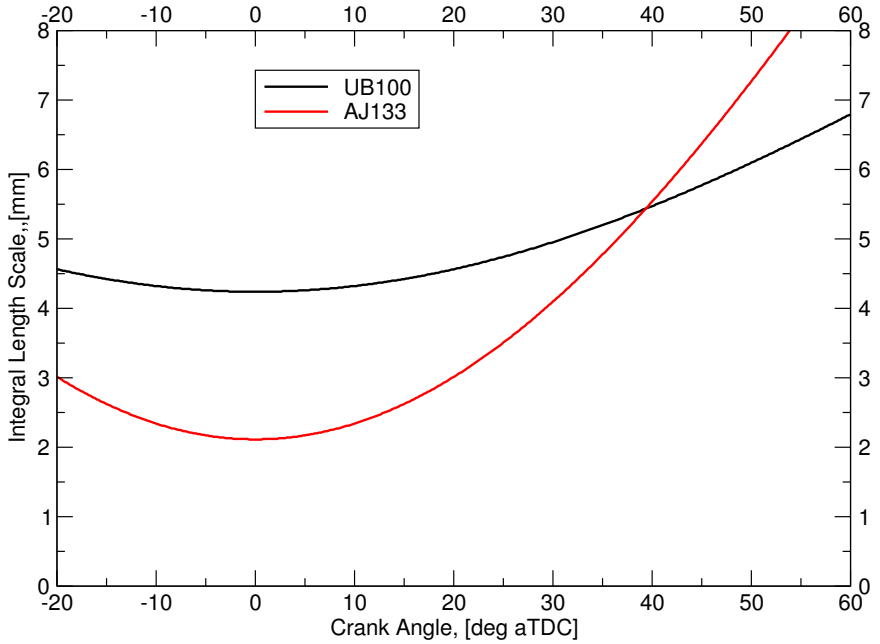

Figure 4.28: Comparing the crank resolved integral length scales in the UB100 and AJ133 engines. The UB100 data are taken directly from CD-Adapco CFD data, the AJ133 data are predicted within LUSIE having calibrated against the CFD data taken from Jaguar Land Rover. NB. UB100 data is taken at 2000 rev/min while AJ133 is at 1500 rev/min.

creased pressure, although the removal of two of the exhaust orifice rings will undoubtedly affect the turbulence, though it is assumed that any differences will be marginal, an assumption which, by the time of writing was being investigated by Ling, 2013. Additionally, by the time of writing the engine was only able to run at 750 rev/min which brings about a possible error with the turbulence data, though it was seen that the 0-D $k-\epsilon$ model accounted for changes in engine speed, and subsequent intake jet velocity, well. The integral scale based on clearance height is deemed to be the same regardless of engine speed, this assumption is verified by the work of Heim and Ghandhi, 2011 who determined, with PIV techniques, that the integral scale value remained fairly constant over a range of engine speeds from 300 rev/min to 1200 rev/min.

Experimental results were obtained from the LUPOE2-D-Boosted engine, by a fellow research student at the University of Leeds (Ling, 2013) at a number of conditions. The conditions presented here are at knock limited, MBT timing, the same as for the LUPOE2-D engine; the conditions were input into LUSIE for a prediction and the comparison can be seen in Figure 4.29. It can be seen that with the same after-burning rate definition, $C_{l_i} = 0.8$, as was used for the LUPOE2-D engine, the combustion is over-predicted compared to experimental cycles, suggesting that the u' is reduced by removal of two exhaust rings, or reduced by the increase in intake pressure, or a combination of the two and that this is not predicted by the 0-D $k-\epsilon$ model.

The exhaust valve, used to increase intake pressure, is shut on the firing cycle to prevent intake charge being exhausted, the influence this has on turbulence can be predicted using the 0-D $k-\epsilon$ model, the results can be seen in Figure 4.30 where the the shut exhaust valve was simulated by setting the exhaust mass flow rate, $\dot{m}_e$ to 0 for the predicted cycle. The increase in u' at TDC is approximately 5%, and is due to to removal of the exhaust term which reduces the kinetic energy. The slower combustion seen in the experimental cycles is not predicted by LUSIE, If the experimental cycles did have higher u' values because of the closed exhaust valve, then there is another factor reducing the rate of combustion, outweighing the increase in u'.

At further increased intake pressure, of approximately 2 bar absolute, it can be seen in Figure 4.31 that combustion, is again over-predicted by LUSIE. Knocking cycles are highlighted which give an exaggerated representation of the peak pressures reached in the LUPOE2-D boosted engine. Nevertheless it can be seen that the peak pressure, as predicted by LUSIE, is earlier than seen experimentally. The over-prediction appears to be greater than the one found at the lower intake pressure of 1.6 bar, suggesting that the increase in pressure results in an increase of predicted burn rate which may not be experienced in the LUPOE2-D-Boosted engine. Laminar burning velocities are known to

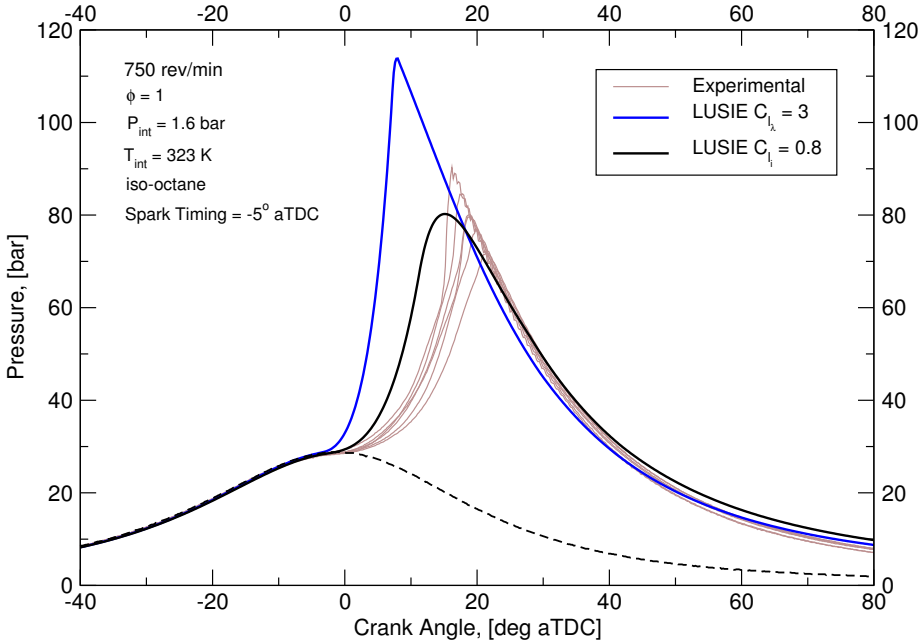

Figure 4.29: The crank resolved in-cylinder pressure plot for the LUPOE2-D-Boosted engine. Here the LUSIE predictions of pressure trace with the integral and Taylor length scale after-burning definitions is presented as well as experimental tests data at 750 rev/min.

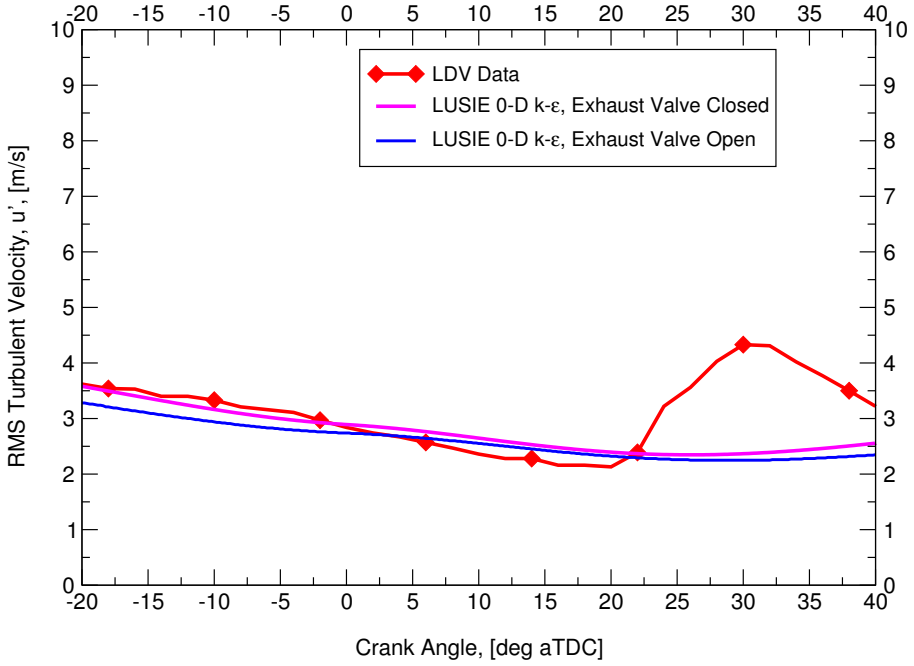

Figure 4.30: Rms turbulent velocity, within the LUPOE2-D as predicted by the 0-D $k-\epsilon$ model compared to experimentally gathered LDV data. The effect of closing the exhaust valve before the firing cycle, can be seen here.

reduce with an increase in pressure while the turbulent flame speeds are expected to rise because of additional flame wrinkling due to reduction of the laminar flame thickness, the model accounts for these interactions, seen in Figure 4.32 where the higher pressure simulation shows a lower laminar burning velocity but larger turbulent burning velocity. An additional observation of note is that the faster burning rate, and subsequently early location of maximum pressure does not result in an increased peak pressure.

The rate of pressure rise appears to be greater than that seen experimentally, and significantly earlier. It is possible that the delay time between the point of ignition and a kernel of sufficient size to result in a self-propagating flame forming, is increased at higher pressures. The standard delay time in LUSIE is 0.111 msec, it is the time between a spark appearing at the electrode and kernel of 2mm being formed, as measured by Cairns, 2001 on the LUPOE1-D engine. It is noted however that there appeared to be no disparity in the early stages of the boosted production engine cases. It is possible that the energy supplied to the coil in the boosted engine was greater resulting in a larger initial flame kernel. The LUSIE predicted cycle using the standard delay time as well as a prediction with a delay time 4x greater than the original can be seen in Figure 4.33. The experimental flame radii were measured using natural light techniques and a high speed camera by Ling, 2013. Caution should be taken at both the early and later stages of combustion. Initially the light given off by the flame is not sufficient to register on the camera, hence the poor quality data at small flame radii. At the later stages of combustion, reflections from the chamber wall can lead to erroneous values of the flame radii. A four fold increase in the delay time was invoked to bring the early stage flame radii in line with a middle radius seen experimentally.

It can be seen that the predicted flame radius has a significantly faster rate of increase than those seen experimentally. Even if the delay time is increased to ensure the predicted cycle is aligned with a middle experimental cycle at the beginning of combustion, the increase in the burning velocity is significant by the end of the flame propagation. The faster entrainment velocity is reflected in the over-predicted crank-resolved in-cylinder pressure profile, as can be seen in Figure 4.34, where knocking cycles have been removed. Here, the delay time appears to have little influence on the overall in-cylinder pressure and it is seen that the cycle is significantly faster than the experimental cycles. The implication of the observation is that, the delay time is not the cause of the over-prediction. Leaving the erroneous prediction of the turbulent entrainment and mass burning velocities to be the likely sources of overall model error.

The two constants, A, (Eq. 3.13) and $C_{\tau b}$ (displayed in this section as C_{l_i} to denote that the integral scale is being used in the after-burning definition) , (Eq. 3.5) which

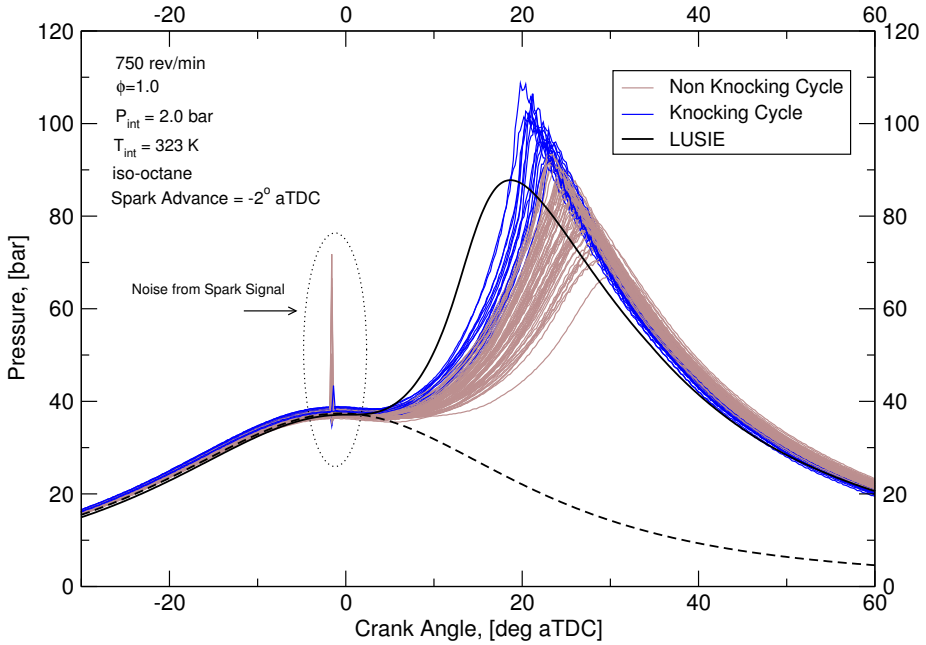

Figure 4.31: The crank resolved in-cylinder pressure plot for the LUPOE2-D-Boosted engine against experimental cycles. Here the LUSIE predictions uses the integral scale for after-burning, C_{l_i} = 0.8, at the higher pressure condition of 2.0 bar intake.

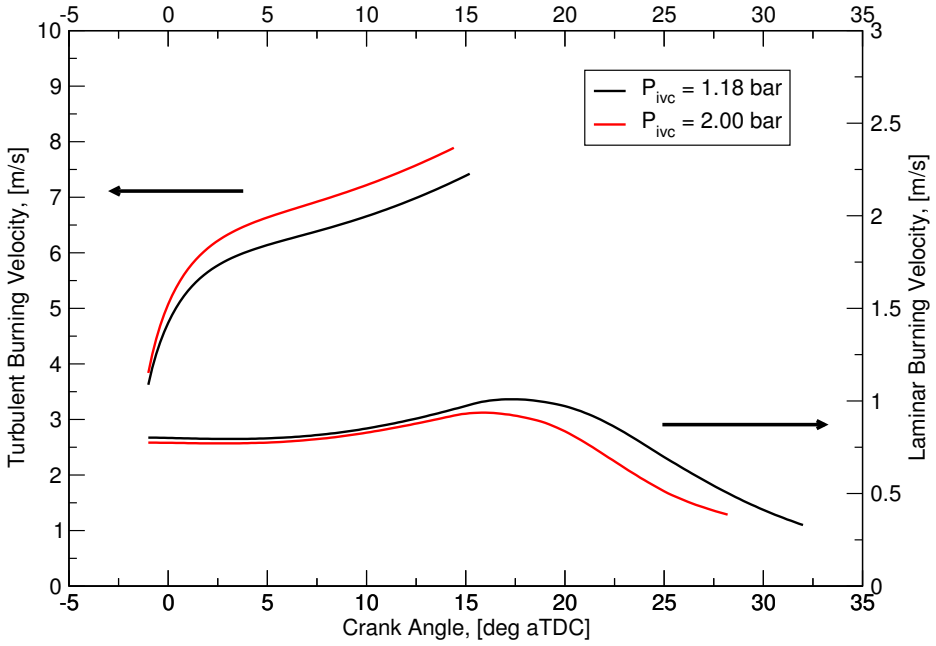

Figure 4.32: Turbulent burning velocity, u_{tr}, and Laminar burning velocity, u_l, predictions from LUSIE at different pressures, temperature remains constant, assuming ideal intercooling. Simulations are based on the LUPOE2-D and LUPOE2-D-Boosted engines.

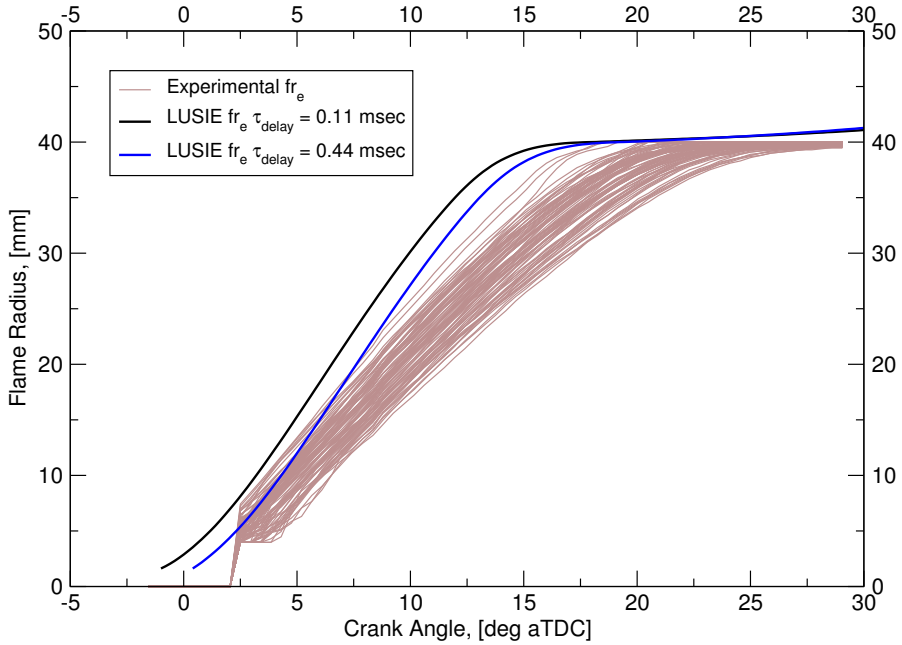

Figure 4.33: The crank resolved flame radius for the 90 cycles captured using the LUPOE2-D boosted engine, as obtained by optically using natural light. In addition the entrained radius predicted by LUSIE at two different kernel delay times is plotted.

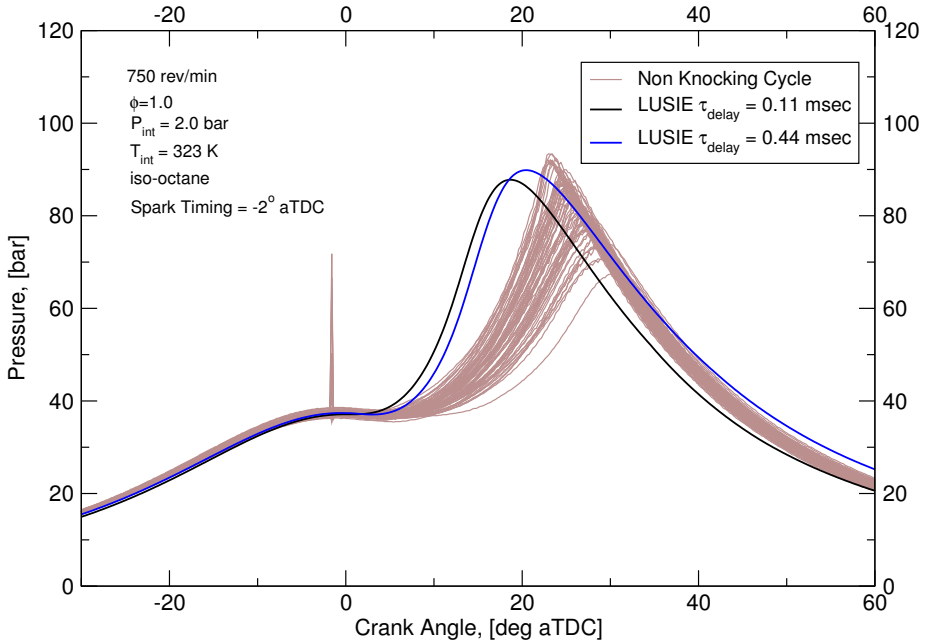

Figure 4.34: The crank resolved in-cylinder pressure for the 90 cycles captured on using the LUPOE2-D boosted engine. In addition, the in-cylinder pressure predicted by LUSIE at two different kernel delay times is plotted.

control, in the case of the three-zone model, the turbulent entrainment burning velocity and the rate of mass burn, were adjusted by $\pm$ 20% in order to assess their influence on the crank-resolved in-cylinder pressure. Additionally the laminar burning velocity, u_l was also adjusted by $\pm$ 20%, although the expression for u_l is considered to be of high integrity, it is feasible that the base definition of the model is erroneous and therefore it was of interest to see in the influence on combustion.

The influence that the adjustment of different parameters has on the resulting in-cylinder pressure profile can be seen in Figure 4.35. The laminar flame speed appears to be more sensitive than either the constant, A, or $C_{\tau b}$, with a range of peak pressure of 28 bar, unsurprising as it appears in the equation for both the developed burning velocity (Eq. 3.11), the developing velocity (Eq. 3.14) and also the after-burning definition (Eq. 3.5). The reduction in C_{l_i} increases the rate of combustion owing to the reduced characteristic burning time. An increase in A, increases the rate of combustion and therefore cylinder pressure. Adjustment of a single parameter would not result in a fitted mean predicted cycle for the LUPOE2-D boosted engine. A change in a single parameter to slow the burning rate will result in a slower burn-rate, as can be seen in Figure 4.35, where a reduction of the constant, A, of 20% will result in a reduction in peak pressure of 12 bar (approximately 15%). The location of peak pressure however also reduces (tends towards TDC). The predicted cycle, using the original turbulent burning definitions (A = 0.35, C_{l_i} 0 = 0.8), has a peak pressure which occurs too early, and at too high a pressure. Therefore, to align the prediction with the experimental results, the magnitude needs to be reduced and the peak should occur later in the cycle. Reducing *one* of the constants reduces the magnitude of the pressure significantly, but does not significantly influence the position of peak pressure. It was therefore necessary to alter both A and, in the case of LUPOE2-D boosted, C_{l_i} as well.

To achieve a reasonable match between prediction and experimental cycles, the constant A and C_{l_i} need to both be significantly reduced from 0.35 to 0.15 and 0.8 to 0.3 for A and C_{l_i} respectively. It can be seen in Figure 4.36, that by imposing a slower entrainment velocity, while increasing the after-burning definition, the predicted cycle matches to a middle experimental cycle. Adjustment of the constants to their final values was achieved by use of the multiple regression function (within MATLAB) on P_{max} and θ_{Pmax} separately, where it is known that P_{max} and θ_{Pmax} are outputs to the function whose inputs include A and C_{l_i}. The regression consisted of adjusting A and C_{l_i} incrementally and adding the P_{max} and θ_{Pmax} outputs to the regression database. It is also noted that if the Taylor microscale is used in the after-burning definition, which has its own dependence on pressure, then a different response to constant adjustment would be seen.

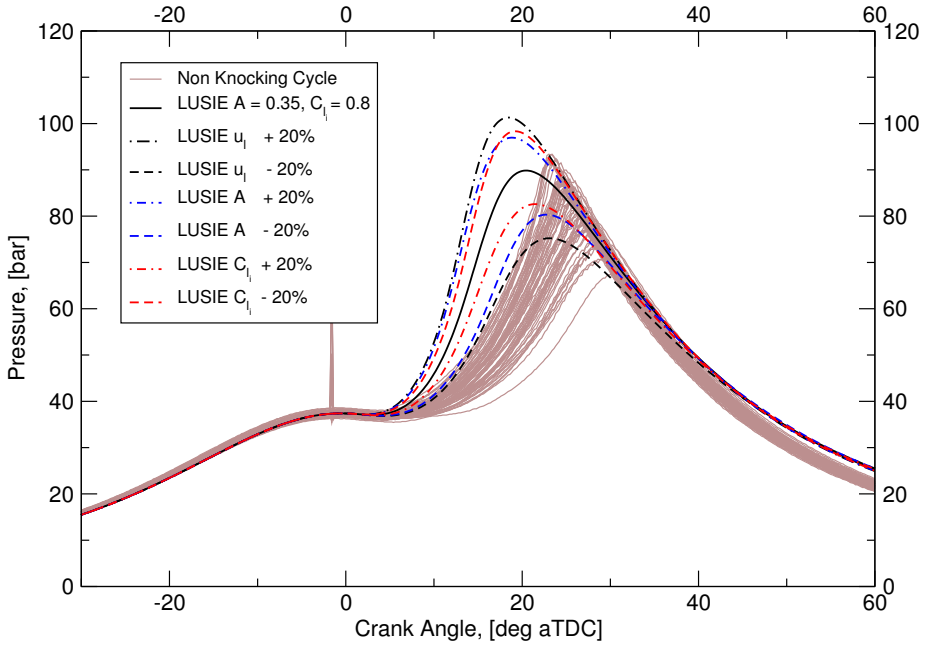

Figure 4.35: The crank resolved in-cylinder pressure for the 90 cycles captured using the LUPOE2-D boosted engine. In addition to the sensitivity of the turbulent combustion constants and laminar flame speed, on cylinder pressure, as predicted by LUSIE.

Although adjustment of the turbulent combustion constants is not satisfying as the fundamental error introduced at higher pressures has not been resolved. It was seen on the boosted production engine, that the after-burning definition had to be reduced in order to achieve an acceptable predicted middle cycle, however no reduction in the constant A, was required. Physically, a reduced entrainment velocity and increased after-burning rate, as required in for the matched LUPOE2-D boosted prediction, would result in a thinner flame thickness. It can be seen that although the cylinder pressure is close to a middle experimental cycle once constants have been adjusted. The entrained flame radius as predicted by LUSIE can be seen in Figure 4.37 to be below, i.e. slower than a middle cycle. Although the predicted middle cycle has been matched in terms of the slope of an experimental middle cycle, the peak pressure is too low as was seen for the 1.6 bar case. The reason for this is, at the time of writing, unknown. Similarly for the cycles with predicted combustion that is too fast, the peak pressure was lower than would be expected. A possible cause is the blow-by model which is over-predicting mass loss for the LUPOE2-D boosted specifically. The constants however for the LUPOE2-D boosted blow-by model were the same as for the LUPOE2-D non-boosted. Also possible is that the initial mass in the cylinder has not been correctly accounted for. It can be seen, however, in Figure 4.38 that trapped mass around TDC, where combustion takes place, that the ratio of trapped mass, is approximately equal to the ratio of pressure in the two engines.

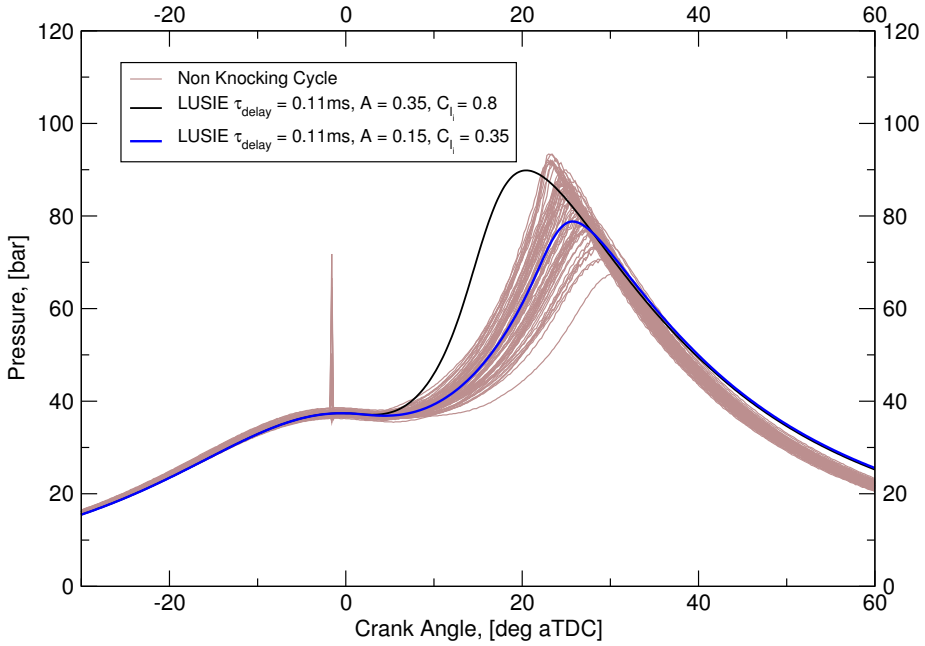

Figure 4.36: The crank resolved pressure in-cylinder pressure, for the 90 cycles captured on using the LUPOE2-D boosted engine with two cycles predicted by LUSIE. 1) with the combustion model as validated with the LUPOE2-D non boosted engine 2) as fitted to the LUPOE2-D boosted engine.

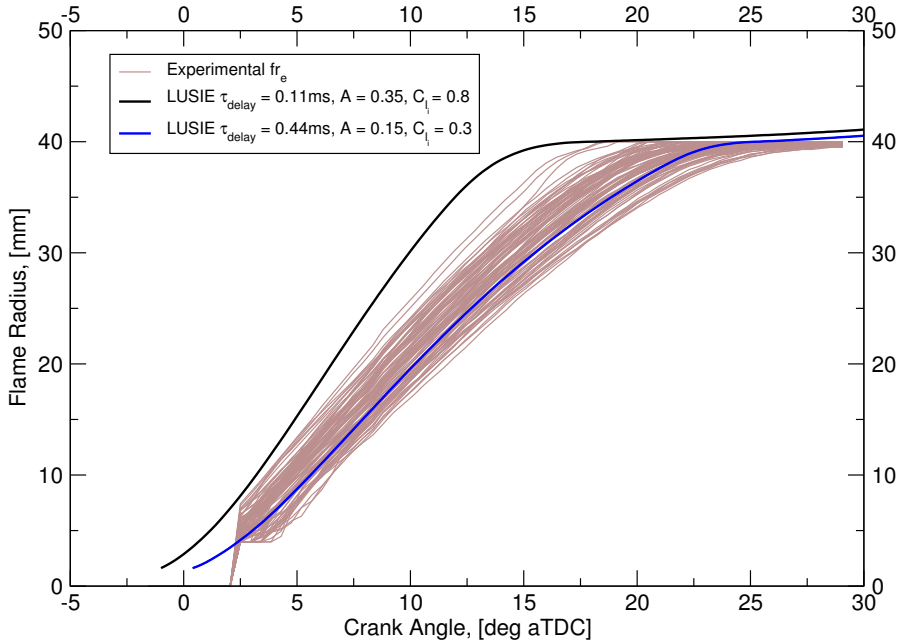

Figure 4.37: The crank resolved flame radius, for the 90 cycles captured on using the LUPOE2-D boosted engine with two flame radii predicted by LUSIE. 1) with the combustion model as validated with the LUPOE2-D non boosted engine 2) as fitted to the LUPOE2-D boosted engine.

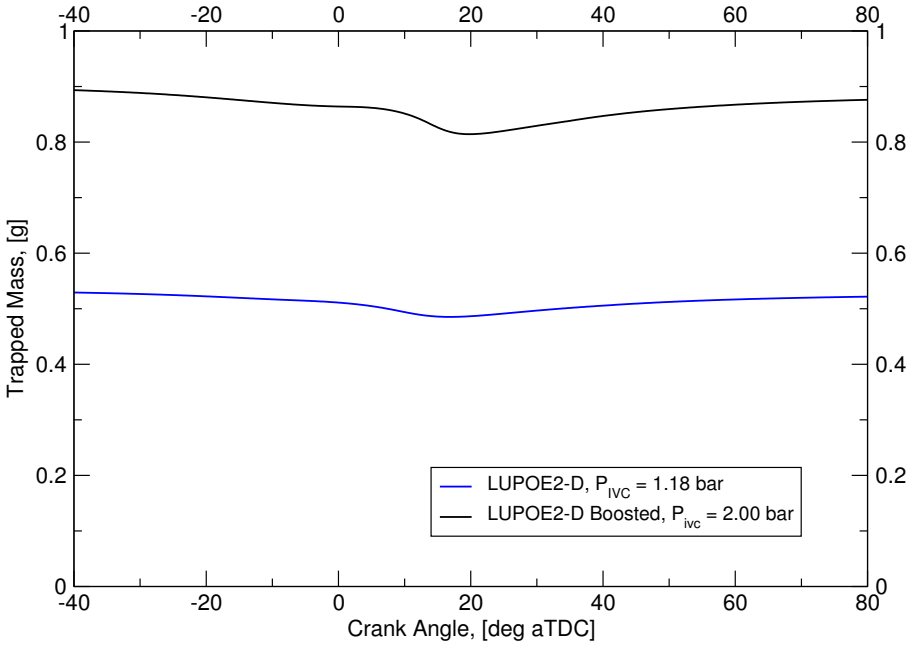

Figure 4.38: The crank-resolved trapped mass within the cylinder, as predicted by LUSIE for the LUPOE2-D non-boosted and LUPOE2-D boosted cases.

$P_{boosted}$ / $P_{non\text{-}boosted}$ = 1.69 while, at TDC, $m_{boosted}$ / $m_{non\text{-}boosted}$ = 1.72. It is therefore unlikely that errors in the initial mass or an over-prediction of mass loss is responsible for the low maximum pressure values.

4.4 General discussion

The application of fast-running engine predictions as a supplementary design and development tool is of great relevance to the automotive industry. With quasi-dimensional thermodynamic models currently offering an efficient method of engine performance prediction, the implications going forward for accuracy with regards to "downsized" engines is of key importance; developed models have historically been validated against engines which fall within a certain pressure-temperature history pattern; moving away from conventional engines into high pressure operating requires re-evaluation of the turbulent combustion model constants.

The 0-D $k-\epsilon$ model was validated against two non-boosted engines, the LUPOE2-D and AJ133; experimentally captured LDV data for the LUPOE2-D was available for validation, while CFD predictions were used as reference data for the AJ133 and engine. It was seen that when using the instantaneous piston speed, $|S_p|$, instead of the mean piston speed, $|\bar{S}_p|$, the predicted u' around TDC and during the combustion phase gave a better

agreement to the reference experimental data. Besides, the model constants were kept the same for the turbulence prediction for both the LUPOE2-D and AJ133 engine. When predicting turbulence characteristics for the UB100 engine, CFD data was again used for the reference owing to the additional time and cost penalties required to adapt the engine to allow collection of turbulence data through experimental methods, was beyond the engine development project scope. The CFD results gave turbulent kinetic energy predicted values at equally spaced theoretical probe locations as well as the mass-averaged u' of the whole chamber, the 0-D $k-\epsilon$ model prediction required further constant optimisation in order to achieve agreement with experiments which was deemed acceptable for UB100. A larger dissipation term constant was needed in addition to a lower production term constant, to produce the higher than predicted rate of dissipation. The reason for the constant alteration is attributed to one of two possibilities: either, the change in pressure influences the turbulence dissipation rate, not predicted by the 0-D $k-\epsilon$ model, or the energy transfer from large scales to smaller ones is not correctly accounted for due to the intricate combustion chamber geometry on the UB100 engine generating turbulence, where the 0-D $k-\epsilon$ model assumes isotropic and homogeneous turbulence and does not account for geometric influence.

Prediction of the integral scale was attempted using five definitions found in the literature. It was seen that although all models predicted values of similar magnitude, the variance between the models was relatively large in terms of the benchmark experimental data. The 0-D $k-\epsilon$ model definition of integral scale was seen to be in good agreement with the LUPOE2-D engine, using the constant validated for the u' predication. Indeed, using the original LUSIE version of l_i as used by Hattrell, 2007 and Abdi Aghdam, 2003 (with the constant, C_L of 2.0), it was seen that the prediction of l_i was too high which resulted in under-predicting the combustion process. For the AJ133 engine, it was seen that the 0-D $k-\epsilon$ model prediction of l_i was too small which would have resulted in combustion that was too fast. It was not possible to attain a reasonable agreement between CFD and the 0-D $k-\epsilon$ model by adjusting the F_d constant which controls both the dissipation and the length scale. It is thought that the pent-roof in the AJ133 and UB100 engine which are accounted for in the CFD predictions are not predicted by either of the 0-D models ($k-\epsilon$ or LUSIE). A potential modification would be to use a separate constant to only affect l_i.

Prediction of the combustion process at a given condition in a given engine was also performed and validated solely against experimentally gathered, crank resolved cylinder pressure data. The prediction of LUPOE2-D combustion process appeared to be in good agreement with experiment using the integral scale definition for after-burning

as used by Hattrell, 2007 and Abdi Aghdam, 2003 with the characteristic burn-up time constant, C_{l_i}, = 0.8. For the LUPOE2-D-Boosted engine, using the same burn-up constant resulted in combustion that is too fast, i.e. the $\frac{dp}{d\theta}$ slope that was far steeper than seen experimentally, the slope becomes steeper still with a further increase in pressure. As the combustion chamber geometry is identical in both cases, any potential influence of localised turbulence produced by combustion chamber geometry can be neglected, leaving the overall turbulence prediction being erroneous. It was seen that the entrained flame radius was considerably over-predicted vis-a-vis the non-boosted LUPOE2-D cycle. An initial assessment would suggest that the increase in pressure causes a reduction in turbulent burning velocity in the LUPOE2-D engine, while the models and fundamental combustion studies, in constant-volume bombs (Lawes et al., 2012), suggest that an increase in pressure should result in an increase turbulent burning velocity. Potentially excessive levels of EGR may exist in the cylinder owing to the removal of two exhaust rings, which would result slower laminar and therefore turbulent burning velocities, however the engine operated with a high level of skip firing, with the intention to eliminate burned gas residuals. It was possible to match a predicted cycle to the experimentally cycles captured on the boosted LUPOE2-D engine, however significant reductions in both three-zone model constants, A and C_{l_i} were required as well as increasing the kernel formation delay time.

It has been seen that the predicted combustion process in the AJ133 engine, is far too slow when using the combustion model validated against the LUPOE2-D engine, combustion prediction is slower still for the UB100 engine. Working on the assumption that the increase in pressure should be accounted for in the model in terms of a higher u_t then the conclusion is that the turbulence data being used is erroneous, most likely it is the integral length scale which is either incorrectly predicted by CFD methods or that the assumption that the integral scale is the optimum scale to use, does not appear applicable for this engine operating. One other possible source of error not investigated might be turbulence induced by the direct injection event itself - possibly a resulting in faster initial flame acceleration which, as can seen in Chapter 5, is likely to have significant influence on overall burn rate.

4.4.1 A discussion on combustion regime and flame instability

The four engines addressed in this chapter are: UB100, AJ133, LUPOE2-D and LUPOE2-D boosted; it was seen that all engines have different requirements of the turbulent combustion model constants. To determine whether or not a fundamental change in the combus-

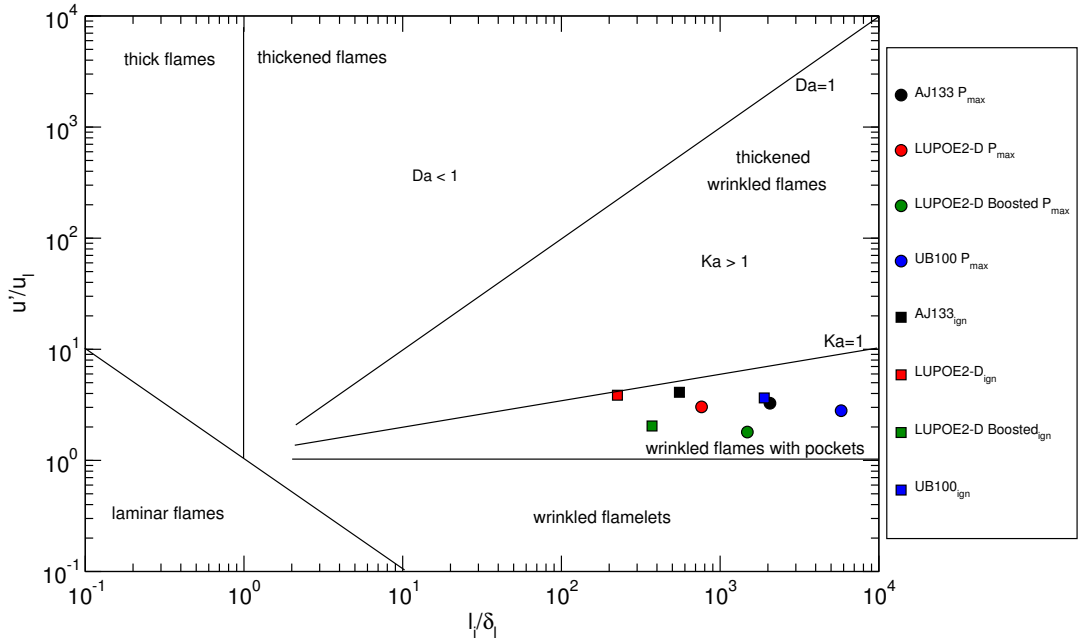

Figure 4.39: A Borghi diagram containing information for the four engines at both the point of ignition and the maximum pressure. The conditions of the engines are as discussed in the above sections when fitting a "mean" cycle to each engine.

tion regime occurs at the different conditions, the "state" of the combustion at the point of ignition, and at maximum pressure, P_{max}, have been plotted on a Borghi diagram (Section 2.3.2.1) and can be seen in Figure 4.39. It can be seen that the combustion process (or at least at ignition and at maximum pressure) occurs in the wrinkled flames regime. One noteworthy observation is that the higher pressure engines (UB100 and LUPOE2-D boosted) appear to have an increased dimensionless length scale (l_i/δ_l), owing to the reduction in laminar flame thickness at lower pressures. It is not however clear, from the diagram, why such a disparity exists between the four engines. It was initially hypothesised that for boosted engines the location on the Borghi diagram would move towards larger Karlovitz, *Ka*, values. However, as the high pressure engine variants in this study utilised idealised inter-cooling, the associated increase in temperature was not realised and therefore *Ka* values reduced.

There appears to be a requirement to change the model constants (seemingly the active turbulent scale) significantly when predicting turbulence for the UB100 engine, as well as for the LUPOE2-D boosted. While the reason for this is as yet, unknown, a possible source of the error could be in accounting for the instability of laminar flamelets as the flame propagates through the turbulent medium. The Zimont model (Section 3.2.8.1) accounts for the thermal diffusivity of the mixture, however it does not account for the mass diffusivity of the mixture and therefore is reliant on indirectly accounting for instability

in the laminar burning velocity routine. The burning velocity at elevated temperatures and pressure possibly also poses an issue when attempting to determine, accurately, u_l. Additionally, in this specific case the behaviour of the test fuel (a RON98 forecourt fuel with 5% ethanol inclusion) may have significantly different instability behaviour than iso-octane and therefore the combustion model would be deficient. It could be suggested, based on the work performed in this chapter, that the Zimont combustion model appears to have deficiencies in accounting for turbulent or laminar burning velocities at elevated pressures. It should be stated that without being able to confirm the integrity of the turbulence data provided to the model, a strict statement regarding fidelity of the Zimont model cannot reasonably be made.

Chapter 5

Cyclic variability in SI engines

5.1 Chapter Overview

Reported in the current chapter is an investigation into the application of a simple cycle-to-cycle variability (c.c.v) model, within a quasi-dimensional thermodynamic model, to sets of cycles which represent a wide range of operating conditions and combustion chamber designs. The dominating causes of cycle-to-cycle variability in engines have been identified as: variations in mixture composition (homogeneity) and random fluctuations in the flow field ahead of the propagating flame. Owing to the turbulence variation, the 0-D $k - \epsilon$ turbulence model, discussed in Chapters 3 & 4, was an integral part of the variability modelling method. A large amount of experimentally gathered data was made available for this project, the majority of which was obtained via testing on the LUPOE2-D research engine at the University of Leeds; additional data on production engines was provided by external parties.

There is a variability between and within cycles, which irrefutably exists in internal combustion engines. Though the variability is clearly visible from any experimentally obtained dataset containing from several to thousands of cycles, quantifying the variability requires some statistical manipulation. There are numerous parameters which can be used to account for combustion variability, and no universally "best" parameter has been identified to suit all types of combustion variability. In this Chapter, previous experimental work has identified that in-cylinder mixture stoichiometry and variations in

cycle-to-cycle turbulence are perhaps the most suitable to use on SI engines regardless of operating pressure.

Finally, this Chapter introduces the influence of variability at different stages of the combustion process in addition to a novel method for quantifying cyclic variability, or more correctly, alluding to the part of the combustion process, within a set of cycles, where such variability occurs.

5.2 Measures of cyclic variability

The cycle-to-cycle variability seen can be characterised by the variations of recorded or calculated, parameters from a set of cycles at a given condition. There are numerous parameters which can be used to assess the degree of variability displayed by any given engine. These have be subdivided into the groups presented in the following sections (Ozdor et al. [1994]).

5.2.1 Pressure related parameters

It has been proposed by Stone [1999] that when ignition timing is set for maximum brake torque, MBT, cycle-to-cycle variability in IMEP is minimised. It has also been identified that c.c.v in P_{max} and $\left(\frac{dp}{d\theta}\right)_{max}$ decreases with advancing ignition up to the point of MBT. Matekunas [1983] proposed that θ_{Pmax} is the best parameter to use to determine early-stage combustion variability arising primarily from a variability in ignition delay times. Belmont et al. [1986] found distinct correlations between pressure related parameters under lean conditions and they suggested that P_{max} is the most convenient basis for c.c.v measurements. The reasons given for this were ease of measurement and that P_{max} is more sensitive to cyclic variations in indicator work than any other parameter. Pressure related parameters are relatively easy to measure with in-cylinder pressure transducers. It has been stated by Samuel et al. [2010] that there is consensus among various researchers that measured cylinder pressure based quantification of cycle-to-cycle variability is the most useful method.

5.2.2 Combustion related parameters

Ozdor et al. [1994] identified that both the mean value and variance of the fluctuations in ignition delay, $\delta\theta_d$, (for SI engines) determine to a great extent cycle-to-cycle variability. Ignition delay time relates to the time between a signal sent to initiate a spark, and a kernel, of a pre-specified size, forming. A smaller $\delta\theta_d$ is associated with smoother engine operation and shows as a good indicator of the early stages of combustion though it does not actually provide any information about the causes for early combustion cycle-to-cycle variability, such as random direction and velocity of the flame kernel convection, local fluctuations in the air-fuel ratio and the amount of diluent. These parameters are also very sensitive to measurement errors as combustion related parameters are derived from in-cylinder pressure data.

5.2.3 Flame front related parameters

Flame-front related parameters, such as flame front position, flame front area and displacement of the flame kernel centre from the spark gap are obtained by means of either visual techniques such as LDV, Schlieren imaging or ionization gap techniques (Ozdor et al. [1994]). It is possible from these techniques to detect small changes in early-stage flame development, such as flame stretch or convection direction. The cost, both in terms of time and resources, renders the application of flame front parameters for cycle-to-cycle variability modelling unsuitable.

The conclusion for cycle-to-cycle characterisation can be summarised as follows:

- If ignition timing is set to MBT then c.c.v in P_{max} will be the most prominent.
- Variability in θ_{Pmax} will allude to variability in ignition delay times, whilst potentially describing variability in the early stages of combustion.
- Cycle-to-cycle variation in IMEP is most useful for indicating the engine response to c.c.v in combustion processes.

As all engines used in this study have been set at MBT, or as close to MBT as is permissible by the knock boundary, the parameter, P_{max} will primarily be used in this study to determine cycle-to-cycle variability.

5.2.4 Measures of Variability

The coefficient of variance (COV) is the most commonly used measure for quantifying the level of variability within a dataset (Heywood [1988]). The coefficient of variance is a measure of the dispersion of a probability distribution showing the extent of variability in relation to the mean of a population. The COV of a given parameter (x) is related to the standard deviation and mean of that given parameter via Eq. 5.1.

$$COV_x = \frac{\sigma_x}{\bar{x}} \cdot 100\% \tag{5.1}$$

5.2.5 Definition of Cycle Types

Throughout this chapter, "typical" cycles are referenced. These typical cycles relate to selected cycles within a dataset when comparing experimental and predicted results, such cycles being referred to as fast, middle and slow cycles. Descriptions of these cycles are as follows:

- Middle cycle is a cycle where the cycle within a dataset where P_{max} is closest to $\bar{P}_{max}$ (the ensemble average of P_{max})
- Fast cycle is a cycle where $\bar{P}_{max}+2\sigma$ P_{max}
- Slow cycle is a cycle where $\bar{P}_{max}-2\sigma$ P_{max}

These are values of typical cycles, rather than the actual definition of a fast, middle or slow cycle. As such a set of fast cycles can have P_{max} values higher *or* lower than the value for a "typical" cycle, see Figure 5.1 for clarification. Additionally, it is not recommended to use an ensemble average of all cycles to represent a mean (middle) cycle; work by Abdi Aghdam [2003] suggests that an ensemble average cycle is unlike any actual cycle within a dataset in terms of $\frac{dp}{d\theta}$.

5.3 Cycle-to-cycle variability validation in the LUPOE2-D engine

The methods employed by LUSIE to predict combustion in S.I. engines has been discussed in Chapter 3. C calibration of the LUPOE2-D for MBT in terms of IMEP has

also been detailed in Chapter 3. It was seen that LUSIE predicted a mean cycle, for the LUPOE2-D engine, with a good degree of accuracy. It was seen that LUSIE also predicted reasonable mean cycles for the UB100, AJ133 and LUPOE2-D boosted engines after adjustment of the after-burning definition of turbulence length scale (Sections 4.3.1, 4.3.2 respectively and 4.3.3); matching of the middle cycle ensures that the accuracy of the variability is not biased towards faster or slower cycles.

The cycle-to-cycle variability exhibited by the LUPOE2-D operating at the standard reference conditions (SRC) can be seen in Figure 5.2. One hundred firing cycles were captured from the LUPOE2-D engine; these 100 cycles were recorded over 10 separate tests with 10 firing cycles being captured in each test; this was undertaken as a result of limitations with the data acquisition (DAQ) software, namely memory limitation within the computer hardware. It can be seen that, despite the design considerations intended to limit cyclic variability (as discussed in Section 3.6.2), there is a considerable amount of cyclic variability present in the LUPOE2-D engine. Because of a large number of non-fired cycles between two fired cycles It was not possible to determine the influence of the combustion process from a previous cycles on the combustion process in the following cycle.

The random distribution of cycles is not uniform, as can be seen in Figure 5.4 & 5.5 from which it can be determined that the random distribution is akin to, but does not fully conform to a perfect Gaussian distribution (see Section 3.4.4 for details), although 100 cycles is not statistically sufficient to determine if the distribution is Gaussian. It is also seen that the crank angle at which peak pressure occurs, θ_{Pmax} varies by around 13^o CA, while the peak pressure, $\mathrm{P_{max}}$, varies by approximately 23 bar.

Attempts to account for the apparently Gaussian cyclic variability via a pseudo-random modelling process has been implemented as described in Chapter 3. Initially, the model was set to assume a variance of the rms turbulent velocity of σ 12.5% (12.5% $\sigma_{u'}$) as the driving parameter behind the variability based on the work of Aghdam et al. [2007] and Burluka et al. [2012a]; the effect of varying the TKE value at the point of ignition on the rms turbulent velocity profile can be seen in Figure 5.3. The initial imposed variation in rms turbulent velocity is allowed to dissipate following the prediction from the 0-D $k-\epsilon$ model with time (crank angle). Though no physical description can be found to validate this methodology, the work of Hussin [2012] suggests that the variation in rms turbulent velocity begins during combustion, whether this is a cause or an effect has not yet been established.

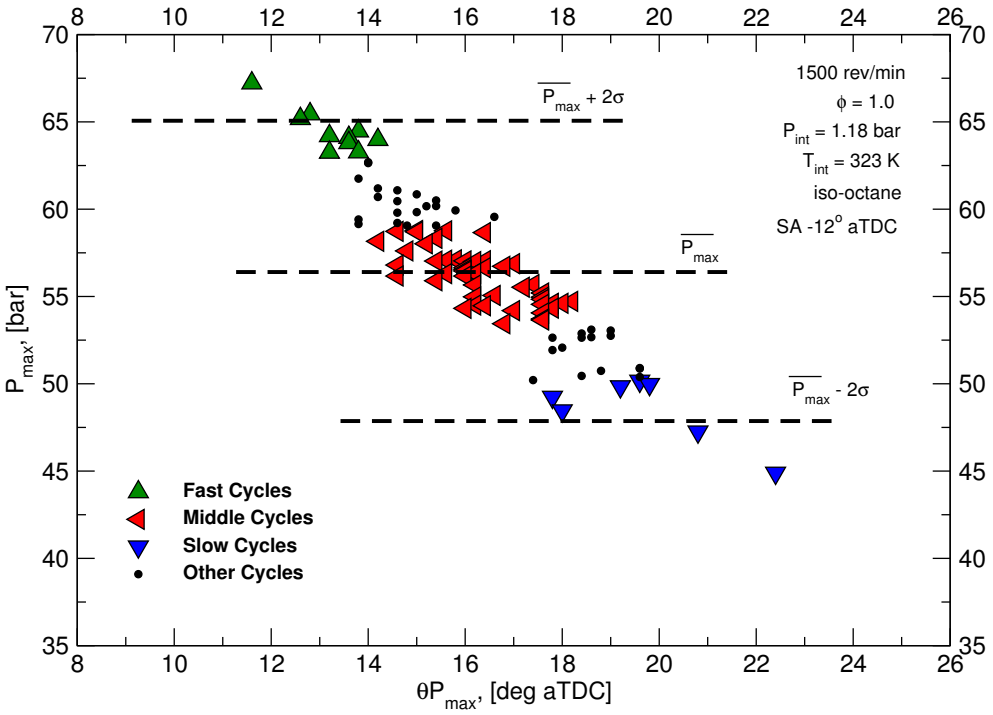

Figure 5.1: Selected 'Fast', 'Middle' and 'Slow' cycles captured experimentally within the LUPOE2-D non-boosted engine. One hundred cycles were captured at the engine's standard reference conditions, detailed within the figure.

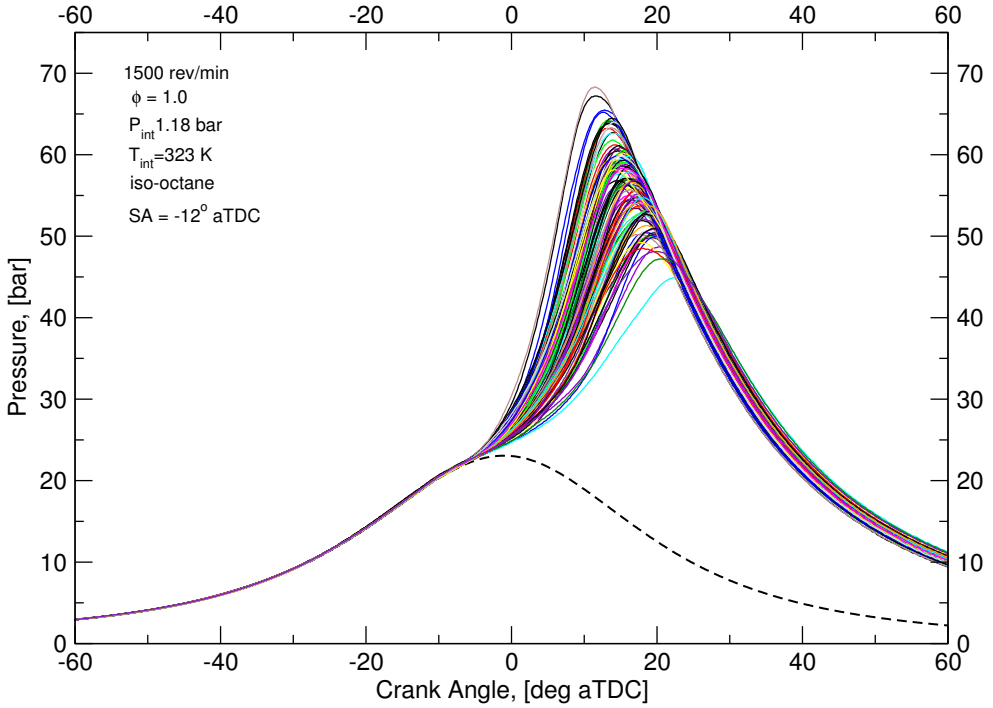

Figure 5.2: One hundred concurrent cycles from the LUPOE2-D experimentally captured. Variation of the combustion from one cycle to the next can be seen here by the spread in-cylinder pressure traces.

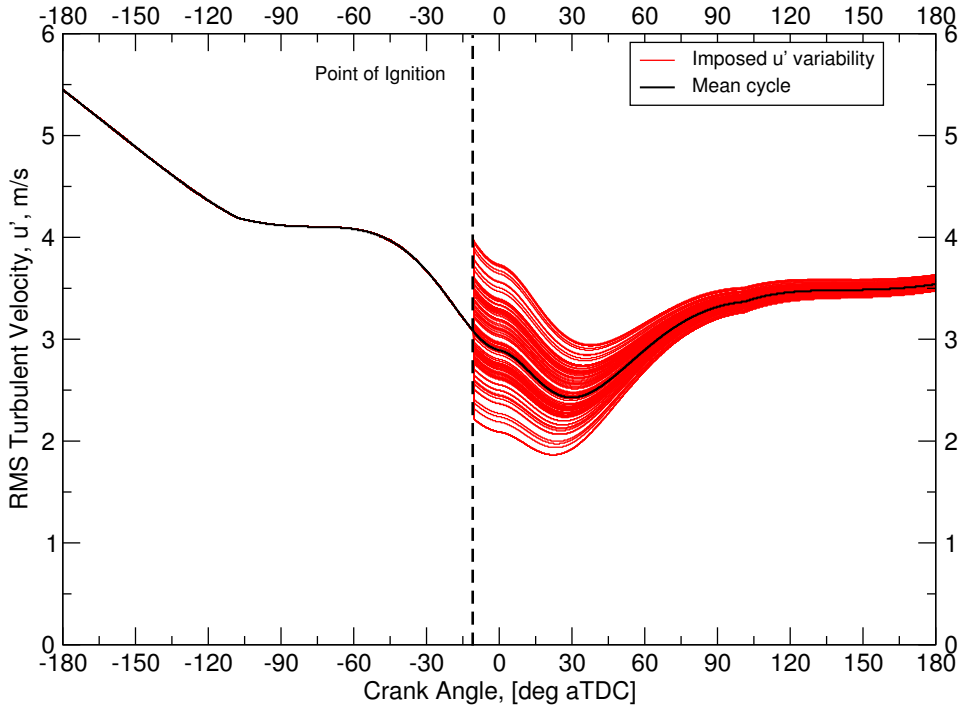

Figure 5.3: Effects of imposed variation of rms turbulent velocity within LUSIE for 100 cycles. Variation occurs at the point of ignition. Up until the point of ignition the standard prediction of rms turbulent velocity by the 0-D $k-\epsilon$ model is used.

The P_{max} vs θ_{Pmax} x-y scatter plot is presented in Figure 5.6 for both experimental results as well as predictions obtained by imposing the variation of u' at the point of ignition. It can be seen that scatter of the data are in good agreement for the experimental and predicted cycles in terms of the arithmetic range (P_{max} - P_{min}), although the predicted cycles appear to show slightly faster combustion than an equivalent experimental cycle, i.e. θ_{Pmax} occurs closer to TDC. As predicted, P_{max} decreases with an increase in θ_{Pmax} as the slower burning cycles have a less severe heat release profile and achieve peak pressure later in the cycle, at a lower magnitude because of the increased cylinder volume. Another observation from this plot is that the horizontal displacement at any given P_{max}, or vertical displacement at any given θ_{Pmax} is not accounted for with this simple variation of one parameter i.e. the relationship is linear. One reason for multiple P_{max} values for any given θ_{Pmax}, and vice-verca, is spatial variations in rms turbulent velocity not accounted for by LUSIE or the homogeneous 0-D $k-\epsilon$ turbulence model.

The experimentally captured crank-resolved pressure signals for selected fast, middle, and slow cycles captured in the LUPOE2-D can be seen in Figure 5.7. Also shown in the figures are LUSIE predictions of fast, middle and slow cycles, the predicted cycles are the extreme cases, i.e. the fastest or slowest possible cases, for a particular set of operating conditions. It can be seen in Figure 5.7, that the fastest predicted cycle is slower than

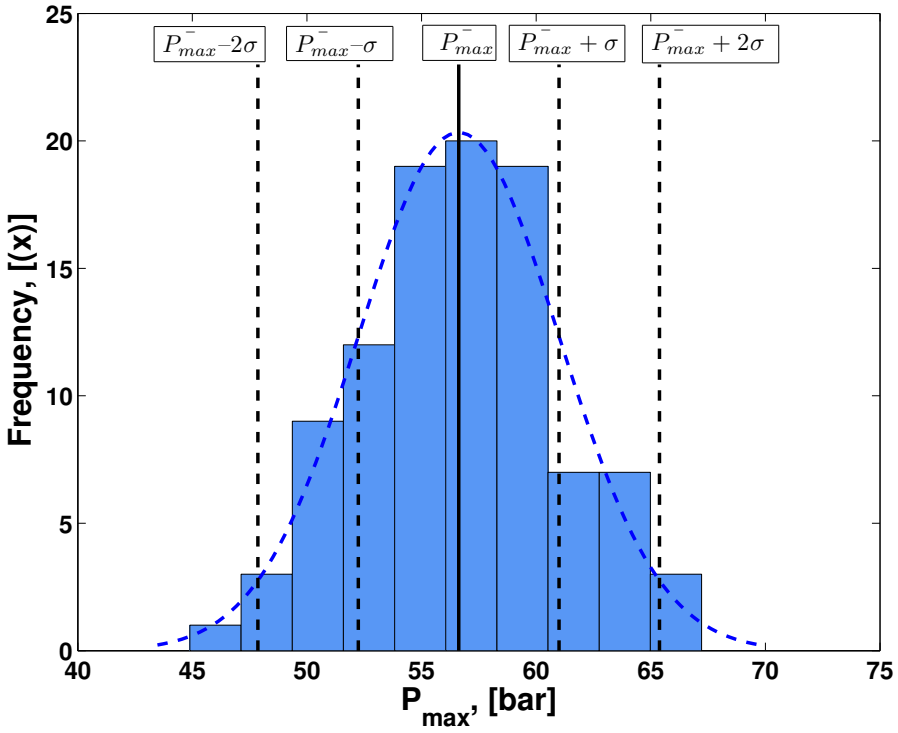

Figure 5.4: Frequency histogram with a bin size of 10 showing the distribution of P_{max} for 100 LUPOE2-D firing cycles with the Gaussian distribution overlayed. μ = 56.4 σ = 4.41.

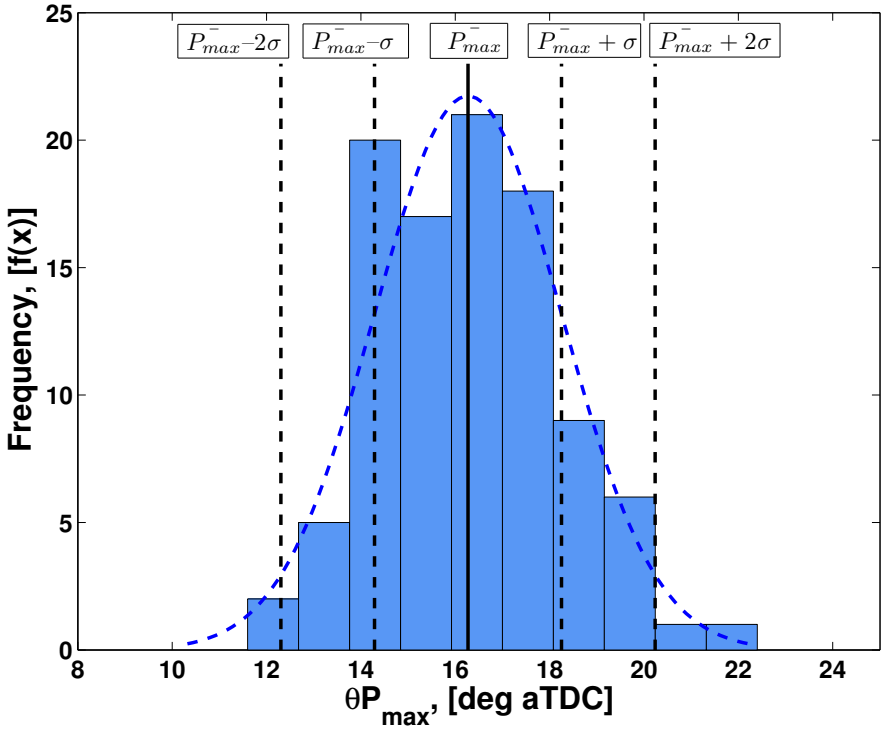

Figure 5.5: Frequency histogram with a bin size of 10 showing the distribution of θ_{Pmax} for 100 LUPOE2-D firing cycles with the Gaussian distribution overlayed. μ = 16.27 σ = 2.0.

the fastest cycles seen experimentally, i.e. the rate of combustion is under-predicted as compared with the experimental cycle. In addition, the slow cycles are under-predicted also; generally, however, the model gives a very good prediction of a fast, middle or slow cycle. If the middle cycle was also under predicted then the reason for the under prediction of fast and slow cycles could be attributed to errors in middle cycle prediction. However it is clear that the middle cycle for this cycle has been validated previously, and is in agreement in this case too. It could be possible that the distribution of the 100 experimental cycles is skewed towards the faster cycles and this is that is the cause of the under-predicted cycles, however the distributions seen in Figures 5.4 and 5.5 do not indicate that the experimental cycles are being skewed in either direction.

A variation of equivalence ratio of σ 5% (5% σ_ϕ) was used to investigate the effect of equivalence ratio variation on combustion in line with the work of Aghdam et al. [2007]. As with the u' variation, the ϕ variation was applied to 100 cycles predicted by LUSIE. The P_{max}, θ_{Pmax} distribution as predicted by LUSIE can be seen in Figure 5.8 compared with the 100 cycle experimental set. It can be seen the scatter of P_{max} is in good agreement between the experimental results and the predicted cycles with respective dispersions of data of 23 bar (67.5 - 44.5 bar) and 22.5 bar (60 - 37.5 bar). It can also be seen that the maximum and minimum predicted values of P_{max} are not aligned with the experimental data.

It is important to identify the response of the test fuel, iso-octane, to changes in equivalence ratio. Iso-octane has a recorded maximum u_l at an equivalence ratio, ϕ = 1.1. Therefore when $\phi > 1.1$, u_l, therefore u_t will be reduced. Hence where an increase in u', from the mean value, will give an increase in u_t, a similar increase in equivalence ratio may not. The maximum ϕ value generated in this set was 1.148. Hence, as LUSIE does not predict the fastest cycles seen experimentally with just a variation in ϕ it can be implied that rich mixtures do not appear to be responsible for the fastest cycle variability. It can also be seen that the linear relationship between P_{max} and θ_{Pmax} has a far steeper slope for variations of ϕ than for variations in the rms turbulent velocity. It can also be seen that when comparing Figure 5.8 with Figure 5.6 ϕ is a more sensitive parameter on variability, compared to rms turbulent velocity, as it was only varied by 5% but resulted in a similar magnitude of difference between the fastest and slowest cycles. It was seen in Figure 4.35 that the laminar flame speed is a more sensitive parameter than the parameters which affect turbulence quantities. Hence, as ϕ changes directly the u_l a similar sensitivity is observed. By observation of Figure 2.11 it can be seen that the slope for rms turbulent velocity is fairly linear around the 2-4 m/s, and therefore a variation around a mean value of 3 will result in a similar sensitivity for slow and fast cycles. For laminar burning

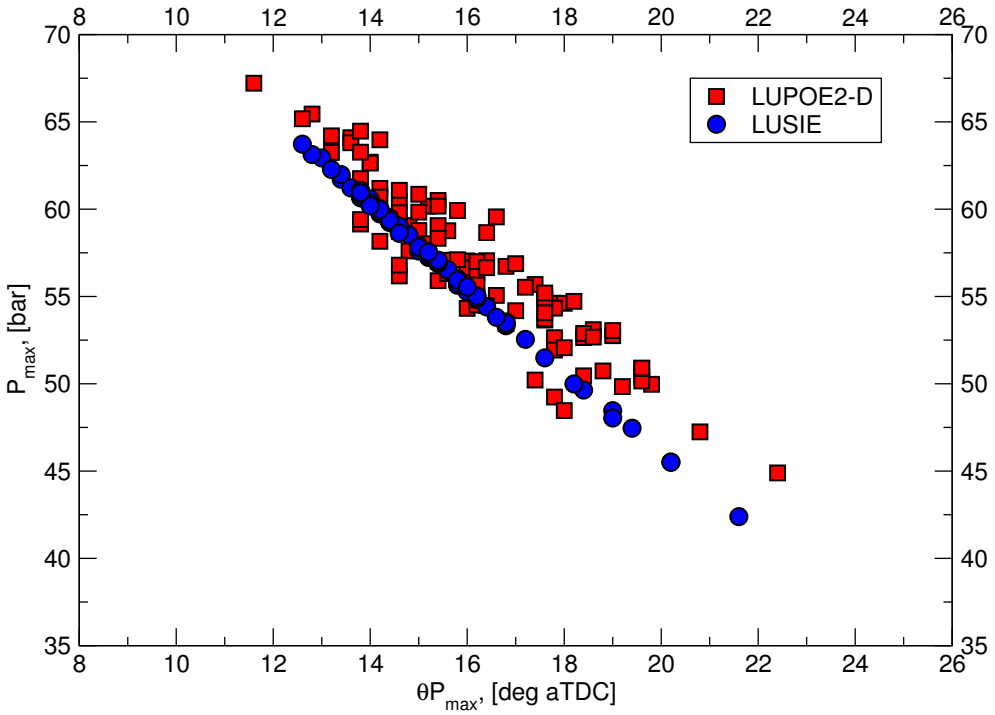

Figure 5.6: The influence of only rms turbulent velocity variation on the distribution of maximum pressure for 100 cycles in the LUPOE2-D engine. Rms turbulent velocity was varied by 12.5%σ.

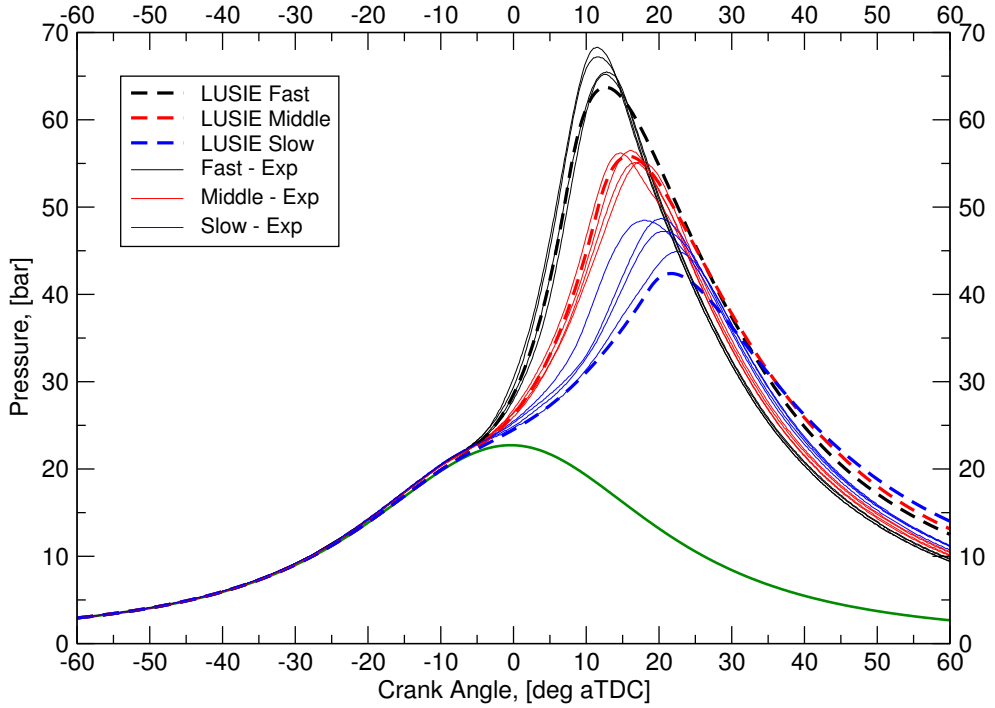

Figure 5.7: Comparison of fast, middle and slow experimental cycles from the LUPOE2-D with cases predicted in LUSIE with variation on only the rms turbulent velocity at a level of 12.5%σ.

velocity however the slope is steeper below ϕ = 1.1 (see Figure 3.3) resulting in a higher sensitivity to u_l.

In order to assess the combined effect of ϕ as well as rms turbulent velocity on variability, both variables were included as variables for a prediction case. As before, 100 firing cycles predictions were performed, for which the results can be seen in Figure 5.9 & Figure 5.10. Combining the two variation parameters gives a better horizontal spread of data at a given P_{max}, or vertical spread at θ_{Pmax}, though it is apparent that the the spread is greater with slower cycles, while at the fastest cycles, the spread is small. The experimental cycles appear to have the minimum spread at the fastest and slowest cycles while the middle cycles have the largest variation at any given P_{max} or θ_{Pmax}. The slope of the line of best fit through the predicted scatter is in better agreement with the experimental cycles compared to the case where only ϕ is varied.

The slope of the line through the scatter plots can be seen more clearly in Figure 5.11 where the slope of the lines of best fit to the dataset can be seen. The slope of the u' only case is 18% steeper than experimental, while the ϕ case is 56% steeper. Fastest cycles are again under-predicted, while slow cycles occur too early with P_{max} values that are too low. From these results it can reasonably be deduced that either variations in ϕ are lower in the LUPOE2-D engine than 5%σ, as such a steep slope is not seen experimentally, or that LUSIE erroneously predicts the influence of ϕ.

Separating the influence of u' and ϕ variations into the four extreme cases, that is, the richest case with the highest turbulence, $\phi+$,$u'+$ down to the leanest cycle with lowest turbulence $\phi-$,$u'-$. These cases are presented as crank resolved pressure traces in Figure 5.12, where it can be seen that a reasonable account of all cycles is captured with the current variability modelling methods. There appears to be a small amount of vertical or horizontal spread which could be attributed to the inter-dependence of ϕ & the rms turbulent velocity during the middle cycles, though the spread does not appear large enough compared to experimental cycles; thus it could be deduced that the suspected spatial variations in turbulence parameters, in a given cycle, are the major cause of the variations in the peak pressure or angle at which it is achieved at any given P_{max} or θ_{Pmax} spread. It should be noted that the richest cycle may not necessarily be the fastest cycle as the richest cycle is in excess of $\phi = 1.1$ which is the the ratio at which the highest laminar flame speeds occur, though the marker seen in the Figure 5.13 is of the richest mixture conceivable with the 5%σ_ϕ for a 100 cycle set, which is a ϕ value of approximately 1.15.

It can be seen from Table 5.1 that the COV of θ_{Pmax} is comparable between experiment and prediction. Interestingly the closest mean value to experiments was found

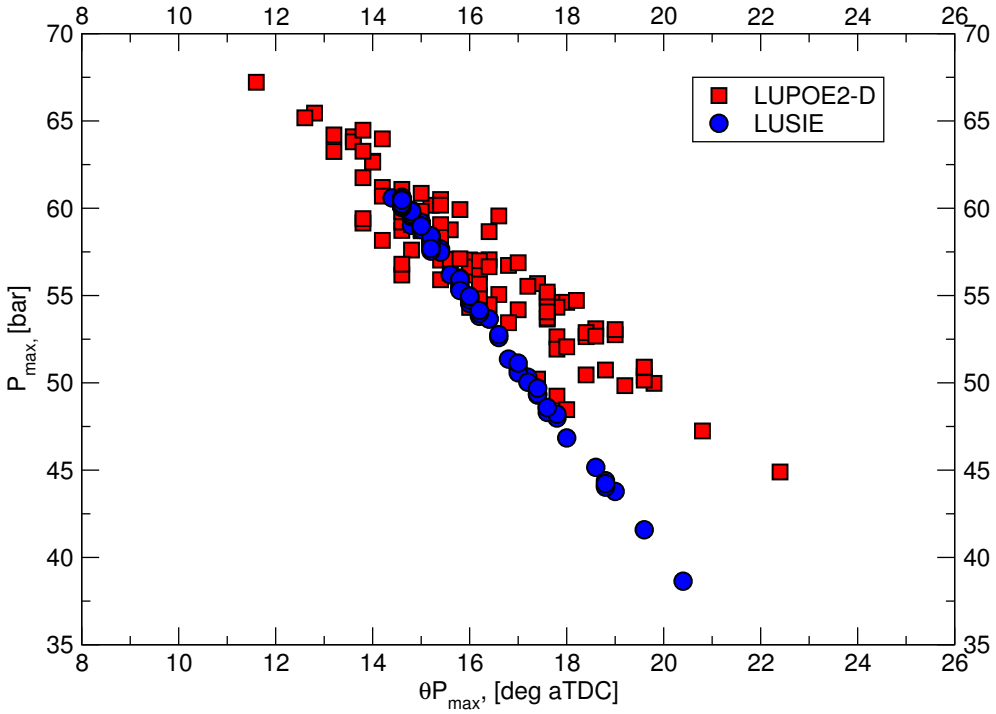

Figure 5.8: The influence of only equivalence ratio on the distribution of maximum pressure for 100 cycles in the LUPOE2-D engine. Equivalence ratio was varied by 5%σ.

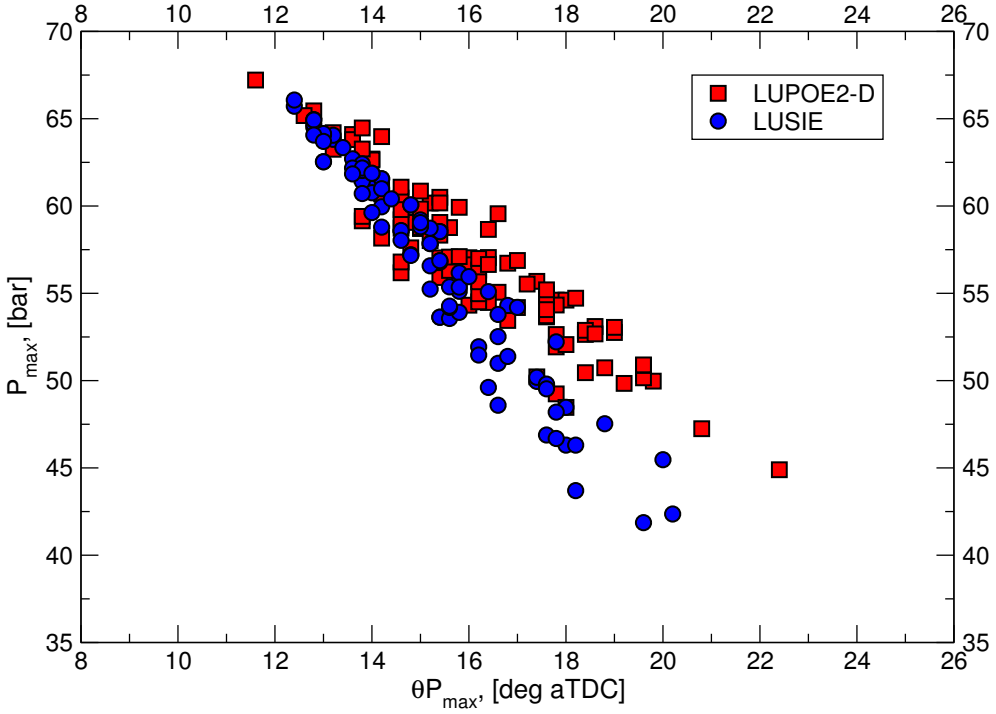

Figure 5.9: The influence of equivalence ratio and rms turbulent velocity variation on the distribution of maximum pressure for 100 cycles in the LUPOE2-D engine. Variation on the equivalence ratio and rms turbulent velocity at levels of 5% σ and 12.5% σ, respectively.

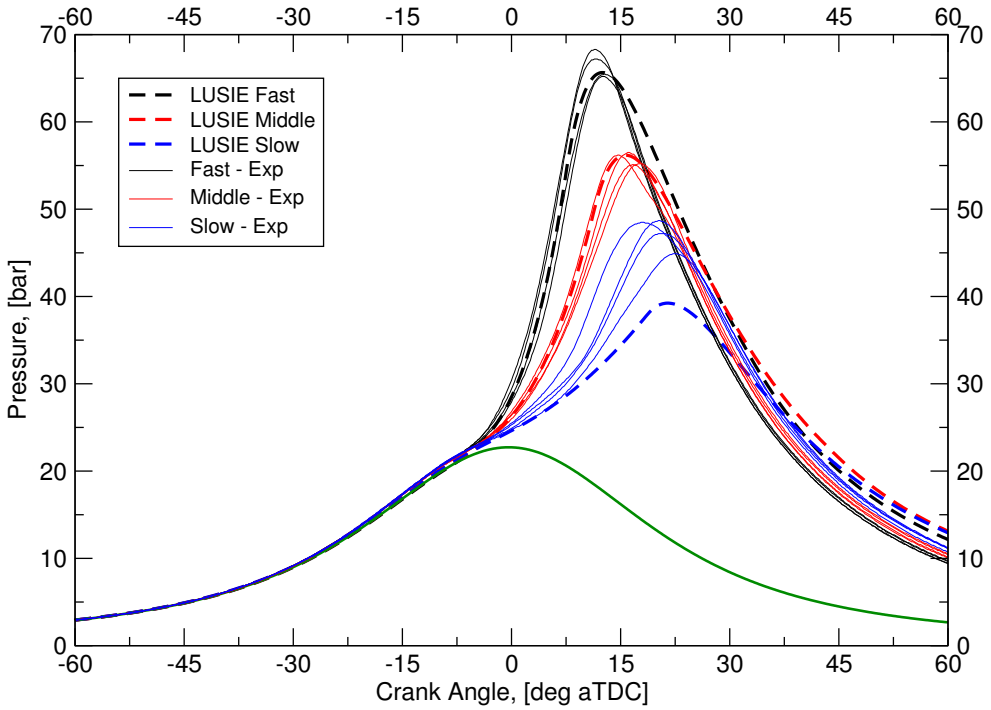

Figure 5.10: Comparison of fast, middle and slow experimental cycles from the LUPOE2-D with cases predicted in LUSIE with variation on the equivalence ratio and rms turbulent velocity at levels of 5% σ and 12.5% σ, respectively.

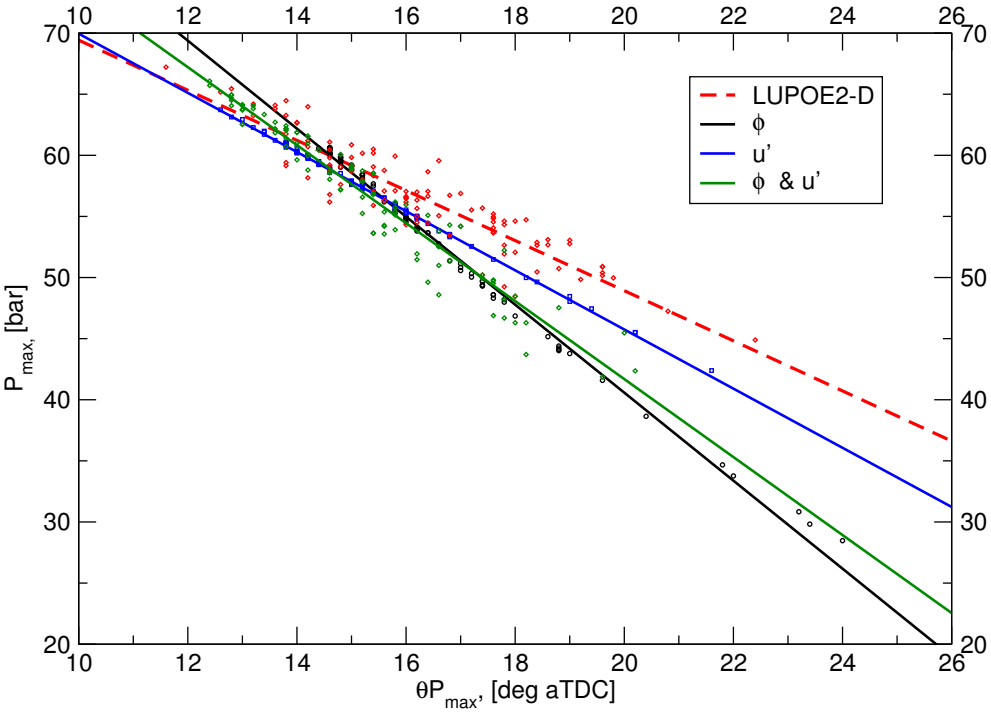

Figure 5.11: The change in slope for least square lines of best fit to the distribution of maximum pressure data. The influence of combinations of the variables used to induce variability, ϕ and u', can be seen.

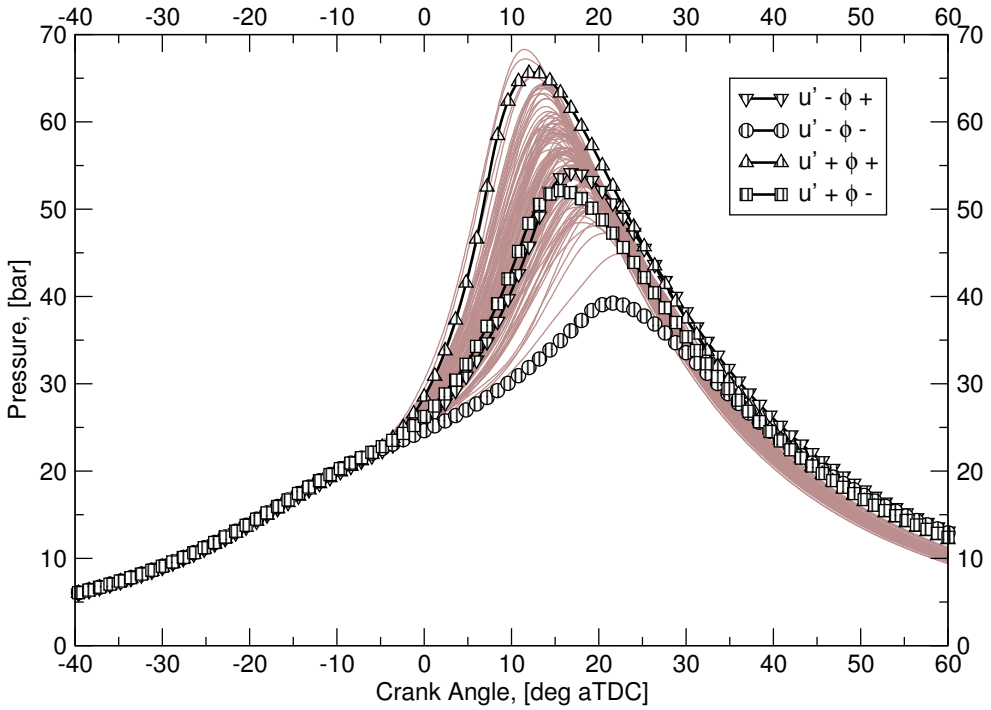

Figure 5.12: Predicted extreme cases with LUSIE where both variability parameters are maximum or minimum, as well as combinations of both. The predicted cases are shown against 100 recorded experimental cycles on the LUPOE2-D.

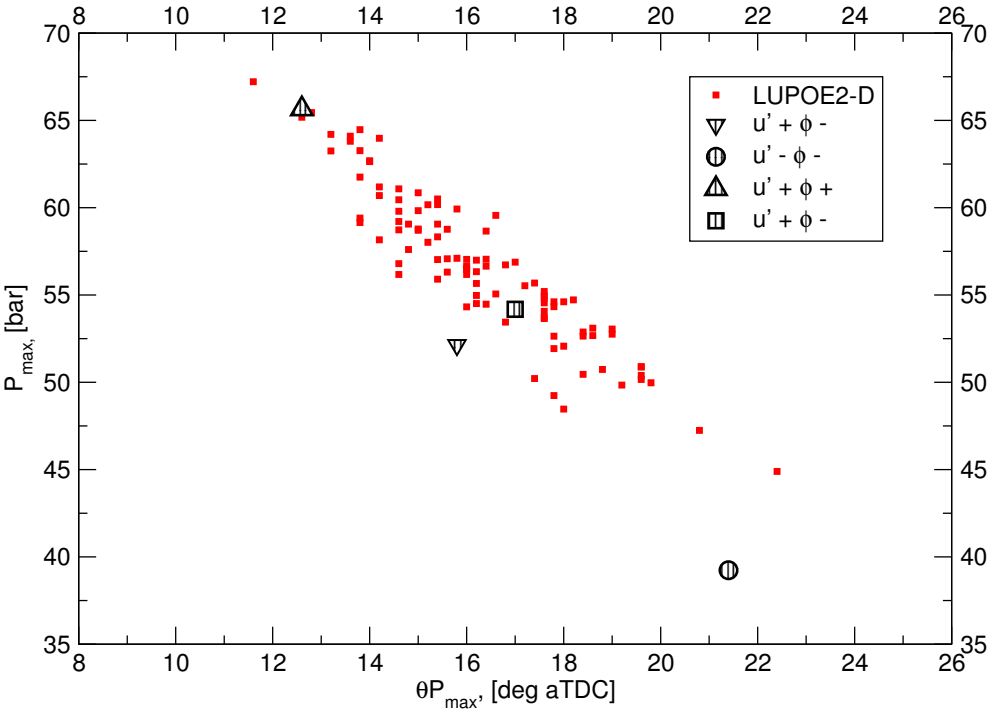

Figure 5.13: Predicted extreme cases with LUSIE where both variability parameters are maximum or minimum, as well as combinations of both. The predicted cases are shown against the maximum pressure distribution for 100 cycles on the LUPOE2-D engine.

	u'	ϕ	Both	LUPOE
Mean (bar)	15.26	15.46	15.28	16.27
Max (bar)	21.60	21.00	20.20	22.40
Min (bar)	12.60	14.40	12.40	11.60
σ (bar)	1.66	1.83	1.79	2.00
COV %	10.88	11.90	11.70	12.27

Table 5.1: COV of θ_{Pmax}, comparing ccv predictive capability of LUSIE to experimental data on the LUPOE2-D engine.

	u'	ϕ	Both	LUPOE
Mean (bar)	57.27	55.01	56.77	56.40
Max (bar)	63.72	64.63	66.47	65.30
Min (bar)	42.39	34.47	41.87	47.89
σ (bar)	4.02	7.48	5.89	4.41
COV %	7.01	13.85	10.37	7.78

Table 5.2: COV of P_{max}, comparing ccv predictive capability of LUSIE to experimental data on the LUPOE2-D engine.

when altering ϕ, even though as discussed earlier, variation in ϕ had the weakest correlation to experiment in terms of a linear fit to P_{max}, θ_{Pmax}. Looking at the maximum and minimum values though it is clear to see that the dataset has a smaller scatter. The COV value for variation in the rms turbulent velocity shows the least correlation with experimental data, though this is likely to be cause by the comparatively small horizontal spread of values at any given P_{max}. Combining both rms turbulent velocity and ϕ results in closer COV values for θ_{Pmax}. The COV value is brought closer to experimental values because of the offset of ϕ Similarly for P_{max} in Table 5.2 the lowest COV is seen for the rms turbulent velocity case and the highest for the ϕ case.

5.4 Normally aspirated production engine variability

The data acquisition capability of the naturally aspirated production engine allowed for a far greater number of consecutive cycles to be captured vis-á-vis the LUPOE2-D engine. In these tests, 1000 consecutive cycles were captured with a resolution of 0.1^oCA for the pressure measurement. Three hundred crank-resolved in-cylinder pressure cycles from the 1000 cycle dataset can be seen in Figure 5.14.

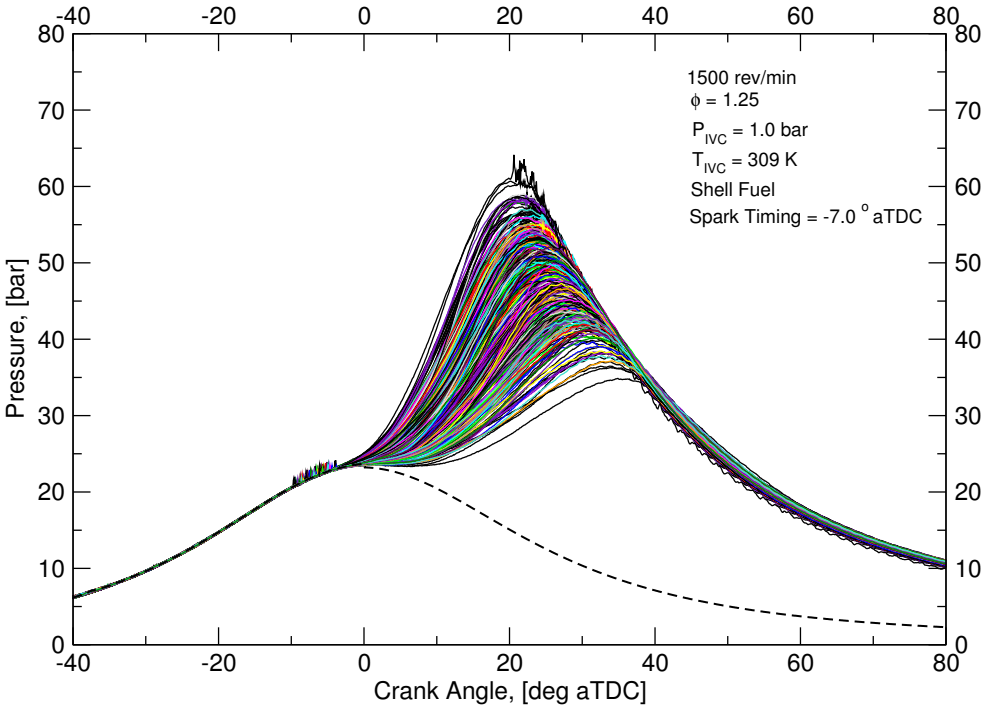

Figure 5.14: Three hundered cycles from the 1000 cycle set captured within the AJ133 engine operating at full load, low speed conditions. Ignition timing was set to MBT; rich operating condition is fixed by calibration requiring component protection.

It can be seen in Figure 5.15 that the middle cycle predicted by LUSIE falls within the middle cycles captured experimentally, in terms of both peak pressure and pressure rise. The validation of this middle cycle can be found in Section 4.3.2. The rate of pressure rise, however, appears to be higher than that seen experimentally during the main to late burn phase, resulting in a higher peak pressure at an earlier crank angle. The arithmetic range (P_{max} - P_{min}) between fast-to-slow cycles appears to be similar for the AJ133 and LUPOE engines for the 1500 rev/min case, though slower cycles, in the AJ133 engine (described in Section 3.6.5 are slower than for the LUPOE2-D engine. It is difficult to directly compare the two engines because of the rich running conditions of the AJ133, which under full load, at 1500 rev/min, is operating at $\phi = 1.25$. In addition it has also been shown Samuel et al. [2010] that GDI engines generally have higher cycle-to-cycle variations than throttle-body-injection or port-fuel-injection engines and as such, cycle-to-cycle variations in the production engine are likely to be more than the LUPOE2-D research engine with its needle fuel system, by the nature of its fuelling system.

The distribution of the 1000 captured cycles can be seen in Figure 5.17 & 5.18, from which it can be determined that the random distribution is Gaussian, specifically for P_{max} which, with a larger quantity of cycles captured vis-á-vis the LUPOE2-D, more closely represents the Gaussian distribution profile. The distribution of θ_{Pmax} has significantly

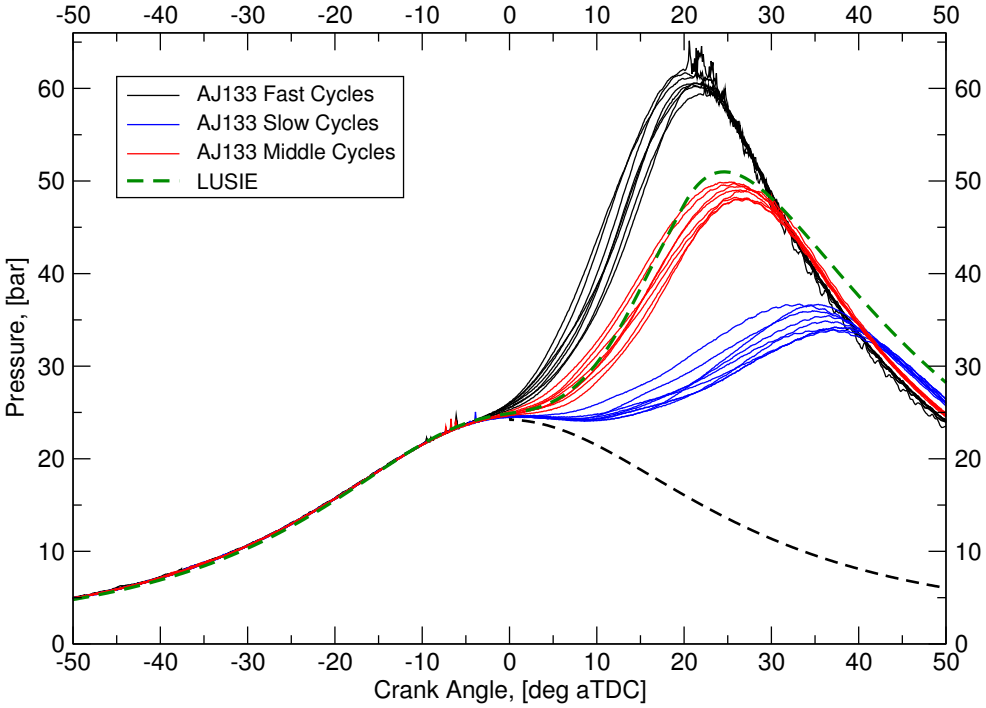

Figure 5.15: Fast, middle and slow cycles from a dataset of 1000 concurrent cycles taken in the AJ133 engine. Compared to a predicted cycle with LUSIE.

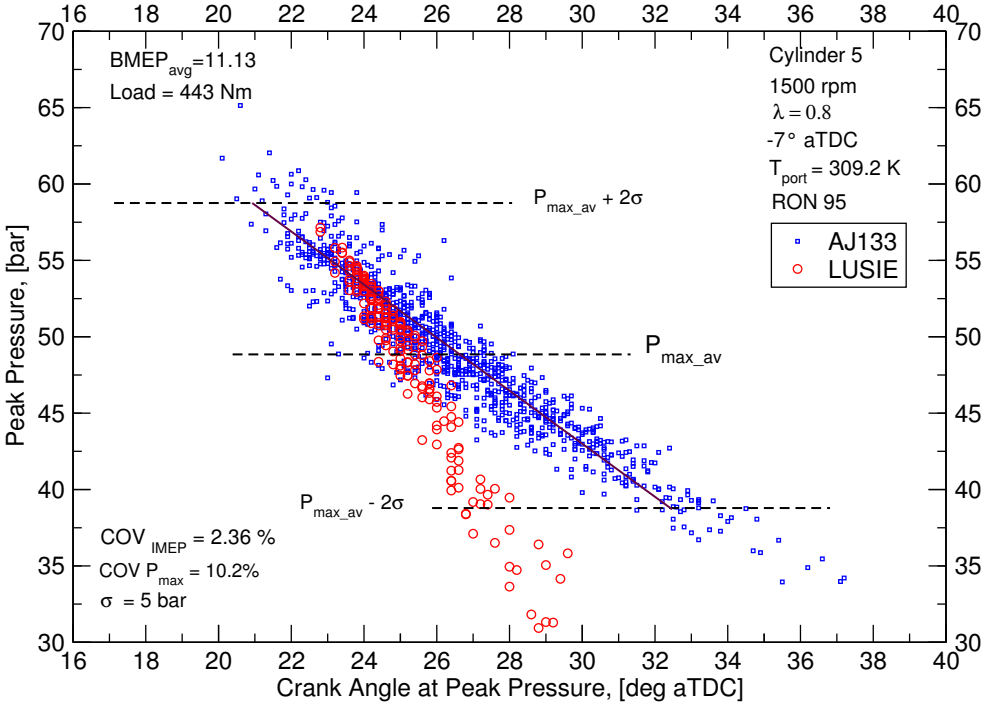

Figure 5.16: The maximum pressure distribution for the AJ133 engine over 1000 cycles compared with 200 cycles predicted with LUSIE. NB the rich equivalence ratio for this case.

lower occurrences of early θ_{Pmax}, fast cycles, compared to slower cycles with a later Pθ_{max} ; reasons for the disparity are discussed later in this section.

Attempts to model the variation in the AJ133 engine were made following the same method as was used for the LUPOE2-D engine, that being a variation of 12.5%$\sigma_{u'}$ and 5%σ_{ϕ}. The acquisition system for the AJ133 enabled the possibility to log 1000 consecutive cycles without interruption. Figure 5.16 contains P_{max} vs θ_{Pmax} data for 1000 experimental cycles compared with only 200 predicted cycles with both ϕ and rms turbulent velocity parameters varied, owing to the increased computational time required when using the GGEOM lookup table (see Section 3.2.12), predictions were limited to 200 cycles. It can be seen that the change in the slope between experimental and simulated data plots is similar to the change seen in the LUPOE2-D engine, that is the fast and middle cycles are in-line with experimental results, while slower cycles are occurring too early. The fastest cycles seen experimentally are not predicted by LUSIE; this is likely to be because of the occurrence of knock in the AJ133 engine for the fastest cycles giving a higher pressure than would be seen with 'normal' combustion, pressure oscillations indicative of knock can be seen in Figure 5.15 in the fastest cycles.

Of interest, though not modelled owing to LUSIE not predicting the intake and exhaust portions of a typical engine cycle, was the influence of a given n^{th} cycle on the following cycle (n+1).There appears to be, in the AJ133 engine a repeated pattern for sets of continuous cycles which appears a number ofl times throughout the 1000 cycles dataset as can be seen in Figure 5.19. The pattern consists of a small increase of P_{max} over approximately 50 cycles, until some value threshold is reached after which there is a steep drop off on the next cycle, or at some point during the next cycles; this pattern repeats over the 1000 cycle set. The explanation for this occurrence is likely because of a calibrated knock control strategy which puts in a large amount of spark retard after a knock event, likely determined by a knock sensor. The spark retard can also be seen in Figure 5.14 where an artifact of the ignition can be seen on the in-cylinder pressure trace. After retarding the following cycle, it appears that the control strategy permits the ignition to be advanced again until some threshold value is again reached. Such a method appears to be detrimental to engine performance owning to the amount of time spent away from the optimum condition. The two variables used to account for variability in the current study should not be influenced by previous cycles, ϕ because it is a controlled parameter, and although over a period of time the global ϕ is altered to achieve the desired air-fuel ratio at a given condition, the control strategy does not affect cycle-to-cycle variability directly as the oxygen sensor data frequency would be far greater than the gap between two cycles, even at low speed. Turbulence properties

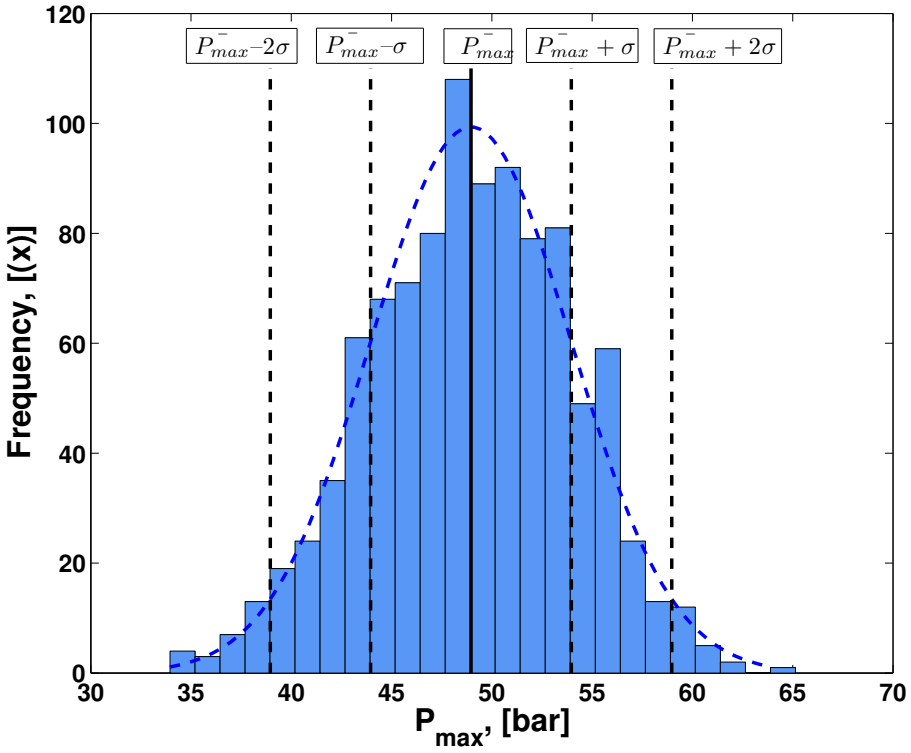

Figure 5.17: Frequency histogram with a bin size of 10 showing the distribution of P_{max} for 100 AJ133 firing cycles with the Gaussian distribution overlayed. μ = 45.75 σ = 5.

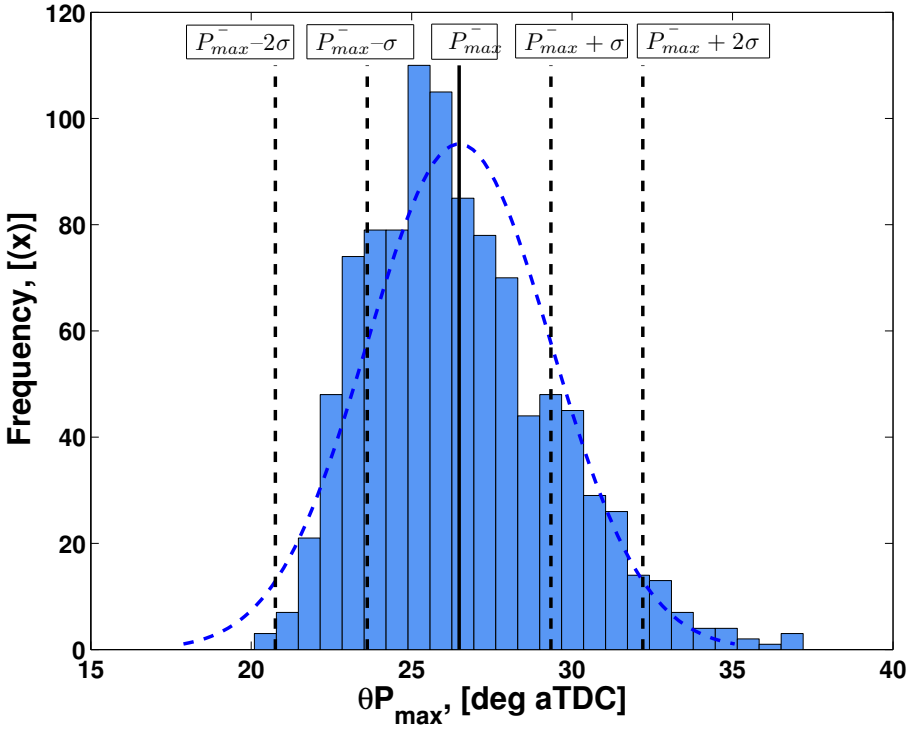

Figure 5.18: Frequency histogram with a bin size of 10 showing the distribution of θ_{Pmax} for 100 AJ133 firing cycles with the Gaussian distribution overlayed. μ = 27.0 σ = 3.0.

between cycles, should not fundamentally be dependent on one another, however it is conceivable that the global rms turbulent velocity is influenced by volumetric efficiency, itself influenced by trapped residuals from a previous cycle. P_{max} was chosen as the parameter for assessment of the dependence between two concurrent cycles.

The return map plot seen in Figure 5.20 plots the P_{max} values from a previous cycle on the x axis $P_{max_{n-1}}$ with the following cycle P_{max_n} on the y axis. It can be seen that, generally there is very little relationship between cycles, in part because of the knock control, although some observations can be made; a very high pressure cycle never follows on from a very low pressure cycle while, as previously mentioned, a low pressure cycle can follow a high pressure cycle. Generally it appears that cycles of similar magnitude follow each other. The reason for this is possibly because of residual formation from previous cycles influencing the next cycle, i.e. a slow cycle may have a high amount of residuals, leading to a slow following cycle.

5.4.1 Variability of combustion caused by variable valve lift technology

The various P_{max}, θ_{Pmax} graphs presented in this report have, until now been analysed from a numerical point of view with respect to the x (P_{max}) and y-axis (θ_{Pmax}). It should, however, be noted that the shape of the P_{max}, θ_{Pmax} scatter plot also provides information regarding cyclic variability. Assuming a Gaussian distribution of u' and ϕ then the scatter of P_{max}, θ_{Pmax} should lie within a spindle shape with the least likely cases (fastest & slowest) representing the end points of the spindle, whilst the common cases can be found in the middle of the spindle (see Figure 5.21), the crescent shape is also sketched here for future reference.

It is of interest to see if the shape of the P_{max}, θ_{Pmax} scatter plots for the AJ133 engine, over the engine operating speed range resembles closely a spindle-shaped distribution. The plots for engine speeds of 1500-3000 rev/min can be seen in Figure 5.22. Figure 5.23 displays the same type of plot but for engine speeds ranging from 4000-6000 rev/min. One observation that can be made is that at lower engine speeds (1000-2500 rev/min), the P_{max}, θ_{Pmax} plots have a more crescent-like appearance, in that they are asymmetrical around the line of best fit for the data. At higher engine speeds the plot shape changes, becoming more symmetrical around the would be line of best fit axis and become more like a spindle. From Figure 5.13 it was determined that the low occurrence cases are those represented by cases where u' is maximum while ϕ is minimum. If this

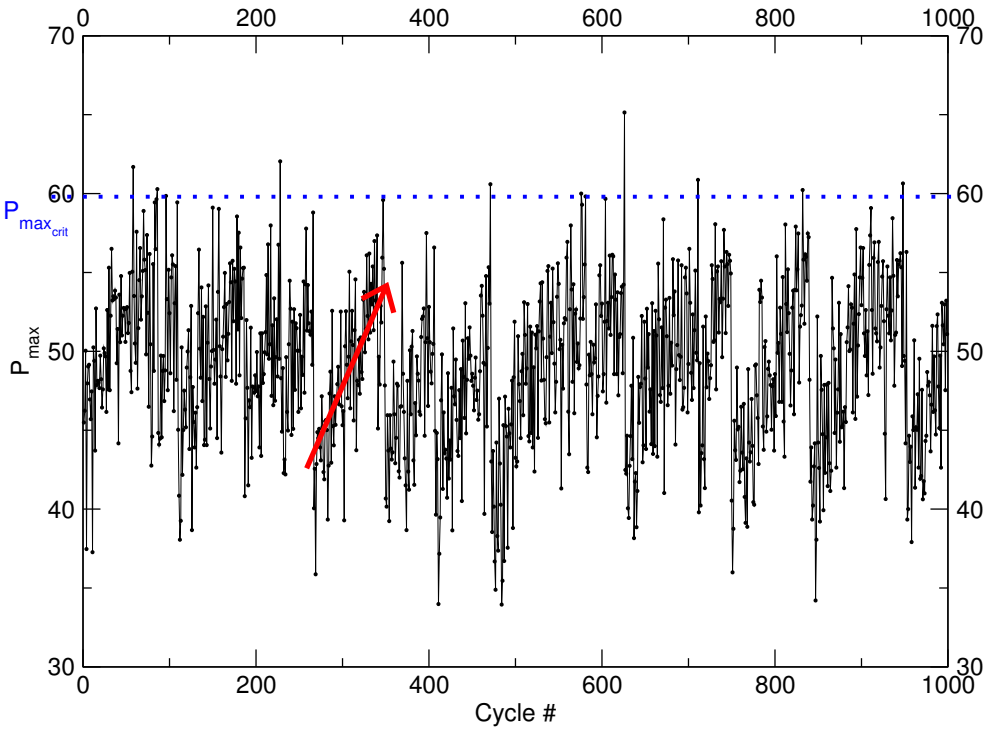

Figure 5.19: Consecutive firing cycles captured within the AJ133 engine. The observable pattern is highlighted by the red arrow showing a general increase in P_{max} with cycle until a threshold is reached.

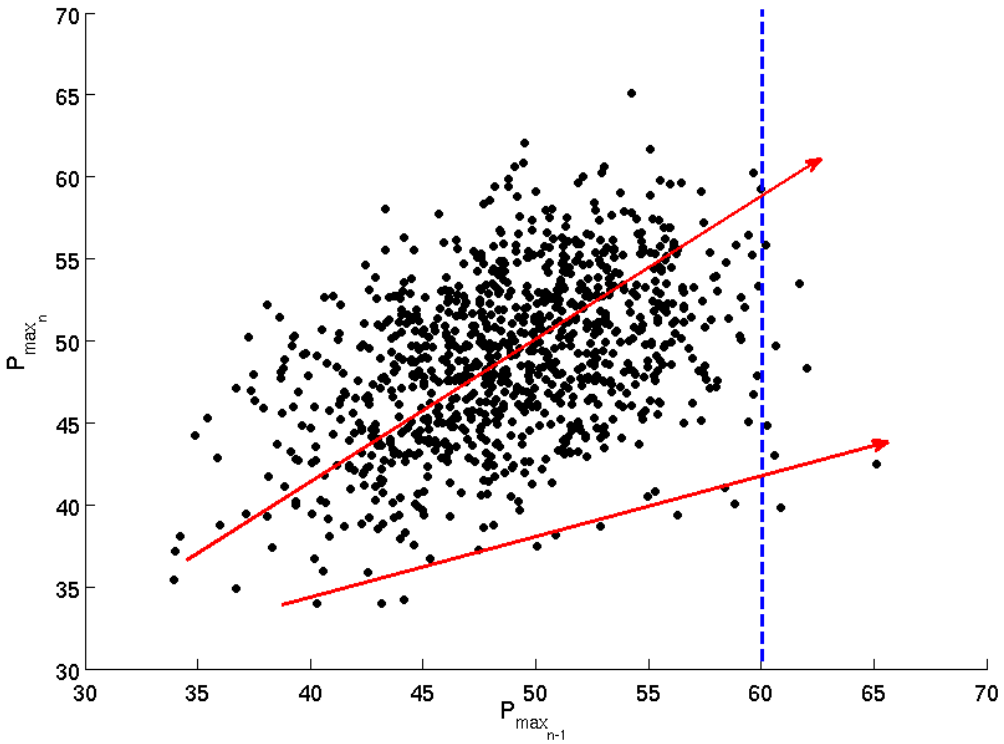

Figure 5.20: Return plot of P_{max} for 1000 firing cycles in the AJ133 engine. The 60 bar threshold is imposed on the plot. There are two distinct lines of best fit which can be extracted from this plot, these have been highlighted in red.

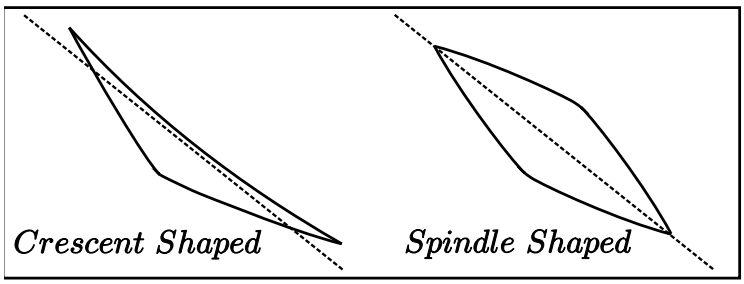

Figure 5.21: Definition of shapes used in text for describing the distribution of maximum pressure graphs.

prediction is correct then the hypothesis is that the asymmetry seen in the low-speed AJ133 P_{max}, θ_{Pmax} scatter plots is because of either, the lack of, high u' cycles or the lack of cases where ϕ is minimum; the occurrence of this asymmetry occurring only at low speeds gives an insight into the possible cause, discussed below.

Information regarding the equivalence ratio can be extracted from the testbed logs, it can be seen in Figure 5.24 that under wide-open-throttle (WOT) conditions the engine is running with a rich ($\phi > 1$) mixture[1] and that the already rich operation could influence the occurrence of the richer cycles, through "natural" variability; as all cycles are already, on average, rich and hence further fuel addition would slow cycles owing to the lower associated u_l. There does not appear to be a definite change in the air-fuel ratio log that would cause the definite change in shape of the P_{max}, θ_{Pmax} scatter plots after 2500 rev/min however. A more likely cause is the camshaft technology on the engine (described in Section 3.6.5) which involves switching from a low-lift to a high-lift cam profile at 2700 rev/min (under WOT conditions), see Figure 5.25. The valvetrain strategy results in 5.5 mm of valve lift up until 2700 rev/min, after which, at full load, it increases to 10.5 mm by 2900 rev/min, the P_{max}, θ_{Pmax} scatter plots show a distinct change in shape between 2500 and 3000 rev/min where this camshaft lift profile changes. The increased valve lift reduces intake velocity which has the apparent effect of increasing the propensity for cycles with unusually high rms turbulent velocity values to occur; or said alternatively, at low lift, with higher intake velocities, the propensity for high u' cases is low.

It was necessary to prove that the P_{max}, θ_{Pmax} scatter plots, were indeed spindle or crescent like, rather than just an assumption from visual analysis. The general change in shape occurs after 2500 rev/min therefore a case before and a case after this critical speed are shown in Figures 5.26 and Figures 5.27. Here, only the maximum and minimum P_{max}

[1]It is common for production engines to run rich at WOT and high engine speeds for component protection by reducing exhaust gas temperatures.

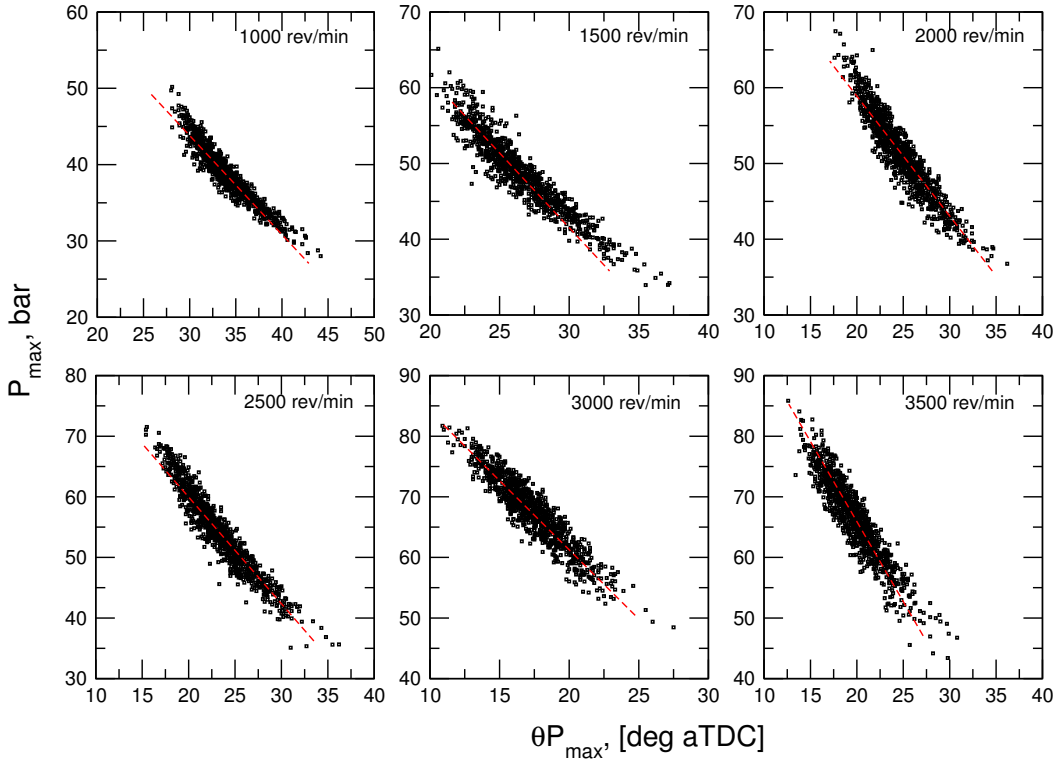

Figure 5.22: The maximum pressure distribution for six full load engine speed cases from 1000-3500 rev/min in 500 rev/min increments captured in the AJ133 engine. Each speed condition contains 1000 cycles.

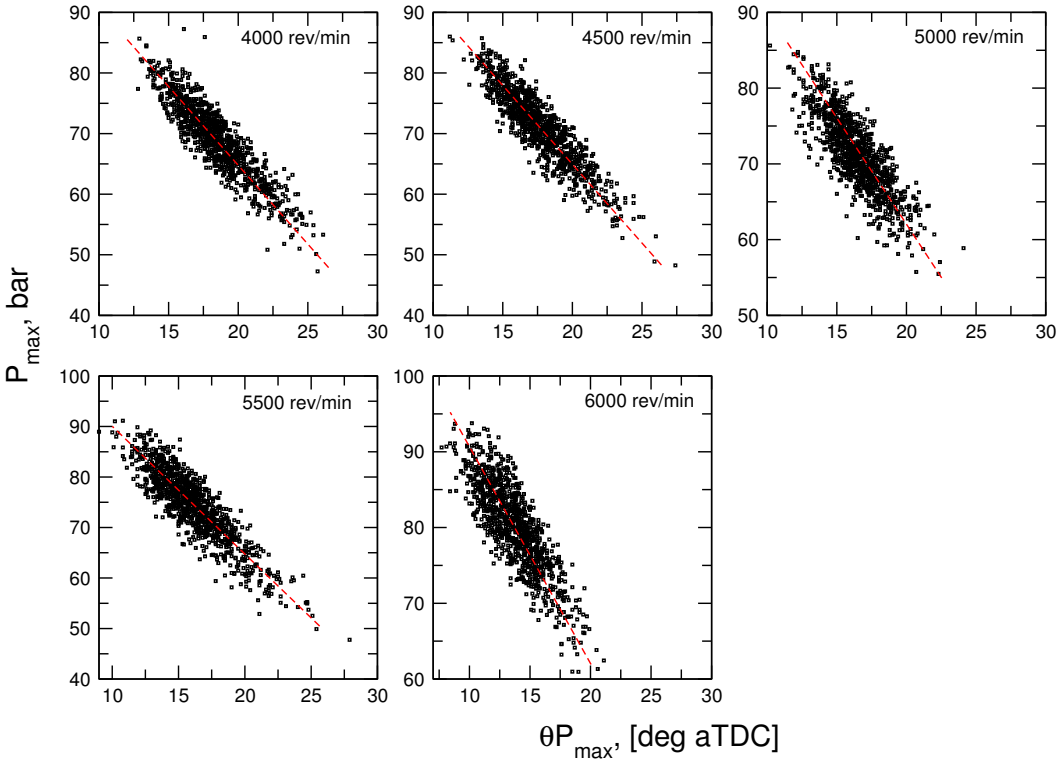

Figure 5.23: The maximum pressure distribution for five full load engine speed cases from 4000-60000 rev/min in 500 rev/min increments captured in the AJ133 engine. Each speed condition contains 1000 cycles.

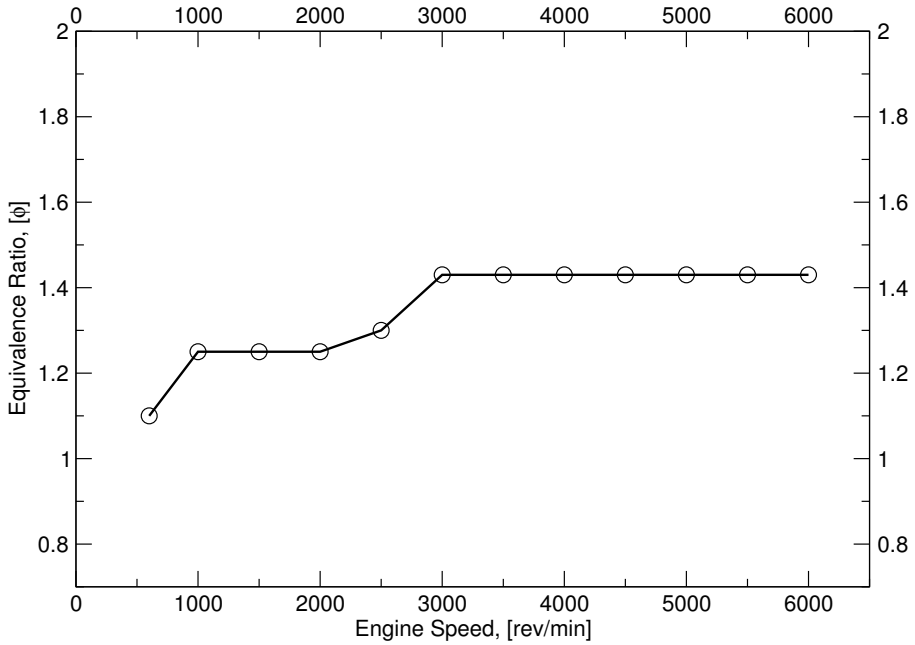

Figure 5.24: The equivalence ratio, ϕ, within the non-boosted production engine, as a function of engine speed. All cases at WOT were run rich because of the calibration dictating engine cooling at this condition.

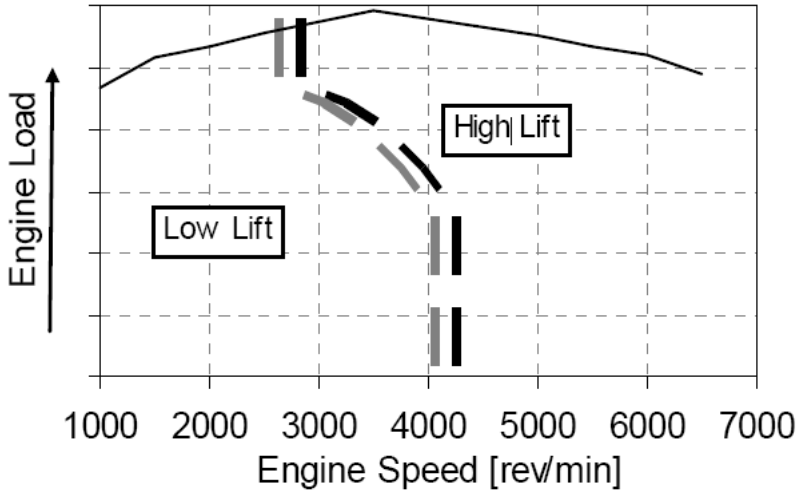

Figure 5.25: The intake valve lift strategy operating within the non-boosted production engine. For this study, only full engine load operation was investigated, the switching point can therefore be seen close to 3000 rev/min with the actual value being 2700 rev/min. The image has been taken from Sandford et al. [2009].

values for any given θ_{Pmax} were taken to give an outline of the shape. The second degree, least squares regression lines of best fit were applied to both the maximum (y_{max}) and minimum (y_{min}) datasets and the corresponding equations of the lines are added. For the case of the 1000 rev/min case they are:

$$y_{max} = 0.02x^2 - 2.765x + 110.6 \tag{5.2}$$

$$y_{min} = 0.05x^2 - 4.62x + 136.2 \tag{5.3}$$

Differentiating the two equations twice leaves the second derivative (double the original x^2 value). If the term representing the maximum values is divided by the minimum, then a single value remains, this value is referred to as the shape factor. A positive shape factor denotes a crescent shape and that the maximum line is concave. A negative shape factor shows that the maximum line is convex and thus the shape is more spindle like. A shape factor of -1 would represent a perfectly symmetrical shape.

The shape factor method was repeated for all engine speed cases for the 1000 cycle logs on the AJ133 engine to prove the observation of changing variability performance. It can be seen in Figure 5.28 & Figure 5.29 that the P_{max}, θ_{Pmax} scatter plots at different engine speeds conform to the predicted spindle, or crescent shapes based on the position of the speed and load dependent valve-lift profile, i.e. that after the valve-lift switch, spindle shapes are dominant.

The increase in engine speed results in faster combustion, in terms of crank angle, because of increased turbulence. An increase in the rate of combustion should bring about a reduction in variability because of lower residency times for different processes, such as heat transfer for example. It can be seen in Figure 5.30 that the COV_{imep} decreases generally with an increase in engine speed; the same can be said for P_{max}. Of note for $COV_{P_{max}}$ is the sporadic increase in COV from 3000-3500 rev/min and 5000-5500 rev/min as well as the general increase in COV from 1000-2500 rev/min, an event which coincides with the low lift cam event.

5.5 JLR downsized research engine variability

The prediction performance of the cyclic variability model has, up until now been compared with what are, essentially, naturally aspirated engines operating at intake pressures

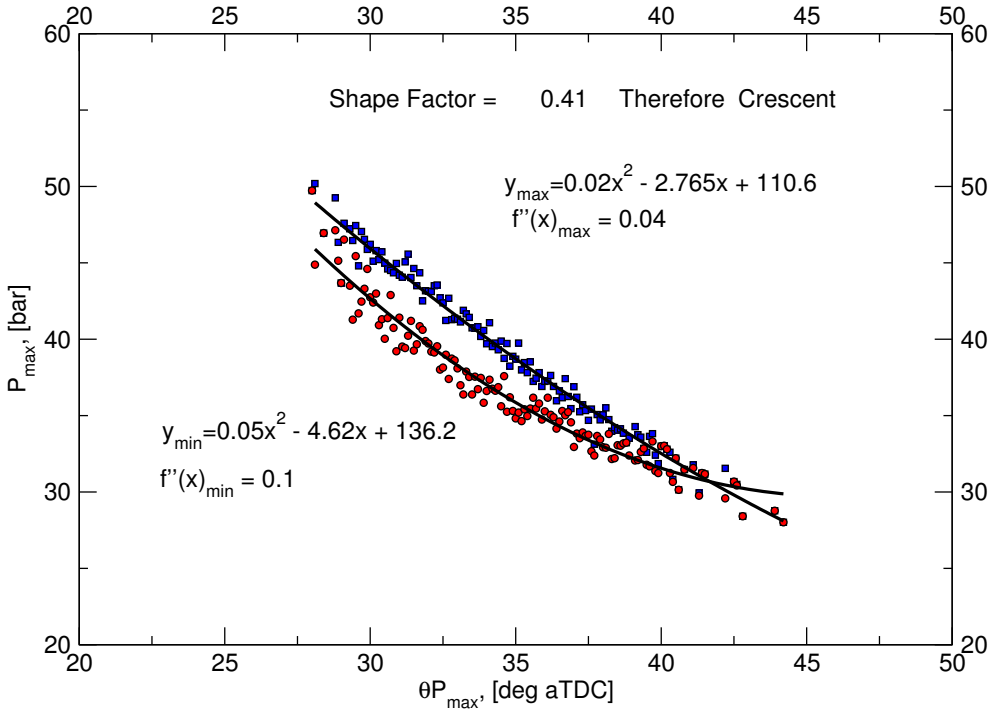

Figure 5.26: The maximum and minimum values of maximum pressure, at a given crank angle for the 1000 rev/min case in the AJ133 engine with a least squares line of best fit to maximum and minimum data, showing the positive shape factor and distinct crescent shape.

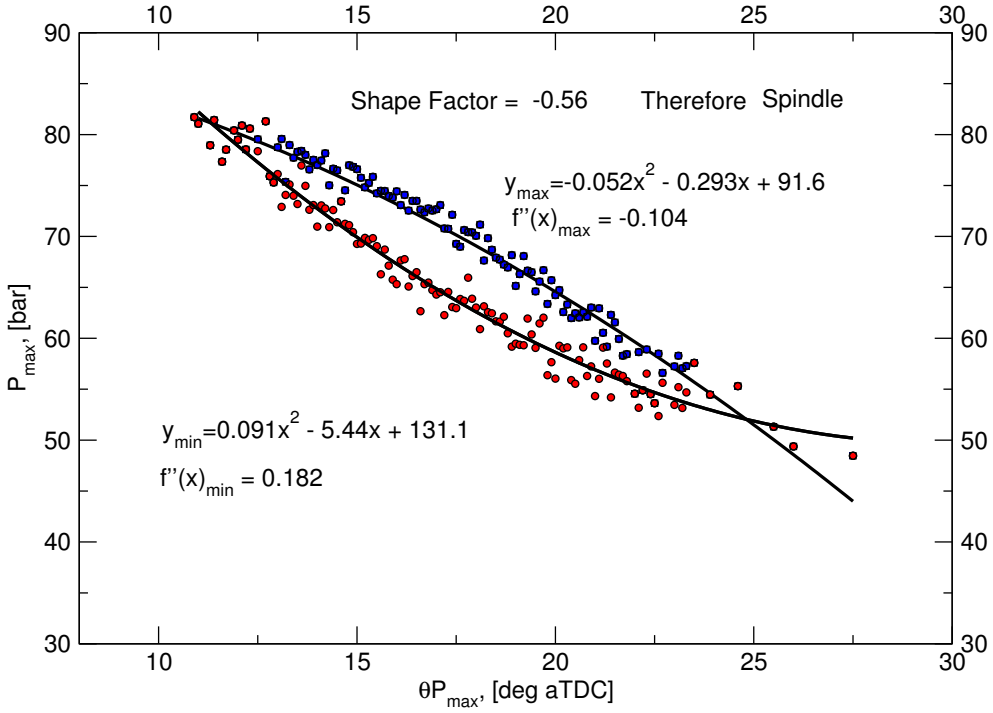

Figure 5.27: The maximum and minimum values of maximum pressure, at a given crank angle for the 3000 rev/min case in the AJ133 engine with a least squares line of best fit to maximum and minimum data, showing the negative shape factor and distinct spindle shape.

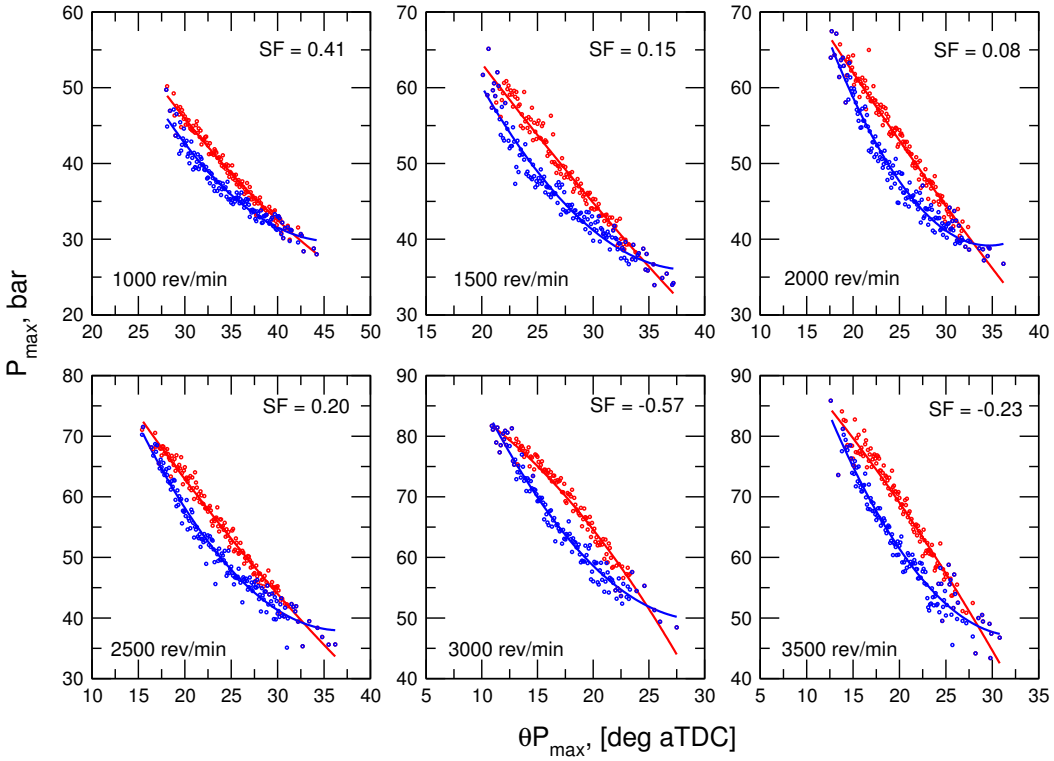

Figure 5.28: The maximum and minimum values of maximum pressure, at a given crank angle for engine speed cases from 1000-3500 rev/min in the AJ133 engine with a least squares line of best fit to maximum and minimum data, the shape factor is included in each case.

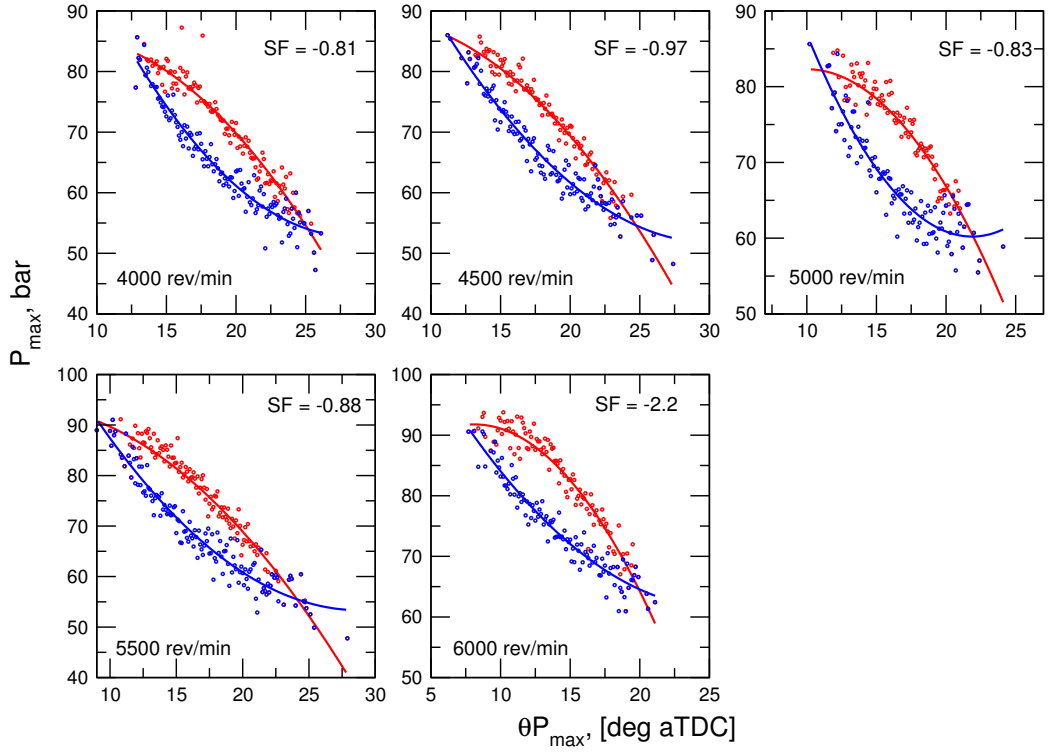

Figure 5.29: The maximum and minimum values of maximum pressure, at a given crank angle for engine speed cases from 4000-6000 rev/min in the AJ133 engine with a least squares line of best fit to maximum and minimum data, the shape factor is included in each case.

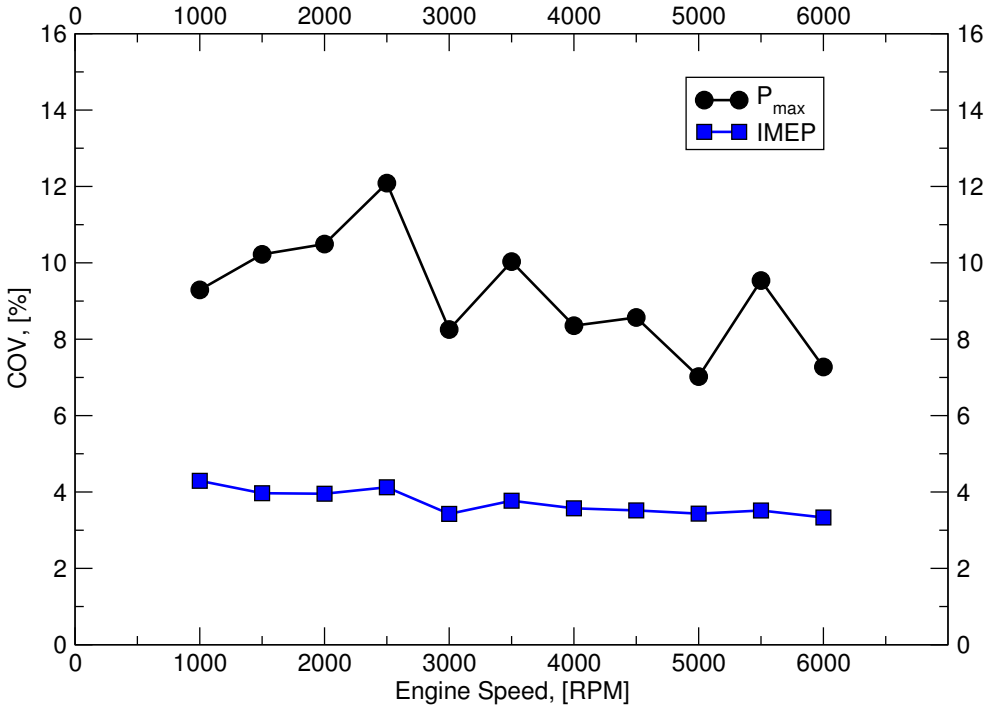

Figure 5.30: The influence of engine speed on the coefficient of variance of IMEP and maximum pressure for the AJ133 engine.

close to ambient conditions of approximately 1 bar. The ability of the LUSIE to predict variability at higher pressures, as would be found in downsized engines, is of interest. The data collected from the Jaguar Land Rover downsized research engine (UB100) contained 100 continuous cycles at both a high and low pressure condition. Combined with the fitted middle cycle as predicted by LUSIE to each condition (discussed in Section 4.3.1), it was possible to assess the variability model fidelity at intake pressures higher than 2.5 bar, and intake pressures less than 1.5 bar, using the same engine hardware.

Shown in Figure 5.31 are 100 experimentally captured cycles from the UB100 engine at high pressure conditions. Two cycles within this set exhibited signs of pre-ignition, with one featuring a 'super-knock', post pre-ignition event; these two cycles were omitted from further statistical analysis. The 100 cycles captured at the low intake pressure condition can be seen in Figure 5.32, no pre-ignition events were observed within the 100 captured cycles at this condition. For both high and low pressure conditions, spark timing was set to MBT so as to ensure alignment with testing on both the LUPOE2-D, LUPOE2-D boosted and AJ133 engines.

The random distribution of cycles for the 100 captured high pressure UB100 cycles can be seen in Figure 5.33 & 5.34, from which it can be determined that the distribution of the maximum pressure is fairly close to Gaussian. A similar trend is observable with the

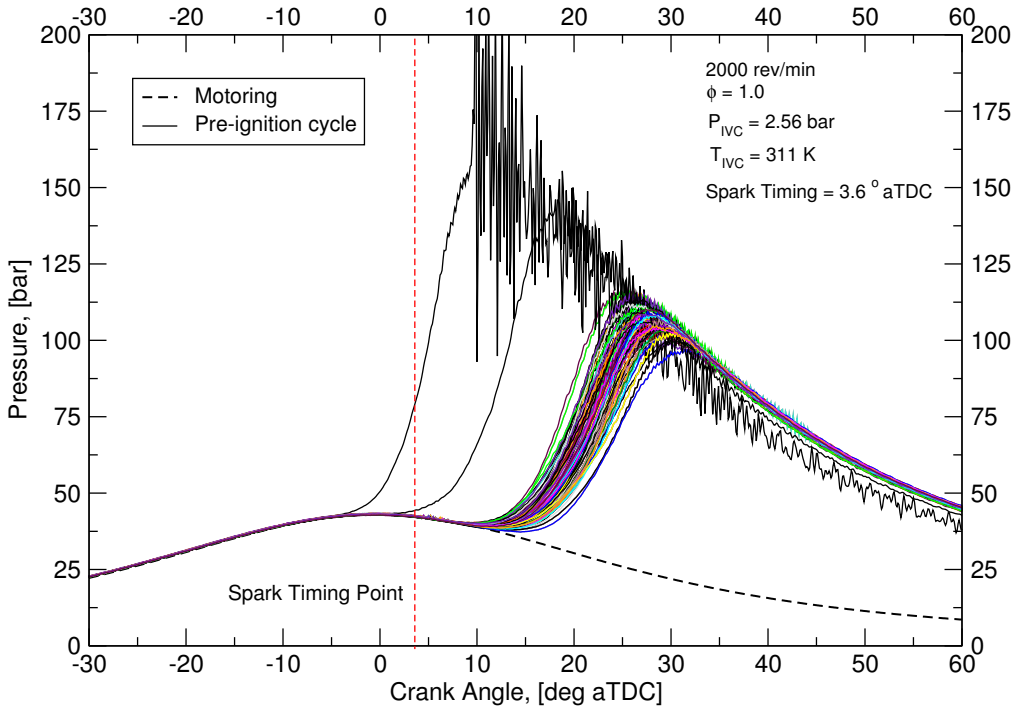

Figure 5.31: One hundred cycles captured within the UB100 engine, the operating conditions are set for high-pressure operation with a high intake pressure. Spark timing is set for MBT.

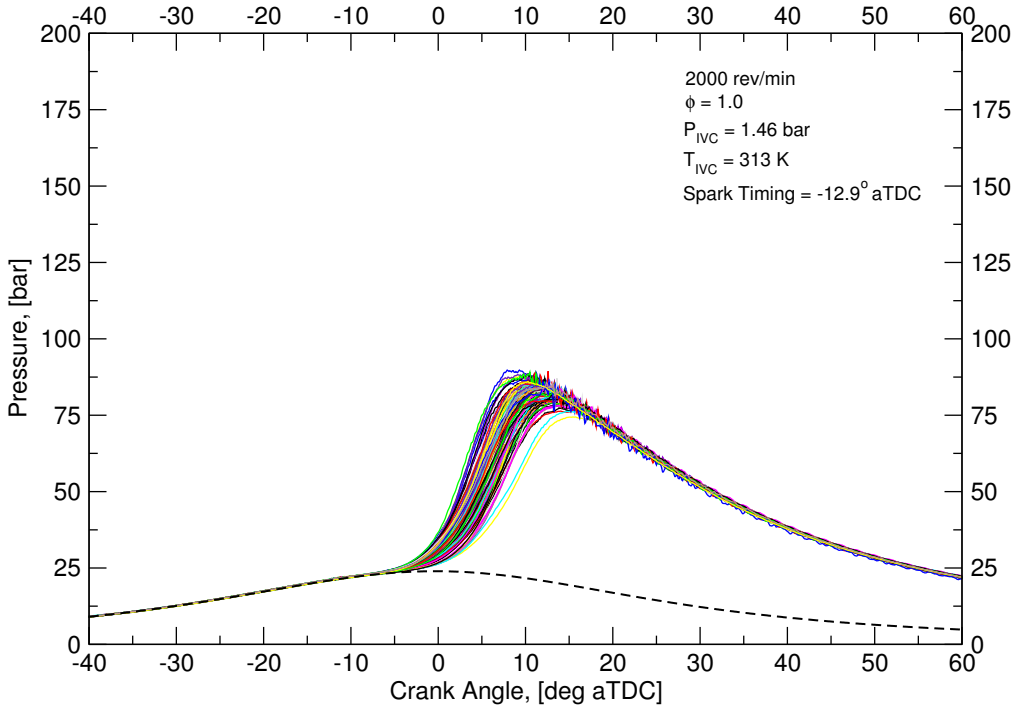

Figure 5.32: One hundred cycles captured within the UB100 engine, the operating conditions are set for low-pressure operation with a low intake pressure. Spark timing is set for MBT.

low pressure condition seen in Figure 5.35 & 5.36. The small size of the dataset prevents an ideal Gaussian distribution being formed.

It can be seen in Figure 5.37 that, with the 5% σ_ϕ and 12% $\sigma_{u'}$ variability imposed, the predicted cycles are in good agreement, in terms of both P_{max} and θ_{Pmax} with those captured experimentally. The slope of the P_{max}, θ_{Pmax} plots appears to be in better agreement than in either the LUPOE2-D or AJ133 engines and that the prediction of the slowest cycles, although slower than seen experimentally, is not as overly slow as those predicted for the LUPOE2-D and AJ133 engines. The Gaussian nature of the cycles appears to be present in the UB100 engine, though these are seen experimentally and not predicted as with the AJ133 engine. The high pressure predictions and experimental data can be seen in Figure 5.38. It can be seen here that the slope of the plot appears to be in agreement with experimental data, though the data spread predicted does not display the large spread of P_{max}, θ_{Pmax} points at slow cycles as seen in the low pressure UB100 and AJ133 cases, the spread also appears to be more Gaussian than in either of the previous cases; the experimental data, as with previous engines and conditions, conforms to Gaussian distribution. The predicted cycles appear to have higher pressure than seen experimentally, though this can be attributed to errors in the mean cycle rather than an error in the variability modelling itself. The greater scatter of P_{max}, θ_{Pmax} can be seen in the crank-resolved predictions seen in Figure 5.39. It is apparent that the method of variability which was applied, with good correlation, to the LUPOE2-D and non-boosted production engine does not have such strong correlation when a) applying the same variability to the UB100 engine, even at low pressure, b) applying the variability to high pressure conditions, where the predicted variability accuracy appears to decrease.

The variability between the experimentally measured results and predicted results for the high pressure and low pressure condition can be viewed in Table 5.3. It can be seen that the a reduction in COV for θ_{Pmax} is seen both experimentally and through predictive techniques when the operation changes from low pressure to high pressure; also clear is that the predicted COV is significantly greater compared to experimentally gathered data. In addition the θ_{Pmax} values for the low pressure condition are, on average, quite close to TDC, or when $\theta = 0$. Possible issues appear to arise with using the COV in relation to θ_{Pmax} as it is not a ratio[1] variable, as $\lim_{\bar{\theta}\to 0}$ COV=∞, which is clearly undesirable. It would appear that calculating the COV for θ_{Pmax} when the $TDC_{combustion}$ is referred to as 0 is not acceptable. Hence, in this instance it was decided to offset the θ_{Pmax} values by 360^o to increase the mean value. This has the unsurprising effect of reducing the COV, as

[1]A ratio variable is a type of continuous variable which has a clear definition of the 0 point for that variable. For example when temperature or pressure (both ratio variables) = 0, there is no temperature or pressure.

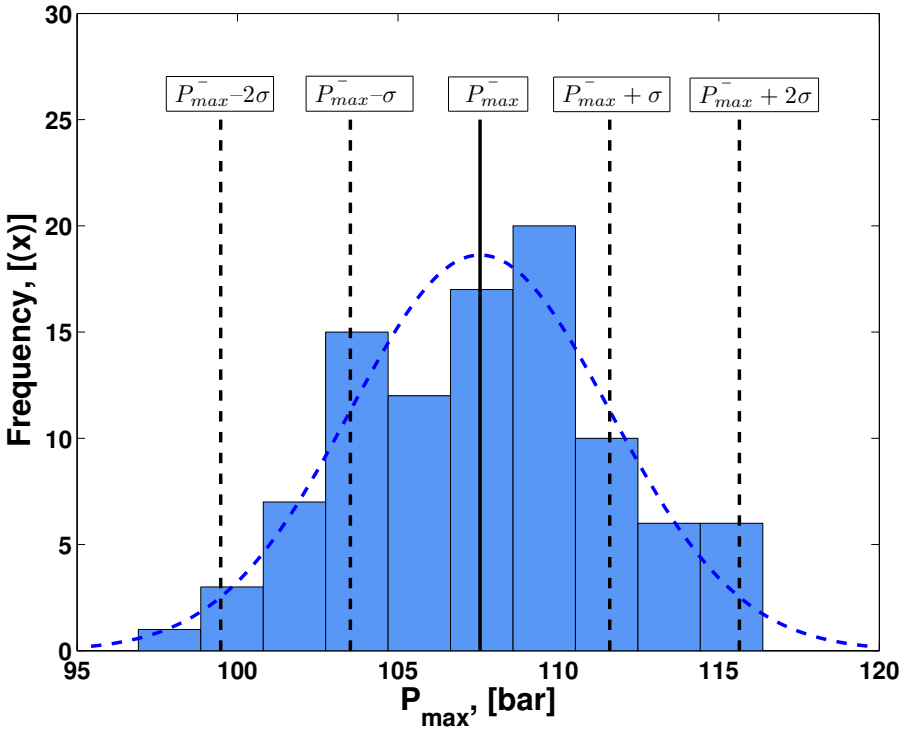

Figure 5.33: Frequency histogram with a bin size of 10 showing the distribution of P_{max} for 100 UB100 high pressure firing cycles with the Gaussian distribution overlayed. μ = 107.8 σ = 4.8.

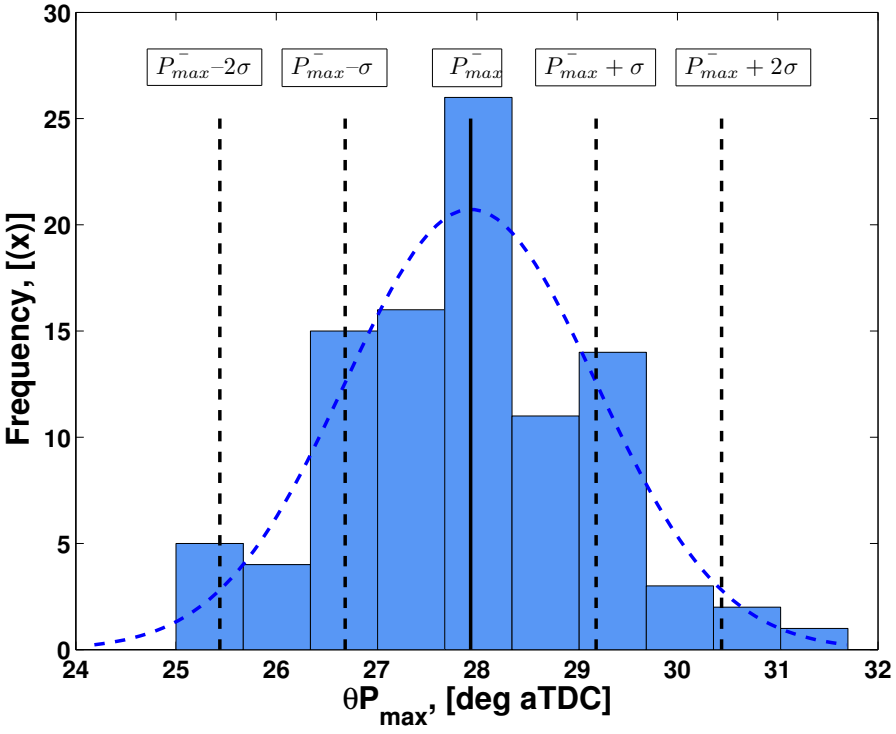

Figure 5.34: Frequency histogram with a bin size of 10 showing the distribution of θ_{Pmax} for 100 UB100 high pressure firing cycles with the Gaussian distribution overlayed. μ = 27.9 σ = 1.4.

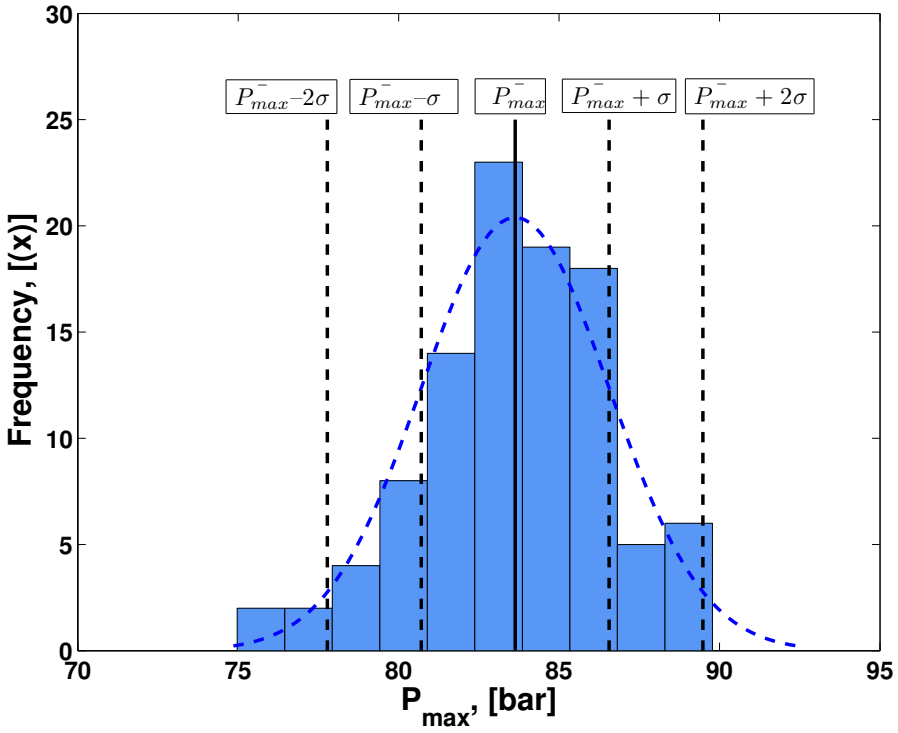

Figure 5.35: Frequency histogram with a bin size of 10 showing the distribution of P_{max} for 100 UB100 low pressure firing cycles with the Gaussian distribution overlayed. μ = 83.6 σ = 2.93.

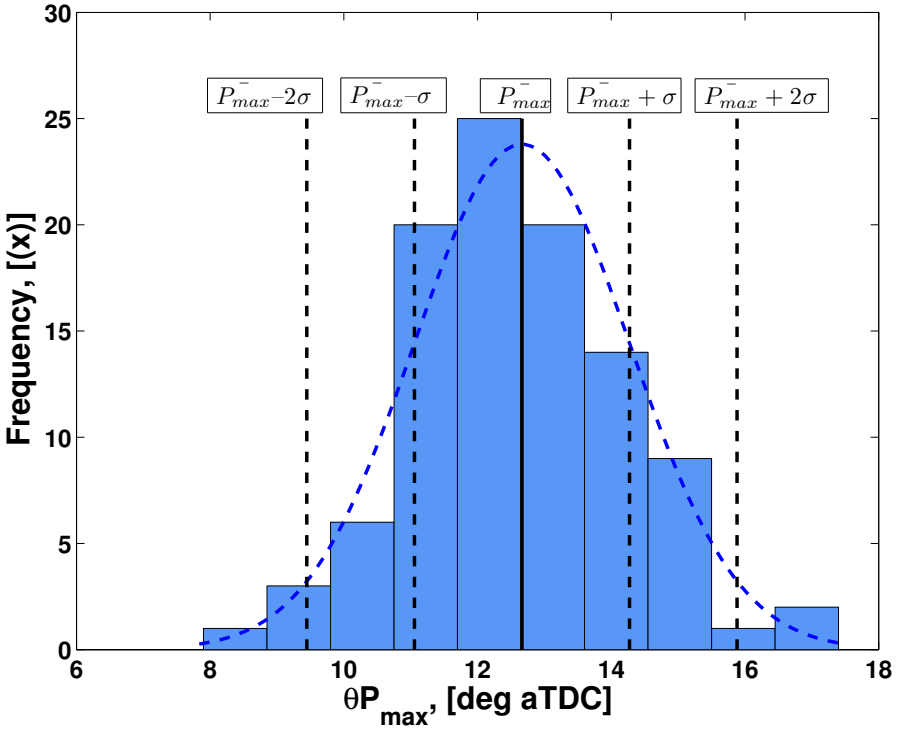

Figure 5.36: Frequency histogram with a bin size of 10 showing the distribution of θ_{Pmax} for 100 UB100 low pressure firing cycles with the Gaussian distribution overlayed. μ = 12.7 σ = 1.6.

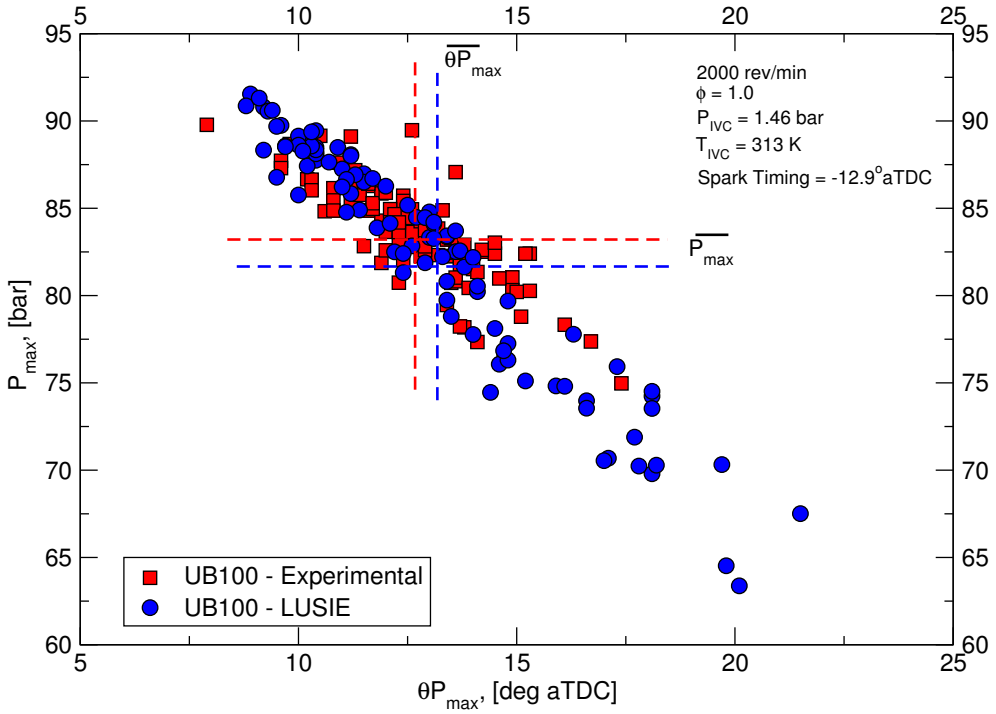

Figure 5.37: The influence of equivalence ratio and rms turbulent velocity variation on the distribution of maximum pressure for 100 cycles in the UB100 engine at low boost conditions. Variation on the equivalence ratio and rms turbulent velocity were set at 5% σ_ϕ and 12.5% $\sigma_{u'}$, respectively.

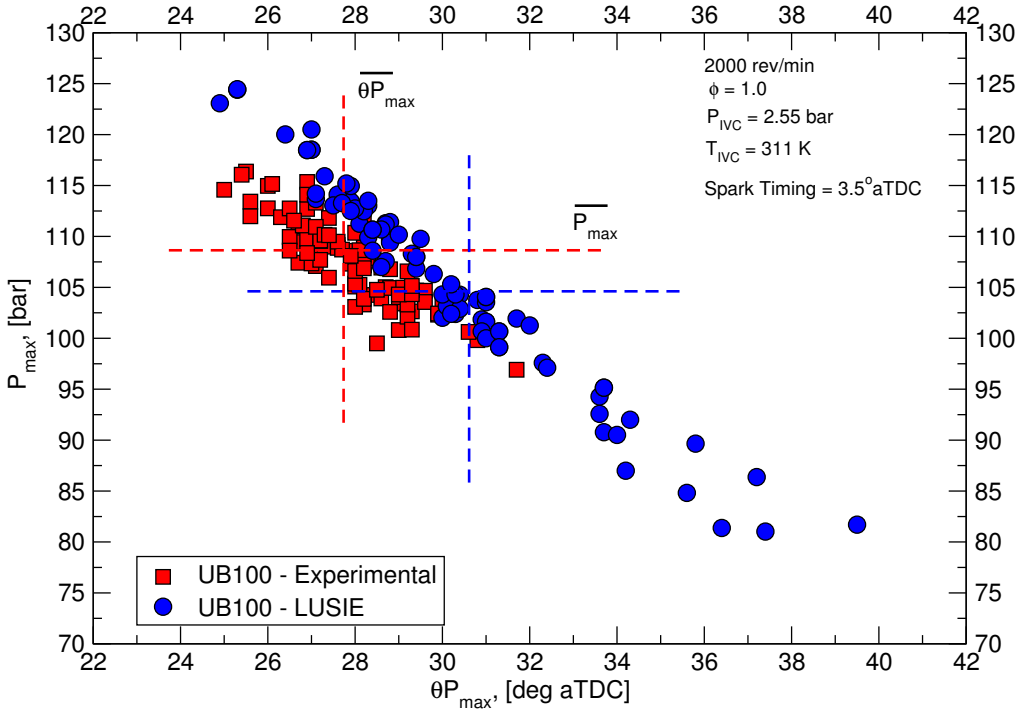

Figure 5.38: The influence of equivalence ratio and rms turbulent velocity variation on the distribution of maximum pressure for 100 cycles in the UB100 engine at high boost conditions. Variation on the equivalence ratio and rms turbulent velocity were set at 5% σ_ϕ and 12.5% $\sigma_{u'}$, respectively.

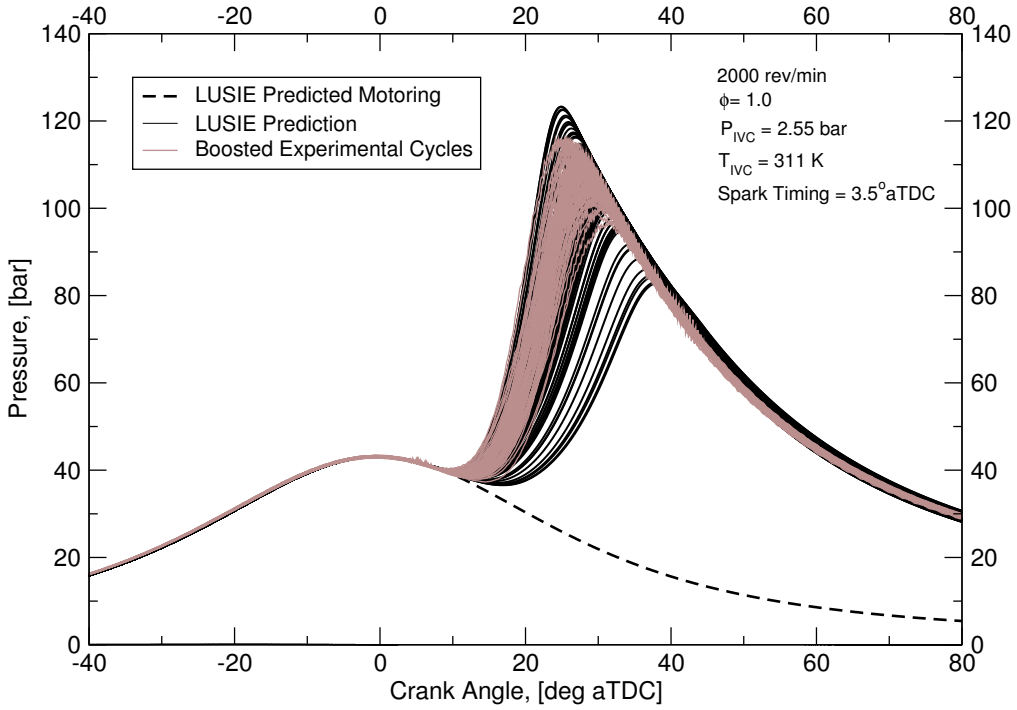

Figure 5.39: 100 crank-resolved in-cylinder pressure traces as predicted by LUSIE compared to 100 experimentally captured cycles in the UB100 engine. Operating conditions are detailed within the figure.

seen in Table 5.4, it can be concluded that it is not appropriate to compare COV values of two different parameters, such as P_{max} θ_{Pmax} as their magnitudes are different and the proximity of θ_{Pmax} to TDC leads to overly large COV values. It can be seen that the relative change in COV from the high pressure and low pressure experimental condition changes from 250% to 120% depending on which base θ_{Pmax} value is used. Interestingly the P_{max} COV is lower for the low pressure condition, a trend which is replicated by prediction; COV values for the predictions, however, are significantly higher than seen experimentally, as seen in Table 5.5.

5.6 LUPOE2-D boosted engine variability

Experimental data was captured on the LUPOE2-D boosted engine by Ling [2013] and this Section is devoted to its analysis. The operating condition of the engine was at a significantly increased intake pressure, 2 bar, vis-á-vis the non boosted configuration, 1.18 bar. Ninety cycles captured at a condition where the engine was operating close to the knock boundary can be seen in Figure 5.40. 15 of the fastest cycles were deemed to have experienced knock, or autoignition, as derived from the slope of the of the derivative of

	Low Pressure Experimental	Low Pressure Prediction	High Pressure Experimental	High Pressure Prediction
Max (bar)	17.4	24.6	31.7	39.5
Min (bar)	7.9	8.8	22.1	24.9
Mean (bar)	12.7	13.2	27.9	30.5
σ (bar)	1.6	3.3	1.4	3.4
COV %	12.7	24.85	4.94	11.3

Table 5.3: Comparison of experimental and predicted θ_{Pmax} values on the UB100.

	Low Pressure Experimental	Low Pressure Prediction	High Pressure Experimental	High Pressure Prediction
Max (bar)	377.4	384.6	391.7	399.5
Min (bar)	367.9	368.8	382.1	384.9
Mean (bar)	372.7	373.2	387.9	390.2
σ (bar)	1.6	3.3	1.4	3.4
COV %	0.43	0.88	0.36	0.80

Table 5.4: Comparison of experimental and predicted θ_{Pmax} values with 360 θ offset on the UB100.

	Low Pressure Experimental	Low Pressure Prediction	High Pressure Experimental	High Pressure Prediction
Max (bar)	89.8	91.6	133.4	124.5
Min (bar)	75.0	51.6	96.9	81.02
Mean (bar)	83.6	81.8	107.8	105.3
σ (bar)	2.9	7.6	4.8	10.4
COV %	3.5	9.3	4.5	9.9

Table 5.5: Comparison of experimental and predicted P_{max} values captured on the UB100 engine operating at both the low and high pressure condition.

the cylinder-pressure trace, a technique discussed in Section 6.5.2, in-line with the work of Roberts [2010].

The P_{max}, θ_{Pmax} distribution for all cycles, both knocking and non-knocking, can be seen in Figure 5.41. The knocking[1] cycles are highlighted and are removed from further analysis. LUSIE does not predict an accurate heat release profile after the onset of autoignition, in fact, it assumes that all remaining unburned fuel is burnt instantly. Inclusion, therefore, of such cycles in a variability study where LUSIE is not predicting autoignition cycles would skew the mean P_{max} towards the faster knocking cycles, detracting from the main focus of the variability study.

The middle cycle predicted by LUSIE (as discussed in Section 4.3.3), compared with selected, fast, middle and slow non-knocking experimental cycles, can be seen in Figure 5.42. With the middle cycle validated against middle cycles observed experimentally, as close as was permissible my combustion constant adjustment (see Section 4.35) variability was then imposed onto the middle cycle as with the LUPOE2-D, non-boosted production and UB100 engines. The variability consisted of varying the parameters of rms turbulent velocity by 12.5% of σ and the equivalence ratio by 5% of σ.

The resulting P_{max}, θ_{Pmax} distribution can be seen in Figure 5.43. A number of cycles which are slower than observed experimentally were predicted by LUSIE. The slow cycles, in part contribute to the mean P_{max} and θ_{Pmax} values which are lower and later respectively, for the prediction than those seen experimentally. The general agreement however is very satisfactory and would be further enhanced if a better match between the experimental and predicted middle cycles was achieved.

5.6.1 Comparison of all engines

A comparison of P_{max} for all engines is presented in Table 5.6. The mean P_{max} value, the standard deviation and the COV parameters have been included; it should be noted that all engines apart from the LUPOE2-D boosted were operating at MBT. It can be seen that generally the higher pressure variants of a base engine configuration appear to have a higher COV. Moreover, the P_{max} COV was vastly reduced on the UB100 engine vis-á-vis the LUPOE2-D engine despite its various strategies to reduce variability. The AJ133 engine has the highest COV of all engines and configurations. It should be noted however, the standard deviation was slightly lower on the LUOPE2-D engine compared to the high

[1]Cycles which displayed autoignition but no knocking oscillation are considered as knocking cycles here, for the sake of brevity. The implications are for either case are that the rate of pressure rise exceeds that which would be observed from a "normal" flame propagation.

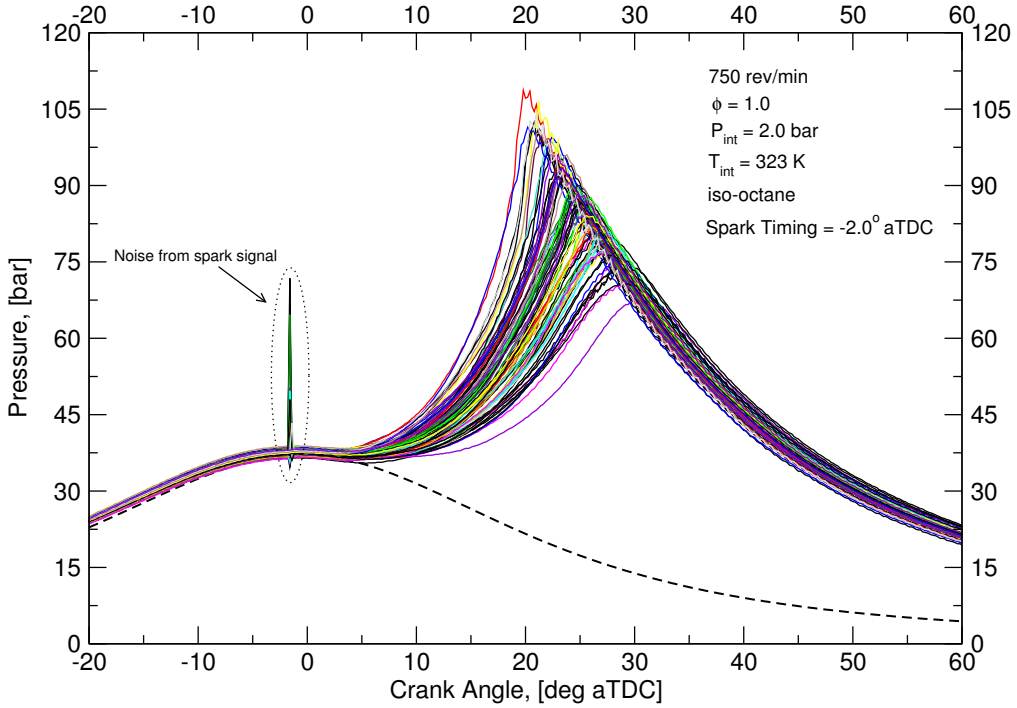

Figure 5.40: Ninety cycles captured within the LUPOE2-D boosted engine operating at the displayed conditions.

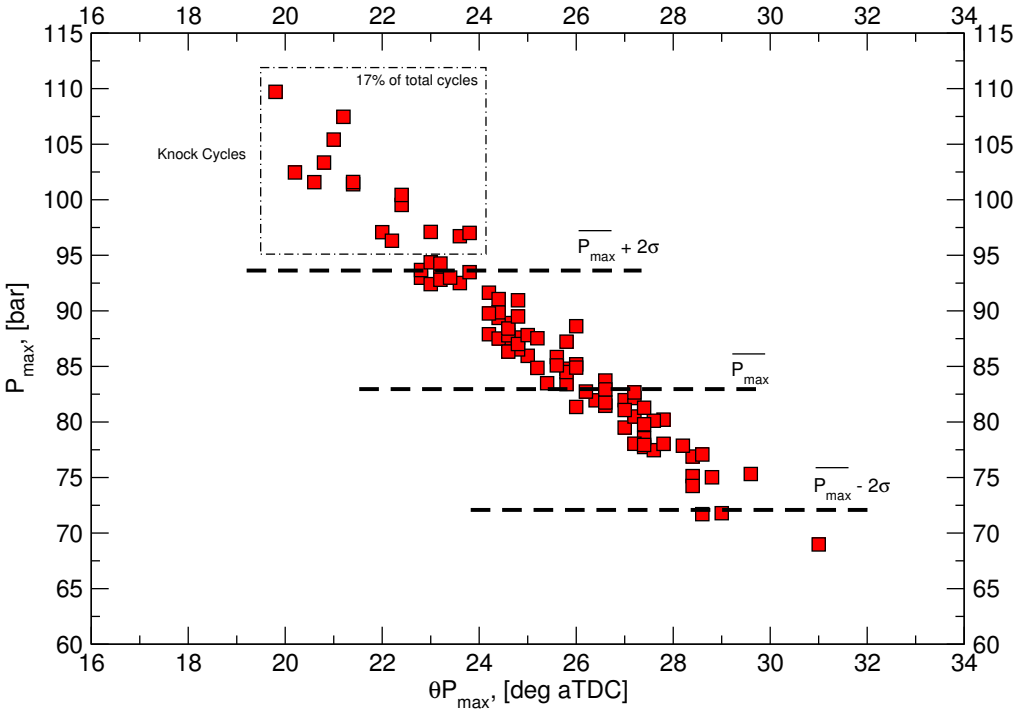

Figure 5.41: The P_{max}, θ_{Pmax} distribution of the 90 cycles from the LUPOE2-D boosted engine. Cycles identified as knocking cycles are highlighted.

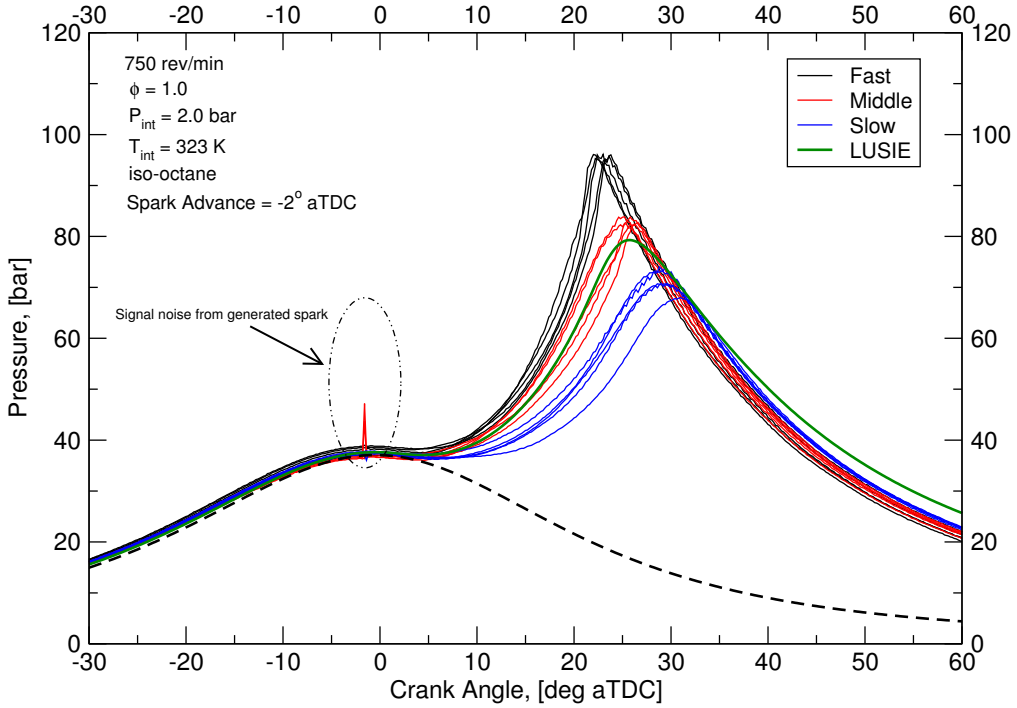

Figure 5.42: Fast, middle and slow cycles identified from the 90 cycle LUPOE2-D boosted dataset. Knocking cycles removed. A middle cycle predicted by LUSIE is also plotted.

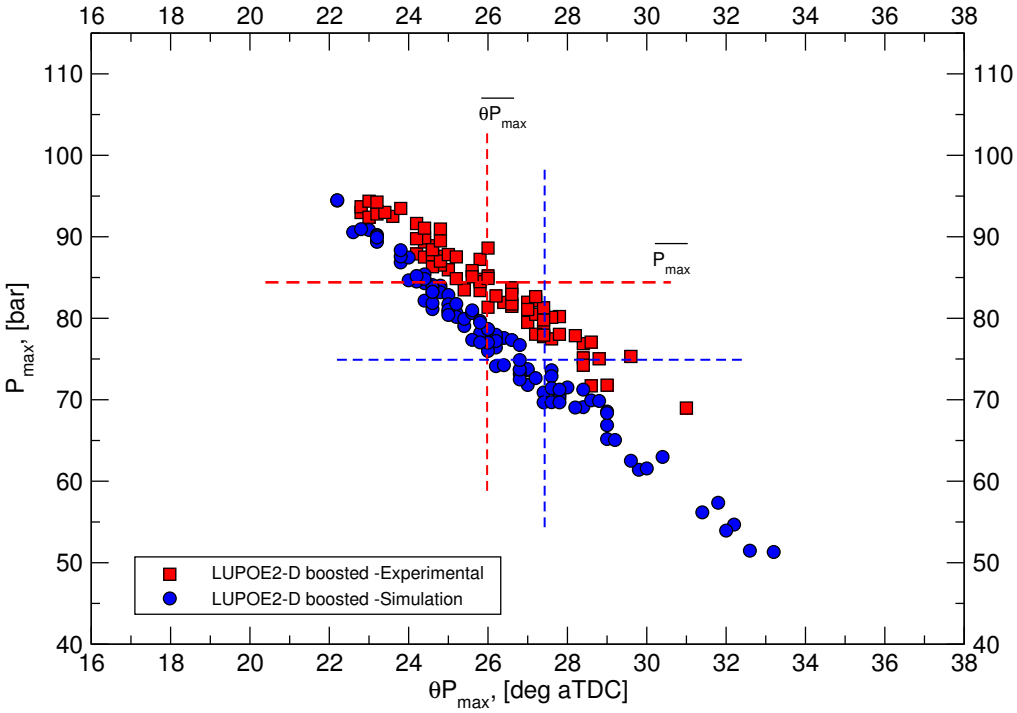

Figure 5.43: The P_{max}, θ_{Pmax} distribution of the non-knocking experimentally obtained cycles and the P_{max}, θ_{Pmax} distribution predicted by LUSIE in the dashed line.

	UB100 - Low	UB100 - High	AJ133	LUPOE2-D	LUPOE2-D boosted
Mean (bar)	83.6	107.8	49.8	56.4	84.3
σ (bar)	2.9	4.8	4.6	4.4	6.1
COV %	3.5	4.5	9.2	7.8	7.2

Table 5.6: Comparison of experimental P_{max} values captured on four engines.

pressure UB100 case. Indeed when assessing the variability by the standard deviation it appears that the LUPOE2-D non-boosted, AJ133 and UB100 (high boost) have very similar standard deviations but vastly differing COV values. The reason for this is the mean value. A higher mean value results in a lower COV (for the same σ). It can therefore be seen that the COV value does not truly reflect the levels of variability in the engines. Indeed it would only be acceptable to compare the UB100 (low) and LUPOE2-D boosted cases where the mean value is comparable; in this case the UB100 shows significantly reduced variability. When comparing standard deviations it can be seen that an increase in pressure appears to increase the levels of variability, not shown by the COV measure for the LUPOE2-D boosted and non-boosted cases. It could therefore be concluded that the COV measure cannot be applied to datasets with significantly different mean values and that the standard deviation, in such cases, would be a better measure. A more detailed analysis of variability in the engines, based on this table alone should be reserve; in part because of the low number of non-knocking cycles captured in the LUPOE2-D boosted engine (75 cycles). While a small amount, it is still felt that that the amount was significant for a back-to-back comparison with prediction.

5.7 Analysis of the variability of combustion in SI engines

Variability of combustion has been attributed to variations in the turbulent flow-field between cycles both in terms of motion and mixture stoichiometry (see Section 2.7.1 for details). Quantification of variability during these stages, or a more rigorous assessment of exactly where the variability occurs is presented in this section. The novel method used to quantify variability is based on the Pearson correlation coefficient, R^2. The R^2 value is commonly used to assess the quality of fit of data in determining trends or model accu-

rately[1]. By determining the influence of a parameter at some point in the cycle compared to a value defining the cycle "speed", i.e. fast, middle or slow, for example the P_{max} value of a cycle, it is possible to observe a relationship between different stages of combustion and the final state of that cycle. It should be noted that previous work has correlated combustion parameters using the R^2 value previously; such as the correlation between P_{max} and CA_{50} for example (Rimmer et al. [2009] & Gao et al. [2012]). However, the author of this work has not seen a the correlation method used to asses the combustion process has a whole.

If the assumption is made that a cycle which has a higher pressure, at any moment, before P_{max} occurs should result in a greater P_{max} value if it is exposed to no variability. Then it can also be assumed that if a cycle with high pressure does not continue onto a cycle with an equally great P_{max}, then it has been affected by variability. Based on the assumption outlined the R^2 method can be used to assess where variability occurs in a dataset consisting of more than 1 cycle.

The proposed method is employed to determine where the combustion variability in LUPOE2-D non-boosted engine, operating at SRC, occurs. A plot of the distribution of $P(\theta)$ vs P_{max} (where $P(\theta)$ is the instantaneous pressure value at a given crank angle, (θ) can be seen in Figure 5.44. It is seen that there exists virtually no correlation between $P(\theta)$ vs P_{max} at -14^{o}CA aTDC i.e. before the spark timing.The poor correlation is given by a low R^2 value. The low correlation is not surprising as it is well known that combustion variability exists, and therefore before the combustion event there is very little relationship between initial pressure and where a cycle will fall in a terms of P_{max} values. The P_{max} vs $P\theta_{max}$ distribution for the LUPOE2-D was seen earlier in this chapter in Figure 5.1. Additionally, it must be noted that a portion of the scatter seen between $P(\theta)$and P_{max} is likely, to be caused by "noise" i.e. experimental error. It can be seen that values of $P(\theta)$ at -14^o aTDC are 18 $\pm$ 0.2 bar. Measurement of 0.2 bar is difficult to achieve accurately, and therefore the proposed R^2 method is likely to be obscured by noise until the variation in combustion causes a greater scatter of $P(\theta)$ values, where the impact of error will be less.

If the R^2 value is calculated at different crank angles throughout the process, as seen in Figure 5.45, then it can be seen that $\lim_{P(\theta)\to\theta_{Pmax}} R^2 = 1$. R^2 will not reach 1 however, as P_{max} does not occur at a single instantaneous crank angle for all cycles and hence, has its own distribution.

[1]In the strictest sense it is appropriate to use R^2 only when either the x or y value used in the correlation is derived from a linear regression model. Where it is used to determine the quality of fit, as in this section, its value indicated how well a regression model would predict data.

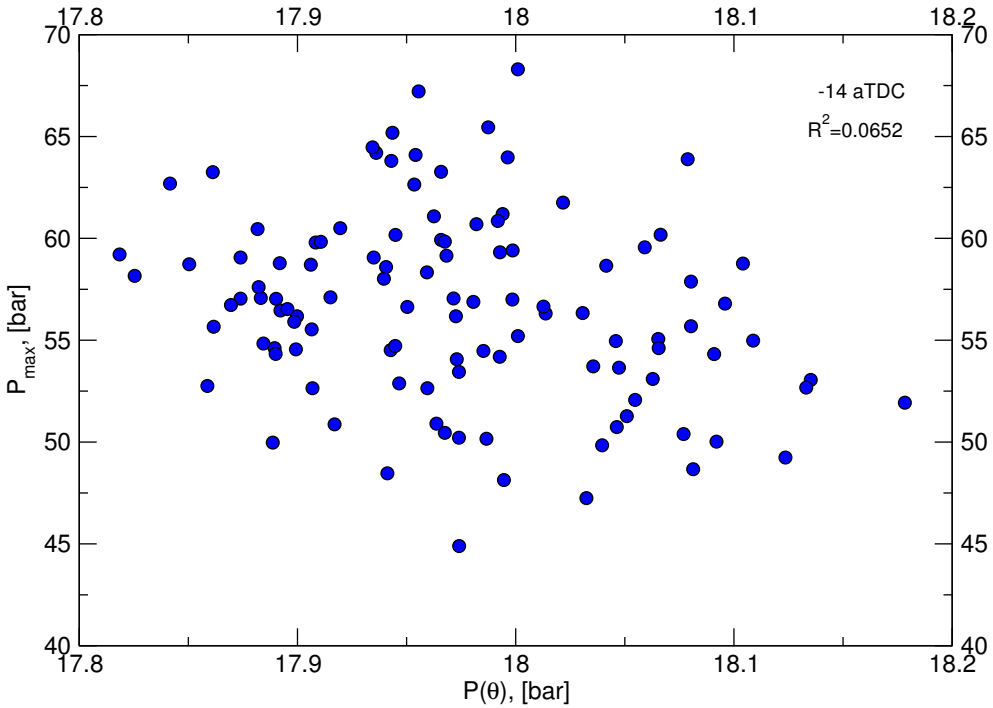

Figure 5.44: P(θ) vs P_{max} scatter at θ=-14 aTDC for the LUPOE2-D operating at SRC (Spark advance is -12 aTDC).

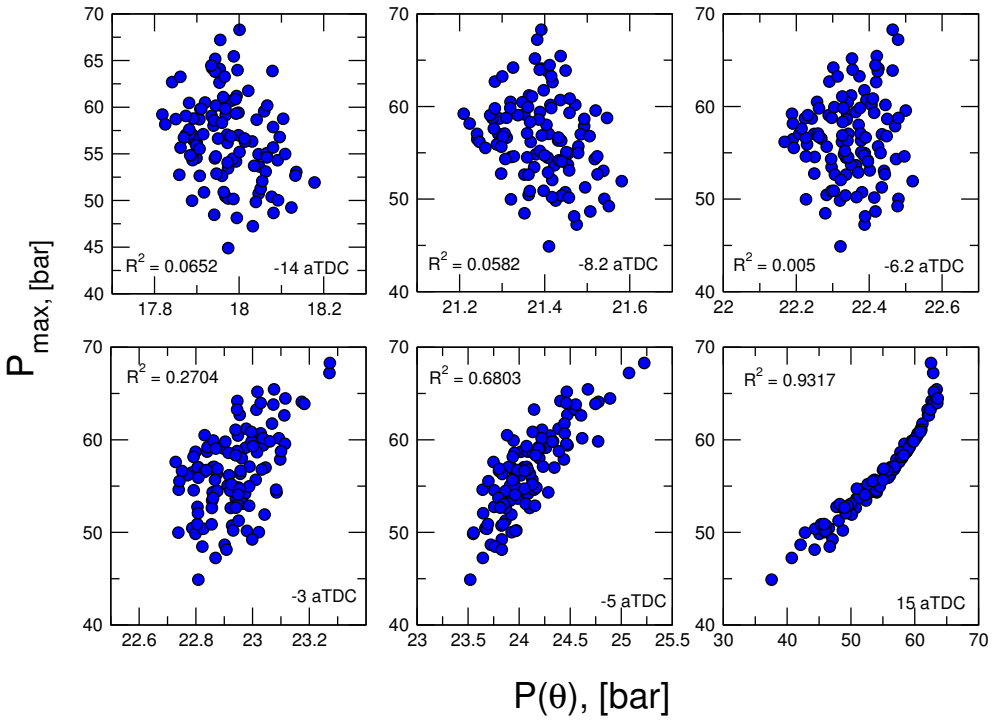

Figure 5.45: P(θ) vs P_{max} in the LUPOE engine at a number of instantaneous crank angles.

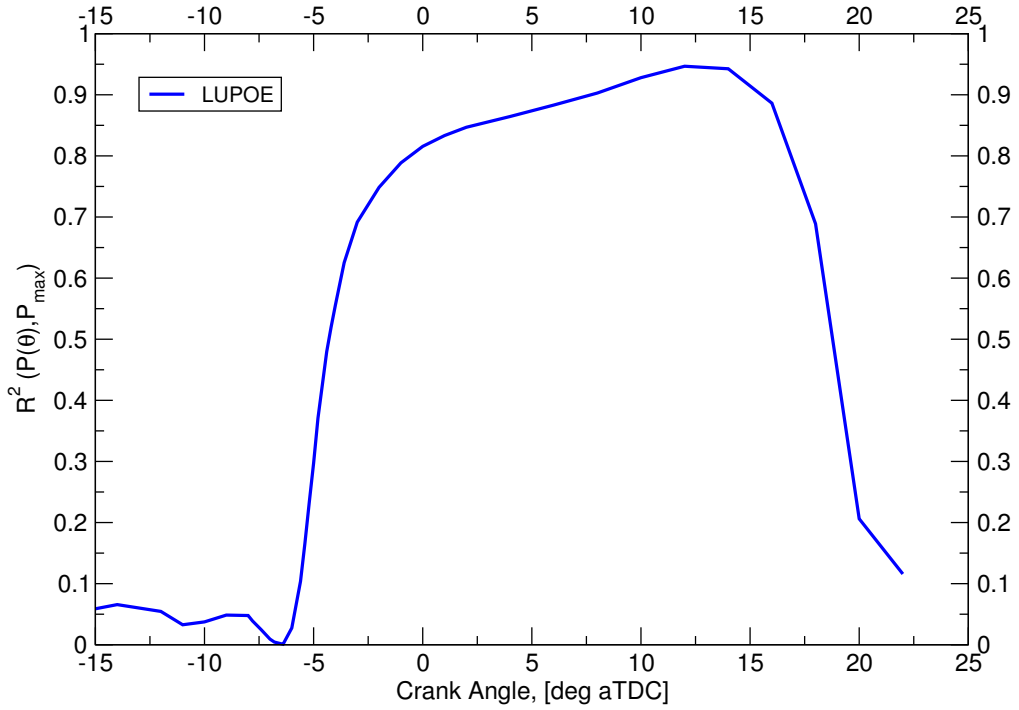

Figure 5.46: The crank resolved R^2 correlation for P(θ) and P_{max} in the LUPOE2-D operating at SRC.

If a sufficient amount of R^2 values are calculated, then a profile of R^2 with respect to crank-angle can be produced. For the LUPOE2-D dataset such a relationship can be seen in Figure 5.46. It can be seen that before the point of ignition (-12^{o}CA aTDC) there exists little correlation between the pressure and the final maximum pressure value. After the point of ignition the value of R^2 tends to 0 at approximately -6 aTDC. After this point, R^2 rapidly increases towards its maximum value until the rate of increase gradually reduces to a slope with substantially lesser rate of change, while R^2 continues to increase until its maximum. The R^2 value then decreases as θ is now greater than the θ at which P_{max} values occur, therefore the distribution of P(θ) vs P_{max} hooks back on itself as can be seen in Figure 5.45 when θ =15^{o}CA aTDC.

From the analysis, as after a certain point the R^2 value increases quickly it can be implied that variability is occurring before this point. In the case of the LUPOE2-D operating at SRC, it can be seen that after approximately θ = -6^{o}CA aTDC, the correlation increases suggesting that less variability is occurring.

The occurrence of cycle-to-cycle variability is often ascribed to the initial stages of combustion as has been seen in the current work; the initial combustion phase is commonly taken as 0-10% of MFB (Heywood [1988]). Of course the relationship between the spherical flame geometry and amount of fuel burned is not linear. Indeed it can be seen

in Figure 5.47 that the time taken (to reach a flame or specific radius) for 10% of fuel to burn in the LUPOE2-D engine, for example, is large, while the amount of flame growth during the main burn phase, usually given as 10-90% of fuel burn, is small. The crank-resolved flame and burned gas radii in addition to the mass fraction burned are plotted in Figure 5.48.

Using the R^2 method, it is possible to quantify the variability in the early stages of combustion and to see if there is a specific link between flame parameters and the onset or, more correctly in this case, subsidence of variability. Having confirmed that the initial stages of combustion are responsible for variability. The R^2 method was further used to see if a critical time to achieve burned gas radii existed; the critical duration would determine the point, or phase, where combustion was most influenced by cycle-to-cycle variability.

In Figure 5.49 the burned gas radius, $fr_b = \left(\frac{3m_b}{4\pi\rho_b}\right)^{1/3}$, as predicted by LUSIEDA, is defined as the radius of the sphere containing the burned products and r_{max}, which is the distance from the centre of the spark electrode gap to a solid wall (Defined in Figure 2.17). The R^2 is given as the relationship between the time taken between ignition and the flame reaching a certain size, $\tau(fr_b/r_{max})$, to the final P_{max} value. It can be seen that the R^2 value increases rapidly while the burned gas radius is still quite small (fr_b/r_{max} <0.15). The small radius can be seen from Figure 5.47 to equate to little burnt fuel, approximately <2%, far lower than 10% suggested by the coarsely defined, initial flame propagation phase. The rapid increase in R^2 shortly after fr_b/r_{max} = 0.15 suggests that the cycles are becoming more "ordered" and less affected by variability. At $fr_b/ r_{max} > 0.22$, only a relatively small level of further correlation increase is seen. Although the increase is only small, the implication is that variability is not confined to the initial stages of combustion only. As can also be seen, the correlation appears to rapidly increase once the flame radius is greater than approximately 6 integral length scales.

A similar result for the LUPOE2-D Boosted engine was seen; the results are presented in Figure 5.50. It can be seen that the correlation value increases again after approximately (fr_b/r_{max} <0.15), and therefore, like the LUPOE2-D engine, where the time for the burned gas radius to reach a size of approximately 6 integral length scales appears to be critical for determining variability (the integral length scale being identical in both engines). The slope depicting the rate of change of the R^2 correlation is less step than for the LUPOE2-D engine. The apparent implication being that the increase in pressure has resulted in the flame being affected by variations in the flow field or mixture stoichiometry, or both, for longer.

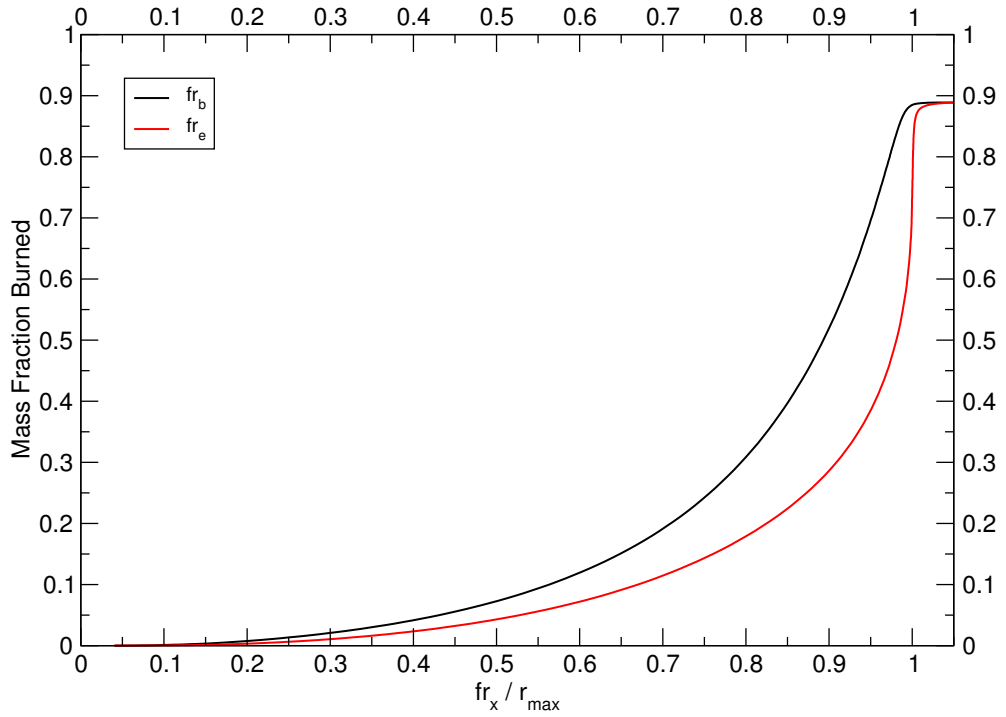

Figure 5.47: The relationship between flame entrainment radius, burned gas radius and the mass fraction of fuel burned as predicted by LUSIE for a middle cycle in the LUPOE2-D operating at SRC.

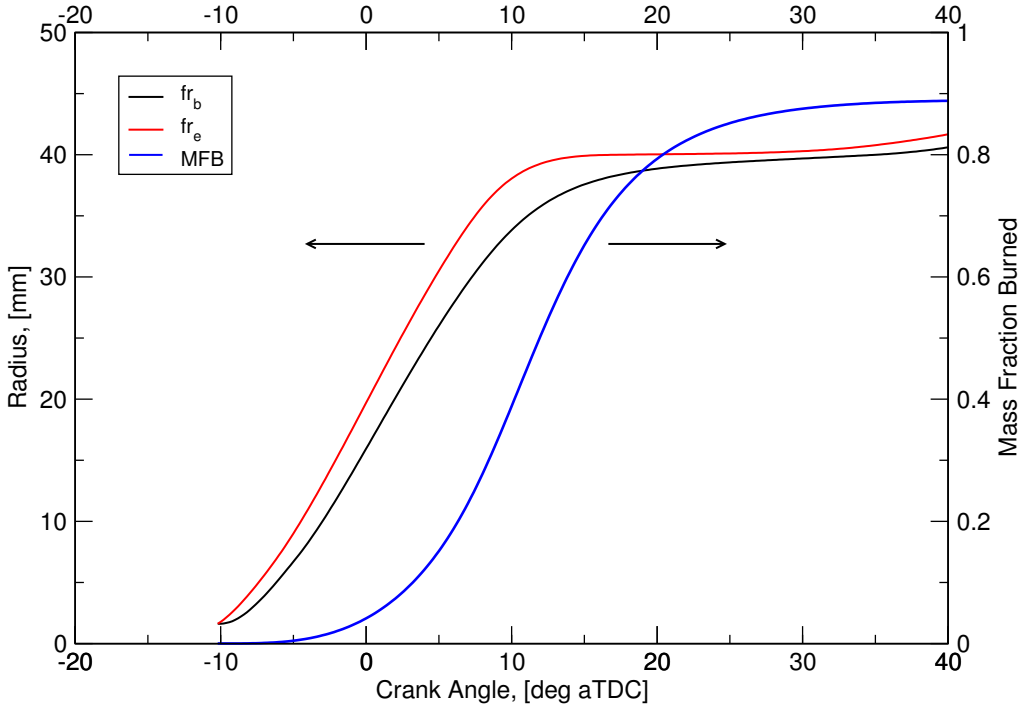

Figure 5.48: Crank-resolved entrained flame radius, burnt gas radius and mass fraction burned values as predicted by LUSIE for a middle cycle in the LUPOE2-D operating at SRC.

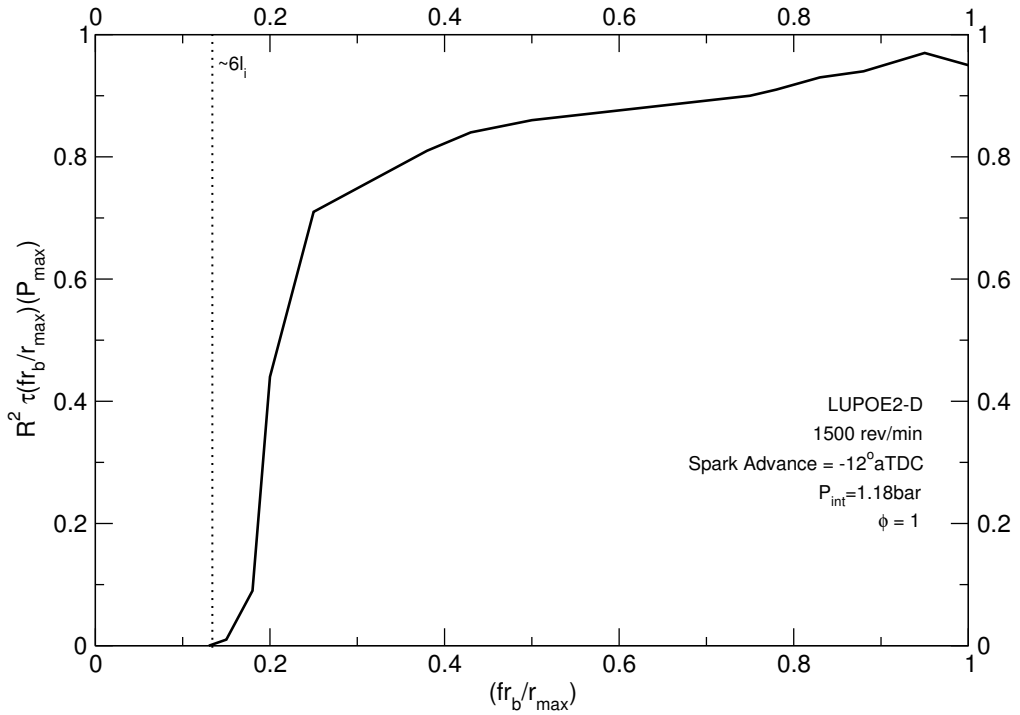

Figure 5.49: The correlation of time taken for the burned gas radius to reach a normalised distance vs peak pressure for the LUPOE2-D engine.

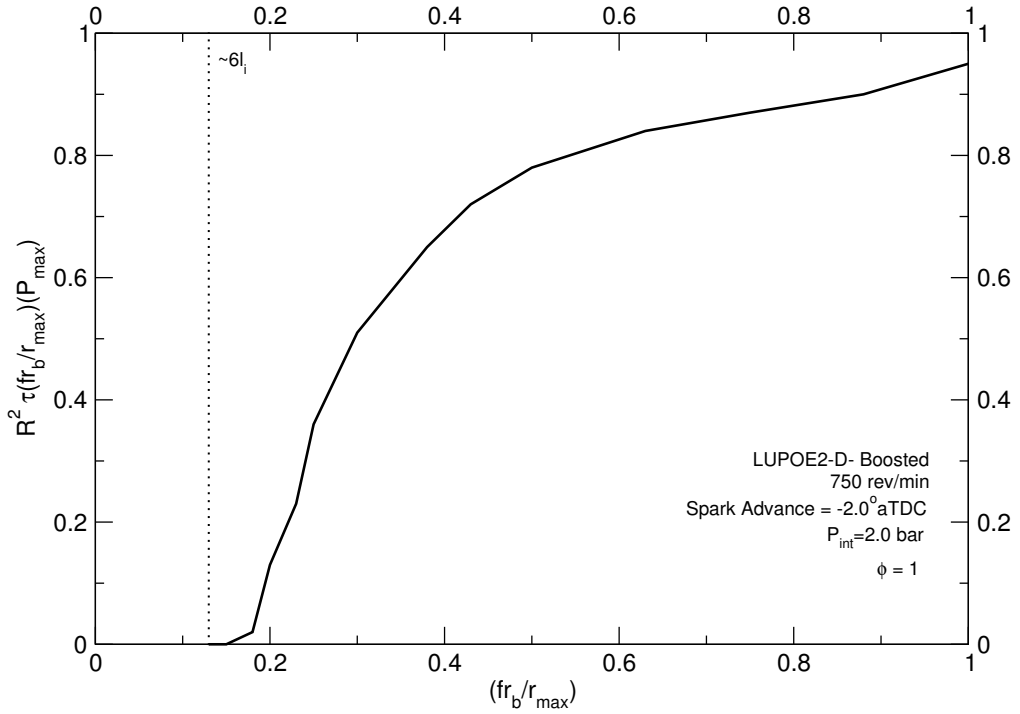

Figure 5.50: The correlation of time taken for the burned gas radius to reach a normalised distance vs peak pressure for the LUPOE2-D boosted engine.

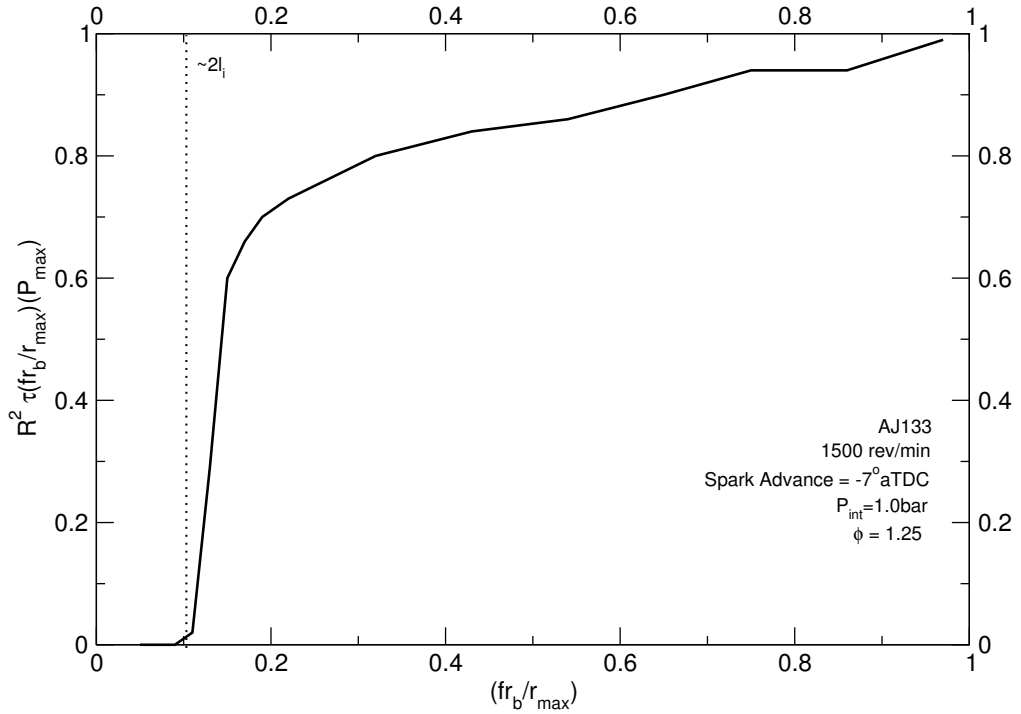

Figure 5.51: The correlation of time taken for the burned gas radius to reach a normalised distance vs peak pressure for the AJ133 engine.

The non-boosted production engine appears to agree with the observations on the two LUPOE2-D configurations; as can be seen in Figure 5.51. Most notably that there is a rapid increase in correlation. The size of the radius in the non-boosted production engine appears to be smaller than for either the boosted or non-boosted LUPOE2-D cases. The rapid increase in correlation appears to occur after approximately two integral length scales, that corresponds to approximately 1/3 of the LUPOE engine radii. A final comment is that the rate of increase of the correlation appears to be aligned with the non-boosted LUPOE2-D engine.

Both high and low intake pressure datasets were available for the UB100 engine. It can be seen in Figure 5.52 that unlike either of the LUPOE2-D configurations or the non-boosted production engine, the increase in the correlation appears to occur at an fr_b/r_{max} value of approximately 0.1 for the high pressure case, and 0.05 for the low pressure case. Indeed the rate of change of the correlation for the high pressure case does not display a rapid increase region after a critical radius, as has been seen on all other engines/operating conditions. Instead a gradual, almost linear increase is seen. The lower pressure case reflects the trend seen in the other engines, where a rapid increase in correlation appears to occur early in the cycle. It is, however, noteworthy that the rate of increase does not reduce at an R^2 value of 0.6-0.7 as is seen in the other engines, the reduction occurs at

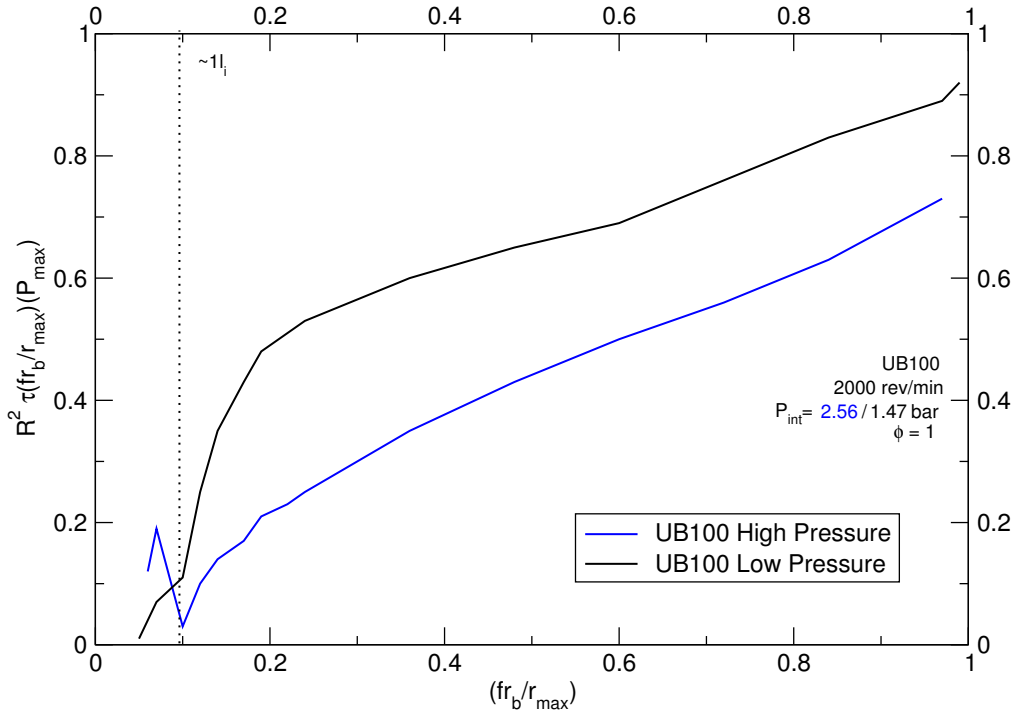

Figure 5.52: The correlation of time taken for the burned gas radius to reach a normalised distance vs peak pressure for the UB100 engine operating at both high and low pressure conditions.

approximately an R^2 value of 0.5. The suggestion of this observation is that the flame is more affected at the later stages of the cycle, while for the high pressure case, it can be said that there does not appear to be a critical radius with regards to correlation between the time taken for the burned gas to reach a certain radius and the final P_{max} value. It could be suggested that variability is not confined to the early flame propagation in the UB100 engine operating at high pressures, although this appears to be a function of both the operating pressure and engine design itself. For the UB100 engine the critical radii appears to correspond to the order of the integral length scale.

A comparison of the R^2 correlation for all engines and all operating conditions is presented in Figure 5.53; where the difference between the UB100 engine and the other engines can be seen, as well as the influence of pressure on the R^2 correlation. It can reasonably be suggested from the presented figures, that an increase in pressure results in the combustion process being influenced by variability at larger flame radii.

The LUSIE predictions of variability in the LUPOE2-D were used to see if the R^2 correlation prediction gave a similar trend to that seen in the data obtained experimentally. The results from the LUSIE predictions can be seen in Figure 5.54. It can be seen that LUSIE does predict a trend of a rapid increase in R^2 correlation, however the increase can

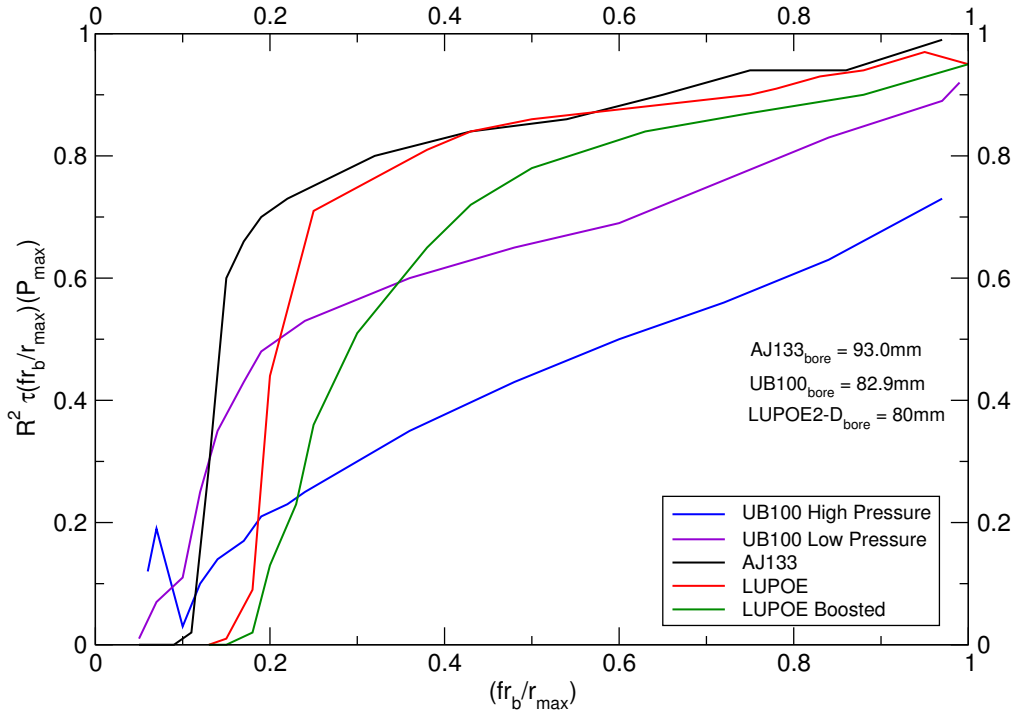

Figure 5.53: The correlation of time taken for the burned gas radius to reach a normalised distance for all engines.

be seen to occur very early on in the cycle and more rapidly than seen experimentally. There also does not appear to be a considerable increase in R^2 after an fr_b/r_{max} value of 0.3, whereas experimentally it was seen that the value would increase until fr_b/r_{max} = 1. The reason for the apparently early converged R^2 value is likely to be caused by the method by which variability is imposed in LUSIE, that being at the point of ignition. Therefore any variability that might be experienced experimentally later on in the flame lifetime, would not be seen in the prediction.

As alluded to earlier in this section, the use of cylinder pressure as the parameter from which to base the R^2 correlation can have inherent errors which may obscure the relationship. LUSIEDA analysis is also "driven" by cylinder pressure and, at the very early stages of combustion i.e. ignition + 1-2^o CA.

Another parameter which was measured was the flame radius, captured by high speed camera and then converted to a crank-resolved flame radius. The luminosity of the flame at the early stages of combustion was low, and therefore the smallest recorded flame radii was 5mm which prevents a correlation between the very early flame growth and the maximum pressure achieved. Shown in Figure 5.55 is the R^2 correlation between the flame radius at a given crank angle, $fr_e(\theta)$ and the final maximum cylinder pressure in the same cycle, as well as the the R^2 correlation between the cylinder pressure at a

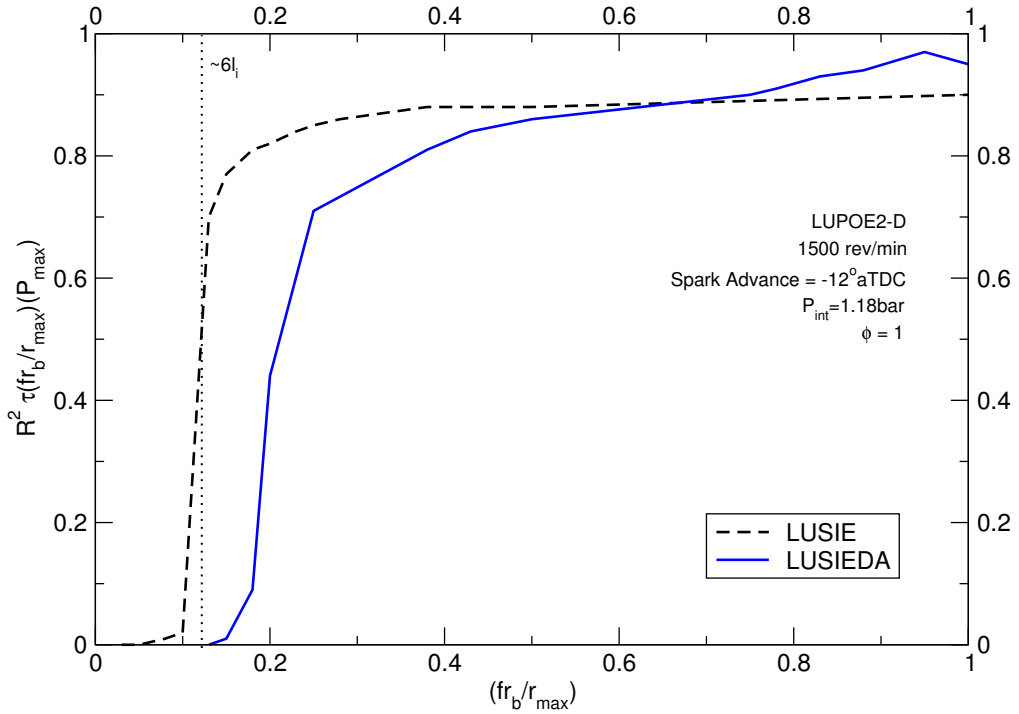

Figure 5.54: The correlation of time taken for the burned gas radius to reach a normalised distance vs peak pressure for the LUPOE2-D boosted engine as predicted by LUSIE and as determined from experimental values by LUSIEDA.

given crank angle, P(θ) and the final maximum cylinder pressure in the same cycle. It can be seen that both parameters show a similar trend in terms of a sharp increase in R^2 approximately 4^o CA after the point ignition. It can be implied from the observation that use of the cylinder pressure, even during the early stages of combustion appears to be a viable parameter for use with the proposed R^2 correlation method. The sharp rise seen in the black P(θ) curve around 20^o CA is caused by the autoignition cycles (see Section 5.6 for details). In addition, it is also observed that the R^2 values, when using the $fr_e(\theta)$ correlation, are seen to be lower vis-á-vis the P(θ) as shown in Figure 5.55.

In Figure 5.56 the time for both the observed flame radius, and burned gas, calculated by LUSIEDA, to reach a certain radius are plotted against their respective R^2 correlation values. It can be seen that R^2 values are higher for $fr_b(\theta)$ vis-á-vis $fr_e(\theta)$, as was also seen between P(θ) and $fr_e(\theta)$ in Figure 5.55. From the observation it is suggested that a variability between the flame radius and the burned gas radius may exist. For example, once the flame front has reached the wall it will no longer affect the final cycle pressure, however the after-burning rate can still influence the maximum pressure. This process is seen in the Figure where the R^2 values for $fr_b(\theta)$ are greater than for $fr_e(\theta)$.

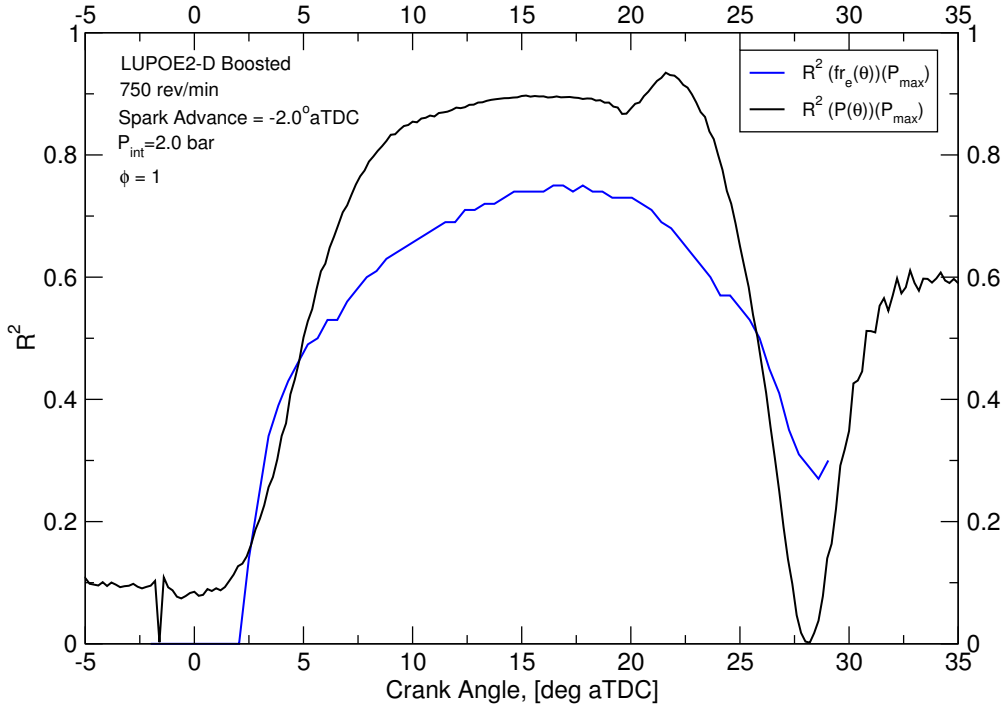

Figure 5.55: The correlation of observed flame radius at a crank angle and the final maximum pressure. Measurements were taken from the LUPOE2-D boosted engine.

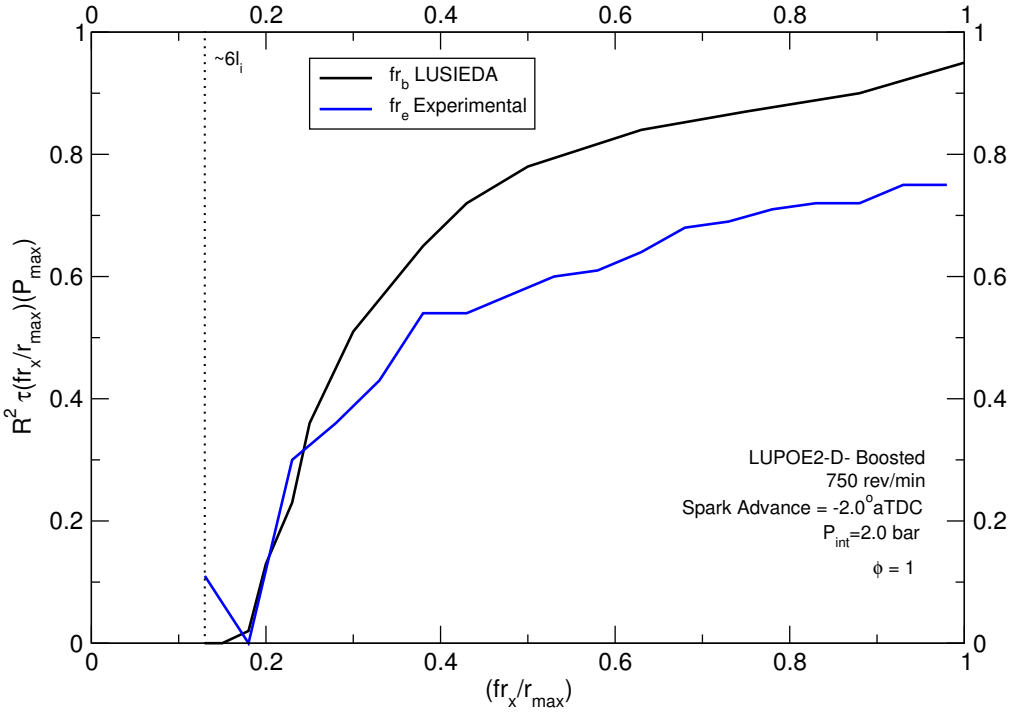

Figure 5.56: The correlation of time taken for the burned gas radius and observed flame radius to reach a normalised distance vs peak pressure for the LUPOE2-D boosted engine.

5.7.1 Prediction of variability at different stages of combustion

Where the variability occurs in a cycle has been suggested to occur at the very early stages of combustion, and appears to have been largely confirmed by the current work (Section 5.7). It was of interest, however to see the impact that imposing variability on different stages of the combustion cycle would have on subsequent variability, measured by a P_{max}, θ_{Pmax} distribution. It was possible to impose variability at different stages of combustion deliberately using LUSIE.

A mean cycle predicted by LUSIE for the LUPOE2-D operating at the SRC, presented in Figure 5.57 highlights the three main stages of combustion; an initial flame development, a constant burning rate and a deceleration of the flame as it nears the cylinder walls. It can be seen that the constant burning rate phase, is not strictly occurring at a constant velocity. However, the rate of change of u_{te} compared with the change in burned gas radius is occurring at a constant rate, while the other two stages demonstrate extreme acceleration or deceleration. The increase in turbulent velocity after the initial development is caused by a number of processes in the model, which combine to result in a net increase in turbulent burning velocity. The first, is that the flame is still continuing to develop and experience the full rms turbulent velocity value, expressed as the ratio of u'_k/u', where u'_k is the effective rms turbulent velocity and is determined by the flame development factor, f_d (see Eq. 3.16) by the relationship $u'_k = u' f_d$. It can be seen in Figure 5.58 that even after the initial development phase, $fr_e/r_{max} > 0.18$, that the u'_k/u' value is increasing, the laminar burning velocity is also increasing as the unburned gas temperature increases. An increase in the laminar burning velocity increases both the rate at which the entrained fuel is burned (see Eq. 3.3), as well as increasing both the developing turbulent entrainment velocity (see Eq. 3.11) and fully developed turbulent entrained burning velocity (see Eq. 3.14).

The variability of u' and ϕ at the point of ignition has been the main focus of the current work. The influence that such a variation has on the turbulent burning velocity of the entrainment radius, ut_e, can be seen in Figure 5.59. In the Figure the burning velocity is given against the growing equivalent burned gas radius, normalised by the maximum radius as determined by the combustion chamber geometry.

Having identified the three main stages of combustion, as predicted by LUSIE, it was possible to deliberately impose the variability to begin at the start constant burn rate phase, as well as the start of the deceleration phase. It can be seen in Figure 5.60 that imposing of the variability after the initial flame development phase, in this case when

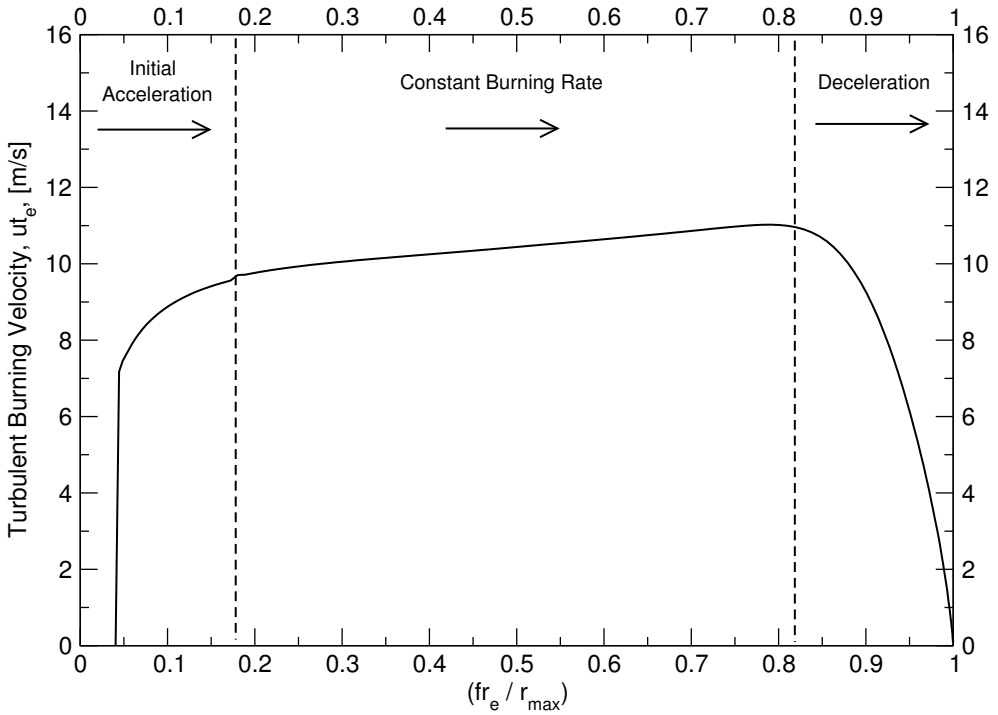

Figure 5.57: The three main stages of flame propagation in S.I. engines as predicted by LUSIE for a LUPOE2-D mean cycle operating at SRC.

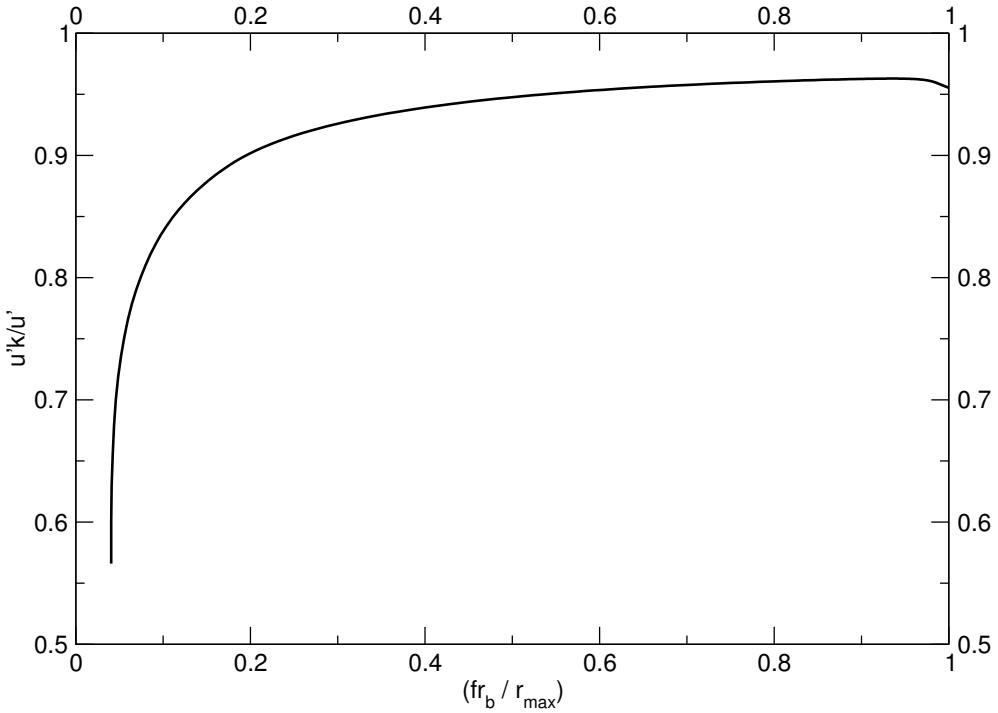

Figure 5.58: u'_{k} normalised by the instantaneous u' value for the mean cycle predicted by LUSIE for the LUPOE2-D operating at SRC.

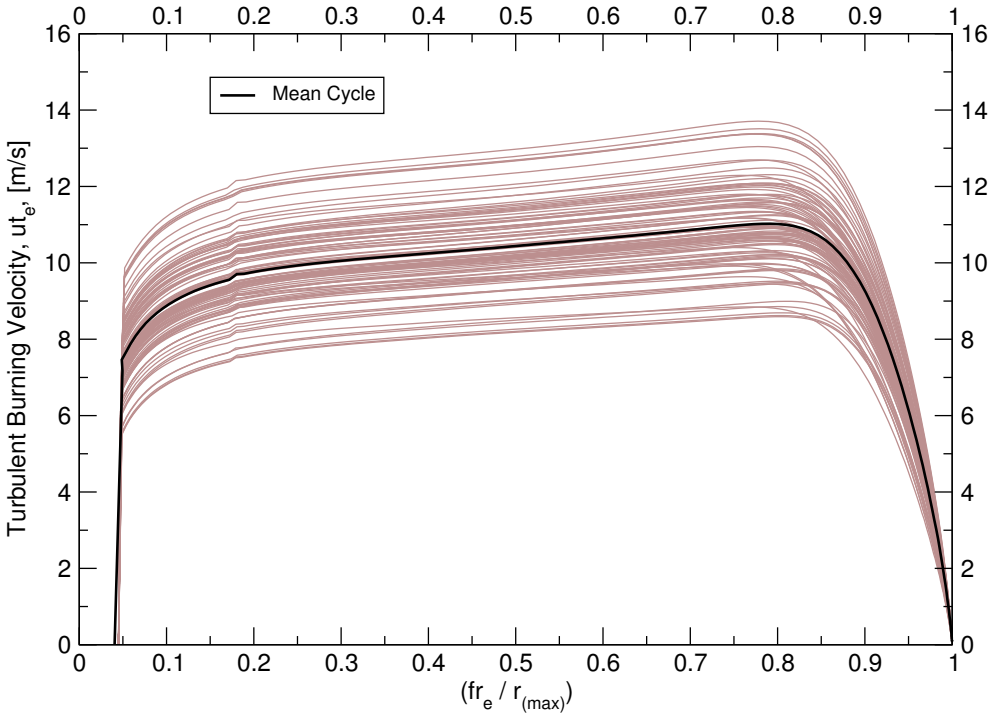

Figure 5.59: Imposing u' and ϕ variability on a mean cycle, at the point of ignition, as predicted by LUSIE for the LUPOE2-D operating at SRC conditions.

$\mathrm{fr_e/r_{max}} > 0.18$, still results in a large variation in the turbulent burning velocity at the later stages of combustion.

Imposing variability at the later stages of combustion, $\mathrm{fr_e/r_{max}} > 0.81$ results in a far lower variability of the turbulent burning velocity during the phase where the flame is decelerating, as can be seen in Figure 5.61. Despite almost 80% of the fuel being burned during the deceleration phase, (seen in Figure 5.47), the variability on burning velocity is low. The active area of the decelerating flame is constantly reducing as parts of it are quenched at the system boundary, as accounted for by the flame deceleration model (see Eq. 3.17).

The effect of varying the combustion rates at different stages of combustion has on the final maximum pressure, can be seen in Figure 5.62. The $\mathrm{P_{max}}$, θ_{Pmax} distribution where variability is imposed at ignition is, unsurprisingly, seen to be very similar to the results of the earlier comparison with experimental results (see Section 5.3). Where variability is imposed after the initial development phase, the $\mathrm{P_{max}}$, θ_{Pmax} distribution has not remarkably reduced, in terms of the prediction of the slowest and fastest cycles vis-á-vis where variability was imposed at the point of ignition. One noteworthy observation is that the spindle-like shape of the $\mathrm{P_{max}}$, θ_{Pmax} distribution appears to be stronger where the variability is imposed after the initial development. Imposing variability at the point

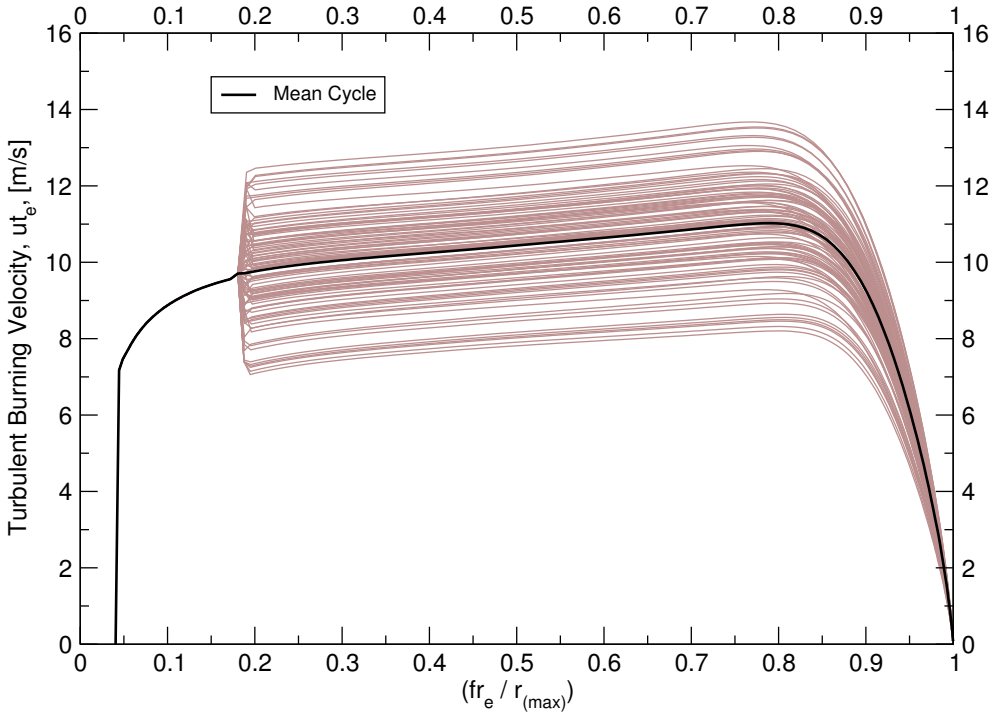

Figure 5.60: Imposing u' and ϕ variability on a mean cycle, after the initial flame development phase, as predicted by LUSIE for the LUPOE2-D operating at SRC conditions.

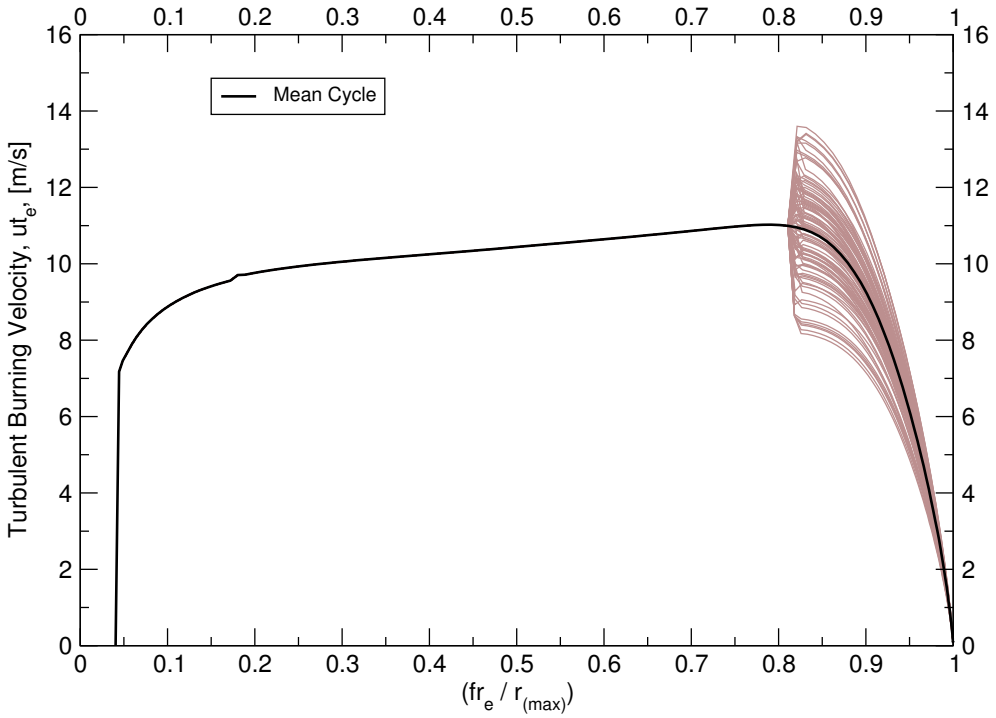

Figure 5.61: Imposing u' and ϕ variability on a mean cycle, at the point of flame deceleration as it comes within close proximity of the cylinder, as predicted by LUSIE for the LUPOE2-D operating at SRC conditions.

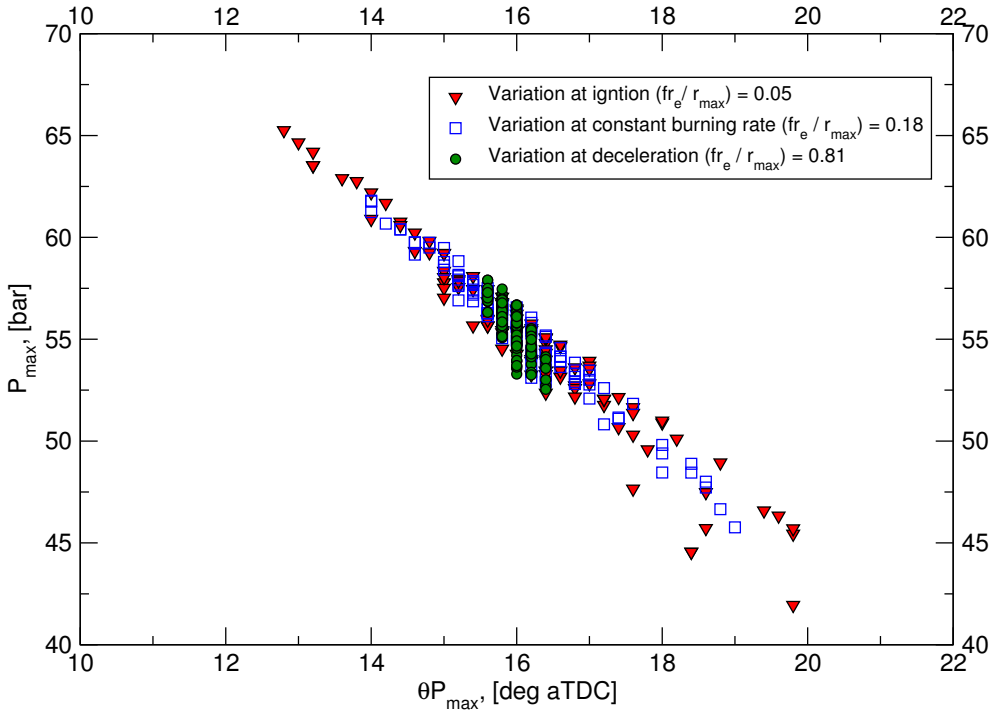

Figure 5.62: The influence of the stage at which variability is imposed on the P_{max}, θ_{Pmax} relationship.

at which the flame begins to decelerate resulted in little change in the turbulent burning velocity As such, the change in the P_{max}, θ_{Pmax} distribution was also minimal.

5.8 Discussion of factors influencing variability and accuracy of modelling

The variability of the combustion processes, which take place under the turbulent and transient conditions within internal combustion engines, is a limiting factor for both engine performance and efficiency. The ability to predict the variability of cycles would be of significant benefit, with specific application to quasi-dimensional predictive models, which have relatively small run-times, in determining initial calibration as well as design limits for engines. Although cyclic-variability modelling has been used in the past, the assessment of previous variability models specifically to combustion in modern "downsized" engines, has not been studied. Experimental and simulated data for both production and research engines has been presented in this chapter; these engines were operated at both at low and high pressure conditions giving an insight into the behaviour of the variability of the combustion events under boosted and naturally aspirated conditions.

Previous experiments suggested that variability from cycle-to-cycle was a result of random fluctuations in both the velocity of the fluctuation turbulent flow field as well as variations in equivalence ratio brought about by imperfect control of injection rates; it was these two parameters which were determined to be the key parameters in accounting for cyclic-variability. A cyclic variability model, based on the Box-Muller transform approach was implemented into the existing LUSIE code which enabled independent variability of both the equivalence ratio and rms turbulent velocity.

The most comprehensive data was available for the LUPOE2-D research engine, including visualised flame propagation as well as cold-flow turbulence data obtained from both LDV and PIV techniques. It was seen that this engine conformed to the expected Gaussian distribution in terms of both P_{max} & θ_{Pmax} although the low amount of captured cycles prevented small bin sizes, which would improve the resolution and Gaussian properties of the data. It could be seen that the variation in only the rms turbulent velocity was in better agreement with the linear, P_{max}, θ_{Pmax} relationship vis-á-vis only a change in equivalence ratio. A change in equivalence ratio resulted in predicting a greater P_{max} mean value for a given θ_{Pmax} mean value, i.e. the slower, lower pressure cycles, were predicted to occur too early in the cycle vis-á-vis experimental data. Variation in the parameter rms turbulent velocity alone, however, did not give an accurate prediction of the spread of data at any given P_{max} or θ_{Pmax} value, that is to say, under experimental conditions it was seen that two cycles with a given P_{max} could have different θ_{Pmax} values. Enabling variation of both the rms turbulent velocity as well as the equivalence ratio resulted in an increased spread in the data for a given P_{max} , in line with the results seen from experiments. Variation of both parameters did however adjust the P_{max}, θ_{Pmax} relationship towards a faster prediction of the lower pressure cycles, as was seen with a variation of only the equivalence ratio. In addition it could be seen that in the experimental cycles the P_{max}, θ_{Pmax} data conformed to a spindle-like distribution while the predictions were more cone-like, where the slower cycles were influenced more by the independent variation of the equivalence ratio parameter which predicted good P_{max}, θ_{Pmax} values for the faster cycles, while the slower cycles were predicted to occur too early, as denoted by the steeper line of best fit slope. As the slopes of the lines of best fit for the independent variation of both variables diverge significantly more in the slower cycles it does not necessarily suggest that the Gaussian nature is not correctly modelled, more likely that the influence of equivalence ratio variation on individual cycles, predominantly the slow cycles, is not correctly predicted.

Data for the AJ133 were overall less comprehensive than for the LUPOE2-D engine, the bulk of the data comprised of 1000 crank-resolved in-cylinder pressure traces,

however, only simulated turbulence data available. In the production engine a similar trend was seen with the prediction of variability as was seen as with the LUPOE2-D engine, that is, that the lower pressure cycles were predicted to occur too early in the cycle. The variability in naturally aspirated production engine cycles was influenced by the engine control strategy, when it realised a cycle approaching knocking conditions it would retard the spark, though this was only viewed on approximately 0.1% of cycles and was not considered to influence the overall variability of the engine, and therefore it was not necessary to include it into the prediction model.

The Gaussian nature of cycle-to-cycle variability results in spindle like P_{max} & θ_{Pmax} shapes. Shown in Figure 5.13 is the scatter of P_{max}, θ_{Pmax} and that other values should fall within this region. Assuming the same response would be exist for the AJ133 engine it can be stated that before the CPS switches, at low engine speeds there are less lean conditions; that is to say conditions which are leaner than the mean equivalence ratio, and less high turbulence conditions. One apparent conclusion is that the switching of the cam profile to a higher lift increases the probability for higher turbulence cases to occur, it could also be attributed to the increasing richness of the air-fuel mixture, as the global air-fuel ratio is already rich, at ϕ =1.25, a decrease, i.e. for those cycles which are leaner than ϕ =1.25 the laminar flame speed would increase up to a leanness of ϕ =1.1. The mixture is however increasing from an already rich condition between 1000 and 2500 rev/min without remarkably changing the shape of the P_{max}, θ_{Pmax} plot; it could therefore be argued that the dominant influence is from the change of cam position which brings about a definite change in the P_{max}, θ_{Pmax} plots. Also plausible is that a combination of these two factors results in the change in shape of the P_{max}, θ_{Pmax} plots.

The effect of increased pressure on cyclic variability could be assessed with the UB100 engine; the engine was capable of operating at both high, and low pressure conditions with a 1.1 bar difference between the absolute intake pressures for the low and high pressure conditions. Using the turbulence data which gave the best mean cycle match, as discussed in Chapter 4, the critical turbulence quantities, rms turbulent velocity and length scale, were not directly affected by an increase in pressure. It was clear that the prediction for the lower pressure case was in better agreement with the experimental data vis-á-vis the higher pressure condition, though the offset mean cycle was in part responsible for this discrepancy. Use of θ_{Pmax} as a measure of variability in terms of COV is a poor choice of variable as it is commonly prescribed as a non-ratio variable in within the -360 to 360 scale; the location of which commonly falls into the near-zero region. Offsetting this by 360 by transforming the data to a 0-720 scale brings about a more correct variance which can be compared between two datasets which may have vastly differing

θ_{Pmax} values. Additionally it was seen that the measure of COV could not reasonably be applied to different engines and used to compare them, when the mean values of a parameter (in this case P_{max}) vary significantly.

Ninety cycles were available from the LUPOE2-D boosted engine. The differences between the LUPOE2-D boosted and non boosted engines are small and constrained to geometric alteration of parts affecting the breathing process. The combustion chambers are identical between the two variants. It was seen that once a middle cycle was predicted with good agreement, that imposing at the point of ignition, a variability of rms turbulent velocity by 12.5% of σ and the equivalence ratio by 5% of σ gave a very satisfying agreement of the P_{max}, θ_{Pmax} distribution, with the caveat that, as with the other engine predictions, cycles which were too slow were seen to be predicted by LUSIE.

It can generally be said that varying the parameters of rms turbulent velocity by 12.5% of σ and the equivalence ratio by 5% of σ can account for the variability present within an engine cycle at low pressure conditions, with the caveat that the lower pressure cycles observed experimentally are predicted to occur too early in the cycle. It is likely that this issue is attributed to the main LUSIE routines rather than the variability model, results suggest that the variation of only the rms turbulent velocity had a better P_{max}, θ_{Pmax} relationship between experimental and prediction, and that it was only when the equivalence ratio variance was introduced that the low pressure cycles were over-predicted.

For the high pressure conditions, such as those seen in the UB100 engine the relationship between P_{max}, θ_{Pmax} appears to be in better agreement between prediction and experiment vis-á-vis the LUPOE2-D or the non-boosted production engine, however the scatter of predicted data is far greater than observed experimentally, the higher pressure cycles have a faster burn-rate which should reduce the residency time for heat-transfer rates, however the LUSIE code accounts for heat transfer and should predict this influence. It is therefore likely that the variability assumption of 12.5% of σ and the equivalence ratio by 5% of σ is too large for high pressure conditions and that an influence of pressure on turbulence stability may be the driving force behind this sensitivity change at higher pressures.

A newly proposed R^2 correlation method identifies where in the combustion process, the influences of variability reduce. It can be implied from the method that there is a certain, critical, radius after which the variability reduces. The critical radius determines where the R^2 correlation increase, and therefore, implies where the influence of factors causing variability begin to decrease. It was seen that variability appears to be a strong

function of the time to reach a certain burned gas radius. There does not appear to be a critical radius of the burned gas, as a function of the integral scale which can be used for all engines. There does however appear to be a relationship between pressure and variability, in terms of where the variability can affect propagation during the combustion process. An increase in pressure was seen, in two separate engines, to result in a larger critical burned gas radius. Moreover, there appears to exist a separate variability between the flame front and the burned gas radii; which can be related to separate variability influences on the processes controlling the entrainment and mass burning velocities.

Imposing variability on different stages of the combustion process in the LUPOE2-D non-boosted engine was predicted using LUSIE. It was seen that when variability was imposed at later stages of combustion a decrease in overall variability was seen, as determined by the spread of a P_{max}, θ_{Pmax} distribution. There appeared to be little difference in the overall P_{max}, θ_{Pmax} distribution when variability was imposed at ignition or at the start of the constant burn rate phase. There was a reduction variability in the slowest and fastest cycles predicted when variability was imposed later in the cycle. It was also seen that the distribution become more like the ideal spindle-like distribution shape, as should be seen with the variation of two parameters with Gaussian distribution.

Chapter 6

Autoignition characteristics in SI engines

6.1 Chapter Overview

The occurrence of an uncontrolled autoignition event in an SI engine may result in detrimental after effects; for example, a high frequency pressure wave, commonly referred to as engine knock. In severe cases, knock may lead to severe engine damage. There are many strategies which can be employed to reduce the propensity of knock. However, if these are calibration rather than design hardware mitigation methods, then they usually result in a reduction in engine performance. It is therefore crucial to have an indication of the possible level of autoignition activity within an engine at the design stage.

The work presented in this chapter investigates a number of autoignition characteristics which are found in both boosted and naturally aspirated SI engines. Primarily, the focus is to assess the performance of two autoignition models; the Douaud and Eyzat (see Section 3.3.1) and the skeletal Keck model (see Section 3.3.2.3) against the four engines reported throughout this work - namely the non-boosted LUPOE2-D, boosted LUPOE2-D, AJ133 and UB100.

Additionally, variations in the cylinder end gas composition which alter the chemical reaction rates and variations in the burn rate within the end gas during a cycle, which

are usually modelled only with a 'mean' cycle. While more advanced studies may include modelling of both 'fast' and 'slow' cycles to determine the autoignition boundary, this is not yet standard practice. Work to assess the inherent variability within autoignition is lacking in the literature.

Finally this Chapter analyses a set of "abnormal" combustion cycles seen within the boosted production engine (UB100). These cycles displayed pressure oscillations which were initially categorised as knock. A detailed frequency analysis of the oscillations however, shows that the frequencies of the phenomena are not considered to reside within the frequency range that is typically associated with knocking conditions.

6.2 Influence of turbulence and heat transfer on autoignition

During the early stages of the current work, parametric studies focussing on autoignition characteristics were undertaken using the LUSIE code. This part of the work was, to some extent, driven by the UltraBoost project where, during the concept and design phase a considerable interest was placed on predicting the potential autoignition levels within the UltraBoost UB100 engine.

The first set of simulations considered the influence of the, rms turbulent velocity, u', on autoignition in LUPOE2-D engine; a trend was seen that an increase in u' resulted in increased autoignition propensity, see the solid black line in Figure 6.1. Higher u' values were imposed on a mean cycle prediction in the LUPOE-2D non-boosted engine, the normal turbulence level cycle having previously been matched to CFD data as discussed in Section 4.2.1. As u' increases, unsurprisingly, the performance of the engine measured here by the IMEP, also increases. The increase in u' however appears to induce autoignition, which is not present at the nominal u' values. The increase in the burn-rate because of higher u' values, leads to a greater heat release rate and therefore system pressure, inducing autoignition. The issue with increasing only the u', with the subsequent increasing the burn-rate, is comparable to advancing the spark timing, where higher pressures are reached by the heat release profile reaching maximum values close to TDC, the smallest volume, resulting in undesirable autoignition. Retarding the spark timing while increasing the u' however can result in an improvement in engine performance without the associated increase in autoignition propensity. It can be seen in Figure 6.1 that when employing the retarded spark in addition to an increase in u' the performance improve-

ment over the variation of u' of 1.5 m/sec from the nominal value is approximately 1 bar of IMEP, or +/- 5% of the nominal value; a significant amount. Adjustment of the spark advance shifts the heat release profile into a less aggressive pressure and temperature regime, away from TDC, while the faster burn rate associated with the turbulence increase reduces the time the end gas spends at higher pressure-temperature regimes. The net result, if the engine is tuned correctly, is an increase in performance, without the increased autoignition propensity.

An additional area of interest to the UltraBoost project was the sensitivity of autoignition to temperatures of the mechanical component. LUSIE was used to perform a study on the sensitivity of the three main surface temperatures within the combustion chamber; the cylinder liner, the piston and the cylinder head. The boosted LUPOE2-D engine was chosen as the platform for the prediction as on this engine it was possible to experimentally manipulate, the cylinder liner and cylinder head temperatures pseudo-independently of temperature increase caused by combustion. It can be seen in Figure 6.2 that a decrease in the temperature of the individual components results in the predicted onset of autoignition occurring later in the cycle. The sensitivity of autoignition to component temperature is higher than initially thought, specifically the cylinder liner temperature; thus a change in liner temperature of only 2^oK can take the engine from an operation where autoignition is predicted to a region one where autoignition is no longer predicted at all. The reason for high sensitivity of the liner compared to the piston, or cylinder head is because of the relatively large surface area exposed to the unburned gas towards the end of the cycle, where most of the flame will have already. truncated the cylinder head and piston.

6.3 Autoignition model performance

Considerable amounts of research at the University of Leeds was devoted to autoignition in SI engines; it has been conducted by researchers at the University of Leeds in an attempt to better understand uncontrolled autoignition characteristics in SI engines; see for example Smallbone [2004] & Roberts [2010]. The latter work (Roberts [2010]) also investigated controlled autoignition, specifically autoignition in HCCI operation. In these works, the performance of predictive autoignition models was assessed using the non-boosted LUPOE engine. The LUPOE variant used by Roberts was the same as the non-boosted LUPOE used in this study, while Smallbone [2004] used an earlier variant of the LUPOE disc engine, with different intake and exhaust geometry. As with Roberts [2010], a change of engine version affects the pressure and temperature history within

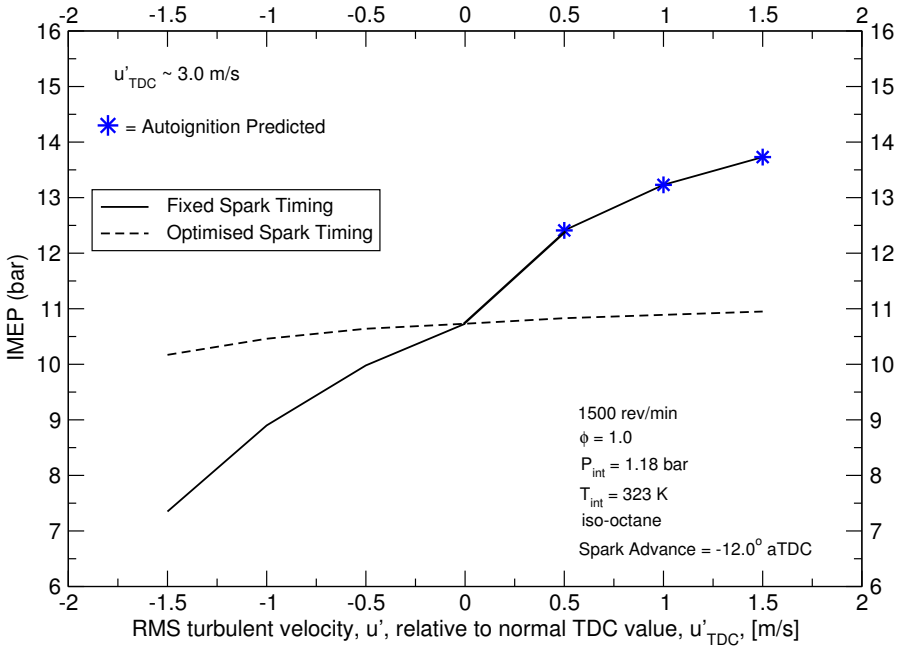

Figure 6.1: The influence of rms turbulent velocity on the engine performance in the LUPOE2-D engine as predicted by LUSIE. Spark timing was fixed at -12^o aTDC (as per the SRC) while u' was adjusted.

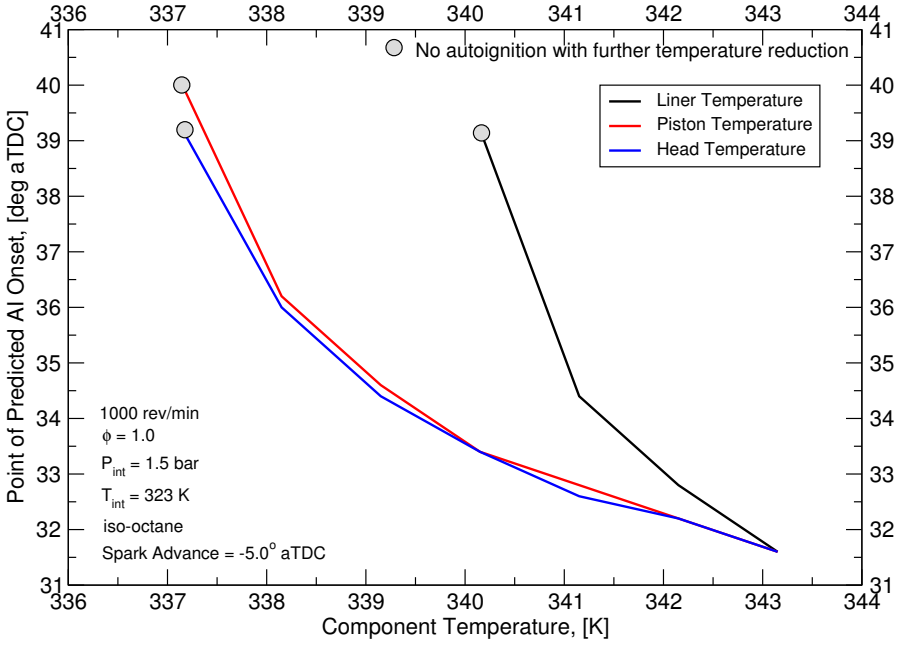

Figure 6.2: The effect of surface temperature on predicted autoignition onset point in the LUPOE2-D boosted engine as predicted by LUSIE. Spark timing was advanced from the autoignition boundary by 1.0^{o}CA.

the combustion chamber leading to a different performance of the empirical autoignition models. The notion that the empirical autoignition models will perform differently with different engines is not surprising, if unsatisfactory, from a modelling point of view because of the different pressure-temperature regimes the engines are operating under. The pressure-temperature regime of the end gas largely determines the autoignition characteristics for a given engine, all else being equal. In other words each empirical model was tuned to a limited range of conditions and its extrapolation outside that range may not necessarily be successful. The interest in the current study lies in the performance of the models under downsized conditions.

6.3.1 Performance of autoignition models on non-boosted engines

Two autoignition models are investigated in this section, of Douad and Eyzat (Section 3.3.1), later referred to as the D&E model, and the skeletal skeletal Keck model (see Section 3.3.2.3). The engines used for comparison in this section are the non-boosted LUPOE2-D engine, the boosted LUPOE2-D variant, the baseline production engine, AJ133, and the JLR downsized research engine, UB100. These engines operate under very different conditions, as can be seen in Figure 6.3, where the pressure and temperature history of the end gas have been plotted for all four engines. All engines conditions investigated here were operated under full load, low engine speed conditions, though the exact operating points are not identical. The pressure for all engines is taken from measured in-cylinder data, while the respective gas temperatures have been calculated using the LUSIEDA reverse cycle analysis package described in Section 3.7. It can be seen that there is a large spread in the unburned pressure - temperature regime between the four engines; it is also noted that the AJ133 engine and the boosted LUPOE2-D have similar pressure temperature regimes, however this is caused by heating of the intakes prior to testing to assist fuel mixture properties. It is well known that the autoignition behaviour of the engine will largely be determined by the pressure-temperature history of the engine, therefore the wide operating range of the four current engines should be an ideal set for testing the predictive capability of the two different autoignition models.

It should be noted here that the octane number input for the D&E model (see Eq. 3.20) is based on the Kalghatgi K factor, discussed in Section 2.6.1, which has been determined for each engine individually based on Eq. 2.33 and 2.32. The T_{comp15}, K and OI for the Shell fuel can be seen in Table, 6.2. It should be noted that for all simulations the non-boosted LUPOE2-D and boosted LUPOE2-D engines were run on iso-octane for

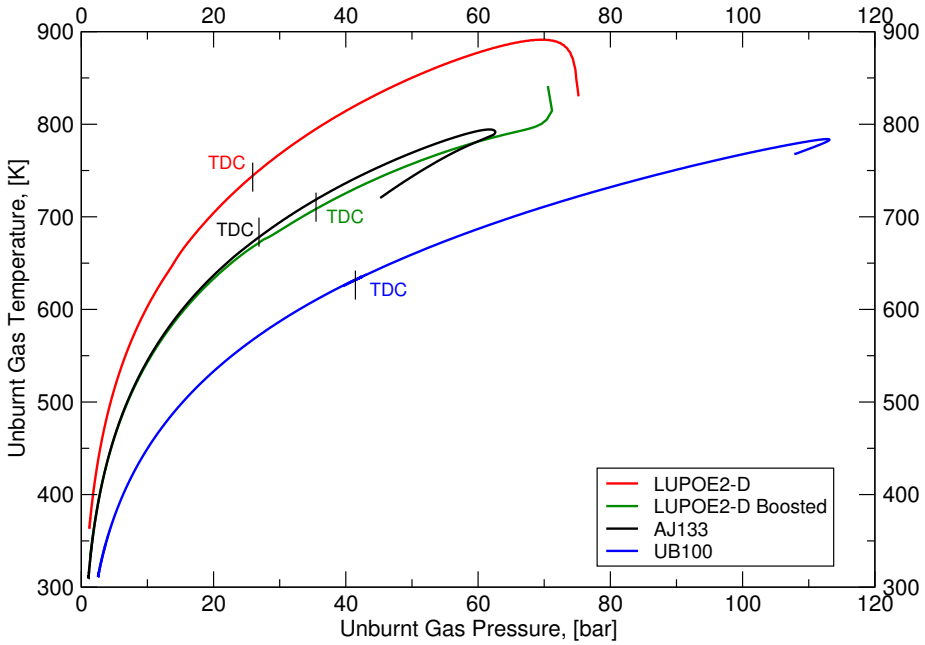

Figure 6.3: The pressure - temperature history of the end gas for the four different engines discussed in this thesis. The reverse cycle software LUSIEDA was used to predict the unburnt gas temperatures based on experimentally gathered cylinder pressure data.

Engine	Engine Speed (rev/min)	Spark Timing (^{o}CA bTDC)	Pressure at IVC/IPC (bar)	Temperature at IVC/IPC (K)
LUPOE2-D	1500	20	1.21	363
LUPOE2-D boosted	750	6	1.6	333
AJ133	1500	7	1.1	309
UB100	2000	3.5	8.5	311

Table 6.1: Summary of the operating conditions of the four engines shown in Figure 6.3.

Engine	T_{comp15} (K)	Kalghatgi K factor	OI
LUPOE2-D	661	-0.98	100
LUPOE2-D boosted	595	-1.35	100
AJ133	602	-1.31	118.5
UB100	497	-1.9	111.75

Table 6.2: The Kalghatgi K factor and Octane Index for the four different engines and two different fuels.

the comparisons seen in this chapter; iso-octane (100RON, 100MON) has a sensitivity (RON-MON) of 0 and therefore is not affected by the K factor.

Experimental cycles containing autoignition events were available for three of the four engines, the UB100 however did not display autoignition. It was decided that it was not within the scope of the testing program to induce autoignition events because of the limitation on parts and the concerns with running the engine at a condition which could be potentially damaging; some cycles captured from the UB100 engine did however display knock-like pressure signals - an observation which will be discussed later in this chapter (see Section 6.5.2).

The majority of cycles within each dataset were normal combustion cycles, however, most sets contained a number of cycles with autoignition and it was these autoignition cycles which resulted in knocking events that were the key to assessing the performance of the two autoignition models. The reverse cycle analysis code, LUSIEDA, was used on each of the experimentally captured crank-resolved pressure traces of firing cycles LUSIEDA is capable of calculating the temperature history of the end gas which, combined with the pressure data, could be used as input to drive an autoignition model, also embeded in LUSIEDA, and obtain a predicted autoignition onset.

Experimental autoignition onset timing vs the predicted autoignition timing, for the four engines, can be seen in Figures 6.4 to 6.7; these figures are based on those found in the thesis of Smallbone [2004] & Roberts [2010]. If the models were perfectly calibrated then all symbols would reside on the 1:1 slope line, which implies that the experimentally seen point of autoignition onset would have been perfectly predicted by the autoignition model, to the nearest 0.2^o CA (the time-step of the autoignition model). The onset point of experimental autoignition was determined manually by observation of the crank-resolved pressure signal as well as the differentiated pressure signal. The first peak of the knock wave was used to determine the point at which the normal flame

propagation event was "interrupted" by the high frequency pressure oscillation which characterises that a knock event has occurred. The base of the first knock peak, where the deviation from the normal cycle occurs is identified as the autoignition onset point. The locations at which the pressure waves initiate will seldom be equidistant to the pressure transducer, introducing a small error into the perceived autoignition onset timing. This error is a function of the operating speed of the engine, the engine bore, *D*, and the speed of the pressure wave (sound), *a*, determined by:

$$a = \sqrt{\gamma RT} \tag{6.1}$$

where γ is the ratio of specific heats, R is the specific gas constant JkgK^{-1} and T is Temperature of the gas (K). For the LUPOE2-D engine operating at 1500 rev/min, with an assumed gas temperature of 800 K, results in approximately a 1^o CA error.

The results for the model prediction of autoignition in the non-boosted LUPOE2-D research engine can be seen in Figure 6.4. It is clear that the Keck model over-predicts the autoignition onset time in the LUPOE2-D engine (over-prediction here means that the autoignition onset time for a cycle is predicted earlier than seen in the corresponding experimental cycle), the mean error of the Keck model predicting autoignition in the non-boosted LUPOE2-D engine is 4.6^o CA earlier than the experimentally observed onset time. The performance of the original D&E model, in this instance, is also poor; although knock events were observed within the set of experimental cycles, these have not been predicted by the D&E model. A possible cause of such a poor model performance is the uncommon operating conditions of the engine where the temperature, at a given pressure, has been artificially increased via heating of the intake air-fuel mixture. The empirical D&E model does not account for the Negative Temperature Coefficient (NTC) (see Section 2.5.1) behaviour (at engine like pressures) observed in the autoignition delay time curves of most fuels. While this could possibly be a source of error for some engine conditions and fuels it should be mentioned that the test fuel, iso-octane (100PRF), does not have as pronounced an NTC region compared to other PRF blends owing to the reduced composition of n-heptane. Moreover, the NTC region tends to reduce with an increase in pressure (Fieweger et al. [1997]), and therefore comparisons of autoignition performance, as determined by the D&E model under boosted conditions, should be made with careful consideration.

The performance of the two autoignition models when applied to the AJ133 engine can be seen in Figure 6.5. The skeletal Keck model under-predicts autoignition compared with the over-prediction of events in the non-boosted LUPOE2-D engine seen previously.

Although there were significantly fewer knocking events in the AJ133 engine vis-á-vis the non-boosted LUPOE2-D engine, it can still be seen that, generally, there exists a trend that the kinetic model under-predicts autoignition. The empirical D&E model appears to largely under-predict some cycles while again it fails to predict any autoignition event for a few of the experimental cycles with autoignition. There is a distinct offset in the model behaviour between the non-boosted LUPOE2-D and the AJ133 engines, most notably that the delay times predicted by the empirical D&E model are shorter for the latter, while the skeletal Keck model now appears to be under-predicting these rates. There are two possible causes for this: a) the first is the different pressure-temperature regime the engine is operating in, as can be seen in Figure 6.3, where at the point of TDC, both engines have a similar pressure but the non-boosted LUPOE2-D engine has an unburned gas temperature 60 K higher than the AJ133 engine. b) Because the fuel used within the test AJ133 engine was a commercially available forecourt pump fuel with a RON of 98, it will behave differently to iso-octane and is likely to have a reduced NTC region vis-a'vis iso-octane used in the non-boosted LUPOE2-D engine tests as it is blended from single-stage autoignition components (such as ethanol), which have little (if any) low intermediate temperature oxidation (Fieweger et al. [1997], Roberts and Sheppard [2013]). The major differences in operating condition which could possibly influence the base autoignition characteristics between the two engines are: the fuel type, the air-fuel mixture and residual levels. The type of fuel will influence the burning rates within the engine, as will the rich operation of the AJ133 engine. In addition to affecting the burning velocity, a rich mixture will introduce a cooling effect to the charge; an effect not considered by LUSIEDA.The interesting observation from this set of results is that only the D&E model appears affected by the difference in fuel; an input exclusive to the D&E model is the RON number which, although adjusted for between the iso-octane (100RON) and pump fuel (98RON), could not account for the NTC behaviour of the fuel. Higher residual gases, in either of the engines, that do not directly influence the temperature of the mixture, would also alter the delay times of the fuel; indeed the D&E model was validated with unkown levels of residuals.

6.3.2 Performance of autoignition models for boosted engines

The ability of the two models to predict autoignition events within an engine operating at high pressure conditions was explored using the boosted LUPOE2-D engine, and also a heavily boosted engine (UB100). Prediction of autoignition in the boosted LUPOE2-D engine can be seen in Figure 6.6; it should be noted that the pressure-temperature histories of the end gas in both the boosted LUPOE2-D engine and the AJ133 engine are very sim-

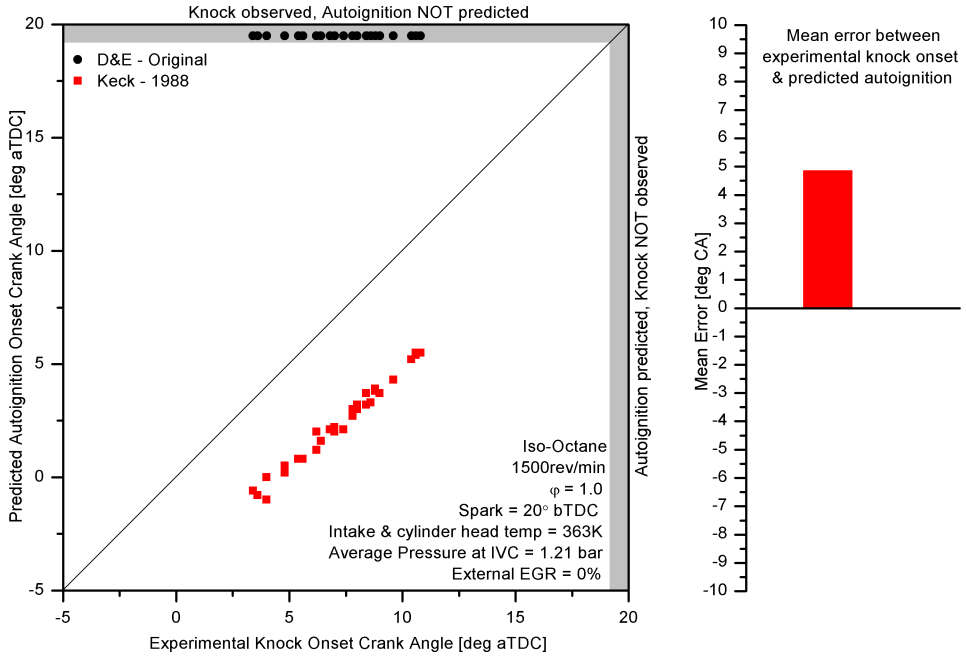

Figure 6.4: Performance of empirical (D&E) model and skeletal (Keck) kinetic model for the non-boosted LUPOE2-D engine.

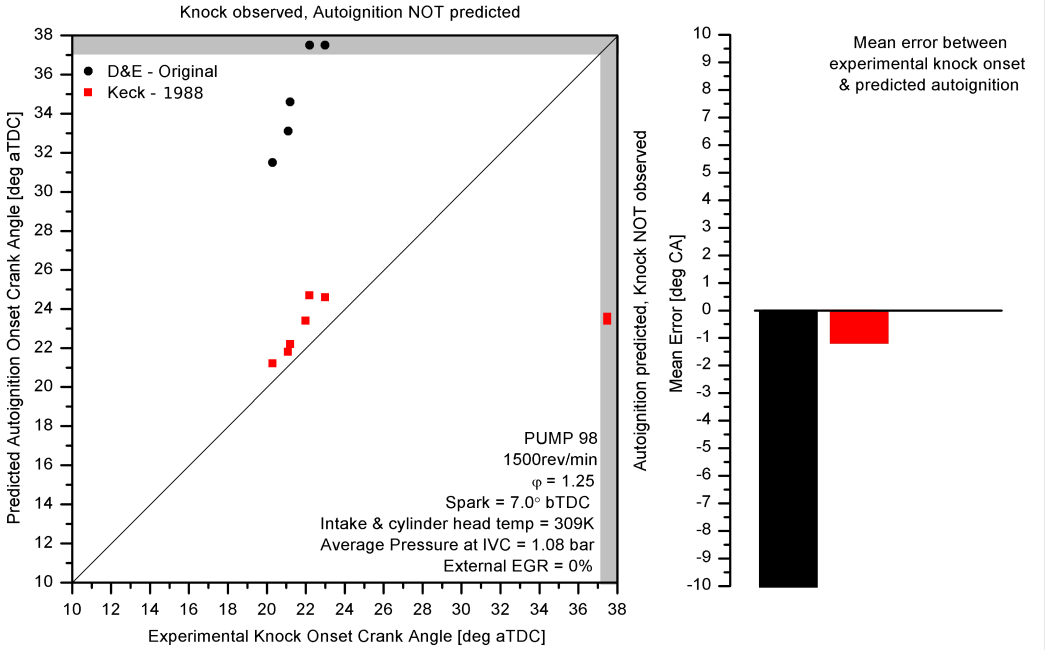

Figure 6.5: Performance of empirical (D&E) model and skeletal (Keck) kinetic model for the AJ133 engine.

ilar, as seen earlier in Figure 6.3. It is therefore not surprising to see that the Keck model perform in a very similar way in predicting the autoignition characteristics on the boosted LUPOE2-D engine as was seen on the naturally aspirated AJ133 engine. Autoignition is still under-predicted by the skeletal Keck model by a mean value of approximately 1^o CA over all of the observed knocking cycles. The D&E model appears to be closer to the experimental data than on the previous two test cases, although still under-predicting the result. When taking into account that the pressure-temperature history of the boosted LUPOE2-D and AJ133 engines are very similar it is remarkable that the performance of the D&E model appears to be in better alignment in the boosted LUPOE-2D vis-á-vis the AJ133 engine .

The heavily boosted UB100 engine operating under a pressure-temperature regime which is significantly lowed compared from the other three engines, did not exhibit knocking cycles throughout the testing, owing to project requirements as previously explained. A prediction of autoignition was still performed on these cycles to see whether or not the models would predict autoignition in the absence of any observed experimentally. It was seen that the D&E model predicted that a significant number of cycles (98 out of 100) had exhibited autoignition, see Figure 6.7. The kinetic model conversely erroneously predicted autoignition in only 2 events out of the 100 cycles.

The mean error bars presented in Figures 6.4 to 6.7 are not representative of the actual error of a model when the majority of cycles are incorrectly predicting autoignition where none is present experimentally, or vice-versa. It can be considered that there are four possible outcomes from model prediction of autoignition compared to experimental results:

1. Knock is seen in an experimental cycle and autoignition is predicted
2. Knock is not seen in an experimental cycle but autoignition is not predicted
3. Knock is seen in an experimental cycle but autoignition is not predicted
4. Knock is not seen in an experimental cycle but autoignition is predicted

Clearly, item numbers 1 and 2 are desirable outcomes from prediction while items 3 and 4 are undesirable. If the experimental and predicted data, presented in Figures 6.4 to 6.7 is categorised into one of the four groups then a better understanding of the model performance over all conditions can be seen. Hence, presenting this data in the format seen in Figure 6.8 provides an overview of the performance of the individual models for each engine.

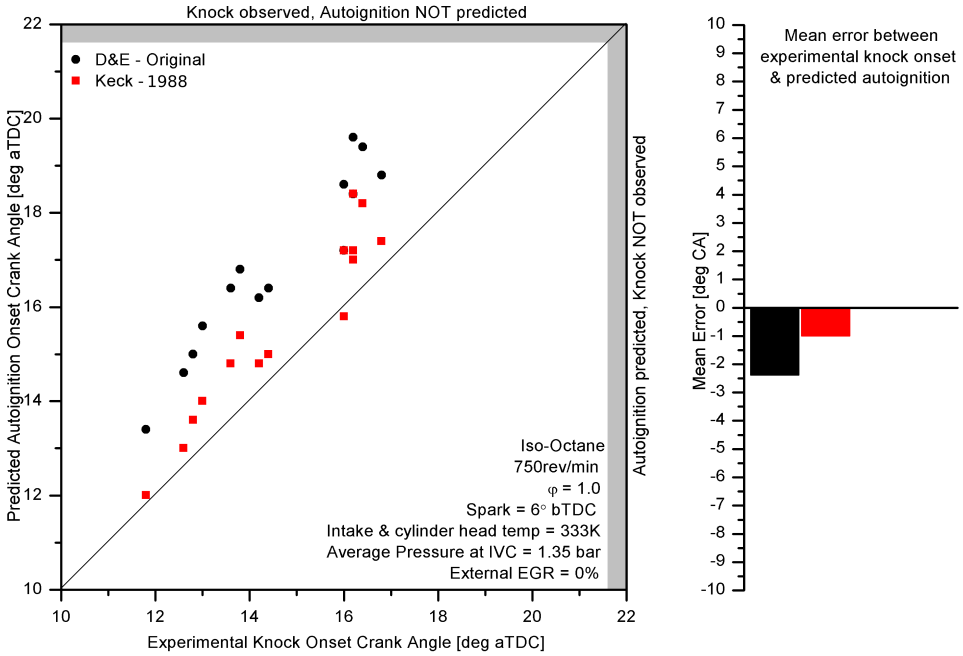

Figure 6.6: Performance of empirical (D&E) model and skeletal (Keck) kinetic model for the boosted LUPOE2-D engine.

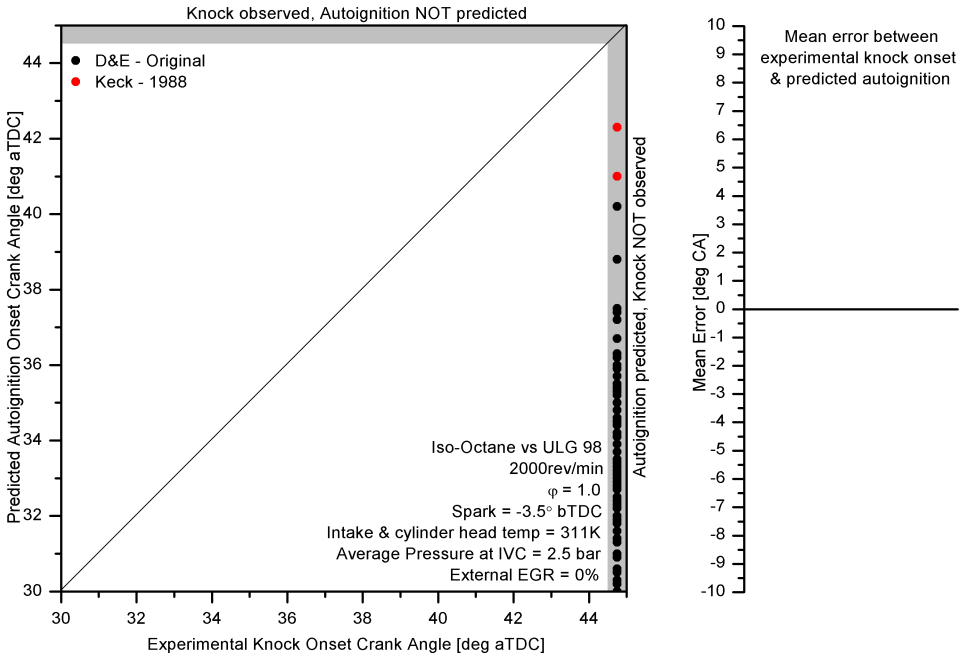

Figure 6.7: Performance of empirical (D&E) model and skeletal (Keck) kinetic model for the UB100 engine. In this example there were no knock cases seen experimentally.

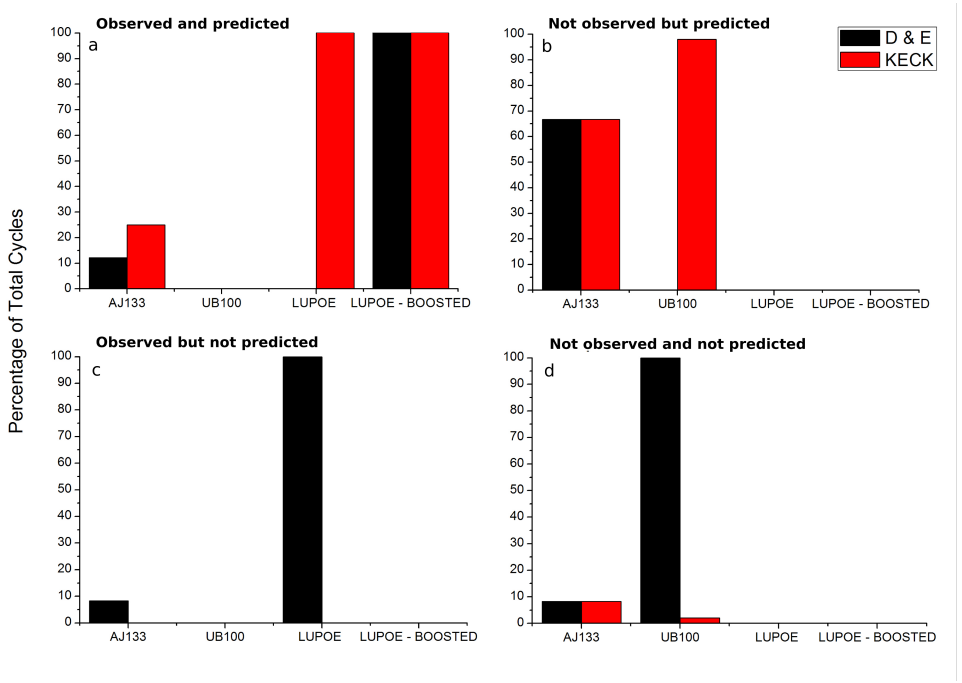

Figure 6.8: A comparison of the performance of two autoignition models for four different engines. a) Knock seen experimentally and autoignition predicted b) Knock not seen experimentally and autoignition not predicted c) Knock seen experimentally but not predicted d) Knock not seen experimentally but predicted.

It can be seen here that the skeletal Keck model gave better performance for the various engine types and operating conditions than the D&E model, although the main functionally of the empirical model (its ability to be tuned) was removed by not allowing adjustment of the model constants; however this step is representative of the issues faced by designers and developers where the pressure-temperature history of the end gas in a given engine is not known. Interestingly, the performance of the D&E model was least accurate for both the non boosted LUPOE2-D engine and the UB100 engine, operating at both extremes of the pressure-temperature history of the end gas for the four engines investigated. The assumption that the empirical model is poorly suited to accounting for changing engine types and conditions appears to have been validated in this study. Although a tuned model would be no worse at predicting autoignition than a chemical one (itself likely requiring tuning); ”out of the box” however, the chemical model appears to be better suited a to an array of engines.

6.4 The variability of autoignition in SI engines

As discussed throughout Chapter 5, variability between two combustion events within SI engines exists, the variation is mainly attributed to fluctuations of $u'$and ϕ. The variability of these quantities results in a variability in burning rates and, subsequently, performance. The likelyhood of an autoignition event occurring in an engine, more specifically an individual cycle's propensity to autoignite is almost solely attributed to the pressure-temperature regime experienced by the unburned gas during the cycle. Results from experimental and predictive methods throughout the course of this work suggest that another variability is observed, a variability that affects the autoignition onset time seemingly independent of the pressure-temperature history.

A number of knocking cycles, captured in the non-boosted LUPOE2-D are shown in Figure 6.9. At the relatively low intake pressure it may be observed that, cycles which exhibit a steeper pressure slope, i.e. faster cycles, have the earlier autoignition onset time. An additional observation is that the severity of the pressure oscillations appears to increase in the slower cycles. A likely reason for higher intensity knock is because of the increased unburned mass fraction of fuel at the point of autoignition in the slower cycle cases. The faster burning cycle consumes the unburned-fuel mixture at a rate that is faster than the chemical reaction rates promote autoignition. In other cases, such as on the AJ133 engine (see Section 5.4), it is seen that the fastest cycles are the only cycles, within a set, which will autoignite and lead to a knock event; in these cases, the rate of heat release attributed to the combustion event acts as the catalyst for the autoignition reactions and therefore the severity of an event and likelyhood it will occur are not intrinsically linked. The non-boosted LUPOE2-D engine is, in this instance, operating in a regime where autoignition is promoted to a point that all cycles exhibit autoignition, thus it is the slower cycles, with a greater unburned mass, which will have higher knock intensity.

At the higher pressure condition in the boosted LUPOE2-D engine, a similar set of knocking cycles were captured; these cycles can be seen in Figure 6.10. Unlike cycles seen in Figure 6.9, there appears to be a larger variability of the onset of autoignition with respect to the cylinder pressure for a given cycle. Again, it is thought that the cylinder pressure-temperature history drives the autoignition characteristics; though there are cycles present which do not appear to conform to this hypothesis, and therefore dispute it by definition. It can be seen however, that cases with an almost identical pressure-temperature history (Cycle 5 & Cycle 6) exhibit an almost identical point of autoignition. It can also be seen that Cycle 2, with lower pressure, and therefore temperature, expe-

riences an autoignition event before Cycle 1, despite the higher cylinder pressure and temperature. It is possible that the faster cycle (Cycle 1) enters the NTC region before the slower cycle at a lower temperature, reducing the delay time; however as disccused by Fieweger et al. [1997] iso-octane does not have a pronounced NTC region at engine like pressures . More likely is that a hot-spot, either component, or hot-spot in the end gas, such as lubricant oil acts as a catalyst for the autoignition reactions. Analysis of the cycles using LUSIEDA, using the skeletal Keck and empirical D&E model was performed to give further insight into the observation.

The cylinder pressure, at -90^o aTDC for each of the six knocking cycles captured in the non-boosted LUPOE2-D engine (seen in Figure 6.9) can be seen in Figure 6.11. The cylinder pressure values at -90^o aTDC, are plotted against the autoignition onset seen experimentally. Also seen in the Figure are the crank-angle of autoignition onset as predicted by the Keck and D&E autoignition models. It can be seen that early on in the cycles there is little or no correlation of cylinder pressure to the eventual time of the autoignition event, the pressure and temperatures in the cylinder at this point, are too low to cause significant reactions to progress. The Keck model predicts autoignition too early, while the D&E model has been modified in order to achieve an aligned fit between predicted and experimental cycles. A successive approximation technique was applied to the activation energy constant, B, from 3800 to 3496 (see Eq. 3.19) in order to predict any autoignition at all. It can be seen that the D&E model does not predict the autoignition event in the cycle with the earliest experimentally observed autoignition (cycle 2), it is likely that this is because of the reasons discussed previously; the fast burn-rate results in combustion that is so fast that it consumes the end gas faster than the heat release promotes autoignition

The cylinder pressure at TDC compared with the crank-angle of autoignition for the six knocking cycles can be seen in Figure 6.12. The autoignition models predict a strong correlation between the cylinder pressure late into the combustion process, compared with the eventual point of autoignition. Conversely the actual experimental cycles do not display such a strong correlation, for example, cycle 5 and cycle 6 are at a similar pressure at TDC, however there is 1^o CA difference in the point of autoignition, while the two autoignition models do not predict this difference; a similar trend is seen between cycle 1 and cycle 3 where the higher pressure cycle has a slightly later autoignition onset timing, not predicted by either model.

Under high-pressure conditions, as seen in Figure 6.10, the autoignition onset timing does appear to have a large variability vis-á-vis the non-boosted condition. As with the non-boosted condition, the cylinder pressure, early in the cycle appears to have little

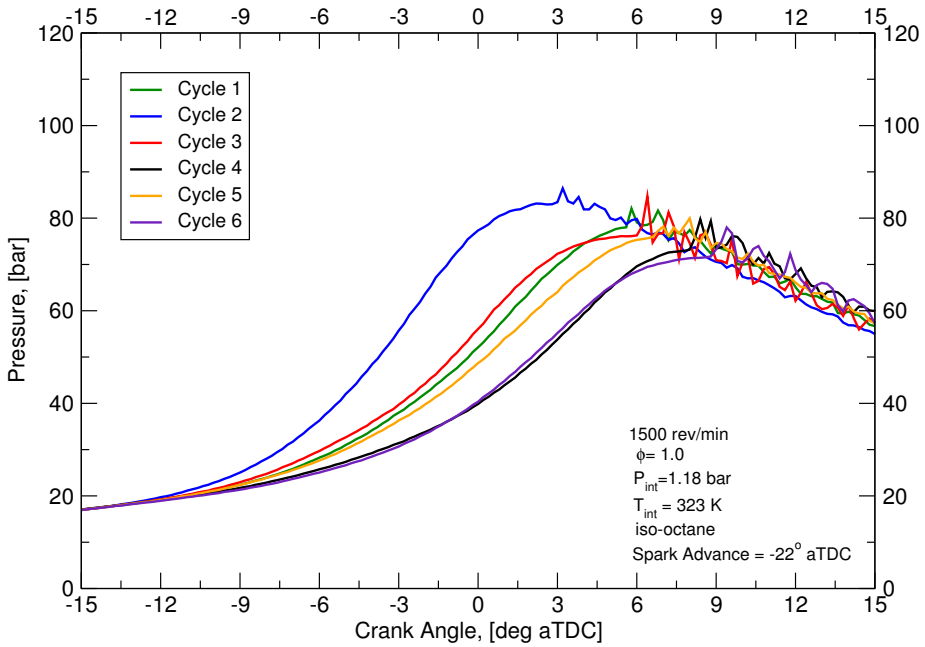

Figure 6.9: Six knocking cycles captured experimentally in the non boosted LUPOE2-D engine; cycle numbers are not representative of order at which they occurred. The operating conditions of the engine can be seen in the figure.

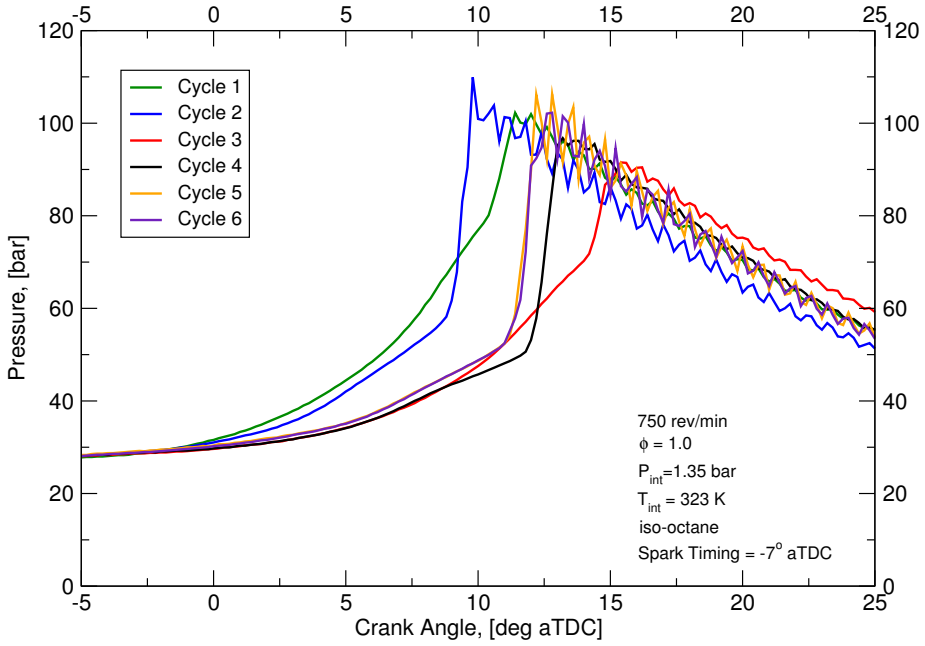

Figure 6.10: Six knocking cycles captured experimentally in the boosted LUPOE2-D engine; cycle numbers are not representative of order at which they occurred. The operating conditions of the engine can be seen in the figure.

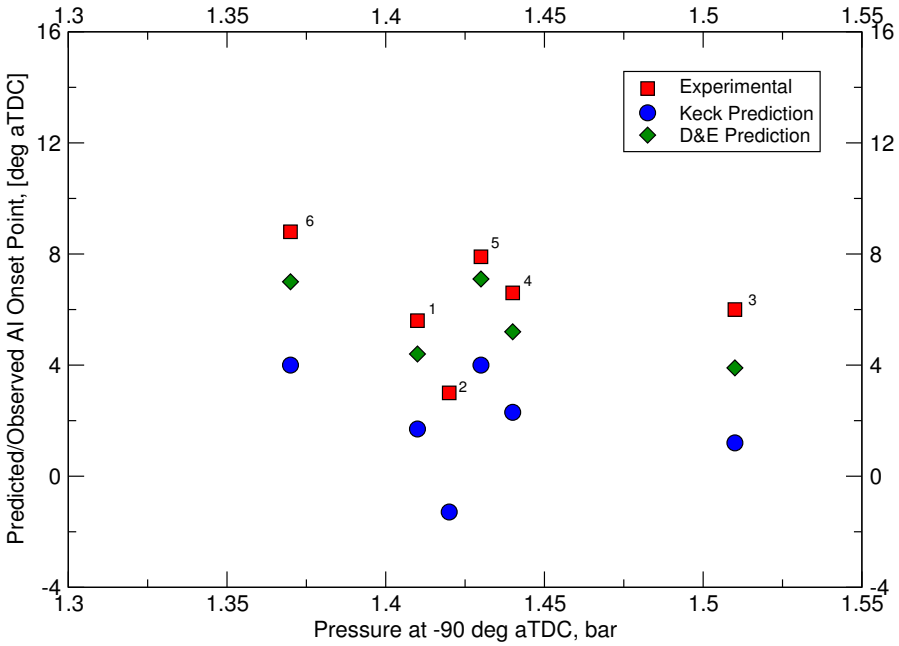

Figure 6.11: Autoignition timing vs pressure at 90^o bTDC for the six knocking cycles captured in the non-boosted LUPOE2-D engine.

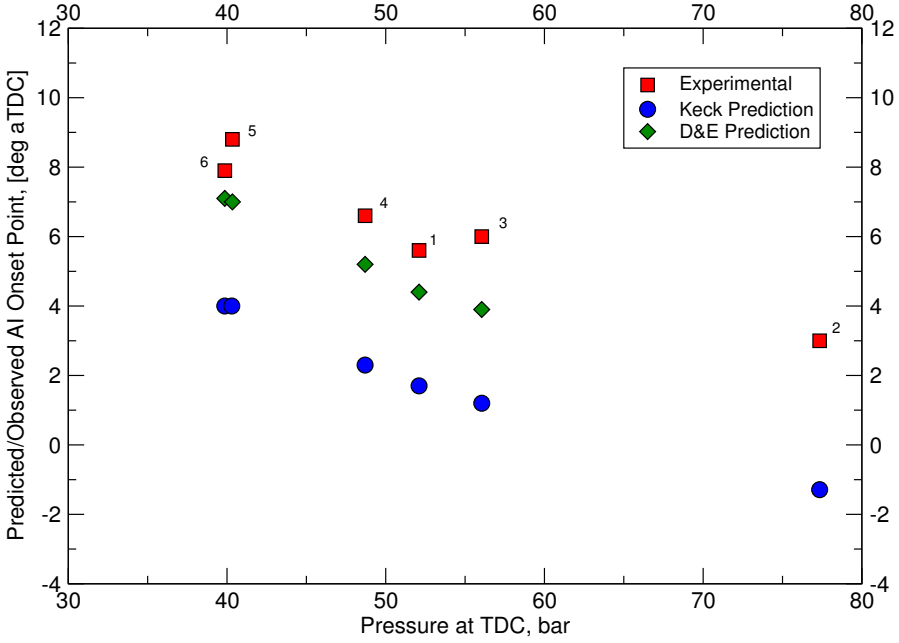

Figure 6.12: Autoignition timing vs pressure at the top dead centre for the six knocking cycles captured in the non-boosted LUPOE2-D engine.

influence on the autoignition onset timing, see Figure 6.13. It was intended to compare the two conditions while the cycles were at similar stages of combustion. Therefore the cylinder pressures at 8^oaTDC were taken, rather than TDC as with the non-boosted case, because of the later spark advance. It can be seen in Figure 6.14 that unlike the non-boosted condition (Figure 6.12), where there was a linear relationship between cylinder pressure at TDC and autoignition timing, at the boosted condition there appears to be much less of a correlation between cylinder pressure and autoignition onset timing; cycles 2, 4, 5 and 6 appear to follow this pattern, while the autoignition delay time of cycle 1 and 3 appear to be delayed based on the lower initial pressure.

The Keck model prediction of autoignition for cycle 1 is 10.3^oaTDC and 10.0^oaTDC for cycle 2, i.e. it predicts the same trend as seen experimentally, if not quite accounting for the magnitude change. The D&E model does not predict the trend correctly, in addition the it does not predict autoignition in the slower cycles (Cycle 4, & Cycle 5), this is contrary to the non-boosted condition where as it was seen that the fastest cycle was not predicted (as discussed in Section 6.3.1. Another observation that can be made is that the D&E model does not predict autoignition for cycle 6 while it does however predict autoignition in cycle 5, which appears to have an almost identical pressure-temperature history. A possible explanation for this is that early on in the cycle, where the pressures and temperatures are low, the cylinder pressure early in the cycle at -90^oaTDC is lower for cycle 6 vis-á-vis cycle 5. The criteria for autoignition with the D&E model is the Livengood and Wu integral which integrates autoignition delay times throughout the entire cycle. It is possible that the influence of early cycle pressures and temperatures are more sensitive in the D&E model compared with the kinetic model.

Having assessed six cycles from both the LUPOE2-D and LUPOE2-D boosted engines in detail, the R^2 method first introduced in Section 5.7 was extended in order to further assess the variability of knock onset timing. It can be seen in Figure 6.15 that the correlation between the point of observed knock onset in the LUPOE2-D engine and the instantaneous pressure value at a given crank angle, $P(\theta)$; as was seen with the correlation between P_{max} and $P(\theta)$, the R^2 value increases shortly after the point of ignition, where the influence of variability appears to be greatest. Experimentally, it is seen that the maximum R^2 value occurs at the earliest observed knock onset, after this point the scatter will begin to curve back on itself (as was seen in Figure 5.45). The maximum value is 0.92, suggesting that a strong correlation between final knock onset cylinder pressure exists. Additionally plotted in the same figure are correlations between experimental cylinder pressure and point of autoignition onset, as predicted by the D&E and Keck autoignition models; the autoignition models being driven by experimental pressure data. It can be

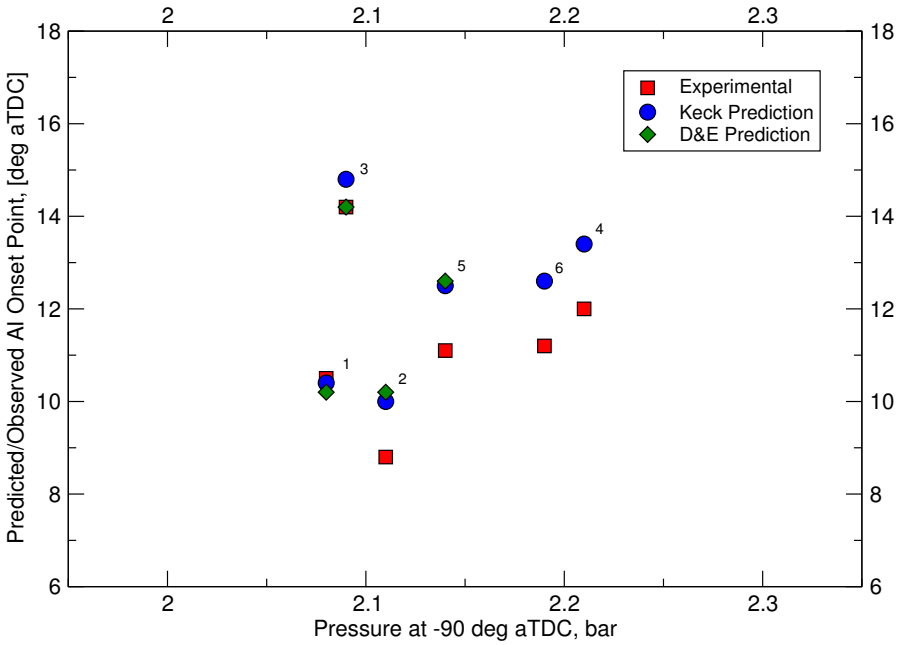

Figure 6.13: Autoignition timing as a function of the cylinder pressure at 90^o bTDC for the six knocking cycles captured in the boosted LUPOE2-D engine.

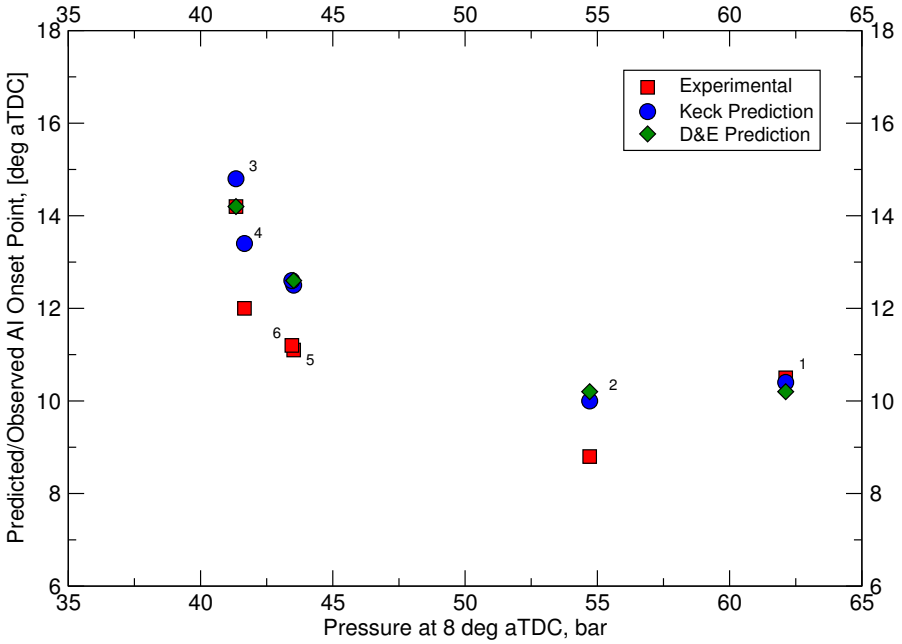

Figure 6.14: Autoignition timing as a function of the cylinder pressure at -8^o bTDC for the 6 knocking cycles captured in the boosted LUPOE2-D engine.

seen that there appears to be a greater correlation between P(θ) and autoignition onset point vis-á-vis the experimental P(θ) and knock onset point. This is likely to be because the models are driven by the experimental pressure and derived temperature only. The reduction in R^2, seen around TDC, for the Keck prediction is caused by the earlier than observed experimental prediction of autoignition. Overall, for the LUPOE2-D engine it can be seen that the point of knock onset is strongly linked to the burn rate.

As with the non-boosted LUPOE2-D case, cycles for the LUPOE2-D boosted engine which contained autoignition have been identified and an R^2 correlation between P(θ) and experimental knock onset point has been performed. Additionally, the Keck and D&E predictions of autoignition onset timing based on the experimental pressures have been plotted. The results can be seen in Figure 6.16. In contrast to the non-boosted case (which had an R^2 value close to 1), it can be seen that the maximum value of R^2 is around 0.5 for the experimental case. The suggestion from this low R^2 value is that a variability of autoignition, aside from the burning rate, appears to exist for the boosted variant of the LUPOE2-D engine. The source of the increased variability is possibly caused by a hot-spot (either surface or oil droplet) which are believed to be causes of pre-ignition under boosted conditions. Another consideration is the dataset size for the LUPOE2-D boosted engine vis-á-vis the non-boosted engine. The boosted engine consisted of only 25 knocking cycles while the non-boosted engine contained 90. Therefore the influence of "outliers" on the R^2 value would be greater for the boosted engine. Also of consideration is that the boosted cycles were captured at 750 rev/min, thus a greater time was available for hot-spots to influence the autoigntiion tendency.

6.4.1 Variability of the Kalghatgi K factor

One variability of autoignition which must be independent of the burn rate is the variability in the response of modern engines to sensitive fuels (fuels which have unequal RON and MON numbers), defined by the K factor (see Section 2.6.1). If a variability in K exists, then a difference in the effective OI of the fuel, and therefore the autoignition performance of the engine must also exist. For a variability in K to exist there must be a variability of T_{comp15} in the compression phase of the engine cycle; clearly before variability in combustion may influence autoignition.

Of the four engines reported in this work, the boosted LUPOE2-D shows the largest variability in T_{comp15} over a 100 cycle dataset. The dataset here contains a large variation between at 15 bar pressure on the compression stroke. The phase of the compression

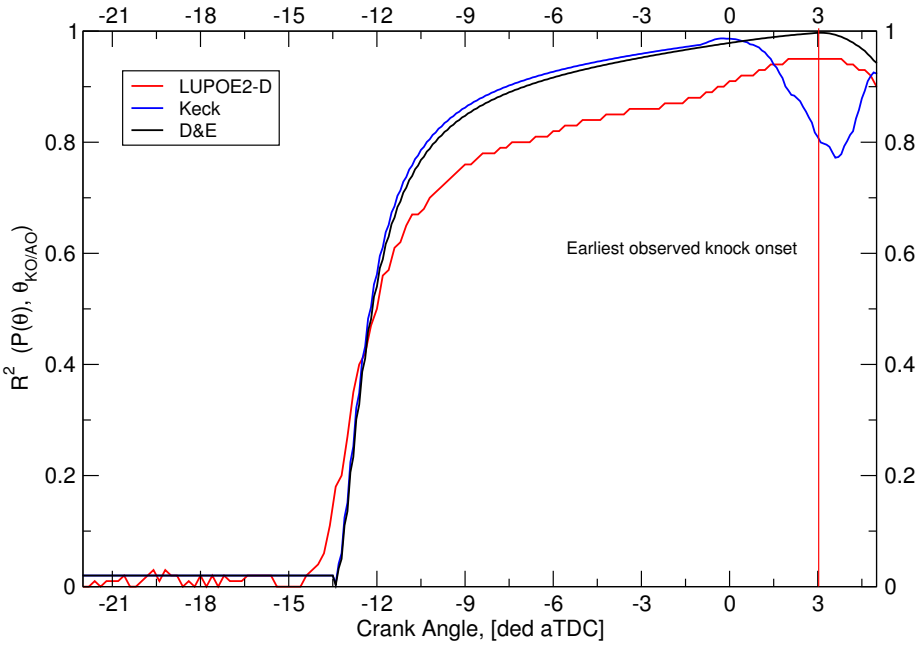

Figure 6.15: R^2 profile of P(θ) vs the crank angle of experimental knock onset and predicted autoignition onset for the LUPOE2-D engine.

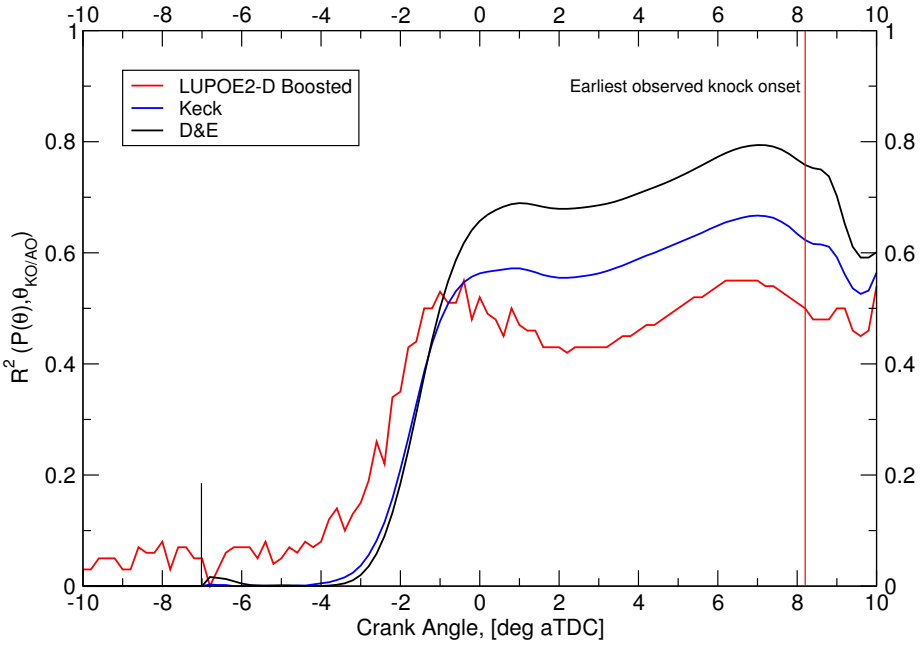

Figure 6.16: R^2 profile of P(θ) vs the crank angle of experimental knock onset and predicted autoignition onset for the LUPOE2-D boosted engine.

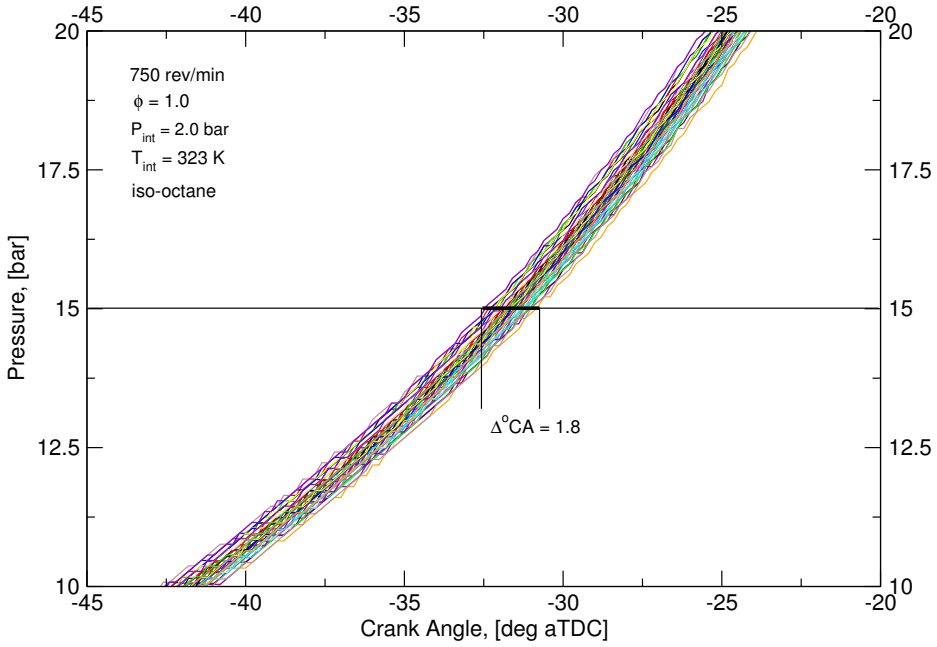

Figure 6.17: The variation of intake pressure at 15 bar in the LUPOE2-D boosted engine.

stroke of interest for the 100 cycles can be seen in Figure 6.17. It can be seen that there is approximately 1.8^{o}CA variation over which the individual cycles reach 15 bar.

In the LUPOE2-D engine at the shown conditions, a difference of 1.8^o CA between -32.5^o CA and -30.7^o CA corresponds to a T_{comp15} difference of 9 K. From Eq. 2.33 this is a difference in K value of 0.05, which, for the Shell fuel corresponds to a variation in OI of 0.5. A difference in OI of 0.5, however between, 114 and 113.5, when used in the D&E model in a LUSIE predictions at knocking conditions on the boosted LUPOE2-D engine such as those seen in Figure 6.17, with a spark timing of -2^o aTDC and corresponds to a small difference in autoignition delay time of 0.1^o CA, see Case 1 and 2 in Table 6.3.

The variability in cycles seen in Section 6.4 was far greater than 0.1^o CA however and it can be seen that the variability in K value is unlikely to contribute significantly to the observed variability which appeared to be independent of the burn rate. In addition, the cause of the difference T_{comp15} values can be traced to a disparity in intake pressure of approximately 0.1 bar. The impact of the different intake pressures on autoignition onset timing can be seen in Table 6.3, case 3 and 4 where the same OI value is set to remove any influence it has. Case 5 and 6 best reflect the actual engine conditions, where the cycle with lower pressure at IPC reaches T_{comp15} later in the cycle. Where the cycle starts at a lower pressure it needs to be compressed further, isentropically, to the same pressure and therefore must be at a higher temperature; the reasonable assumption is that both cycles start at the same temperature despite different dynamic pressures. It can

Case	P_{IPC}	OI_{Shell}	Predicted Onset (^{o}CA aTDC)
1	2.00	114.0	15.7
2	2.00	113.5	15.6
3	1.95	113.75	15.9
4	2.05	113.75	15.4
5	1.95	113.5	15.8
6	2.05	114.0	15.5

Table 6.3: The influence of pressure and K corrected OI on autoignition performance.

be seen in Table 6.3 that when both the correct intake pressure and OI value are used, the variability between cases reduces.

It can be said therefore that although a variability in the K factor, and therefore effective OI, exists in engines, it has a small impact on autoignition. When the correct intake pressures are imposed however, the variability increases for the same OI values. Finally, using the correct pressure and OI value reduces autoignition variability vis-a-vis the case where only pressure is adjusted, while it is greater than where the average intake pressure is used. Moreover the variability is small between all cases compared to variability seen in Section 6.4

6.5 Abnormal combustion in a heavily boosted engine

Throughout the UB100 testing program a number of irregular features were observed in the crank-resolved in-cylinder pressure traces. The two most notable observations were the occurrence of apparently stochastic pre-ignition and also the occurrence of high frequency pressure oscillations, initially mistaken for knocking cycles. This section contains a detailed analysis of these irregular combustion occurrences as well as a discussion of some of the more ”interesting” cycles from the UB100, believed to be on the knock boundary.

6.5.1 Pre-ignition in the UB100

Early in the testing program it became apparent that pre-ignition was occurring within the UB100. These pre-ignition events were being followed by 'super knock', identified by very high amplitude pressure oscillations. A frequent occurrence of these events would lead to damage of engine components. Early analysis was unable to determine clearly whether this pre-ignition was caused by hot-spot ignition, or gas-phase autoignition. Further analysis at Leeds shows that the pressure rise is controlled and progressive, up to the point of the 'super-knock' event, (see for example Figure 6.21).

Three samples of "normal" cycles, characterised by very low noise in the differentiated, $\frac{dP}{d\theta}$, pressure signal, can be seen in Figure 6.18. The pressure rise occurs after a delay period from the point of ignition to a fully propagating pre-mixed flame; pressure oscillations in the cylinder are small in this cycle. A "noisy" cycle (Cycle 2) can be seen in Figure 6.19 ; comparing this cycle with those that can be seen in Figure 6.18 there are similarities. The pressure rise is again consistent with the expected progression after ignition, here denoted by the vertical red line. The difference vis-á-vis Figure 6.18 is seen later in the cycle where apparent pressure oscillations, around the location of maximum pressure, occur. These oscillations will be discussed later in this section. In Figures 6.20 & 6.21 examples of cycles with pre-ignition can be seen.Cycle 90 from the dataset can be seen in Figure 6.20. Upon first inspection, it appears to show a pressure rise due to combustion occurring after the point of ignition, i.e. "normal" combustion, however comparing this cycle with the two previous cycles it can be seen that the delay time is too short, and thus it is likely that ignition began before the point of ignition. The high amplitude pressure oscillations also suggest a higher heat release profile than would be expected for this engine, corroborating the pre-ignition theory for this cycle. Cycle number 83 from this 100 cycle dataset shows definite pre-ignition, as seen in Figure 6.21, with the pressure rise visually occurring before the point of ignition. It can also be seen that the 'super knock' event is more severe vis-a-vis previous cycles. Cycle number 22 and cycle 44 seen in Figures 6.22 & 6.23 respectively, both show early pressure rise before the point of ignition, followed by the most severe 'super knock' seen in this dataset.

A feature of these pre-ignition cycles is that the earlier the start of combustion, the more intense pressure oscillations appear later. Releasing the chemical energy of a fuel into a smaller volume will result in a higher knock intensity; at earlier ignitions the cylinder volume is smaller because of the closer proximity to TDC. Perhaps the most important feature of all of the pre-ignition cycles is that, although the pressure rise is faster vis-á-vis non-pre-ignition cycles, it is not quasi-instantaneous akin to HCCI combustion,

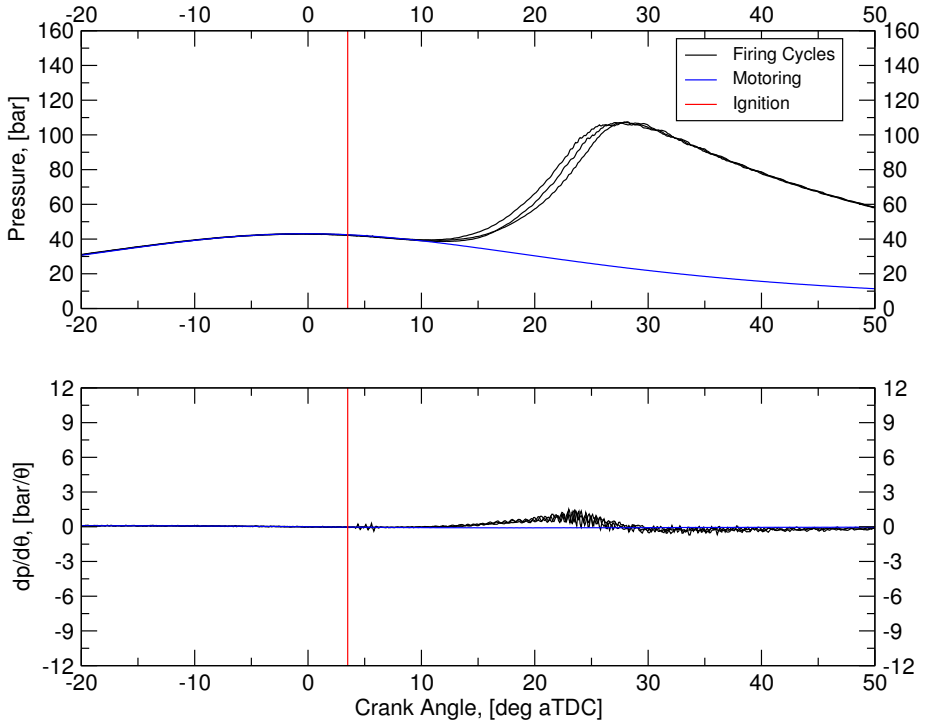

Figure 6.18: Three cycles displaying a ″normal″ pressure rise signal in the UB100 at full load and the differential of that signal.

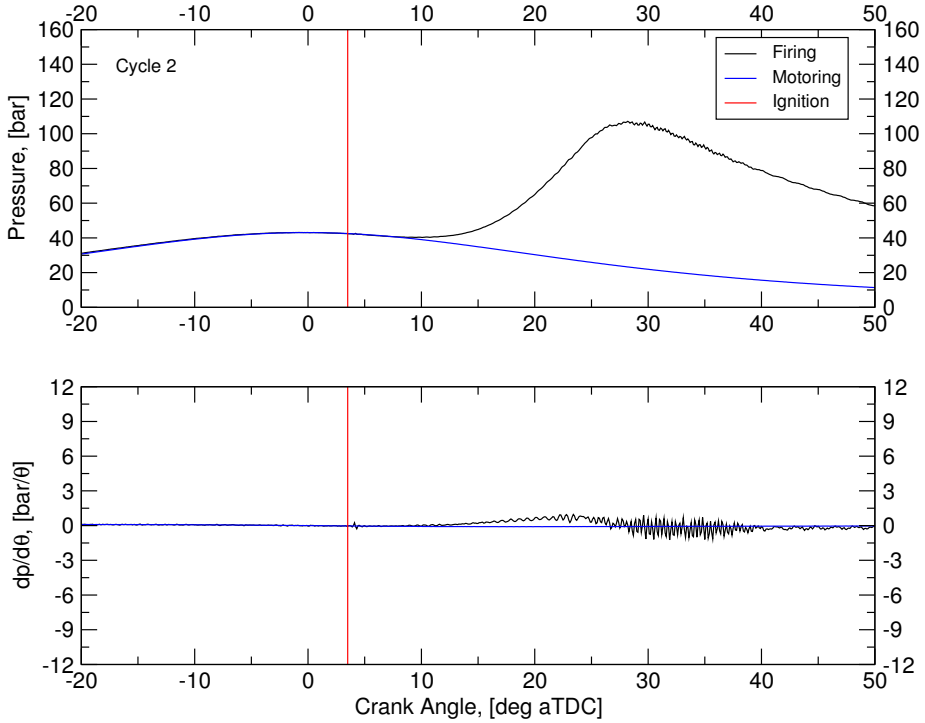

Figure 6.19: A cycle displaying a normal pressure rise in the UB100 with a slight oscillation in the signal at around peak pressure.

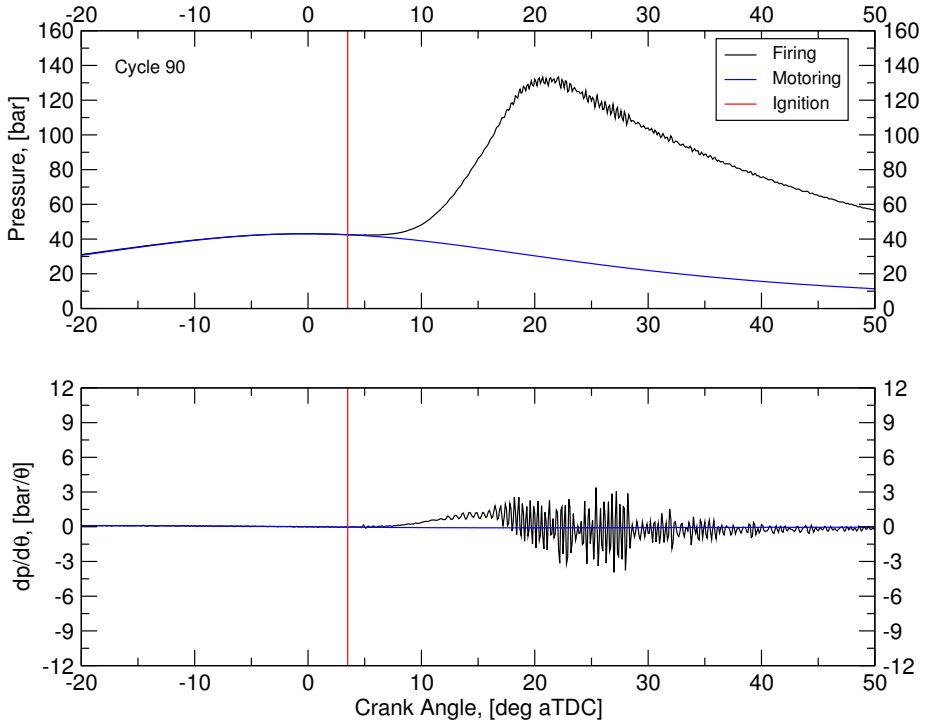

Figure 6.20: A cycle with a pressure rise due to combustion occurring closer to the point of ignition, much earlier than normal combustion cycles as seen in Figure 6.18.

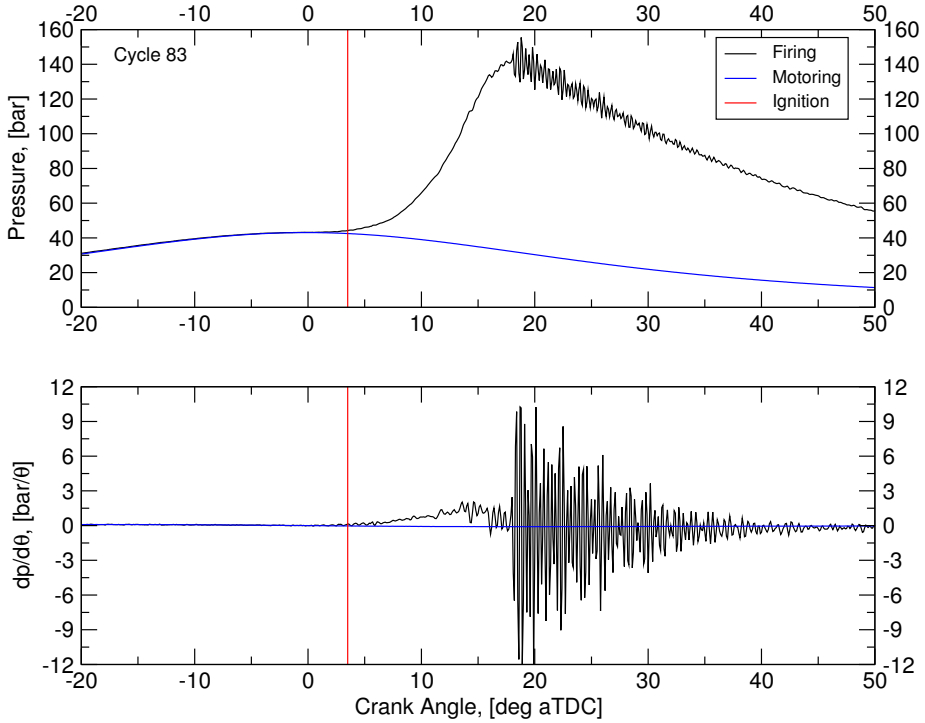

Figure 6.21: Cycle 83 from the dataset showing pressure rise due to combustion occurring before the point of ignition. Followed by moderately severe 'super knock'.

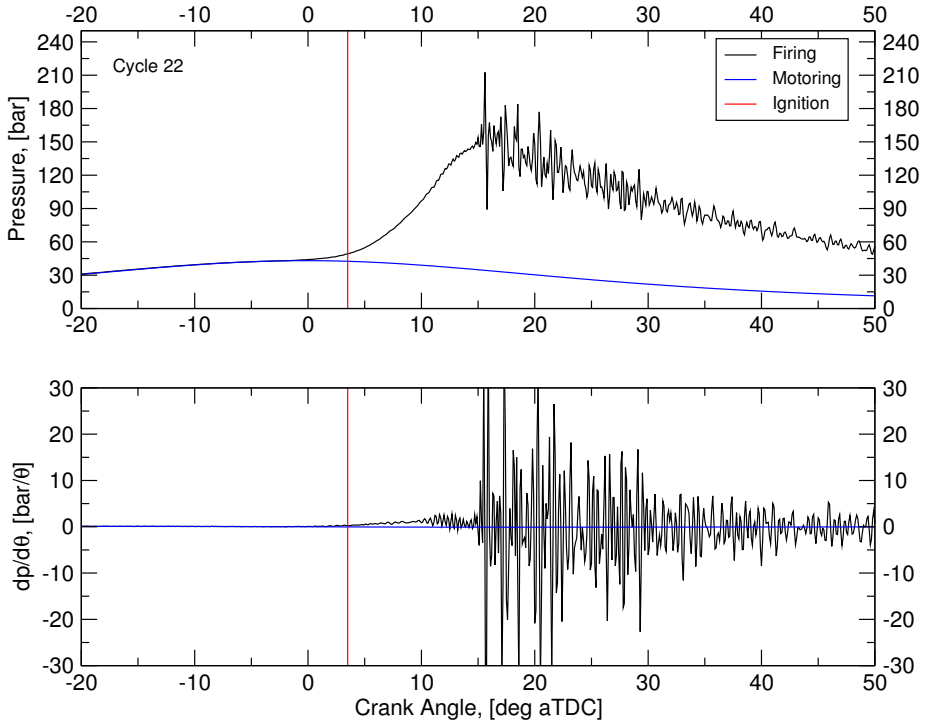

Figure 6.22: A cycle captured in the UB100 engine with a pressure rise, caused by combustion, occurring early in the cycle followed by severe 'super knock'.

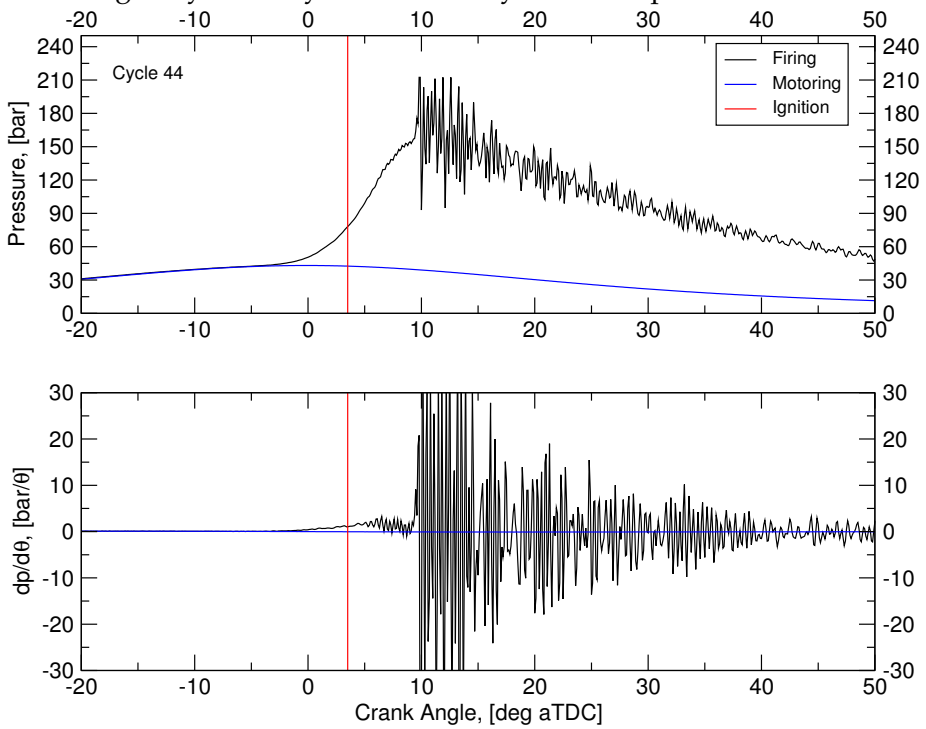

Figure 6.23: A cycle showing extremely early pressure rise due to combustion. The high heat release leads to the most severe 'super knock' of the dataset.

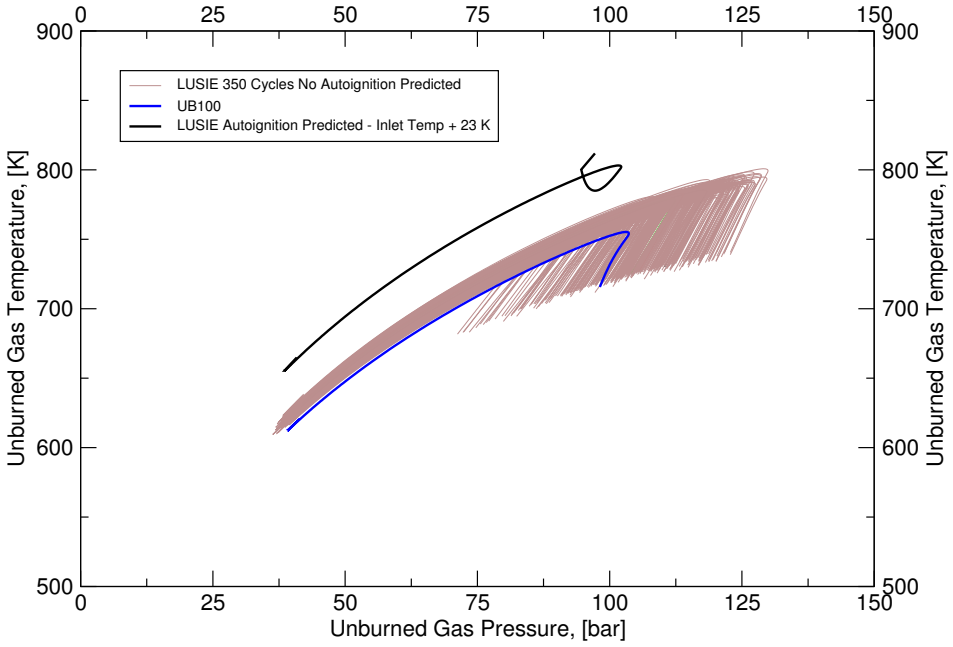

Figure 6.24: Pressure-temperature regime of the UB100 engine as predicted by LUSIEDA and LUSIE at the high pressure condition.

or spontaneous autoignition of the fuel-air mixture. There is a fairly long period of gradual pressure before oscillations set in. This realisation allows the type of pre-ignition to be determined as hot-spot pre-igniting rather than gas-phase pre-ignition. In the latter, the pressure and temperature of the fuel-air mixture reach the point of autoignition, followed by a subsequent quasi-instantaneous pressure rise to maximum. In order to assess whether or not the pre-ignition events observed in the UB100 engine were caused by homogeneous auto-igniting of the end gas, the pressure-temperature histories, predicted by LUSIE, from the variability study in Chapter 5 were abstracted. It can be seen in Figure 6.24 that autoignition was not predicted in the engine at these conditions with the skeletal Keck model, which if anything has been seen to be "overly cautious" when predicting auto-igniting in the UB100. Indeed, separate predictions were run with increasing temperatures until autoignition occurred. As can be seen in Figure 6.24, a significant increase in the temperature of the intake air was required to induce a homogeneous autoignition event. Hot-spot autoignition is caused by local heating of the fuel-air mixture by a surface at elevated temperature; The University of Bath and the Jaguar Land Rover consortium concluded that the likely source in this case was the spark plug, as when a higher heat-rating plug was installed the pre-ignition was abated.

6.5.2 High frequency pressure oscillation

Within the course of the UltraBoost project, a large amount of crank-resolved data were made available to the University of Leeds; this dataset contained many cycles which were considered, by the consortium, to be knocking. Upon analysis of individual pressure curves it became apparent that these cycles were not exhibiting traditional knocking cycle characteristics. To illustrate such characteristics, a comparison of normal and knocking cycles for the Ricardo E6 engine can be seen in Figure 6.25. The non-knocking cycle shows a smooth pressure curve with respect to crank angle. The differentiation of the pressure curve shows the rate at which the pressure rise is increasing. The knocking case, also seen in Figure 6.25 shows a similar progressive pressure rise, though it is clear to see that there is a spike in pressure at around 28^o aTDC. This is the origin of a pressure wave, which continues to traverse the cylinder forwards and backwards reducing in amplitude with time. The cause of the pressure wave is the autoignition of a part of the end gas, ahead of the flame front. The remaining unburnt fuel-air mixture spontaneously ignites; this high rate of heat release causes a pressure wave and the initial pressure spike. The derivative of the pressure signal, $\frac{dP}{d\theta}$, and the Fourier image of the pressure calculated through a Fast Fourier Transform (FFT) function in MATLAB can be seen in Figure 6.26. The frequency is determined by the sample size, N, which, in this case is power of 2 (common for FFT calculations). Therefore the signal was only considered in a window around the area of interest, i.e. the pressure oscillation, and with a data logging rate of 0.1^o CA the resulting sample signal contained 1024 individual data counts. With a knowledge of the sample size and the data log rate, the frequency can be obtained from the real and imaginary parts of the original signal. The y-axis shows the amplitude spectrum of the frequency, |Y(f)|. It can be seen that the first mode, or dominant frequency, is 7 kHz with a secondary mode at 14 kHz. This is consistent with previously seen published knocking data for engines experiencing knock events (Dahl et al. [2011]).

The boosted production datasets at 2000 rev/min and 3000 rev/min display pressure oscillations akin to knocking cycles. However, the general shape as well as frequency of the pressure oscillations suggests that oscillations are not caused by the knock. The 3000 rev/min dataset consists of 100 cycles. All 100 cycles contained pressure oscillations which were, presumably, identified as knocking cycles by the ECU. The disparity between knocking cycles and the phenomena experienced in the UB100 can be seen in Figure 6.27 (Cycle 34). Here, although pressure oscillations are present, the gradual rise in the amplitude of the pressure wave to the point of maximum pressure is not a feature of a knocking cycle since the pressure rise occurs over 10-15^o CA. The decay, although a feature of knocking cycles, is occurring too quickly over approximately 7^o CA or 0.3 msec

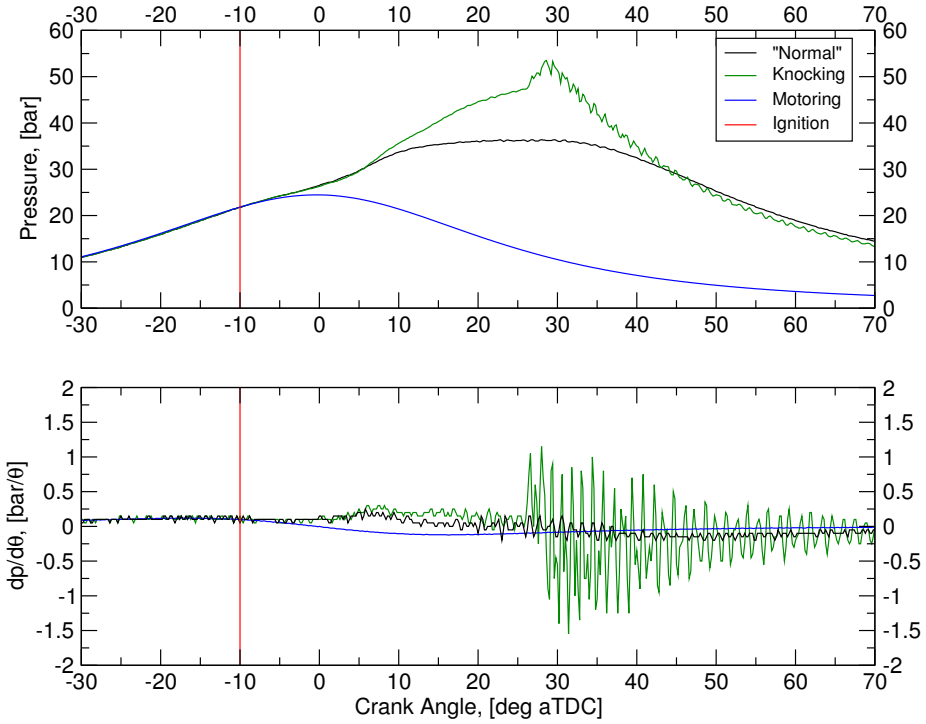

Figure 6.25: Normal and knocking cycles captured within a set of 100 consecutive cycles in a Ricardo E6 engine.

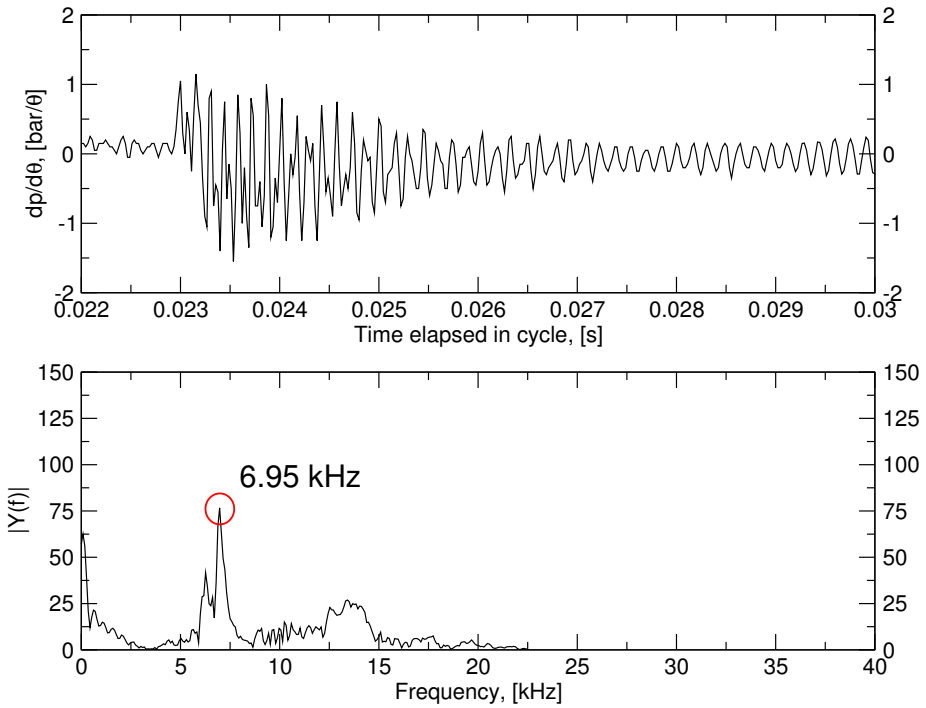

Figure 6.26: A knocking cycle for the Ricardo E6 engine. Note the instantaneous increase in pressure seen in the first derivative of the signal.

at 2000 rev/min. For comparison, in the Ricardo engine the time for decay was around 4ms (albeit at a reduced engine speed). The oscillations seen in the UB100 cycle (Cycle 34) show a clear dominant frequency, which can be seen in Figure 6.28. The value is approximately 33.5 kHz; determining the frequencies inside such a complex combustion chamber as is seen in the UB100 engine would require CFD or Finite Element Methods (FEM) (Vressner et al. [2003]), here a first approximation of the tangential and longitudinal mode frequencies is made by:

$$F_{\text{tan}} = a/D\pi \tag{6.2}$$

$$F_{\text{long}} = a/D \tag{6.3}$$

where, a, is the speed of sound (Eq. 6.1). Assuming an unburned gas temperature from Figure 6.24 of approximately 700 K, and a maximum burned gas temperature of 2500 K from LUSIEDA predictions, the frequency range for F_{tan} and F_{long} are 2.0-3.4kHz and 6.8-10.6kHz respectively. Hence the observed frequency is highly unlikely to be a pressure wave, and certainly not a pressure wave which propagates in the same way as a knocking cycle, across the cylinder.

There do not appear to be any definite secondary frequency modes in this cycle. In contrast to Cycle 34, Cycle 49 shown in Figure 6.29 has a longer decay duration. The cycle shown in Figure 6.30 (Cycle 92) contains oscillations which appear to have almost subsided before being followed by a small increase in amplitude before further decay. The increase in amplitude, after the oscillations had apparently decayed to normal, is in contrast to cycles which showed an increase in amplitude before the oscillations had completely decayed, such as 6.29. Three cycles were chosen at random from the 100 cycle dataset and transformed into the frequency domain, the results are presented in Figure 6.31. In this Figure it can be inferred that, although the three cycles have different decay profiles and the maximum oscillation amplitude occurs at different times, the dominant frequency remains fairly constant around 32-34 kHz. It is noted that the frequency at maximum amplitude in cycle 68 is lower vis á vis cycles 50 and 90, however this is not the case between cycle 50 and 90 where different amplitudes have identical dominant frequencies. A possible explanation for cycle 90 and 50 having identical dominant frequencies at different amplitudes could be explained by the timing of maximum amplitude. The cycle 90 peak occurs later than cycle 68 and therefore in a larger volume than cycle 50, effecting heat release which could contribute to acoustic differences. To de-

termine whether or not the timing of the maximum amplitude has an effect on dominant frequency, a comparison between frequency at maximum amplitude was compared with the time at $\left(\frac{dP}{dt}\right)_{\max}$. This has been plotted in figure 6.32. It can be seen that although there is a very weak trend suggesting higher frequencies occurred earlier on in the cycle, the trend is not strong enough to draw conclusions. The average frequency for the 100 cycles in this at 3000 rev/min set was 34.1 kHz.

A cycle with a remarkable pressure wave can be seen in Figure 6.33; where although there is a significant pressure oscillations occurring, the rise up to the maximum pressure value is gradual, occurring over 3-5 degrees of crank angle and then, after this gradual rise there are signs of decay followed by a further increase in amplitude, followed by a second decay which appears to reduce the oscillations back to a level of permissible noise. The questions: what causes the decay? and what drives the gradual increase in amplitude? arise. The frequency and amplitude of the oscillations in this cycle can be seen in the FFT plot in Figure 6.34. The dominant frequency here is at 33 kHz with no apparent secondary order frequencies in the high frequency range. A pattern of increasing frequency with amplitude and vice-versa can also be seen. A similar pattern can be seen in Figure 6.35 where, although the amplitude is not as high the dominant frequency is the same. The gradual rise to decay is again seen here, though without the dip seen in the previous cycle. The data seen in the final figure in this set, Figure 6.36, has far less noise, though was still recognised as a knocking data set owing to the presence of pressure oscillations. The average dominant frequency for the 2000 rev/min dataset was 32.4 kHz. It is noted that this frequency is lower than the 3000 rev/min set average frequency of 34.1 kHz (see Table 6.4. If the oscillations were caused by vibration of a component system which may be increased by an increase in crankshaft speed, then it would be expected that the observed frequency would also increase. As the increase in frequency is not proportional to the increase in engine speed, it can be reasoned that the relationship between engine speed and the oscillation frequency is small. It can also be said from the similar frequencies that the data logging frequency is unlikely to be the source of spurious frequency peaks. Data were logged every 0.1^o CA at 2000 rev/min and 3000 rev/min; the logging frequencies are therefore the 12 0 kHz and 180 kHz respectively. As the difference between the frequency peaks observed from pressure oscillation does not change proportionally to the logging frequency between 2000 rev/min and 3000 rev/min it is possible to rule out an influence from logging frequency from the analysis.

At lower engine loads, the problem is far less significant; lower loads are achieved in the boosted production test setup by reducing intake pressure. The data presented in Figures 6.37, 6.38, 6.39& 6.40 are of the UB100 operating at 2000 rev/min at low load,

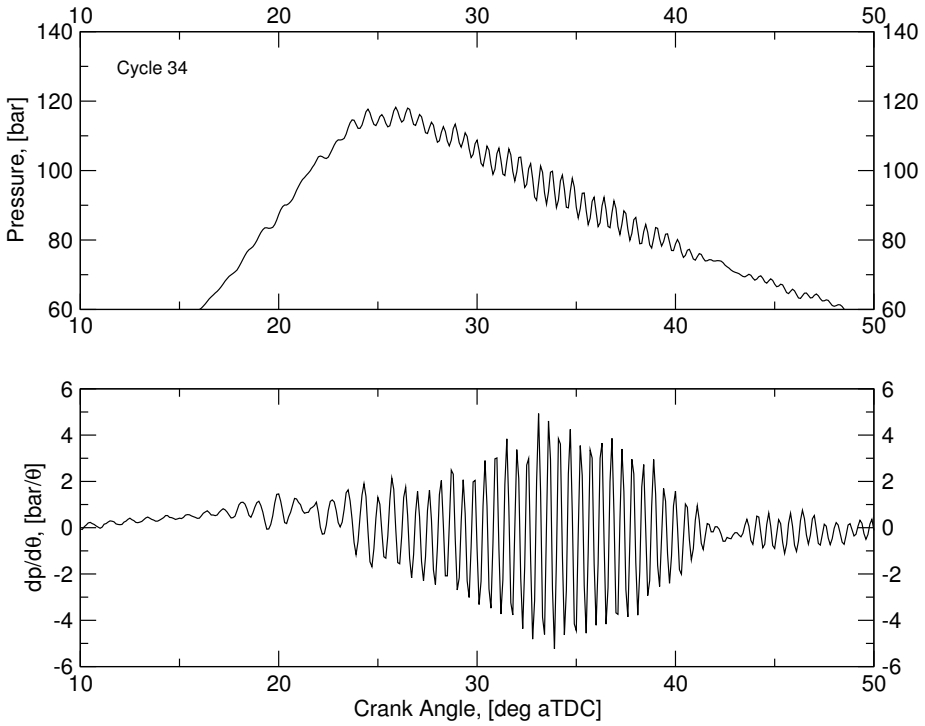

Figure 6.27: A cycle from the UB100 at 3000 rev/min. The gradual increase in pressure followed by sharp decay seen here is not indicative of a knocking cycle.

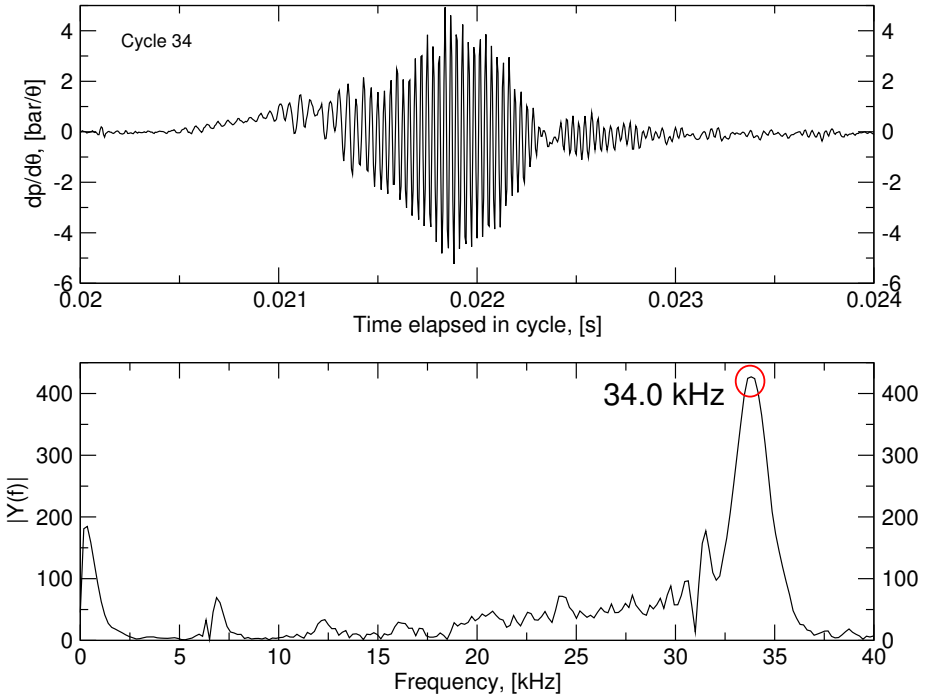

Figure 6.28: The FFT of the differentiated pressure signal shows the dominant frequency is over 4 times greater than seen in the Ricardo knocking cycles. The amplitude is also far greater.

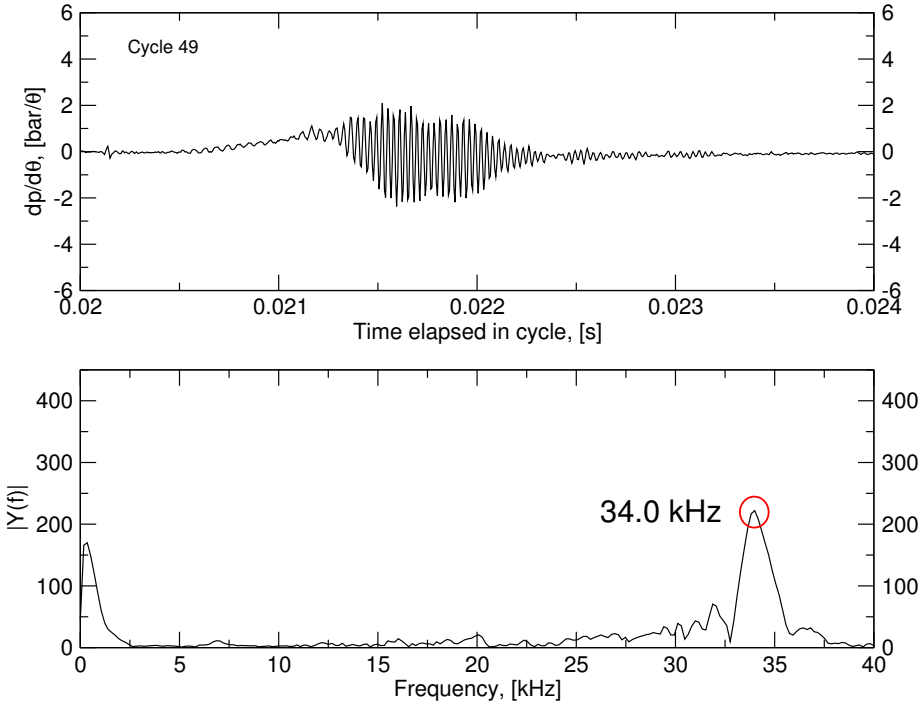

Figure 6.29: This cycle shows a slower decay than the first cycle, though there is an increase in the amplitude of the oscillations during this decay period.

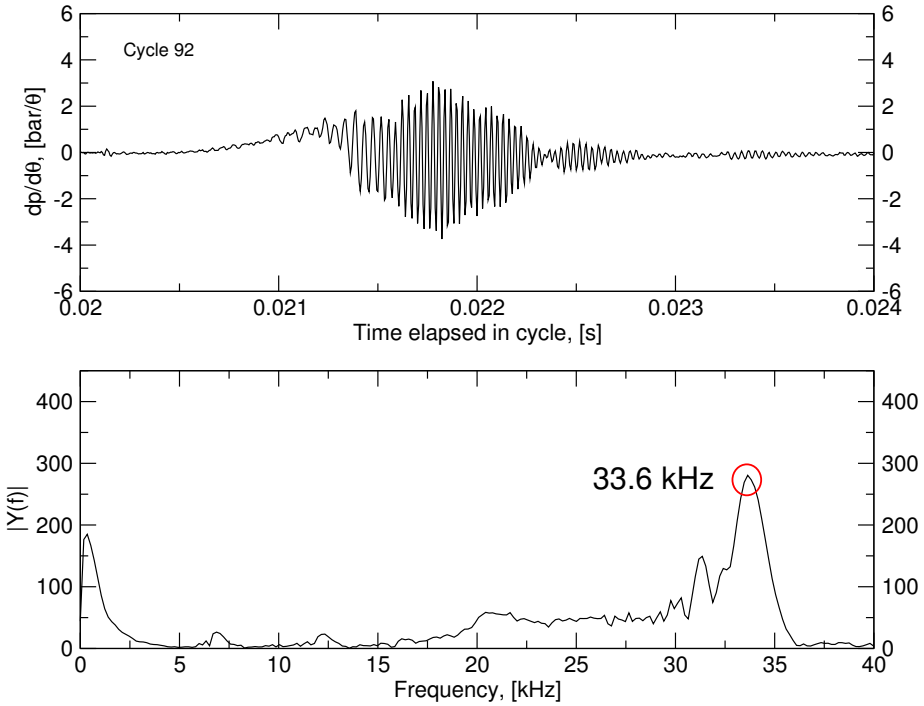

Figure 6.30: It can be seen in this cycle that decay profile is different to the previous cycles in that it shows a further rise after decay.

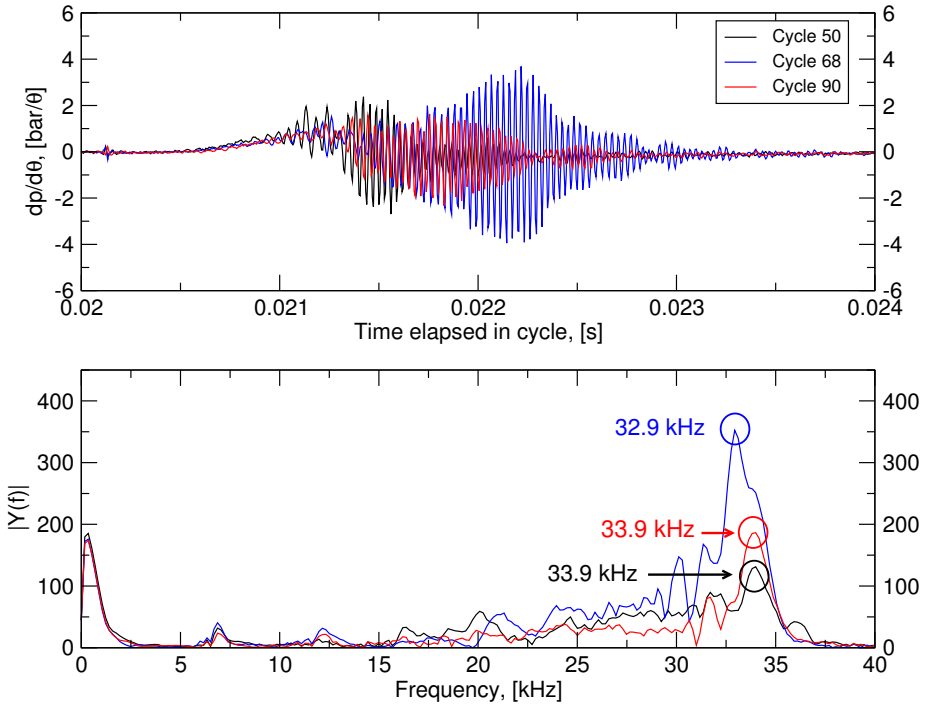

Figure 6.31: 3 Random cycles from the 3000 rev/min dataset. The dominant frequency is similar for the 3 cycles, though the higher amplitude cycle has a slightly lower frequency.

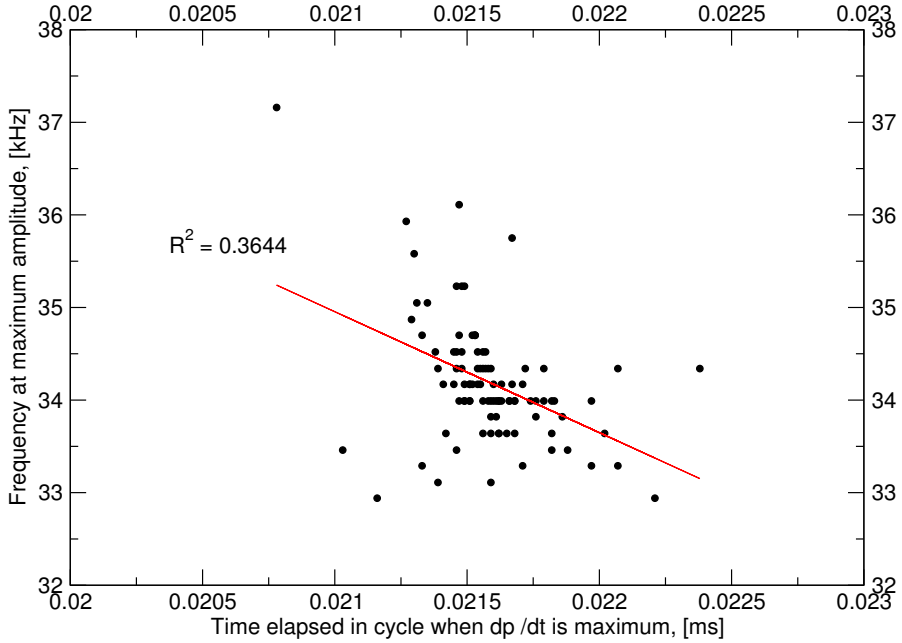

Figure 6.32: The frequency at maximum amplitude against the time elapsed when the absolute $\frac{dP}{dt}$ is maximum. Showing the weak influence of the timing of maximum amplitude of the pressure oscillation on the dominant frequency.

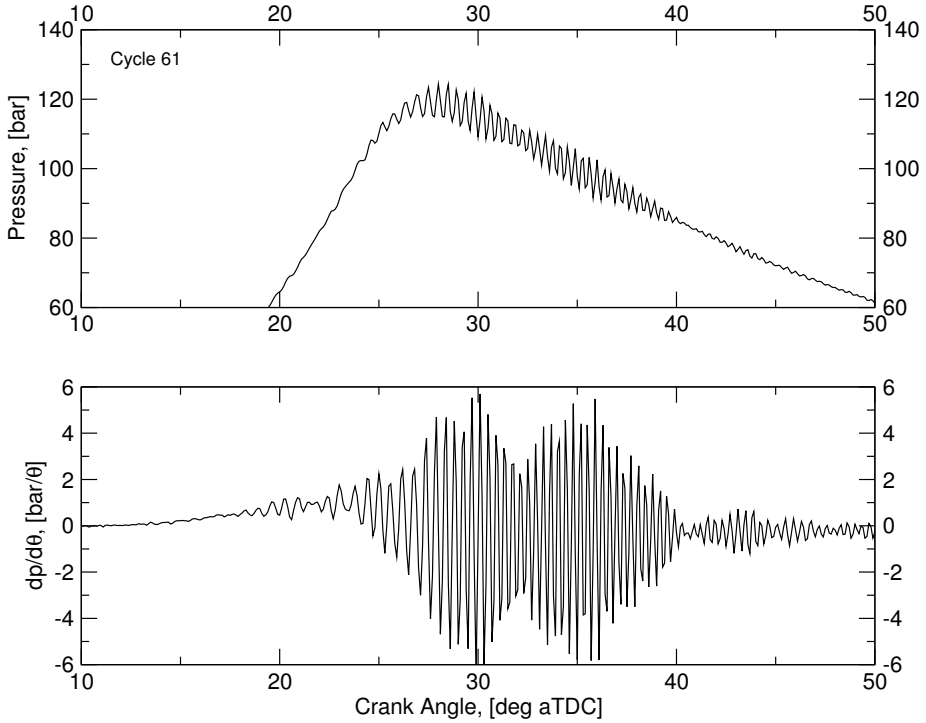

Figure 6.33: A cycle at 2000 rev/min with significant pressure oscillations, a gain in amplitude after initial decay is an interesting feature of this cycle.

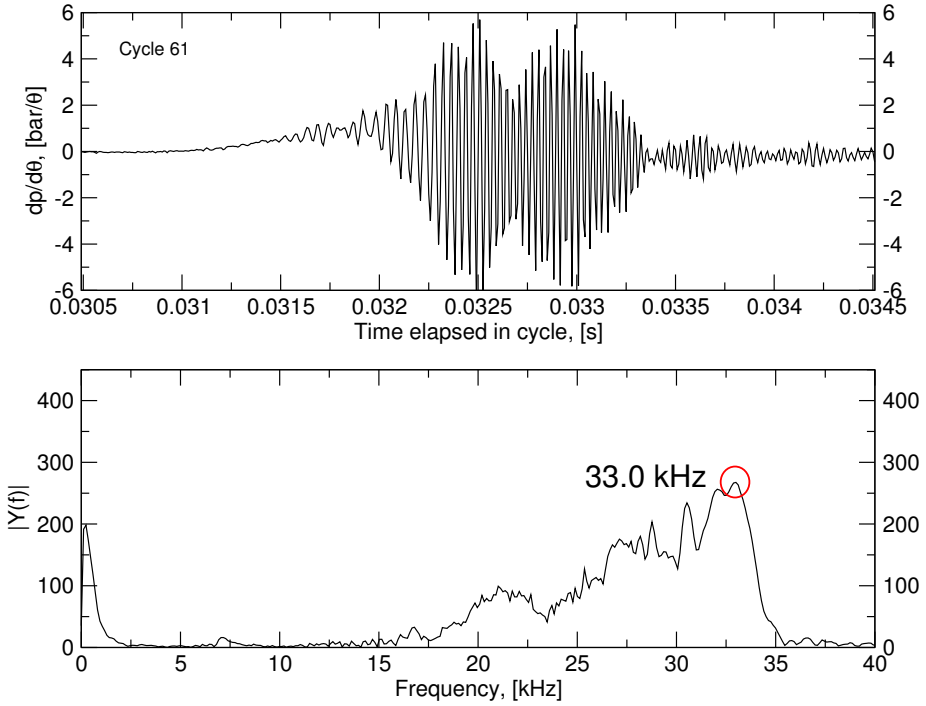

Figure 6.34: Cycle 61 transformed into the frequency domain. The increase in frequency with amplitude is seen in other cycles which are not presented here.

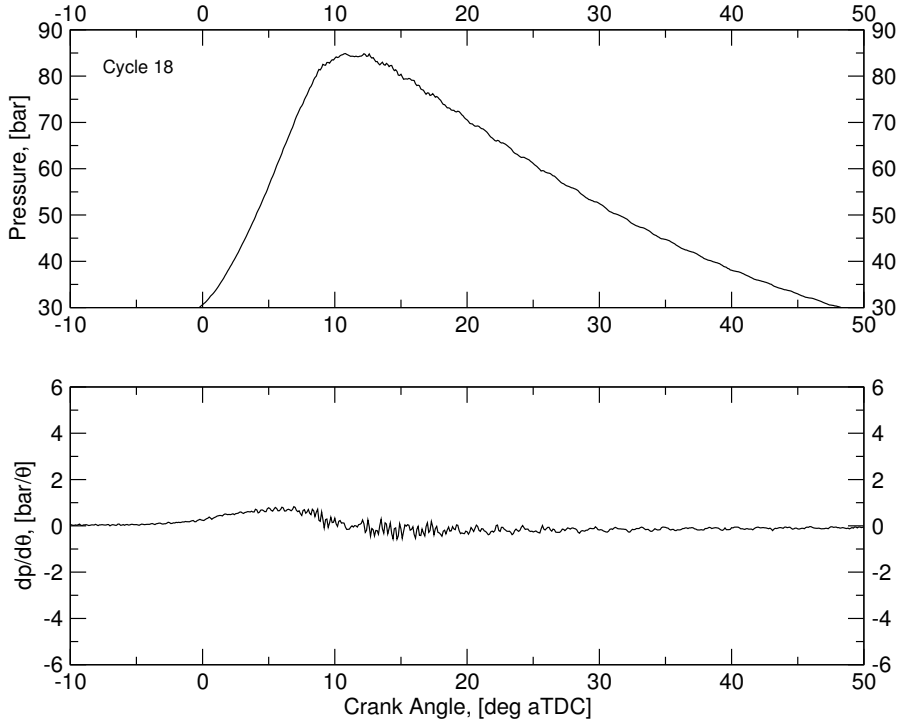

Figure 6.35: A typical cycle at 2000 rev/min and low-load with little oscillation.

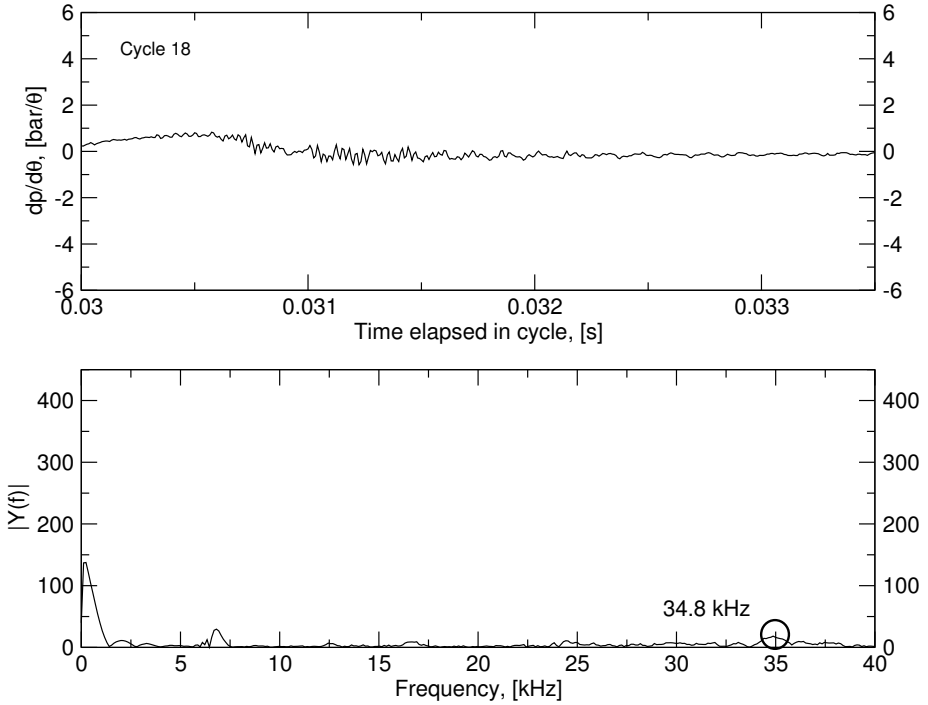

Figure 6.36: This cycle has relatively low amplitude oscillations but still shows the same dominant frequency.

Engine	Engine Speed (rev/min)	Engine IMEP (bar)	Frequency at max Amplitude (kHz)	Variance of Frequency at max Amplitude (%)
UB100	2000	31	32.4	5.6
UB100	3000	31	34.1	3.6
UB100	2000	16	28.8	26.7
Ricardo E6	1500	7	8.5	24.3

Table 6.4: Summary of the UB100 and Ricardo E6 pressure oscillation frequency analysis.

16 bar IMEP compared with 31 bar for the other 2000 rev/min case. The amplitude of the oscillations is far lower vis-á-vis the full load 2000 rev/min and 3000 rev/min cases. Generally significant oscillations are not seen; Figure 6.38 is typical of the majority of cases and does not show significant oscillations. In Figure 6.37 the pressure oscillation profile is more resemblant to that of a knocking cycle than at any of the full load cases, identified by the omission of a gradual rise to peak amplitude. The gradual increased profiles are still present however in other cycles, see Figure 6.39 for example; though occur much less frequently. The dominant frequency for these cycles is not well defined, as can be seen in Figure 6.40. Though generally these oscillations appear to occurring in a region of greater than 10 kHz, higher than would generally be expected for engines. A summary of the frequency data for all cycles in each set can be found in Table 6.4. The full load boosted production cycles have quite distinct dominant frequencies with little variation, where as at high load the frequency has dropped but the variation of these cycles is far higher. A similar large variation can be seen for the Ricardo engine data, the dominant frequency is in the region expected for SI engines but, again has a large variance. The relatively low variance and high frequency cases seen at full load in the UB100 appears to be unique to this engine.

A manual check of wave frequency was made to check that the MATLAB code, created to determine frequency, was accurate. It can be seen in Figure 6.41 that the time elapsed between dominant peaks for the Ricardo E6 engine corresponds to approximately 7 kHz, while the frequency in the UB100 engine, see Figure 6.42 corresponds to approximately 30 kHz; values calculated using the MATLAB code were aligned with these.

A key impact of these pressure oscillations is that they are being identified as knocking signals. The engine is currently limited to these operating conditions as they are believed to be the knock limited operating conditions and the full potential of the engine

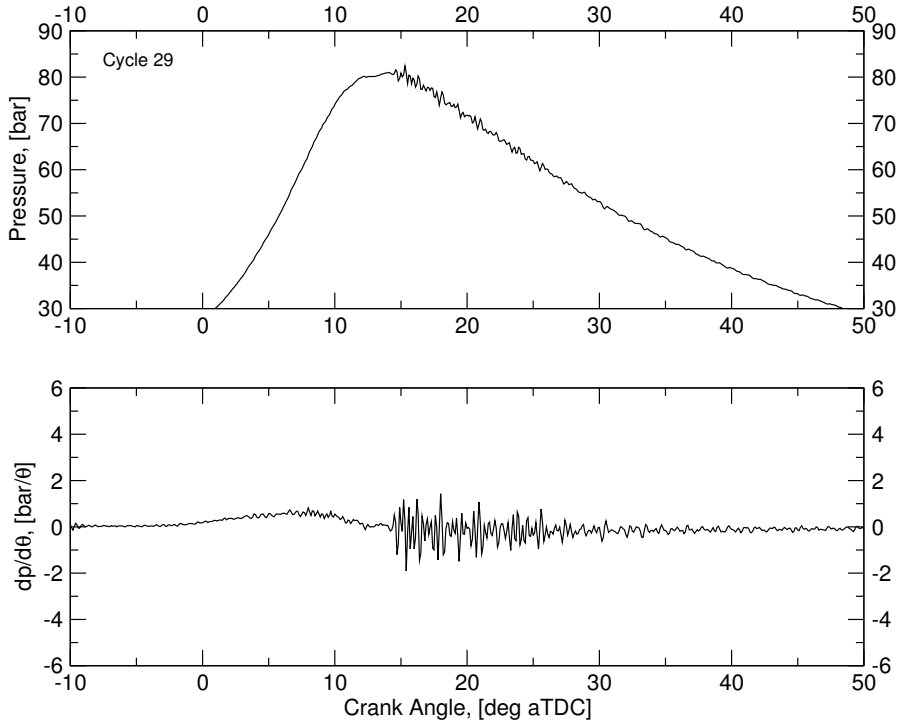

Figure 6.37: Cycle 29 at 2000 rev/min low load with weak oscillations which have similarities to knocking traces.

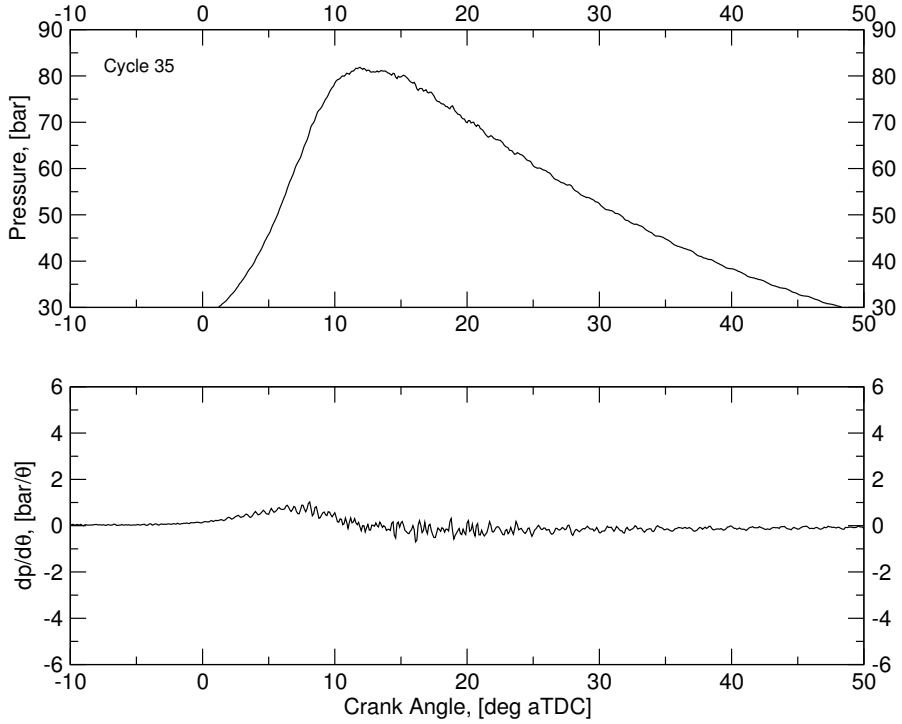

Figure 6.38: Cycle 35 at 2000 rev/min, low-load, with no significant oscillations.

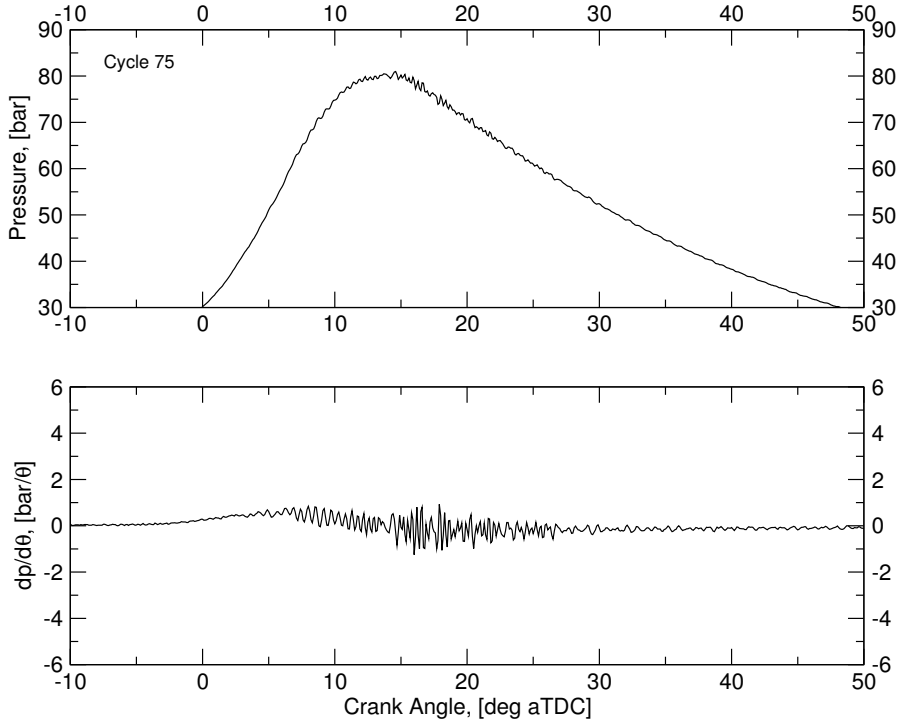

Figure 6.39: Cycle 75 at 2000 rev/min, low-load with pressure oscillations showing similar patterns to full load.

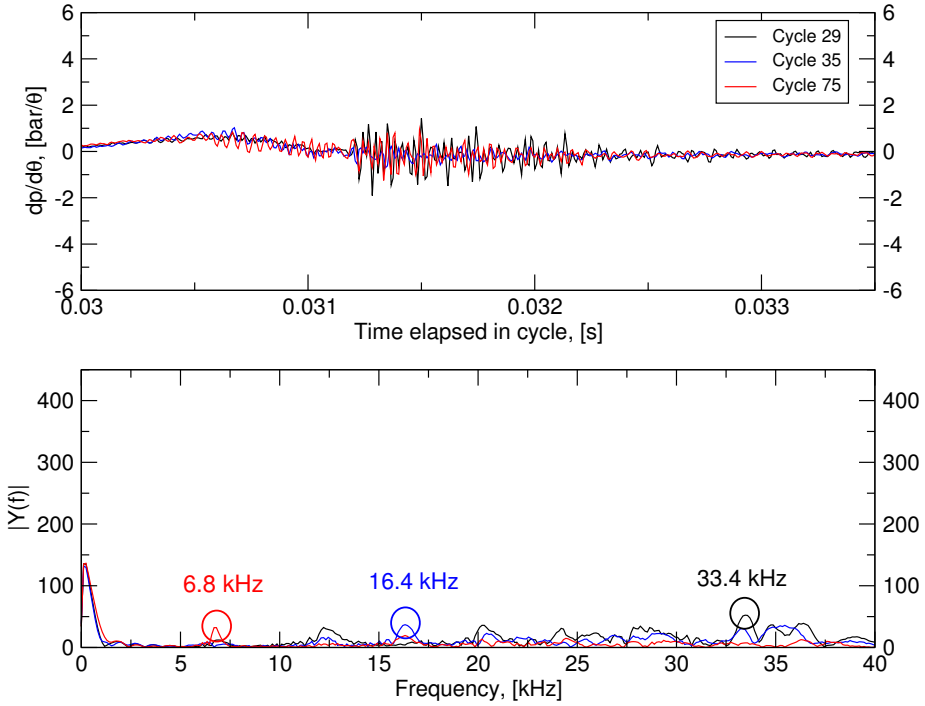

Figure 6.40: The three previous cycles transformed into the frequency domain, note the dominant peak has a large variation in terms of frequency.

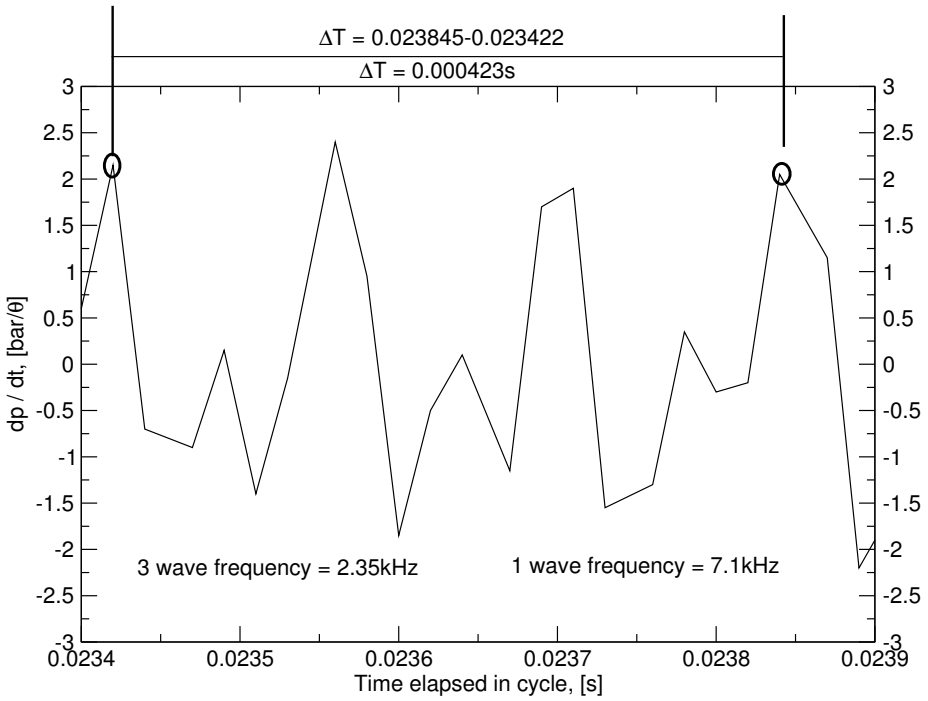

Figure 6.41: Example of frequency calculation by manual observation of wave separation timing within the Ricardo E6 engine.

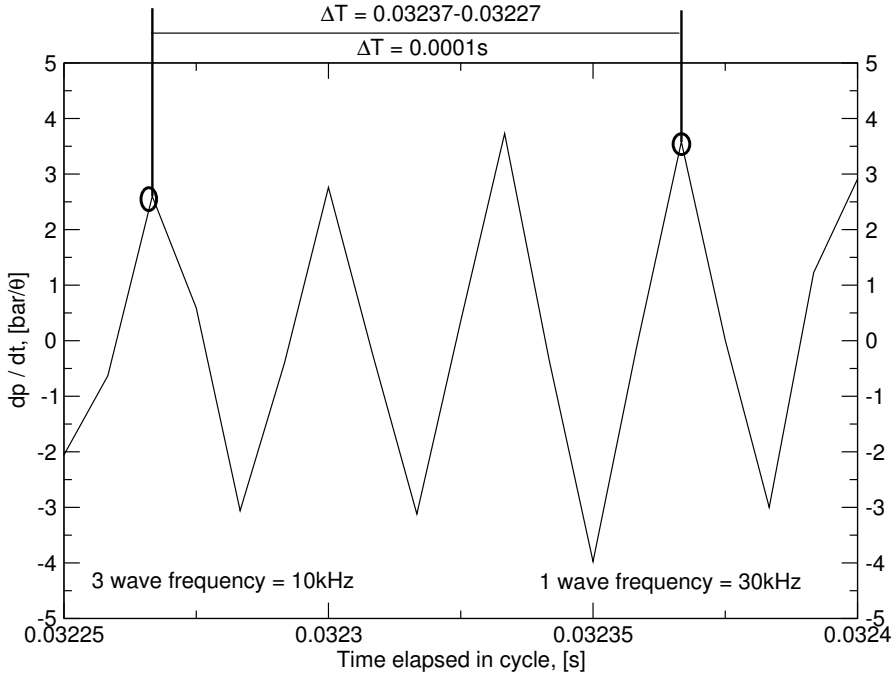

Figure 6.42: Example of frequency calculation by manual observation of wave separation timing within the UB100.

may not, currently, be realised due to the oscillating pressure phenomena. In addition, even at the current conditions the variation in pressure leads to a variation in IMEP and maximum pressure. Figure 6.44 shows a plot of the maximum cylinder pressure and the point at which it occurs in degrees of crank angle. It can be seen that the unsmoothed data has a larger spread than the smoothed data. The individual cylinder pressure traces were smoothed using a 2^{nd} order Butterworth low pass filter, this process removes the pressure oscillations. The smoothed data is also seen in Figure 6.44 plotted against the unsmoothed data. A significant drop in the COV of IMEP is seen with the smoothed cycles, suggesting that if the origins of the pressure oscillations can be found and a solution found to reduce or remove them, then further refinement to the engine may be possible.

The origins of pressure waves within SI engines is not a new phenomena as discussed in the paper of Sheppard et al. [2002]. The occurrence of these waves is often caused by an excessive heat release, coming from rapid combustion events, usually autoignition. In a knocking case, the unburned air-fuel mixture autoignites, usually ahead of the flame front in the end gas region, causing an extremely rapid rate of energy release and local over-pressures that lead to pressure-wave propagation (Heywood [1988]). It has, however, been determined that the cycles within the UB100 engine are not knocking cycles due to the profile of the pressure oscillation curve. In addition to the profile not matching traditional knocking cycles, it has previously been seen that dominant knocking frequencies in SI engines should fall into the range of 2-12 kHz (see Section 6.5.2. Frequencies of 30 kHz and upwards are seen in the boosted production cycles. It is clear that knock by autoignition induced pressure waves are not present in the UB100 engine at the tested conditions. Nonetheless, they are recognised as knocking cases, limiting engine performance. Oscillations of this nature are not limited to SI combustion. Under high load in HCCI applications the chemical reactions are too fast, and the combustion is too rapid, which results in pressure waves that travel back and forth in the combustion chamber (Dahl et al. [2011]). It has been proposed that the pressure waves in HCCI combustion arise from the very fast combustion in a parcel of the fuel/air mixture when the required expansion rate of such a parcel exceeds the speed of sound, resulting in an increase in local pressure (Yelvington and Green [2003]). Typical acoustic frequencies for this combustion mode are again around 6-10 kHz as the frequency is primarily a function of engine geometry (Dahl et al. [2011]), although lower temperatures in HCCI combustion will reduce the speed of sound, and therefore frequency, vis-á-vis SI combustion

The dominant frequency of approximately 33 kHz seen in the UB100 engine corresponds to longitudinal lengths of approximately 17-40 mm respectively depending on the gas temperature, far smaller than the bore of the engine. The combustion chamber was

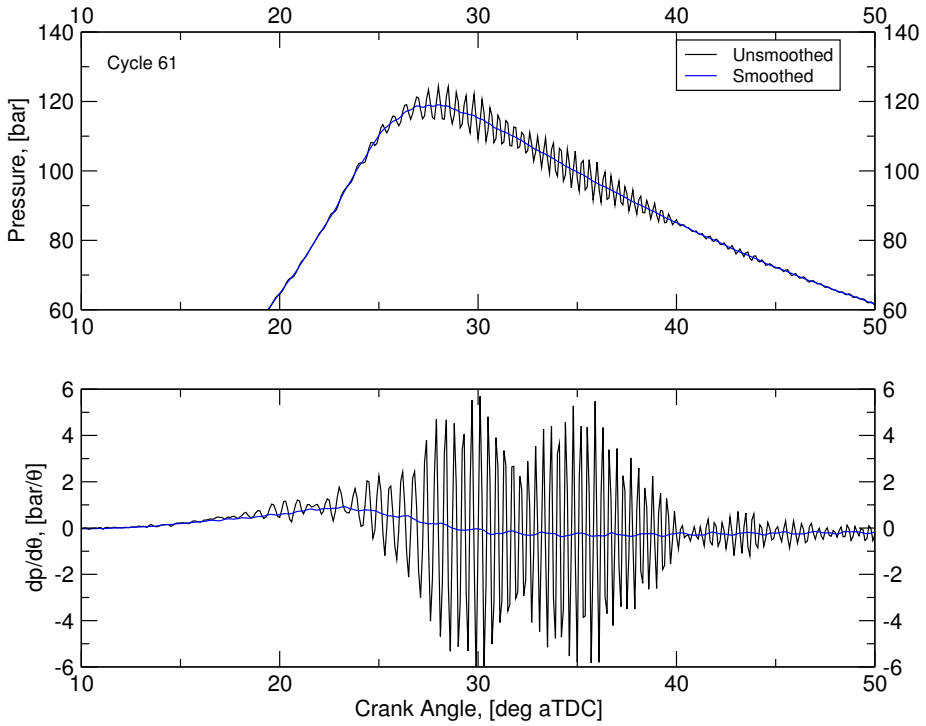

Figure 6.43: An example of data smoothing using a Butterworth filter on the original raw cylinder pressure data in the UB100.

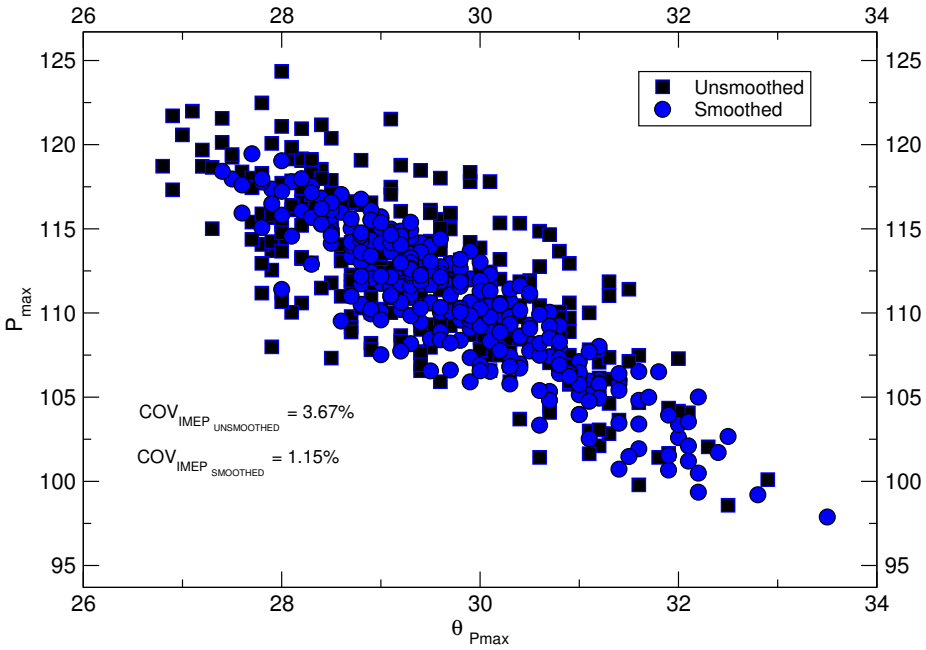

Figure 6.44: A maximum pressure distribution plot for the unsmoothed raw data from 300 cycles in the UB100s compared with the same cycles which have been smoothed through a Butterworth filter.

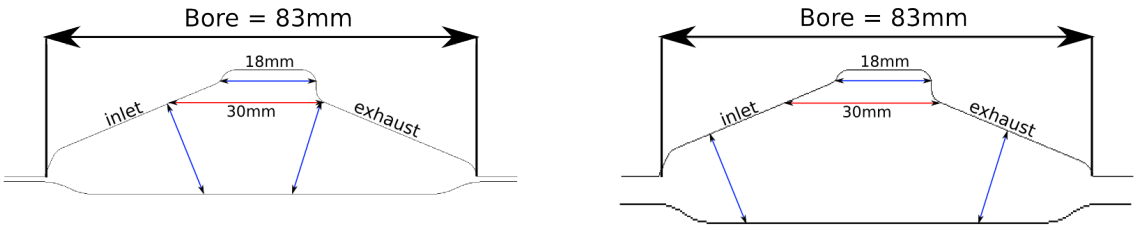

Figure 6.45: A cross section of the boosted production combustion chamber showing an acoustic length of 18 mm (red and blue lines) at TDC and 25^o aTDC.

analysed to determine if any of the combustion chamber features accommodate these lengths and hence, may be responsible for the pressure oscillations. The cross section of the piston and cylinder can be seen in Figure 6.45 along with some relevant acoustic lengths. It can be seen that there is a feature at the top of the chamber which has a bore of 18mm, within the range of possible lengths to be responsible for the pressure oscillations, additionally, the 30 mm length which appears lower down the chamber feature corresponds to a length which could also be responsible for the oscillations. Also of consideration would be pressure waves which travel up and down the cylinder, i.e. normal to, the longitudinal pressure waves. Such waves would be expected to be a function of the clearance height and therefore to appearance of a single dominant frequency would be unlikely. In addition there was poor correlation between the onset of of such waves and their frequency (see Figure 6.32.

The next logical source would be a mechanical issue. Either mechanical fault, or limitation, with the equipment or mechanical noise within the engine. Mechanical noise within the engine includes the cylinder pressure transducer mounting or some other location near the pressure transducer where vibration from the engine as it operates is causing noise. It would generally be expected that this noise would increase in a linear manner with piston speed. It is seen however that, an increase from 2000 rev/min to 3000 rev/min brings about a small change in dominant frequency. It has been suggested that high in-cylinder pressures can increase the propensity for piston slap to occur. Fuel combustion in-cylinder occurs usually at nearly the top dead centre. The rapid rise of pressure in- cylinder causes vibration of the engine block and other components, and then the vibration transmits to the engine surface to form the airborne noise. So the combustion noise usually occurs around TDC. After combustion begins, the piston moves rapidly from one side of cylinder liners to the other side under the high pressure and speed. The excitation of piston slap can also induce an obvious noise radiation. The piston slap occurs after the combustion starts; the noise caused by the piston slap also follows the combustion induced noise emissions (Hao et al. [2007]). Typical frequencies,

even in the most extreme conditions were identified to be 3 kHz, 10 times smaller than the oscillation frequency seen in the UB100 engine.

6.6 General discussion

The performance of two autoignition models has been investigated throughout this chapter. Their application to engines operating under varying conditions was of key interest to the overall work scope. The primary objective of this thesis is: to assess variability of combustion events within non-boosted and boosted engines. In the current chapter, the performance of two autoignition models, a kinetic model and an empirically derived model have been used to predict both the onset of autoignition and validate against experimentally observed knock onset timings. In addition an investigation into whether a variability of the onset of autoignition independent of burning rate exists, this was predicted using in-cylinder pressure and determining heat release rates using LUSIEDA.

The project direction was largely determined by data availability, itself determine by the requirements of the UltraBoost project. In the first instance, LUSIE was employed to predict the level of autoignition activity that might exist in the UB100 and assess possible mitigation strategies that could be employed if autoignition levels were unacceptably high. Autoignition events were captured in the UltraBoost engine during the testing program, though they were not the expected end gas autoignition events which normally lead to knock events, instead they were pre-ignition events, with associated super-knock events. A lack of autoignition data for the UB100 and AJ133 engines limited autoignition model validation and variability analysis primarily to the non-boosted LUPOE2-D and boosted LUPOE2-D engines.

The models used to predict autoignition in this project were, the empirical Douad and Eyzat model, a model created in 1978 and based on a lumped reaction rate driven by the end gas pressure and temperature, and the skeletal Keck model, a skeletal kinetic scheme comprising of a limited number of species and reactions. The D&E model is traditionally used in a number of 1D engine simulation packages as it offers flexibility and very fast computational times. Recently however some 1D packages are beginning to include chemical kinetic autoignition solvers in their routines (Gamma-Technologies [2012]). Because of the wide-spread usage of this specific model in the automotive industry, particularly for parametric studies, it was important to determine if the D&E model is able to account for autoignition in boosted engines without first having experimental data to calibrate the model constants to, effectively removing the predictive capability of

the model. It was seen that predictions from the D&E model were not well correlated to any of the engine data sets and that the model behaviour changed with different engines and operating conditions, from over-predicting the event, to under-predicting the event to predicting cycles which did not autoignite and vice-versa. Unsurprisingly the model is sensitive to the pressure of the engine, but that it does not correctly account for changes in intake pressure. The theory is that because the model does not account for the NTC region, itself pressure and temperature dependent, it cannot predict autoignition behaviour of a real fuel. It could be concluded from the analysis that the D&E model is not well suited to application on boosted engines, unless a validation process can take place with actual engine data. Conversely the skeletal Keck model appears to have a better ability to account for autoignition characteristics in different engines although, as with the D&E model, the model performance changed between the boosted and non-boosted conditions where the increase in intake pressure resulted in the model under-predicting the autoignition event in the engine.

A set of other limitations, specifically concerning models which are incorporated in quasi-dimensional packages, is the inability to account for hot-spots within the engine which will locally increase the temperature of a pocket of end gas causing autoignition before the bulk gas has reached the point of homogeneous autoignition. Despite these limitations, kinetic autoignition modelling can give an indication of the likelihood that an engine operating under certain conditions will result in autoignition, specifically if the end gas composition reaches the correct conditions, also it can approximately indicate at which point in the cycle and therefore estimate how much unburned fuel is spontaneously ignited by the uncontrolled autoignition event, which to an extent, will determine the severity of the event. It was seen in this study, that the variability of autoignition could be predicted by the autoignition models, however in the majority of cases the variability of autoignition was directly linked to the variability of the burn rate. Where variability, independent of the burn-rate, appeared to occur, the skeletal Keck model gave a better prediction of these rogue autoignition cycles, however the reasons for this could not be directly attributed to the model accounting for the NTC region. A possible source of the variability could be attributed to possible hot-spot ignition which would not be predicted by the homogeneous autoignition models used in this study.

There is no definitive conclusion to be made as to the source of the high frequency oscillations in the UB100. If they are mechanically based, the source is not obvious and the frequencies do not scale with engine speed, suggesting they are not related to engine operating frequency. Although a possible reason for this is because of the high frequency the oscillations are associated with the natural frequency of a dense object, such as the

piston which may be excited by the combustion pressure. If the oscillation are related to an, as yet, undetermined combustion related phenomena then they have not been seen in other applications tested at Leeds. The oscillations appear most at high load conditions suggesting that they are related to the chamber composition, inferring a combustion phenomena is a possibility. What is apparent is that they are present in the engine and are erroneously being identified as knocking cycles, limiting the engine performance.

Chapter 7

Conclusions and Recommendations

7.1 Introduction

The aim of the reported work was to primarily determine if a quasi-dimensional combustion model which shares many routines with industry software, can still be applied to engines which operate with considerably higher intake pressures, as dictated by the automotive industry's trend towards downsized engines. Criteria of assessment was centred around three main areas:

- The rates of combustion, consisting of the initiation, propagation and termination stages of a flame in a "typical" cycle.
- Variability of the combustion process at high and low combustion pressures by considering the influence of the turbulent flow field, mixture homogeneity and stoichiometry
- Autoignition behaviour for high and low pressure engines as predicted by two different types of autoignition models.

Four engine platforms were used to assess model fidelity. Two of the engines were multi-cylinder, direct injection (GDI) engines, one naturally aspirated, the other with considerable levels of boosting, permitting approximately 50 bar pressures at the start of the

combustion event. The other two engines reported are bespoke single-cylinder research engines developed at the University of Leeds. The engines operate with a near-quiescent flow field at top dead centre and have an indirectly controllable intake pressure.

The quasi-dimensional combustion model used throughout this work is identified as LUSIE ([the] Leeds University Spark Ignition Engine [code]). LUSIE shares many combustion definitions with several commercially available models, therefore its ability to account for high-pressure operation will be of interest to the majority of industry programs which employ simulation in their research and development programs.

Overall it could be said that the model can be used to predict combustion and variability at high pressures, however only once mean burning rates have been matched to experimental data. Therefore the predictive capability of the models is heavily dependent on a better understanding of very high pressure combustion.

7.1.1 Summary of turbulent combustion conclusions

Presented in the current section are conclusions from the investigation into prediction of turbulence and their influence on combustion characteristics for the four reported engines.

- A 0-D $k-\epsilon$ model was validated against three engines, the LUPOE2-D engine with experimental data while the non-boosted and boosted production engines were validated against turbulence data predicted by CFD data. A good agreement was seen for the LUPOE2-D and non-boosted production engine for u' prediction with a single set of model constants; the Jaguar Land Rover boosted research engine (UB100) required adjustment of the model constants in order to obtain a reasonable fit to CFD data.

- The integral length scale, l_i, predicted by the 0-D $k-\epsilon$ model was in good agreement for the LUPOE2-D engine. However, the predicted the length scale for complex pent-roof geometries was not in agreement with CFD predictions.

- Prediction of the LUPOE2-D combustion was in good agreement with experiment using the integral scale definition for after-burning constant, C_{l_i} = 0.8; as used by previous researchers at the University of Leeds.

- When using the after-burning constant of C_{l_i} = 0.8 for the boosted LUPOE2-D engine the resulting combustion was too fast vis-á-vis experimental data; the suggestion being an influence of pressure in the engine was slowing the combustion

process over that which is predicted, or that the turbulence characteristics were not correctly predicted for the engine.

- It was seen that the combustion process predicted in the AJ133 engine, was too slow when using the same combustion model which was validated against the LUPOE2-D engine. The combustion process appears to be slower still for the UB100 engine. A situation which is contrary to that seen in the LUPOE2-D boosted engine where an increase in pressure led to the model over-predicting the combustion rates.

- Adjusting the size of the turbulent scale in the after-burning definition of the model gives a better account of the combustion event in the UB100 and AJ133 engines. The apparent implications of this are, that in the production engine a smaller scale exists, or that the flame structure is more affected by a small turbulence structure. Moreover it was seen that an even smaller scale was required to predict combustion in the UB100 engine, implying that for the boosted engines as pressure increases the active scale reduces in size.

- For prediction of a satisfactory LUPOE2-D boosted middle cycle, the turbulent burning velocity constant A and the afterburning constant C_{l_i} were adjusted according to a multiple regression fit. For a middle cycle to be attained, A and C_{l_i} were reduced significantly, from the reference values validated for the LUPOE2-D engine. Reduction of both parameters was required in order to slow the cycle sufficiently that both maximum pressure and location of maximum pressure were representative of an experimental cycle.

7.1.2 Summary of cycle-to-cycle variability conclusions

Presented in the current section are conclusions from the prediction of cycle-to-cycle variability for the four reported engines.

- It was seen in the LUPOE2-D engine that the distribution of P_{max} & θ_{pmax} was of a spindle shape, suggesting a Gaussian distribution of more than one parameter was the reason behind the variability. Prediction of the cases observed a boundary where the maximum and minimum cycles would lie and that this boundary was dependent on the extremity of each variable.

- When a variation in only rms turbulent velocity or only equivalence ratio was imposed on the variability model within LUSIE then the distribution was more linear. The gradients of the linear distributions were different depending on whether the

rms turbulent velocity or equivalence ratio was changed; also the equivalence ratio was seen to be the more sensitive parameter. The predicted P_{max} & θ_{pmax} distribution was cone-shaped and in good agreement with the fastest cycles seen experimentally while the slower cycles were under-predicted significantly and had too large a spread.

- For the naturally aspirated production engine, the spindle-like distribution was also seen experimentally while again the prediction was similar to the trend seen on the non-boosted LUPOE2-D engine where slower cycles were considerably under-predicted.

- An interesting observation seen in the AJ133 engine was the change in the shape of the P_{max} & θ_{pmax} distribution at increasing engine speeds. After 2500 rev/min the distribution was seen to be more akin to a crescent shape. This was attributed to the variable valve lift system on the engine which changes the turbulence characteristics at a certain speed.

- It was further seen that in the UB100, throttled to reduce intake pressure, the distribution predicted by LUSIE was in very good agreement with the experimentally seen data. For the full-load i.e. high pressure cases however it was seen that, while the variability was generally well predicted around the mean cycle, it was far larger than seen experimentally and that cycles which were both too fast and too slow were predicted.

- For the LUPOE2-D boosted engine, it was seen that once a middle cycle have been successfully fitted to experimental data, the variability measures of f 12.5% of σ for the rms turbulent velocity and by 5% of σ for the equivalence ratio gave a very satisfactory fit to the experimental P_{max} & θ_{pmax} distribution, albeit with several slower cycles as seen with the other engines.

- Generally it was seen that the variability measures of 12.5% of σ for the rms turbulent velocity and by 5% of σ of the equivalence ratio, on the whole, accounted for the cycle-to-cycle variability seen in all the engines.

- It has been observed that caution should be exercised when using the coefficient of variance (COV) for θ_{pmax} owing to the fact it can produce a 0 mean value which will artificially increase the COV. In addition, comparing engines with considerably different mean quantities can not be approached with the COV measure.

- The R^2 correlation coefficient method of determining the dependence of the different stages of combustion, in terms of pressure or time to reach a flame radii, on the

final maximum pressure appears to be a valid approach to quantifying early stage variability.

- The R^2 correlation method was applied to several engines and operating conditions. By using the method it was possible to determine where in the cycle lifetime the influence of the parameters which affect variability reduce. As denoted by a rapid increase in the R^2 value after a certain time to reach a prescribed burned gas radii, determined by LUSIEDA. The time for the burned gas to reach a certain radii was not seen to be a function of the turbulent scale. Additionally it was seen that in the boosted engines the rate of increase of R^2 was less than for the non-boosted engines, both production and research.

- An analysis into the effect of imposing variability at different stages of the combustion process was performed using LUSIE. It was seen that imposing the variability after the initial development phase when $fr_e/r_{max} \approx 0.2$, then that the over distribution of P_{max}, θ_{pmax} was reduced, in terms of the ranges of P_{max} & θ_{pmax} vis-a-vis where variability was imposed at ignition. When variability was imposed at the final stages of combustion where the flame reaches the wall, where it was seen that most of the unburned gas remains, the level of variability was small.

7.1.3 Summary of autoignition modelling conclusions

Presented in the current section are conclusions from the autoignition for the four different engines as well as an analysis of an anomalous autoignition event in the boosted production engine.

- It was seen that the D&E model was not well correlated to any of the engine data sets and that the model behaviour changed with different engines and operating conditions, from over-predicting the event, to under-predicting the event to predicting cycles which did not auto-ignite and vice-versa. The NTC region was considered as a possible cause of the error, however the NTC region of iso-octane and gasoline fuels at engine-like pressures and temperatures barely exists. More likley was the fact that the original model was formulated using experiments with unknown quantities of residuals. It could be concluded from the analysis that the D&E model is not well suited to application on boosted engines, unless a validation process can take place with actual engine data.

- The kinetic Keck model appears to have a better ability to account for autoignition characteristics in different engines although, as with the D&E model the model per-

formance changed between the boosted and naturally aspirated conditions where the increase in intake pressure resulted in the model under-predicting the autoignition event in the engine.

- It was seen in this study that the variability of autoignition could be predicted by the autoignition models, however the variability of autoignition was directly linked to the variability of the burn rate.
- Where variability, independent of the burn-rate, appeared to occur the kinetic Keck model gave a better prediction of these "rogue" autoignition cycles. However, the reasons for this could not be directly attributed to the model accounting for the NTC region. A possible source of the variability could be attributed to possible hot-spot ignition which would not be predicted by the homogeneous autoignition models used in this study; such a mechanism would not be accounted for by the Keck model..
- No definitive conclusion could be made as to the source of the high frequency oscillations in the UB100. If they are mechanically based the source is not obvious, the frequencies do not scale with engine speed suggesting they are not related to engine operating frequency. The nature of the high frequency oscillations suggests that it is the vibration of a component itself, likely a large component such as the piston.
- A potential variability of the Kalghatgi K number caused by a variability in intake pressure is unlikely to cause significant variability of autoignition, independent of the burn rate. Moreover, the cause of the variability in K factor, namely variability in intake pressure, was more sensitive than the affect on K.

7.1.4 Recommendations for future work

Throughout the reported work, a number of areas of future investigation have been identified that were either beyond the scope of the current work or that would have required additional experimental testing that was not feasible owing to equipment or resource restrictions. Suggestions for future research are details as follows:

- It was seen on a number of occasions, specifically in the two higher pressure engines, that the location at which compression began was before system closure i.e. before intake port closure/intake valve closure (IPC/IVC). Correctly identifying

where the onset of "isentropic" compression begins is of importance when determining the "dynamic" compression ratio (V_{IVC} / V_{TDC}) as well as the initial pressure condition for the model; this will ultimately effect the start of combustion pressure and where the Livengood and Wu integral is calculated from.

- The empirical D&E model was seen to poorly predict autoignition in the LUPOE2-D engine for both naturally aspirated and boosted conditions. With the LUPOE2-D boosted engine now having an almost continuous control over intake pressure up to 4 bar, it would be of interest to see if a relationship between pressure and the activation constant in the D&E model, which satisfies a wide range of pressures, could be proposed.

- Investigate the autoignition properties of various lubricants and lubricant-fuel combinations. This would give a better understanding of the potential mechanisms that can cause preignition in engines which operate at elevated temperatures and pressures.

- Implement a bulk flow model into the $k - \epsilon$ model. Corroborate the data with either experimental data, likely to be gathered from PIV or from predictions made via CFD. A zero-dimensional tumble flow model has been suggested by Ramajo et al. [2007]

- The influence of engine speed on the predictive capability of LUSIE is an area of interest. LUSIE, traditionally, has been validated against low speed conditions. Production engines typically also operate at low engine speeds during legislative emissions cycles, however for performance it is higher engine speeds which are of interest.

- Throughout this work the variability of ϕ and u' to account for cycle-to-cycle variability. The magnitude of variation is based on 5%σ for ϕ and 12.5%σ for u'; however as the amount of variability data increases it would be of interest to determine whether or not better variability magnitudes of each parameter exist for different conditions.

- The R^2 correlation method proposed in Chapter 5 is original work, formulated during this program. It could be extended to investigate the relationships between other parameters; for example, the relationship between burning rates and knock intensity would provide a valuable insight into the phenomena. Other parameters for investigation, not solely related to P_{max}, might include θP_{max}, MFB_{50}, MFB_{10-90} and IMEP to name a few.

- The ignition delay time within LUSIE, between the point of ignition and a kernel of defined size being formed, is based on experiments conducted at near-atmospheric conditions. Of interest for modelling engines operating at high pressures would be impact of pressure on this delay time.

7.1.4.1 Recommendations for LUSIE

- An up-to-date user manual for LUSIE would be advantageous for new students to the Combustion Research Group at the University of Leeds. Modifications to the code itself and, more importantly for users, the input file format since the last manual, makes the requirement for a new one all the more relevant.

- The multi-spark routines employed currently have instability when the second flame is initiated. The current work never extended to a study of multiple sparks and as such, the location of the error was not found. It is likely to be in either the pressure equalisation, thermodynamic or flame geometry routines.

- Currently LUSIE has fuel properties for eight fuels, however laminar burning velocity coefficient data is only available for: iso-octane, "BP 4-Star" propane and methanol. The database should be extended to include burning velocities for other fuels, most notably, methane and ETBE (of which the current author has proposed a relationship for ETBE based on iso-octane burning velocities). Additionally the laminar burning velocities for these fuels should be updated with recent experimental or computational results to better account for the burning velocity of gasoline-like fuels.

- A modification to the "*swept.f90*" routine to include an offset crankshaft should be implemented. Offset crankshafts are used to reduce engine friction primarily through a reduction in the piston-to-wall side loading. Of interest to combustion research is that an offset crankshaft will change the location of piston TDC away from 0^o CA, it will also influence the piston motion and, more importantly the instantaneous piston velocity which has implications for turbulence prediction using the $k - \epsilon$ effect on piston motion and therefore turbulence.

- The $k - \epsilon$ model currently assumes a constant flow rate through the intake and exhaust valves/ports. A more realistic representation of the actual flow through the intake and exhaust should account for the variation in flow rates with a transient valve/port opening area.

- If future work is concerned with variability modelling then there are a number of improvements which could be made to significantly reduce computational time:
    1. Currently the flame look-up table is loaded at the start of every cycle. For engines which use a look-up table generated by the GGEOM routines for complex combustion chamber shapes, this takes a considerable portion of the total run-time. For more efficient variability calculations, where a significant number of cycles are run, then this file should be loaded into LUSIE and stored in arrays where the data can be accessed for the next cycle.
    2. In line with the previous recommendation LUSIE as a whole should be modified to better account for variability. LUSIE runs a cycle individually, more than one cycle is run where the user explicitly defines the run files which LUSIE then runs one after the other without further user input. This means that knowledge of previous cases is "forgotten", resulting in all the input data being re-parsed and reinitialised, a motoring cycle is re-run for the turbulence and heat-transfer routines. It would be possible to enclose the firing cycle routine within the main "*lusie.f90*" file within a loop which reruns for a predetermined number of cycles. Revision of the way files are output, as well as resetting certain variables between each cycle, would be required.
    3. LUSIE operates with a fixed time-step solution, by implementing an adaptive method it could identify the optimum time-step which might permit a reduction in computing time for large numbers of cycles. The simplest method of implementing this is time-step doubling as suggested by Hattrell [2007].

References

Abdel-Gayed, R. G., Bradley, D., and Lawes, M. (1987). Turbulent burning velocities: A general correlation in terms of straining rates. *Proceedings of the Royal Society of London. A. Mathematical and Physical Sciences*, 414:389–413.

Abdel-Salam, H. (1992). *Modelling and Experimental Validation of Turbulent Flame Propagation in Spark Ignition Engines*. PhD thesis, Department of Mechanical Engineering, The University of Leeds.

Abdi Aghdam, E. (2003). *Improvement and Validation of a Thermodynamic S.I. Engine Simulation Code*. PhD thesis, Department of Mechanical Engineering, The University of Leeds.

Acroumanis, C., Bicen, A. F., Vafidis, C., and Whitelaw, J. H. (1984). Three-dimensional flow field in four-stroke model engines. *Society of Automotive Engineers*, SAE Technical Paper 841360.

Aghdam, A. E., Burluka, A. A., Hattrell, T., Liu, K., Sheppard, C. G. W., Neumeister, J., and Crundwell, N. (2007). Study of cyclic variation in an SI engine using a quasi-dimensional combustion model. *Society of Automotive Engineers*, SAE Technical Paper 2007-01-0939.

Al-Mamar, F. (1986). *Combustion in a dual chamber spark ignition engine*. PhD thesis, Department of Mechanical Engineering, The University of Leeds.

Al-Shahrany, A. S., Bradley, D., Lawes, M., and Woolley, R. (2005). Measurement of unstable burning velocities of iso-octane-air mixtures at high pressure and the derivation of laminar burning velocities. *Proceedings of the Combustion Institute*, 30:225–232.

Andrews, G, E. and Bradley, D. (1972). The burning velocity of methane-air mixtures. *Combustion and Flame*, 56:275–288.

Annand, W. J. D. (1963). Heat transfer in the cylinders of reciprocating internal combustion engines. *Proceedings of the Institution of Mechanical Engineers*, 177(36):973–990.

Atashkari, K. (1997). *Laser Diagnostics in Combustion and In-Cylinder Flow*. PhD thesis, Department of Mechanical Engineering, The University of Leeds.

Belmont, M. R., Hancock, M. S., and Buckingham, D. J. (1986). Statistical aspects of cyclic variability. *Society of Automotive Engineers*, SAE Technical Paper 860324.

Blizard, N. C. and Keck, J. C. (1974). Experimental and theoretical investigation of turbulent burning models for internal combustion engines. *Society of Automotive Engineers*, SAE Technical Paper 740191.

Borghi, R. and Destriau, M. (1998). *Combustion and flames: chemical and physical principles*. Editions Technip, Paris, 1st edition.

Box, G. E. and Muller, M. E. (1958). A note on the generation of random normal deviates. *The Annals of Mathematical Statistics*, 29:610611.

Bozza, F., Fontana, G., Galloni, G., and Torella, E. (2007). 3D-1D analyses of the turbulent flow field, burning speed and knock occurrence in a turbocharged si engine. *Society of Automotive Engineers*, SAE Technical Paper 2007-24-0029.

Bozza, F., Siano, D., and Torella, E. (2009). Cycle-by-cycle analysis, knock modelling and spark-advance setting of a "Downsized" spark-ignition turbocharged engine. *Society of Automotive Engineers*, SAE Technical Paper 2009-24-0020.

Bradley, D., Hicks, R. A., Lawes, M., and Sheppard, C. G. W. (1998). The measurement of laminar burning velocities and markstein numbers for iso-octane-air and iso-octane-n-heptane-air mixtures at elevated temperatures and pressures in an explosion bomb. *Combustion and Flame*, 115:126–144.

Bradley, D., Hynes, J., Lawes, M., and Sheppard, C. G. W. (1988). Limitations to turbulence-enhanced burning rates in lean burn engines. *Proceedings of the Institution of Mechanical Engineers*, C46/88:17–24.

Bradley, D., Lau, A. K. C., and Lawes, M. (1992). Flame stretch rate as a determinant of turbulent burning velocity. *Philosophical Transactions of the Royal Society : Physical and Engineering Sciences*, 338(1650):359–387.

Bradley, D., Pan, J., and Sheppard, C. G. W. (1993). Turbulence and flow field effects. *Gas/Surface Interactions and Damaging Mechanisms in Knocking Combustion*, JOUE-00280-D(MB).

Bradley, D., Sheppard, C. G. W., Woolley, R., Greenhalgh, D. A., and Lockett, R. D. (2000). The development and structure of flame instabilities and cellularity at low markstein numbers in explosions. *Combustion and Flame*, 122:195–209.

Bray, K. N. C. (1980). *Turbulent Reacting Flows*. Springer-Verlag, New York, 1st edition.

Bruun, H. H. (1985). *Hot-Wire Anemometry: Principles and Signal Analysis*. Oxford University Press, New York, 2nd edition.

Burluka, A. A., El-Dein Hussin, A. M., Ling, Y. Z., and Sheppard, C. G. W. (2012a). Effects of large-scale turbulence on cyclic variability in spark-ignition engines. *Experimental Thermal and Fluid Science*, 43:13–22.

Burluka, A. A., Liu, K., Sheppard, C. G. W., Smallbone, A., and Woolley, R. (2012b). The influence of simulated residual and NO concentrations on knock onset for PRFs and gasolines. *Society of Automotive Engineers*, SAE Technical Paper 2004-01-2998.

Cairns, A. (2001). *Turbulent Flame Development in a Spark Ignition Engine*. PhD thesis, Department of Mechanical Engineering, The University of Leeds.

Chen, C. and Riley, J. J. (1991). A study of favre averaging in turbulent flows with chemical reaction. *Combustion and Flame*, 87:257–277.

Chun, K. M., Heywood, J. B., and C., K. J. (1988). Prediction of knock occurence in a spark ignition engine. *Twenty-Second Symposium (int) on Combustion*, pages 455–463.

Conway, G. (2010). *High Pressure Autoignition Modelling in S.I. Engines - Transfer Report*. Department of Mechanical Engineering, The University of Leeds.

Cowart, J. S., Keck, J. C., Heywood, J. B., Westbrook, C. K., and Pitz, W. J. (1990). Engine knock predictions using a fully-detailed and a reduced chemical kinetic mechanism. *Twenty-Third Symposium (Int) on Combustion*, pages 1055–1062.

Cox, R. A. and Cole, J. A. (1985). Chemical aspects of the auto-ignition of hydrocarbon-air mixtures. *Combustion and Flame*, 60:109–123.

Cruz, P., Vianna, J., and Moreira, C. S. (2003). Study of the turbulence intensity variation within the combustion chamber of an S.I engine due to turbocharging. *Society of Automotive Engineers*, SAE Technical Paper 2003-01-3687.

Dahl, D., Andersson, M., and Denbratt, I. (2011). The origin of pressure waves in high load HCCI combustion: A high-speed video analysis. *Combustion Science and Technology*, 183:11:1266–1281.

Dahnz, C. and Spicher, U. (2010). Irregular combustion in supercharged spark ignition engines- pre-ignition and other phenomena. *International Journal of Engine Research*, 11:485–499.

Dai, W. Trigui, N. and Lu, Y. (1995). Modeling of cyclic variations in spark-ignition engines. *Society of Automotive Engineers*, SAE Technical Paper 2000-01-2036.

Dai, W., Davis, C. D., Hall, M. J., and Matthews, R. D. (1995). Diluents and lean mixture combustion modelling for si engines with a quasi-dimensional model. *Society of Automotive Engineers*, SAE Technical Paper 952382.

Darabiha, N., Candel, S. M., and Marble, F. E. (1986). The effect of strain rate on a premixed laminar flame. *Combustion and Flame*, 64:203–217.

Darrieus, G. (1938). Propagation d'un front de flamme: Assai de théorie des vitesses anomalies de déflagration par developpment spantané de la turbulencel. *Presented at the 6th int. Cong. Appl. Mech.*, Paris.

Dawood, A. (2010). *Combustion and Flow Characteristics in a Disc-Shaped Spark Ignition Engine*. PhD thesis, Department of Mechanical Engineering, The University of Leeds.

Desoky, A. (1981). *An experiental and theoretical study of the combustion process in a divided chamber spark ignition engine*. PhD thesis, Department of Mechanical Engineering, The University of Leeds.

Douaud, A. M. and Eyzat, P. (1978). Four-octane-number method for prediction the anti-knock behaviour of fuels and engines. *Society of Automotive Engineers*, SAE Technical Paper 780080.

Ferguson, R. C. and Kirkpatrick, T. A. (2001). *Internal Combustion Engines: Applied Thermosciences*. John Wiley & Sons, New York, 2nd edition.

Fieweger, K., Blumenthal, R., and Adometi, G. (1997). Self-ignition of s.i. engine model fuels: A shock tube investigation at high pressure. *Combustion and Flame*, 109:599–619.

Fluent (2006). User's guide version 6.3. Technical report, Fluent. Page 287.

Fraser, R. and Bracco, F. (1989). Cycle-resolved ldv integral length scale measurements in an IC engine. *Society of Automotive Engineers*, SAE Technical Paper 890615.

Gamma-Technologies (2012). Gt-suite engine simulation application manual 7.3. Technical report, Gamma Technologies.

Gao, Z., Wu, X., Huang, Z., Yoshiyama, S., Tomita, E., Tamazaki, Y., and Higashi, T. (2012). The interdependency between the maximal pressure and ion current in a spark-ignition engine. *International Journal of Engine Research*, 14(4):320–332.

Ghandi, J. B., Herold, R. E., Shaka, J. S., and Strand, T. E. (2005). Time resolved particle image velocimetry measurements in an internal combustion engine. *Society of Automotive Engineers*, SAE Technical Paper 2005-01-3868.

Gillespie, L., Lawes, M., Sheppard, C. G. W., and Woolley, R. (2000). Aspects of laminar and turbulent burning velocity relevant to si engines. *Society of Automotive Engineers*, SAE Technical Paper 2000-01-0192.

Glassman, I. and Yetter, R. A. (2008). *Combustion*. Elsevier, California, 4th edition.

Gosman, A. (2012). Progress on LES using Star-CD. Japan Star Conference.

Griffiths, J. F. and Barnard, J. A. (1995). *Flame and Combustion*. Blackie Academic & Professional, Glasgow, 3rd edition.

Gürbüz, H., Buran, D., and Akçay.I (2013). An experimental study on performance and cyclic variations in a spark ignition engine fuelled with hydrogen and gasoline. *Journal of Thermal Science and Technology*, 33:33–41.

Hall, M. J. and Bracco, F. V. (1987). A study of velocities and turbulence intensities measured in firing and motored engines. *Society of Automotive Engineers*, SAE Technical Paper 870453.

Halstead, M. P., Kirsch, L. J., and Quinn, C. P. (1977). The autoignition of hydrocarbon fuels at high temperatures and pressures fittings of a mathematical model. *Combustion and Flame*, pages 45–60.

Halstead, M. P., Kirsch, L. J., Quinn, C. P., and Prothero, A. (1975). A mathematical model for hydrocarbon autoignition at high pressures. *The Royal Society, Mathematical and Physical Sciences*, 346(1647):515–538.

Hao, Z., Yan, J., and Yang, C. (2007). Study of engine noise based on independent component analysis. *Jzus*, 8(5):772–777.

Haq, M., Sheppard, C. G. W., and Woolley, R. (2002). Wrinkling and curvature of laminar and turbulent premixed flames. *Combustion and Flame*, 131:1–15.

Hattrell, T. (2007). *A Computational and Experimental Study of Spark Ignition Combustion*. PhD thesis, Department of Mechanical Engineering, The University of Leeds.

Hattrell, T. (2009). Ggeom. Technical manual, University of Leeds.

Heim, D. and Ghandhi, J. (2011). A detailed study of in-cylinder flow and turbulence using PIV. *Society of Automotive Engineers Int. J. Engines*, 4:1642–1668.

Heravi, H. M., Azarinfar, A., Kwon, S. I., and Bowen, P. J. (2007). Determination of laminar flame thickness and burning velocity of methane-air mixture. *ECM*, Third European Combustion Meeting:1–6.

Heywood, J. B. (1988). *Internal Combustion Engine Fundamentals*. McGraw-Hill, New York, international edition edition.

Hill, P. G. (1988). Cyclic variations and turbulence structure in spark-ignition engines. *Combustion and Flame*, 72:73–89.

Hill, P. G. and Zhang, D. (1994). The effects of swirl and tumble on combustion in spark-ignition engines. *Prog Energy Combus Sci*, 20:373–429.

Hinze, J. (1975). *Turbulence: an introduction to its mechanism and theory*. McGraw-Hill, New York, 2nd edition.

Hong, C. W. and Chen, D. G. (1997). Direct measurements of in-cylinder integral length scales of a transparent engine. *Experiments in Fluids*, 23:113–120.

Hülser, T., Grünefeld, G., and Brands.T. (2013). Optical investigation on the origin of pre-ignition in a highly boosted si engine using bio-fuels. *Society of Automotive Engineers*, SAE Technical Paper 2013-01-1636.

Hussin, A. (2012). *New and Renewable Energy:Renewable Fuels in Internal Combustion Engines*. PhD thesis, Department of Mechanical Engineering, The University of Leeds.

Hynes, J. (1986). *A Computational and Experimental Study of Spark Ignition Combustion*. PhD thesis, Department of Mechanical Engineering, The University of Leeds.

Ishima, T., Obokata, T., Nomura, T., and Takahashi, Y. (2008). Analysis on in-cylinder flow by means of LDA, PIV and numerical simulation under steady state flow condition. *Society of Automotive Engineers*, SAE Technical Paper 2008-01-1063.

James, H. (1987). Laminar burning velocities of iso-octane-air mixtures a literature review. *Society of Automotive Engineers*, SAE Technical Paper 870170.

Jerzembeck, S., Peters, N., Pepiot-Desjarins, P., and Pitsch, H. (2009). Laminar burning velocities at high pressure for primary reference fuels and gasoline: Experimental and numerical investigation. *Combustion and Flame*, 156:292–301.

Kalghatgi, G. (2001a). Fuel anti-knock quality - part i. engine studies. *Society of Automotive Engineers*, SAE Technical Paper 2001-01-3584.

Kalghatgi, G. (2001b). Fuel anti-knock quality- part ii. vehicle studies - how relevant is motor octane number (MON) in modern engines? *Society of Automotive Engineers*, SAE Technical Paper 2001-01-3585.

Kalghatgi, G. (2004). The available and required auto-ignition quality of gasoline-like fuels in hcci engines at high temperatures. *Society of Automotive Engineers*, SAE Technical Paper 2004-01-1969.

Kalghatgi, G. (2005). Auto-ignition quality of practical fuels and implications for fuel requirements of future SI and HCCI engines. *Society of Automotive Engineers*, SAE Technical Paper 2005-01-0239.

Kalghatgi, G. and Bradley, D. (2012). Pre-ignition and 'super-knock' in turbo-charged spark-ignition engines. *International Journal of Engine Research*, 0:1–16.

Karlovitz, B., Denniston, D. W., Knapschaffer, D. H., and Wells, F. E. (1953). Studies on turbulent flames : A. flame propagation across velocity gradients b. turbulence measurement in flames. *Symposium (International) on Combustion*, 4:613–620.

Keck, J. C., Heywood, J. B., and Noske, G. (1987). Early flame development and burning rates in spark ignition engines and their cyclic variability. *Society of Automotive Engineers*, SAE Technical Paper 870164.

Khan, A, F. (2013). *Chemical kinetics models for autoignition of modern fuels in strongly boosted engines- thesis in preparation*. PhD thesis, Department of Mechanical Engineering, The University of Leeds.

Kobayashi, H., Nakashina, T., Tamura, T., Maruta, K., and Niioka, T. (1997). Turbulence measurements and observations of turbulent premixed flames at elevated pressure up to 3.0mpa. *Combustion Institute*, 108(1-2):104–110.

Konig, G. and Sheppard, C. G. W. (2004). End gas autoignition and knock in a spark ignition engine. *Society of Automotive Engineers*, SAE Technical Paper 902135.

Lake, T., Stokes, J., Murphy, R., Osborne, R., and Schamel, A. (2004). Turbocharging concepts for downsized D.I gasoline engines. *Society of Automotive Engineers*, SAE Technical Paper 2004-01-0036.

Landau, L. D. (1944). On the theory of slow combustion. *Acta Physiochim URSS*, 90:77–85.

Landry, L., Halter, F., Foucher, F., Samson, E., and Rousselle, C. (2008). Effect of pressure and dilution on flame front displacement in boosted spark-ignition engine combustion. *Society of Automotive Engineers*, SAE Technical Paper 2008-01-1625.

Langridge, S. (1995). *Imaging and thermodynamic analysis of autoignition and knock in SI engines*. PhD thesis, Department of Mechanical Engineering, The University of Leeds.

Larsson, G. (2009). *Turbulence Related Cyclic Variation in Combustion*. PhD thesis, Department of Mechanical Engineering, The University of Leeds.

Law, C. K. (2006). *Combustion Physics*. Cambridge University Press, Cambridge, 1st edition.

Lawes, M., Ormsby, M. P., Sheppard, C. G. W., and Woolley, R. (2012). The turbulent burning velocities of iso-octane/air mixtures. *Combustion and Flame*, 159:19491959.

Lecointe, B. and Monnier, G. (2003). Downsizing a gasoline engine using turbocharging with direct injection. *Progress in Energy and Combustion Science*, 28:1–74.

Ling, Z. (2011). *Characterization of Knock and Autoignition in a Boosted Spark Ignition Engine*. PhD thesis, Department of Mechanical Engineering, The University of Leeds - Ph.D. Transfer Report.

Ling, Z. (2013). *Characterization of Knock and Autoignition in a Boosted Spark Ignition Engine*. PhD thesis, Department of Mechanical Engineering, The University of Leeds - Ph.D. Thesis writing in progress.

Liou, T. and Santaviccia, D. (1983). Cycle resolved turbulence measurements in a ported engine with and without swirl. *Society of Automotive Engineers*, SAE Technical Paper 830419.

Liou, T. M., Hall, M., Santaviaa, D. A., and Bracco, F. V. (1984). Laser dopper velocimetry measurements in valve and ported engines. *Society of Automotive Engineers*, SAE Technical Paper 840375.

Lipatnikov, A. N. (2012). *Fundamentals of Premixed Turbulent Combustion*. CRC Press, Boca Raton, Florida, 1st edition.

Lipatnikov, A. N. and Chomiak, J. (1997). A simple model of unsteady turbulent flame propagation. *Society of Automotive Engineers*, SAE Technical Paper 972993.

Lipatnikov, A. N. and Chomiak, J. (1998). Randomness of flame kernel development in turbulent gas mixture. *Society of Automotive Engineers*, SAE Technical Paper 982617.

Lipatnikov, A. N. and Chomiak, J. (2000). Modeling of pressure and non-stationary effects in spark-ignition engine combustion: A comparison of different approaches. *Society of Automotive Engineers*, SAE Technical Paper 2000-01-2034.

Lipatnikov, A. N. and Chomiak, J. (2002). Turbulent flame speed and thickness: phenomenology, evaluation and application in multi-dimensional applications. *Progress in Energy and Combustion Science*, 28:1–74.

Liu, K. (2004). LUSIE manual. Technical manual, University of Leeds.

Liu, K., Burluka, A. A., and Sheppard, C. G. W. (2013). Turbulent flame and mass burning rate in a spark ignition engine. *The Science and Technology of Fuel and Energy*, 107:202–208.

Livengood, J. C. and Wu, P. C. (1955). Correlation of autoignition phenomenon in internal combustion engines and rapid compression machines. *Proceedings of Fifth International Symposium on Combustion*, page 347.

Lotus (Accessed 15 May 2013). Ultra Boost for Economy. `http://lotusproactive.wordpress.com/2012/05/07/ultra-boost-for-economy`.

Lumley, J. L. (2006). *Engines: An Introduction*. Cambridge University Press, Cambridge, 1st edition.

Mallard, E. and Le Chatelier, L. H. (1883). *Annal of Mines*, 4:379–568.

Mandilas, C. (2008). *Laminar and Turbulent Burning Characteristics of Hydrocarbon Fuels*. PhD thesis, Department of Mechanical Engineering, The University of Leeds.

Marsaglia, G. and Bray, T. A. (1964). A convenient method for generating normal variables. *SIAM Journal on Scientific and Statistical Computing*, 6:260–264.

Marsaglia, G. and Tsang, W. W. (1984). A fast, easily implemented method for sampling from decreasing or symmetric unimodal density functions. *SIAM Journal on Scientific and Statistical Computing*, 5:349–359.

Marshak, A. and Davis, A. e. (2005). *3D Radiative Transfer in Cloudy Atmospheres*. Springer Berlin Heidelberg, New York, 1st edition.

Matekunas, F. A. (1983). Modes and measures of cyclic combustion variability. *Society of Automotive Engineers*, SAE Technical Paper 830337.

Merdijani, S. and Sheppard, C. G. W. (1993). Gasoline engine cycle simulation using the leeds turbulent burning velocity correlations. *Society of Automotive Engineers*, SAE Technical Paper 932640.

Metghalchi, M. and Keck, J. C. (1980). Laminar burning velocity of propane-air mixtures at high temperature and pressure. *Combustion and Flame*, 38:143–154.

Metghalchi, M. and Keck, J. C. (1982). Burning velocities of mixtures of air with methanol, isooctane, and indolene at high pressure and temperature. *Combustion and Flame*, 48:191–210.

Minter, A. H. and Spangler, S. R. (1996). Observation of turbulent fluctuations in the interstellar plasma density and magnetic field on spatial scales of 0.01 to 100 parsecs. *Astrophysical Journal*, 458:194.

Mittal, V. and Heywood, J. B. (2008). The relevance of fuel RON and MON to knock onset in modern SI engines. *Society of Automotive Engineers*, SAE Technical Paper 2008-01-2414.

Mittal, V. and Heywood, J. B. (2009). The shift in relevance of fuel RON and MON to knock onset in modern SI engines over the last 70 years. *Society of Automotive Engineers*, SAE Technical Paper 2009-01-2622.

Miyamoto, K., Hoshiba, Y., and Hosono, K. (2006). Enhancement of combustion by means of squish pistons. *Mitsubishi Motors Technical Review*, Edition 18.

Morel, T. and Mansour, N. N. (1982). Modelling of turbulence in internal combustion engines. *Society of Automotive Engineers*, SAE Technical Paper 820040.

Muller, U. C., Bollig, M., and Peters, N. (1997). Approximations for burning velocities and markstein numbers for lean hydrocarbon and methanol flames. *Combustion and Flame*, 108:349–356.

Nomura, H., Kawasumi, I., Ujiie, Y., and Sata, J. (2007). Effects of pressure on flame propagation in a premixture containing fine fuel droplets. *Proc. Combustion Institute*, 31(2):2133–2140.

Ormsby, M. (2005). *Turbulent flame development in a high-pressure combustion vessel*. PhD thesis, Department of Mechanical Engineering, The University of Leeds.

Ozdor, N., Dulger, M., and Sher, E. (1994). Cyclic variability in spark ignition engines a literature survey. *Society of Automotive Engineers*, SAE Technical Paper 940987.

Peters, N. and Kerschgens, B. (2103). Super-knock prediction using a refined theory of turbulence. *Society of Automotive Engineers*, SAE Technical Paper 2013-01-1109.

Poulos, S. G. and Heywood, J. B. (1983). The effect of chamber geometry on spark-ignition engine combustion. *Society of Automotive Engineers*, SAE Technical Paper 830334.

Pulkrabeck, W. W. (2004). *Engineering Fundamentals of the Internal Combustion Engine*. Pearson Prentice-Hall, Glasgow, 2nd edition.

Ramajo, D., Zanotti, A., and Nigro, N. (2007). Assessment of a zero-dimensional model of tumble in four valve high performance engine. *International Journal of Numerical Methods for Heat & Fluid Flow*, 17:770–787.

Rao, R. S. V. (2010). *Computational Fluid Dynamics*, pages 285–305. Intech, 1st edition.

Reynolds, A. J. (1974). *Turbulent Flows in Engineering*. John Wiley & Sons Ltd., London, 1st edition.

Rhodes, D. B. and Keck, J. C. (1985). Laminar burning speed measurements of indolene-air-diluent mixtures at high pressure and temperatures. *Society of Automotive Engineers*, SAE Technical Paper 850047.

Rimmer, J. E. T., Long, E. J., P., G. C., Hargrave, G. K., Richardson, D., and Wallace, D. (2009). The influence of single and multiple injection strategies on in-cylinder flow and combustion within a disi engine. *Society of Automotive Engineers*, SAE Technical Paper 2009-01-0660.

Roberts, P. (2010). *Fuel and Exhaust Residual Effects in Spark Ignition and HCCI engines.* PhD thesis, Department of Mechanical Engineering, The University of Leeds.

Roberts, P. and Sheppard, C. G. W. (2013). The influence of residual gas no content on knock onset of iso-octane, prf, trf and ulg mixtures in si engines. *SAE International Journal of Engines*, SAE Technical Paper 13JENG-0068.

Ryan, T. W. I. and Lestz, S. S. (1980). The laminar burning velocity of isooctane,n-heptane,methanol,methane, and propane at elevated temperature and pressures in the presence of a diluent. *Society of Automotive Engineers*, SAE Technical Paper 800103.

Samuel, S., Moreey, D., Whelan, I., and Hassaneen, A. (2010). Combustion characteristics and cycle-by-cycle variation in a turbocharged-intercooled gasoline direct-injected engine. *Society of Automotive Engineers*, SAE Technical Paper 2010-01-0348.

Sandford, M., Page, G., and Crawford, P. (2009). The all new AJV8. *Society of Automotive Engineers*, SAE Technical Paper 2009-04-20.

Scott, M, J. (1992). *Distributions of strain rate and temperature in turbulent combustion*. PhD thesis, Department of Mechanical Engineering, The University of Leeds.

Semenov, N. N. (1935). *Chemical Kinetics and Chain Reaction*. The Clarendon Press, Oxford, 1st edition.

Shahbakhti, M., Lupul, R., and Koch, C. (2007). Predicting HCCI auto-ignition timing by extending a modified knock-integral method. *Society of Automotive Engineers*, SAE Technical Paper 2007-01-0222.

Shahed, S. M. and Bauer, K. H. (2009). Parametric studies of the impact of turbocharging on gasoline engine downsizing. *Society of Automotive Engineers*, SAE Technical Paper 2009-01-1472.

Sheppard, C. G. W., Tolegano, S., and Woolley, R. (2002). On the nature of autoignition leading to knock in HCCI engines. *Society of Automotive Engineers*, SAE Technical Paper 2002-01-2831.

Sjeric, M., Kozarac, D., and Bogensperger, M. (2012). Implementation of a single zone $k-\epsilon$ turbulence model in a multi-zone combustion model. *Society of Automotive Engineers*, SAE Technical Paper 2012-01-0130.

Smallbone, A. (2004). *Fuel and Residual Effects in Spark Ignition Engines*. PhD thesis, Department of Mechanical Engineering, The University of Leeds.

Sokolik, A. S. (1963). *Self-Ignition Flame and Detonation in Gases*. Israel Program for Scientific Translations, Jerusalem, 1st - translated from russian edition.

Soltau, J. P. (1960). Cylinder pressure variations in petrol engines. *Institution of Mechanical Engineers*, pages 99–116.

Sounasis, J. (Accessed 23 June 2013). World vehicle population tops 1 billion units. `http://wardsauto.com/ar/world_vehicle_population_110815`.

Stokes, J., Osborne, R., and A.Lake, T. (2000). A gasoline engine concept for improved fuel economy - the lean boost system. *Society of Automotive Engineers*, SAE Technical Paper 2000-01-2902.

Stone, C. R. (1999). *Introduction to Internal Combustion Engines*. Palgrave Macmillan, New York, 3rd edition.

Syed, I. Z., Abhijit, Y., Naber, J. D., and Michalek, D. (2010). Numerical investigation of laminar flame speed of gasoline-ethanol-air mixtures with varying pressure,temperature and dilution. *Society of Automotive Engineers*, SAE Technical Paper 2010-01-0620.

Tabaczynski, R. J. (1976). Turbulence and turbulent combustion in spark-ignition engines. *Progress in Energy and Combustion Science*, pages 143–165.

Tabaczynski, R. J., Ferguson, C. R., and Radhakrishnan, K. (1977). A turbulent entrainment model for spark-ignition engine combustion. *Society of Automotive Engineers*, SAE Technical Paper 770647.

Tabaczynski, R. J., Trinker, F. H., and Shannon, B. A. S. (1980). Further refinement and validation of a turbulent flame propagation model for spark-ignition engine. *Combustion and Flame*, 39:111–121.

Tennekes, H. and Lumley, J. L. (1972). *A First Course in Turbulence*. MIT, Cambridge, MA, 1st edition.

Tripathi, N. (2012). *Dynamics of Confined Premixed Laminar Explosion Flames*. PhD thesis, Department of Mechanical Engineering, The University of Leeds.

Turns, S. R. (2000). *An Introduction to Combustion: Concepts and Applications*. McGraw-Hill, New York, 2nd edition.

Verhelst, S. and Sheppard, C. G. W. (2009). Multi-zone thermodynamic modelling of spark-ignition engine combustion - an overview. *Energy Conversation and Management*, 509:1326–1335.

Versteed, H. K. and Malalasekera, W. (2007). *An Introduction to Computational Fluid Dynamics, The Finite Volume Method, second edition.* Pearson Education, Glasgow, 2nd edition.

Vibe, I. (1964). Halbempirishe formel dur die verbrennungsgeschwindigkeit, in krafstoffaufbereitung und verbrennung bei dieselmotoren. *Springer Verlag*, pages 156–159.

Vressner, A., Lundin, A., Christense, M., Tunestoal, P., and Johansson, B. (2003). Pressure oscillations during rapid HCCI combustion. *Society of Automotive Engineers*, SAE Technical Paper 2003-01-3217.

Woschni, G. (1967). A universally applicable equation for the instantaneous heat transfer coefficient in the internal combustion engine. *Society of Automotive Engineers*, SAE Technical Paper 670931.

Wu, C. M., Roberts, C. E., Matthers, R. D., and Hall, M. J. (1993). Effects of engine speed on combustion in si engines: Comparison of predictions of a fractal burning model with experimental data. *Society of Automotive Engineers*, SAE Technical Paper 932714.

Yelvington, P. E. and Green, W. H. (2003). Prediction of the knock limit and viable operating range for a homogeneous-charge compression-ignition (HCCI) engine. *Society of Automotive Engineers*, SAE Technical Paper 2003-01-1092.

Zahdeh, A., Rothenberger, P., Nguyen, W., Anbarasu, M., Schmuch-Solda, S., Schaefer, J., and T., G. (2011). Fundamental approach to investigate pre-ignition in boosted SI engines. *Society of Automotive Engineers*, SAE Technical Paper 2011-01-0340.

Zeldovich, Y. B., Barenblatt, G. I., Librovich, V. B., and Makhviladze, G. M. (1985). *Mathematical Theory of Combustion and Explosions*. Consultants Bureau, New York, 1st - translated from russian edition.

Zel'dovich, Y. B. and Frank-Kamenetskii, D. A. (1938). A theory of thermal flame propagation. *Acta Physicochem*, 9:341–346.

Zhao, Z., Conley, J., Kazakov, A., and Dryer, F. (2003). Burning velocities of real gasoline fuel at 353 k and 500 k. *Society of Automotive Engineers*, SAE Technical Paper 2003-01-3265.

Zheng, J. (2001). Prediction of pre-ignition reactivity and ignition delay for HCCI using a reduced chemical kinetic model. *Society of Automotive Engineers*, SAE Technical Paper 2001-01-1025.

Zimont, V. L. (1979). Theory of turbulent combustion on a homogeneous fuel mixture at high reynolds numbers. *Combustion, Explosions & Shockwaves*, 15:305–311.

Zolfagharifard, E. (Accessed 15 May 2013). "burning desire: The Ultra Boost project". *http://www.theengineer.co.uk/burning-desire-the-ultra-boost-project/1006277.article*.